MICROSTRUCTURE EVOLUTION DURING HOMOGENIZATION AND ITS EFFECT ON THE HIGH TEMPERATURE DEFORMATION BEHAVIOUR IN AA6082 BASED ALLOYS

by

Chenglu Liu

M.ASc., Chongqing University, 2011

B.ASc., Chongqing University, 2008

A THESIS SUBMITTED IN PARTIAL FULFILLMENT OF

THE REQUIREMENTS FOR THE DEGREE OF

DOCTOR OF PHILOSOPHY

in

THE FACULTY OF GRADUATE AND POSTDOCTORAL STUDIES

(MATERIALS ENGINEERING)

THE UNIVERSITY OF BRITISH COLUMBIA

(Vancouver)

November 2017

Abstract

There is a current trend in increased use of aluminum extrusion alloys in automotive applications. This trend is driven by the need to reduce the vehicle weight, which in turn, is to decrease energy use and/or emissions of the vehicles. In this work, Al-Mg-Si alloys, and especially variants of AA6082 with different Mn and/or Cr additions have been studied.

The objectives of the study are to i) experimentally characterize the evolution of the constituent particles (phase, volume fraction and size) and dispersoids (chemistry, crystal structure, size and volume fraction), ii) rationalize the mechanisms of dispersoid evolution and iii) develop a physically based constitutive law for the high temperature flow stress.

The characterization of microstructure evolution during homogenization was done using a combination of i) transmission electron microscopy, ii) field emission gun scanning electron microscopy, iii) electron microprobe microanalysis and iv) electrical resistivity measurements. The high temperature flow stress was characterized by uniaxial compression tests.

The main results on microstructure evolution during the process of homogenization show that i) there is a transformation of the constituent particles from the β to α phase during homogenization and a concurrent speriodization of the particles, ii) dispersoids with the size range of 20-200 nm and a volume fraction of 0.25 – 1.3 % are initially formed during homogenization but they eventually dissolve as Mn is transported to the constituent particles and iii) a steady-state flow stress of between 20 and 45 MPa was measured for the test temperature between 550 °C and 580 °C with strain rates of 0.1 – 10 s^{-1}.

The evolution of dispersoids during homogenization was rationalized by considering their nucleation, growth and coarsening. It is proposed that dispersoid coarsening initially involves

long-range diffusion of Fe from the constituent particles to dispersoids and later Mn and Fe diffuse to the constituent particles. The Kocks-Chen constitutive model was extended to include the role of dispersoids on high temperature flow stress using an Orowan type model for precipitation hardening. This was found to predict the flow stress ± 5 % in ≈ 95 % of the cases that were studied.

Lay Summary

There is currently a large interest to replace steel components with aluminum in automobiles to decrease vehicle weight and thereby reduce their environmental impact. This work focuses on changes in a commonly used alloy during the homogenization heat treatment. Heat treatment is an important process to improve the ability for the alloy to be manufactured and its final strength. A systematic experimental study has been conducted to study how alloy additions affect the structure during the homogenization heat treatment and the high temperature strength of the alloy. The main findings of this work were that the precipitation of manganese containing particles during homogenization is closely related to the iron in the alloy which was confirmed experimentally and through the use of mathematical model. Finally, the high temperature strength was found to be related to manganese precipitation and a mathematical model to describe this behaviour was developed and validated.

Preface

The majority of this work was conducted and completed by Chenglu Liu at The University of British Columbia. The TEM work has been conducted in collaboration with Dr. Xiang Wang at McMaster University, where the material for TEM samples was provided by Chenglu Liu and the operation of the TEM and indexing of the selected area diffraction (SAD) patterns was done by Dr. Xiang Wang. The quantitative X-ray diffraction (XRD) work on the constituent particles was conducted in collaboration with Dr. Zhijun Zhang at the University of British Columbia, where the samples were provided by Chenglu Liu and the dissolution and extraction for the constituent particles were performed together with Dr. Zhijun Zhang. The XRD quantitative analysis was done using the Reitveld method with the help of Dr. Mati Raudsepp at the department of Earth and Ocean Sciences at UBC. Finally, the homogenization modeling work was done in collaboration with Dr. Qiang Du at SINTEF, Norway. The multi-component homogenization model was developed for AA3xxx alloys by Dr. Qiang Du. The application to AA6xxx alloys in the current study was done with his assistance.

Some of the experimental results and discussion have been published in the following journals:

[1] **C.L. Liu**, H. Azizi-Alizamini, N.C. Parson, W.J. Poole, Q. Du, Microstructure evolution during homogenization of Al-Mg-Si-Mn-Fe alloys: Modelling and experimental results, Trans. Nonferrous Met. Soc. China. 27 (2017) 747–753.

[2] **C.L. Liu**, H. Azizi-Alizamini, N.C. Parson, W.J. Poole, The effect of Mn on microstructure evolution during homogenization of Al-Mg-Si-Mn alloys, Mater. Sci. Forum. 794–796 (2014) 1199–1204.

Table of Contents

List of Tables

List of Figures

List of Symbols

Symbols	Definitions/Values
A	Pre-exponential diffusion constant (s^{-1})
b	temperature dependent Burger's vector (m)
$C^{at.}_{Al,disp.}$	estimated concentration of Al in dispersoids (at.%)
$C^{at.}_{Cr,disp}$	estimated concentration of Cr in dispersoids (at.%)
$C^{wt.}_{Cr,matrix}$	estimated concentration of Cr in Aluminum matrix (wt.%)
$C^{at.}_{Fe,disp.}$	estimated concentration of Fe in dispersoids (at.%)
$C^{at.}_{Mn,disp.}$	estimated concentration of Mn in dispersoids (at.%)
$C^{wt.}_{Mn,disp.}$	estimated concentration of Mn in dispersoids (wt.%)
$C^{wt.}_{Mn,matrix}$	estimated concentration of Mn in Aluminum matrix (wt.%)
$C^{wt.}_{Mn,S.S}$	estimated concentration of Mn in solid solution (wt.%)
$C^{at.}_{Si,disp.}$	estimated concentration of Si in dispersoids (at.%)
D	diffusion coefficient (m^2s^{-1})
d	diameter (mm)
f_{disp}	volume fraction of dispersoids
$f^{disp.}_{Al(FeMn)Si}$	volume fraction of Al(FeMn)Si dispersoids
$f^{disp.}_{Al(FeMnCr)Si}$	volume fraction of Al(FeMnCr)Si dispersoids
$f_{\alpha\text{-Al(MnFe)Si},eq}$	volume fraction of Al(FeMn)Si from equilibrium calculation

$f_{\alpha\text{-Al(MnFe)Si},Scheil}$	volume fraction of Al(FeMn)Si from Scheil calculation
$f_{\alpha\text{-AlFeSi},Scheil}$	volume fraction of α-AlFeSi from Scheil calculation
$f_{\beta\text{-AlFeSi},Scheil}$	volume fraction of β-AlFeSi from Scheil calculation
$K_{Mn,S.S}^{wt.}$	Constant which relates S.S. contribution to amount of Mn
$K_{Cr,S.S}^{wt.}$	Constant which relates S.S. contribution to amount of Cr
k	Boltzmann constant ($Pa \cdot m^3 K^{-1}$)
M	Taylor factor
Q	activation energy ($kJ \cdot mol^{-1}$)
R	universal gas constant ($Jmol^{-1}K^{-1}$)
r	average particle radius
T	temperature (K)
V_{molar}^{Al}	molar volume of aluminum
$V_{molar}^{disp.}$	molar volume of dispersoids
$V_{disp.}$	estimation of volume fraction of dispersoids
$V_{eq.}$	volume fraction of particles from equilibrium calculation
V_{scheil}	volume fraction of particles from Scheil calculation
$\dot{\varepsilon}$	strain rate (s^{-1})
θ	the angle between Burgers vector and dislocation line
μ	temperature dependent shear modulus (GPa)
ν	Poisson's ratio

ρ	measured resistivity (nΩ·m)
$\rho_{solutes}$	solid solution component of resistivity (nΩ·m)
$\rho_{thermal}$	thermal component of resistivity (nΩ·m)
$\rho_{dislocations}$	dislocation component of resistivity (nΩ·m)
$\rho_{precipitation}$	precipitation component of resistivity (nΩ·m)
$\rho_{grainboundaries}$	grain boundary component of resistivity (nΩ·m)
ρ_{base}	base measured resistivity for 0Mn alloy (nΩ·m)
σ_0	base athermal stress (MPa)
$\sigma_{athermal}$	athermal stress (MPa)
σ_{flow}	steady state flow stress (MPa)
σ_{Orowan}	Orowan stress (MPa)
σ_{ppt}	athermal stress caused by dispersoids (MPa)
$\sigma_{ppt(HT)}$	athermal stress caused by dispersoids at high temperature (MPa)
$\sigma_{thermal}$	thermal stress (MPa)
τ	shear stress (MPa)

List of Abbreviations

BCC	Body Center Cubic
BSE	Backscattered Electron
CALPHAD	Computer Coupling Phase Diagrams
DC	Direct Chill
EDS	Energy Dispersive X-ray spectroscopy
EPMA	Electron Probe Micro Analysis
FCC	Face Center Cubic
FE	Finite Element
FEGSEM	Field Emission Gun Scanning Electron Microscope
HAABF	High Angle Annular Bright Field
SADP	Selected Area Diffraction Pattern
SC	Simple Cubic
SDAS	Secondary Dendrite Arm Spacing
TEM	Transmission Electron Microscope
WDS	Wavelength Dispersive Spectroscopy
XRD	X-ray Diffraction

Acknowledgements

In the first and foremost, I would like to express my sincere gratitude to my supervisor Dr. Warren Poole for guiding me step-by-step for years while enlightening me with his vast knowledge throughout the course of the Ph.D. project.

My gratitude also goes to the industry collaborator Dr. Nick Parson from Arvida Research & Development Centre (ARDC) of Rio Tinto and the academic collaborators Dr. Mary Wells at the University of Waterloo and my co-supervisor Dr. Qiang Du from SINTEF, Norway for their continuous encouragements and suggestions for my career planning.

My special thanks go to Dr. Hamid Azizi-Alizamini, Dr. Xiang Wang and Dr. David Embury at McMaster University for the invaluable support and comments that they provided me with in the past few years.

I would also like to mention the professional help that I received from the staff at UBC, especially the technicians Ross Mcleod, Carl Ng and David Torok at the machine shop, Jacob Kabel the SEM technician, and Dr. Mati Raudsepp and Edith Czech from the department of Earth and Ocean.

I would like to thank the UBC microstructure group members from the last few years, including Dr. Thomas Garcin, Dr. Zhijun Zhang, Dr. Qingquan Lai and Jingqi Chen for providing help and ideas in the experiments and discussions.

I am very fortunate to have Rui Zhai, my girlfriend study together with me at UBC. She brought me immense joy, happiness and hope during all the years that we lived at Vancouver. I would also like to express my heartfelt gratitude to my father Keliang Liu and my mother Xiaoping Yu for their endless and unconditional support.

Finally, I am deeply honored by the financial support that I received from the China Scholarship Council (CSC) during my Ph.D. studies at UBC.

1. Introduction

Aluminum alloys belong to the group of the most used metals in our daily lives and find many applications in the packaging, automotive and aerospace sectors [1–8]. There are two main categories of aluminum alloys in terms of processing, i.e. cast alloys and wrought alloys. Cast aluminum alloys are usually used to fabricate engines and wheels into complex shapes, such as engine blocks, cylinder heads and automotive wheels. Wrought alloys include extrusions, flat-rolled products and products for which applications include crash boxes, body panels and suspension components, respectively. Among the wrought alloys, AA6xxx alloys (Al-Mg-Si) are the preferred alloys with growing applications in the automobile industry. The reason why they have attracted applications in the field of transportation, is related to their excellent combination of high strength, low density, high extrudability and good resistance to corrosion. Driven by the ideal of replacement of steels by aluminum alloys to reduce weight in the automobile industry, aluminum producers are now emphasizing the manufacturing of these new, high value-added AA6xxx alloys. The automobile applications of AA6xxx alloys can be found in both rolled products as well as extrusions. Many complex aluminum components such as door sills and door pillars are produced using extrusion as the principal manufacturing process. AA6xxx alloys are good candidates for extrusion production because of their flexibility they display in producing complex shapes. The aluminum alloy, AA6082, is commonly used as extrusion alloy in automotive applications as a result of its good combination of formability and corrosion resistance [9,10].

Rio Tinto Aluminum, the industrial partner for this project, has a long-term vision to be a leader in the supply of advanced aluminum alloys to the ever-expanding automobile market. In

order to maintain the leading role in supplying high quality wrought aluminum alloys, Rio Tinto Aluminum has been collaborating closely with The University of British Columbia and the University of Waterloo, launching a through process modeling project for AA3xxx (Al-Mn) and AA6xxx alloys (Al-Mg-Si). With the successful completion of the through process model for AA3xxx alloys, the focus of the collaboration has currently shifted to AA6xxx alloys.

The general extrusion processing sequence for AA6xxx alloys involves direct chill (DC) casting, homogenization (a high temperature heat treatment at 500 – 600 °C), billet re-heating, high temperature extrusion (often combined with accelerated cooling), solution heat treatment (optional for many AA6xxx series alloys) and artificial aging [10]. The complex manufacturing route starts with the casting process including the precise addition of the alloying elements such as Mg and Si (for strengthening) and also some transition elements like Mn, Cr and Fe. These transition elements will result in the formation of micron-sized intermetallic particles known as constituent particles and dispersoids which are nanometers in size. The size, fraction and distribution of these particles will not necessarily strongly affect the strength of the final products at room temperature, but they do play a key role in i) controlling the grain structure during deformation, ii) influencing the high temperature deformation behaviour and iii) affecting the quench sensitivity. All of those considerations are of practical concern for the industry.

The microstructure [i.e. the grain structure, Mn/Cr dispersoids, (MgSi) precipitates and constituent particles] is controlled by both the processing parameters and the alloying additions. To tailor a suitable combination of physical and mechanical properties, a proper design of the microstructural features is required. Even though much work has been done on the homogenization heat treatments in the past, there is still a strong need from industry to have physically-based through process models available, so as to make predictions for the quantitative

microstructure features at a given chemistry and processing condition. The first requirement is to quantify the microstructure evolution in terms of the constituent particles and dispersoids with different Mn/Cr additions through various homogenization thermal cycles. The fast development of the modern characterization techniques has enabled a better quantification of the second phase particles from the nanometer scale to micrometer scale.

The ability to accurately measure the microstructure parameters is important for the calibration of analytical model for microstructure evolution during homogenization and also for the physically-based constitutive models for the high temperature deformation regime. Then, the models developed for the homogenization heat treatment can be used as the input for a constitutive model describing high temperature deformation behaviour. Finally, the new knowledge generated from this thesis will be passed on to the other team members, with the objective of producing an integrated through process model which the industry can use as a cost effective tool for the design of the high value added products.

2. Literature Review

2.1 Review of Al-Mg-Si (6xxx) alloys

Al-Mg-Si alloys (AA6xxx series) are widely used for extrusions, comprising up to 80 % of the Aluminum extruded shapes due to easy fabrication and good combination of mechanical properties and corrosion resistance [10,11]. A large body of literature related to 6xxx extrusion alloys has been generated in the past decades [11–24]. This review will focus on the role of the homogenization treatment after casting on extrusion and post-extrusion behaviour for the Al-Mg-Si based alloys. It is generally accepted that the microstructure goes through changes during homogenization such as i) the transformation of large constituent particles [25–27], ii) the formation of dispersoids [28–31] and iii) the precipitation/dissolution of precipitates [32,33] during homogenization remarkably influence the downstream extrusion behaviour and also the subsequent microstructure development [11,34,35]. The development of microstructure during homogenization and the effect on the final properties are affected by both the alloying elements and the heat treatment processes.

The structure of this review has been organized as follows: first, background information on AA6xxx alloys is briefly provided in terms of their chemical composition, extrusion route and mechanical properties; second, microstructure changes, including the constituent particles and dispersoids, associated with homogenization scenario and chemistry are reviewed; third, microstructure models developed for simulating homogenization are discussed; fourth, the constitutive laws proposed for high temperature flow behaviour are evaluated; and finally, the effect of homogenized microstructure on subsequent high temperature deformation behaviour is reviewed.

2.1.1 Chemical composition of AA6xxx alloys

AA6xxx alloys have Mg and Si as their main alloying elements, where Mg ranges from 0.20 to 1.20 wt.% and the Si content varies between 0.20 and 1.25 wt.% as shown in Figure 2.1. Mg and Si are added to form metastable Mg-Si precipitates which are the source of precipitation hardening in these AA6xxx alloys. The general accepted precipitation sequence is supersaturated solid solution→ GP zones → β" →β' →β [36]. More detailed High Resolution Transmission Electron Microscopy (HR-TEM) studies reveal the precipitation sequence are more complex in terms of the more classified metastable transitions, which is as follows SSSS→ Clusters → Co-Clusters, GP (Mg_4AlSi_6) → β" (Mg_5Si_6)→β' (Mg_9Si_5), B' ($Mg_9Al_3Si_7$), U1 ($MgAl_2Si_2$), U2 ($MgAl_2Si_2$) →β (Mg_2Si) [37,38]. The amount of Mg and Si additions determine the potential peak strength after the T6 heat treatment. Among the Al-Mg-Si alloys, AA6082 alloys are alloyed with higher levels of Si and Mg, and therefore are of higher strength for a similar heat treatment.

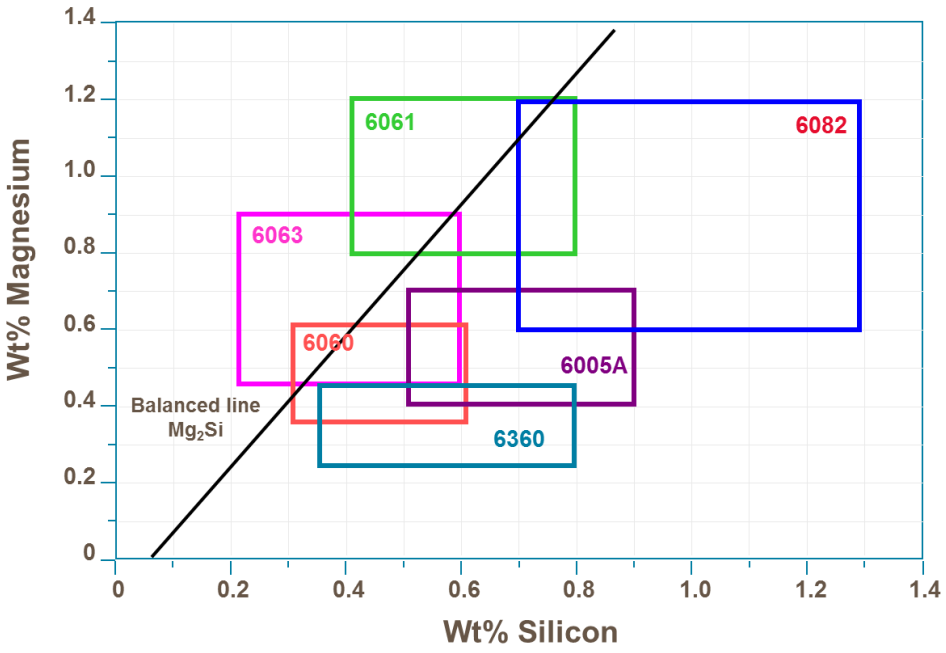

Figure 2-1 Chemical composition of major 6xxx series extrusion alloys (wt.%) [39]

In addition, the transition elements as Mn, Cr and Fe are usually in AA6xxx alloys. Typical upper limits for Mn, Cr and Fe are 0.5 wt.%, 0.2 wt.% and 0.3 wt.% respectively [24]. Fe is a common impurity found in Al, which has a low solubility and is typically observed as micron sized constituent particles [40,41]. Mn is added to form dispersoids, which modify the grain microstructure and influence the fracture properties [34,42]. Cr tends to form constituents or dispersoids together with Mn; these phases will also modify the recrystallization during the extrusion process.

2.1.2 The extrusion route of AA6xxx extrusion alloys

Homogenization, reheating, extrusion and aging are conducted in a sequence for an extrusion product [11]. An example of the thermal history for an AA6082 alloy is shown in Figure 2.2.

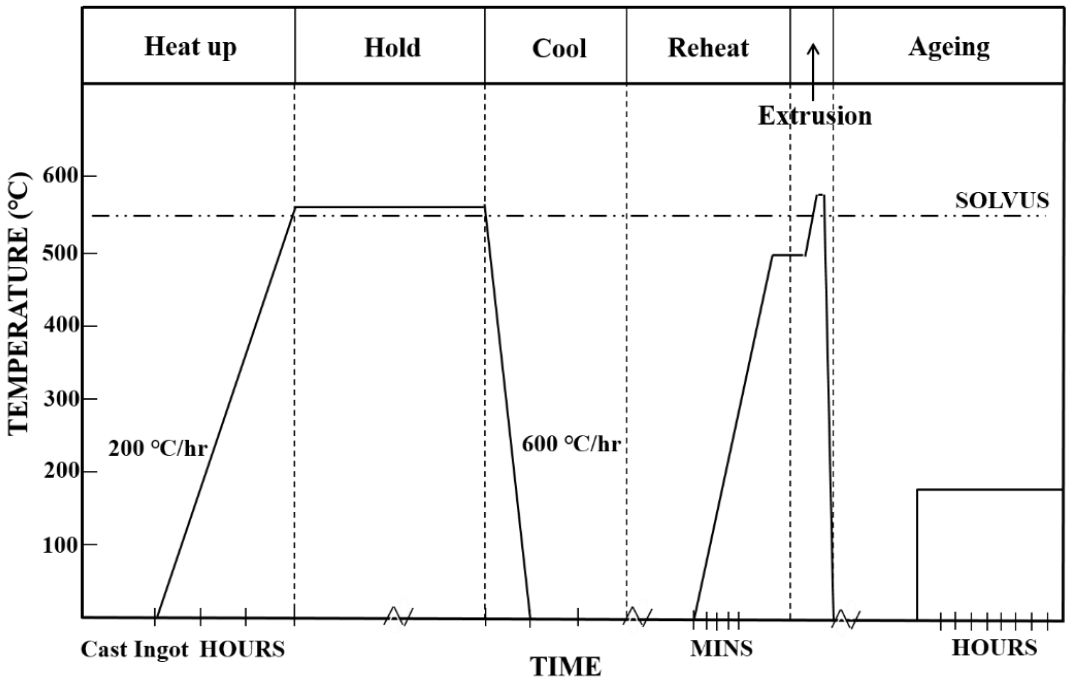

Figure 2-2 Extrusion processing route for AA6xxx series alloys expressed as a thermal-mechanical history [11]

After DC casting, AA6xxx series alloys experience a homogenization treatment before extrusion to eliminate the micro-segregation and improve extrudability [43]. Microstructure changes such as transformation of large constituent particles, formation of dispersoids and precipitation/dissolution of Mg-Si precipitates during the homogenization and reheating will influence the extrusion behaviour and the microstructure development of AA6xxx alloys. The billets are then reheated to the desired extrusion temperature. After extrusion, the extrudate is cooled to room temperature. The extrudate typically stays at room temperature for some time and is then "aged" at a temperature at 150˚C to 200˚C [23].

2.1.3 Mechanical properties and microstructures of AA6xxx alloys

The mechanical properties can be controlled by varying the processing parameters such as the homogenization treatment, the extrusion conditions, artificial aging, deformation and alloying [17,34,44–47]. AA6xxx alloys can be divided into two groups in terms of their strength. Lean alloys, such as AA6060 and AA6063, with low Mg and Si addition possess high extrudability and are used for general purposes. For example, AA6063 (0.42 wt.% Mg, 0.45 wt.% Si) has a T6 ultimate tensile strength (UTS) of approximately 230 MPa after solution heat treatment and artificial aging, while AA6082 (0.68 wt.% Mg, 0.87 wt.% Si) has a T6 UTS of about 350 MPa and belongs to the medium strength alloy family [9,24]. In general, the strength increases with an increase in the Mg and Si concentrations. AA6xxx alloys are often alloyed with Mn/Cr depending on purpose of the application of the products. Mn is added in AA6xxx alloys to change the micromechanism of crack propagation and modifies the fracture toughness [42,48] due to the formation of Mn containing dispersoids [49]. In addition, dispersoids can affect the transition from recrystallized to non-recrystallized microstructures, working hardening and

quench sensitivity of extruded products depending on the chemistry and the heat treatment applied.

The suppression of recrystallization during or after extrusion can be attributed to the Zener pinning pressure, Equation 2-1 [50], This is usually calculated by the drag of particles on the grain boundaries and is given by:

$$P_z = \frac{3F_v\gamma}{2r} \tag{2-1}$$

where F_V is the volume fraction of particles, r is the mean radius and γ is the interfacial energy between the grain boundary and the particle. Although this equation is of a simple form, it applies quite widely, including the effect of dispersoids on retarding recrystallization in Al alloys during or after the extrusion.

Homogenization process parameters, such as the heating rate and soak temperature, will change the morphology, inter spacing and the size of dispersoids. These changes will lead to a different effect on recrystallization by modifying the degree of Zener drag (Equation 2-1) [51]. For example, Eivani et al. [52] observed that low temperature homogenization could result in a stronger inhibition of recrystallization, presumably since homogenization at low temperature would produce fine dispersoids with a high number density. Cr dispersoids are also used to control grain structure and to prevent recrystallization in extruded Al-Mg-Si alloy [43]. Røyset et al. [53] investigated the influence of Mn and Cr on the recrystallization layer in extruded rods and suggested that the dispersoid number density from different Mn/Cr content and homogenization treatments are of the highest impact on the recrystallization inhibition, compared to extrusion billet temperature. In a study by Jeniski et al. [54], the volume fraction of

dispersoids was determined to increase with an increase in the Mn content as expected and thus, raises the resistance to the recrystallization of AA6013.

The presence of dispersiods may also modify the work hardening behaviour in aluminum alloys. Zhao et al. [55] studied the work-hardening effect in an Al-Mn alloy with different initial dispersoid densities. A higher work hardening rate was found in the samples that had smaller dispersoid spacing, thereby indicating that the high density of disperoids increases the work hardening rate [55].

Another effect of dispersoids was observed on the fracture toughness. A higher volume fraction of dispersoids is capable of increasing the fracture toughness as a result of homogenizing the slip distribution. Finely distributed slip was found at the crack tip in the samples with improved fracture toughness [42]. Dowling and Martin noted that the addition of different levels of Mn in AA6xxx alloys and the associated change in the amount of dispersoids effectively changed the deformation behaviour i.e. the slip band spacing [34]. Evensen et al. also found that the dispersoids reduced the coarse slip bands, and ameliorate the chance of the intergranular fracture [56].

Finally, Mn and Cr have been observed to contribute to the higher quench sensitivity, as compared to AA6xxx alloys without Mn or Cr after solution heat treatment and aging [43]. The effect of adding 0.23 wt. % Cr and 0.5 wt. % Mn separately to Al-Mg-Si alloys was analyzed by Lohne and Dons [57] where it was confirmed that both Mn and Cr-bearing dispersoids were effective nucleation sites for β'-Mg_2Si particles. Further, equal for dispersoid densities, Cr-containing dispersoids are better nucleation sites for Mg_2Si as compared to the Mn-containing dispersoids [57].

2.1.4. Characterization of microstructure

The morphology and distribution of Fe bearing constituent particles in AA6xxx alloys is usually characterized by using Scanning Electron Microscopy (SEM) [40,58–61], where the composition can either be obtained simultaneously from the Energy Dispersive X-ray spectroscopy (EDS) [41,62,63] or Wavelength Dispersive Spectroscopy (WDS) [59,63,64]. The crystal structure of the constituent particles can be either characterized by X-ray Diffraction (XRD) [41,58] and Electron Backscatter Diffraction (EBSD) [40]. Turning to the characterization of Mn bearing dispersoids in AA6xxx alloys, Transmission Electron Microscope (TEM) is more frequently used in order to characterize the morphologies of dispersoids [29,51,65] and EDS in TEM is used for determining the chemistry [30,31,66–70]. The crystal structure of dispersoids is usually determined by the Selected Area Diffraction (SAD) in TEM [28,67,71].

The formation of dispersoids also leads to the reduction of Mn/Cr solute levels, which could be characterized using the electrical resistivity measurements on homogenized AA6xxx samples [29,65,70]. The relationship between the resistivity and the solute content is described by Mathiessen's rule [43] in Equation 2-2

$$\rho = \rho_{thermal} + \rho_{solutes} + \rho_{dislocations} + \rho_{precipitations} + \rho_{grainboundaries} \quad (2\text{-}2)$$

where $\rho_{solutes} = \sum_{i=1}^{n} K_i C_i$ (K_i is the resistivity coefficient and C_i is the concentration)

The resistivity coefficients for the solutes in Al alloys are varied depending on the references [43,72–76]. The ranges of resistivity coefficients for Mn and Cr are summarized reported to be from 24 to 36 nΩ·m/wt.% and 36 to 41 nΩ·m/wt.%, respectively taken from Mondolfo [74] and Hatch [43].

2.2 Homogenization of AA6xxx alloys

2.2.1 Initial microstructure

The majority of extrusion billets are produced by the method of direct chill (DC) casting. The non-equilibrium nature of solidification (i.e. relatively high cooling rates and growth velocities) leads to micro-segregation and also boots the formation of a wide range of intermetallic phases [77]. In aluminum alloys, micro-segregation is caused by the low solubility of alloying elements in the solid compared to that in the liquid [78]. Transition elements such as Mn are usually supersaturated in the aluminum matrix after solidification and cooling to room temperature. In AA6xxx alloys, many intermetallics including α-Al(MnFe)Si, β-AlFeSi and Mg_2Si precipitates can form during solidification, depending on the cooling rates and alloy composition through either eutectic or peritectic reactions [79,80].

As-cast billets fabricated by direct chill (DC) casting typically have two types of major Fe bearing constituent particles, α-Al(MnFe)Si and β-AlFeSi [40]. The first phase is the α-Al(MnFe)Si which may or may not contain Mn or Fe and has a complex variable chemistry. The early work of Cooper et al. [81,82] examined the crystal structure of this α-Al(MnFe)Si phase. In the Al-Mn-Si system, this phase possesses a simple cubic structure [81], but phase changes to a BCC structure when Fe replaces Mn [82]. In as-cast samples, the α-Al(MnFe)Si phase is suggested to be $Al_{19}Fe_4MnSi_2$ with a BCC structure [40]. However, the α-Al(MnFe)Si is sometimes found in the form of α-$Al_{12}(FeMn)_3Si$ [35,58,83], although there are no lattice parameters reported in the literature for this stoichiometry and the stoichiometry was largely estimated by conducing the EDX. The second important phase is the β-AlFeSi which is commonly accepted as monoclinic β-Al_5FeSi [40,62].

In this work, α-Al(MnFe)Si and β-AlFeSi will be used to represent the families of the cubic and monoclinic constituent particles, respectively. In addition to the α-Al(MnFe)Si and β-AlFeSi phases, another Fe bearing contain phase named the π-$Al_8FeMg_3Si_6$ can sometimes be observed in the Fe bearing Al-Mg-Si alloys [40,64]. The π-$Al_8FeMg_3Si_6$ was observed under TEM on either side of β-AlFeSi phase [40]. Samuel et al. described that the addition of Mg resulted in the transformation of β-AlFeSi phase into π-$Al_8FeMg_3Si_6$ [64]. Dons [12] pointed out that low Mg concentration would allow the transformation of π-$Al_8FeMg_3Si_6$ to β-AlFeSi during the subsequent homogenization stage. The β-AlFeSi phase was also identified to nucleate on Mg_2Si precipitates during solidification [41]. In some cases, both α-Al(MnFe)Si and β-AlFeSi are found in as-cast samples e.g. XRD analysis on the extracted intermetallics that are produced by dissolving the aluminum matrix in AA6063 with boiling butanol [41]. The presence of α-Al(MnFe)Si phase in the as-cast microstructure is probably because of the non-equilibrium eutectic reaction [79]; while the β-AlFeSi phase would be dominant at the growth velocity range of 30 to 60 mm/min [80]. Onurlu and Tekin [84] and Tanihata et al. [26] also concluded that the β-AlFeSi is the main phase in a cast sample of AA6063 alloy with 0.2 wt.% Fe addition, obtained under an industrial relevant cooling rates. A summary of the constituent phases which have been observed in AA6xxx alloys is shown in Table 2.1.

Table 2.1 Summary of constituent particles observed in frequently used AA6xxx alloys

Alloys (wt.%)	Stoichiometry	Lattice parameters	Ref.
Al-Fe-Si-(Mn)	bcc $Al_{19}Fe_4MnSi_2$	a=1.256nm	[82]
0.40Mg-0.56Si-0.20Fe 0.39Mg-0.53Si-0.28Fe	monoclinic β-Al_5FeSi bcc $Al_{19}Fe4MnSi_2$ hcp π-$Al_8FeMg_3Si_6$	a=2.081,b=0.618,c=0.616 β=90.42° a=1.256nm a=0.663, c=0.794nm	[40]
0.7Mg-0.83Si-0.18Mn-0.27Fe	monoclinic β-Al_5FeSi cubic $Al_{12}(FeMn)_3Si$	-	[58,83]
0.46Mg-0.63Si-0.13Mn-0.21Fe	monoclinic β-Al_5FeSi cubic $Al_{12}(FeMn)_3Si$	-	[35]

Significant levels of microsegregation are typically found in as-cast materials. To reduce the amount of micro-segregation, homogenization is usually conducted before hot extrusion. In AA6xxx alloys, relatively short homogenization times, (e.g. less than 1 h, at high temperature, e.g. at 580 °C) is enough to remove Mg and Si segregation [43,85,86]. However, longer time spans are needed to homogenize Mn and Cr due to their low diffusivity in Al matrix [86]. The length scale of segregation after the solidification process depends on the thermal gradient and growth velocity. Typically, as-cast specimens with a larger grain size and a greater inter dendrite arm spacing will have longer characteristic diffusion lengths and therefore take longer times to reduce segregation [87].

The diffusion coefficient for the substitutional element can be described by [86]:

$$D = D_0 \exp(-\frac{Q}{RT}) \tag{2-3}$$

where D_0 is the pre-exponential constant, R is the universal gas constant and Q is the activation energy for diffusion.

There is a wide range of data for diffusivities of Mg [88–90], Si [91,92], Mn [93–96], Cr [94,96–98] and Fe [93,96,99] in Al. Further, there is relatively little variation for the diffusivities of Mg, Si, Mn and Fe based on the selected references. However, this is less clarity about this for Cr. Du et al [86] conducted a critical assessment for a large dataset of diffusion coefficients in Aluminum and their final suggested values in their work have been summarized in Table 2.2. In addition, diffusivities values at 550 °C and 580 °C and the characteristic diffusion length ($\sqrt{Dt}$) for the case of 1 h at 580 °C are also reported in the table in such order that the diffusion lengths of the different elements can be compared. It can be observed that the diffusion rates of Mg and

Si are much faster as compared to Mn, Cr and Fe. Among the transition metals, Fe is ≈ 4x faster than Mn and Cr is ≈ 0.25x of Mn.

Table 2.2 The constants for diffusivity of the selected substitutional elements in Al and the diffusivity values at 550 °C and 580 °C and also the calculated characteristic diffusion length for 1 h at 580 °C [86]

Element	D_0 (m^2/s)	Q (kJ/mol)	D_{550C} (m^2/s)	D_{580C} (m^2/s)	1h@580 °C $\sqrt{Dt}$ (m)
Mg	1.14×10^{-5}	120.5	2.6×10^{-13}	4.8×10^{-13}	4.1×10^{-5}
Si	1.38×10^{-5}	117.6	4.8×10^{-13}	8.7×10^{-13}	5.6×10^{-5}
Mn	1.35×10^{-2}	211.4	5.1×10^{-16}	1.5×10^{-15}	2.3×10^{-6}
Cr	0.679	261.9	1.6×10^{-17}	6.2×10^{-17}	4.7×10^{-7}
Fe	0.262	214.0	6.9×10^{-15}	2.1×10^{-14}	8.6×10^{-6}

2.2.2 The transformation of β to α constituent particles during homogenization

One of the objectives behind conducting the homogenization treatment before extrusion is to modify the intermetallic phase type and morphology in order to improve extrudability [43] The β-AlFeSi phase has sharp boundaries and is poorly bonded with the Al matrix which leads to poor hot workability [62]. A transition from plate like β-AlFeSi phase to a more spheroidized α-Al(FeMn)Si phase has been reported after homogenization in the AA6xxx alloys [25,58]. It is believed that the presence of the α-Al(FeMn)Si phase improves both the surface finish and formability [25]. The addition of Mn/Cr has been found to modify the type of constituent particles formed after casting [25,58]. It is also [25] reported that the transformation of plate shape β-AlFeSi phase to α-Al(FeMn)Si is greatly accelerated during post cast homogenization when Mn is added. The transformation of β-AlFeSi phase to α-Al(FeMn)Si phase was observed with laser scanning confocal microscopy to initiate the nucleation of the α phase on the β-AlFeSi constituent particles, in an alloy with 0.18 wt.% Mn homogenized at 540 °C for 8 h [60,100]. In the same alloy, the relative fraction of the α-Al(FeMn)Si phase was measured for a series of

homogenization treatments conducted at 540 °C up to 32 h [58] and it was claimed that the transformation was incomplete after the longest soaking time under the aforementioned temperature. The complete transformation was achieved at 590 °C after 32 h [58]. The typical SEM images of β-AlFeSi phase and α-Al(FeMn)Si phase were shown in Figure 2.3. The Si content has also been observed to play a role in the transformation of the constituent particles. For example, Lassance et al. [101] found that the β-AlFeSi to α-Al(FeMn)Si phase transformation occurred more rapidly in AA6063 alloy with a lower Si content than in the AA6005 alloy with higher Si level. Also, Kumar et al found that after homogenization at 580 °C for 5 h in AA6063 alloy with 0.07 wt.% Mn addition [41], the β-AlFeSi type constituent particles broke up and ended up with only spherical morphology intermetallics. To distinguish between these two constituent particles, generally three criteria are employed [58]: geometrical aspect ratio, Mn presence in the intermetallics and the intensity ratio of (Fe+Mn)/Si. The mean aspect ratio of the plate-like β-AlFeSi phase is > 10 whereas the spheroidized α-Al(FeMn)Si particles have a mean value of near unity. The Mn intensity and the ratio (Fe+Mn)/Si could be obtained automatically using EDX in a SEM. A combination of EBSD and EDX was suggested to identify different intermetallics by analyzing the diffraction pattern and the chemistry of the constituent particles, respectively [102]. Sweet et al. [40] used this method to differentiate β-AlFeSi and α-Al(FeMn)Si in as-cast Al-Mg-Si alloys with various Fe levels. Moreover, X-ray diffraction (XRD) is another tool that can help differentiate the types of intermetallics, but this involves a rather difficult process of dissolving the aluminum matrix so as to release the intermetallics [41,58,80].

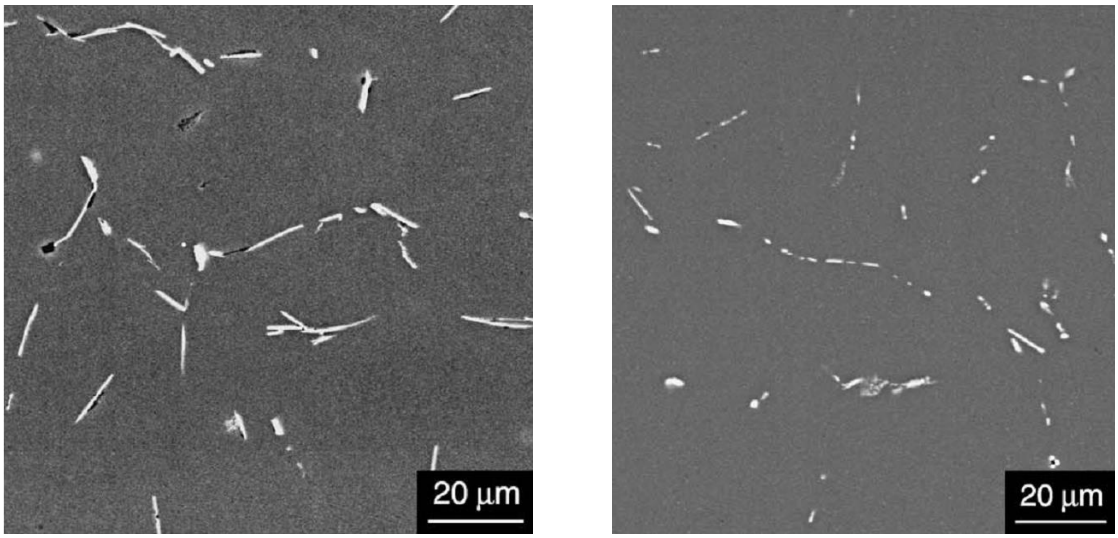

Figure 2-3 SEM images of AA6005 alloy (a) as-cast sample with plate like β-AlFeSi phase (b) fully homogenized sample at 590 °C for 32 h with more spheroidized α-Al(FeMn)Si phase [58]

To summarize, it is apparent that the kinetics of the β-AlFeSi to α-Al(FeMn)Si transformation is dependent both on the chemistry and the homogenization scenario. Although there are qualitative and quantitative techniques to distinguish the two main types of iron bearing constituents, relative little data is available on the transformation when changing the Mn level under different homogenization processing conditions.

2.2.3 Dispersoid formation during homogenization

Due to the low solubility of Mn and Cr in aluminum at the homogenization temperatures, the as-cast structure which is supersaturated in Mn and Cr decomposes by the precipitation of the dispersoids. Dowling and Martin [34] studied two Fe-free Mn-bearing 6xxx alloys and found that the dispersoids are incoherent α-$Al_{12}Mn_3Si$ particles. In the case of iron containing alloys, the crystal structure of the dispersoids is dependent on the Mn/Fe atomic ratio [28,34] i.e. simple cubic structure is observed for higher Mn/Fe ratios while the bcc structure favors the lower Mn/Fe ratios. Cr can also be added to form dispersoids [103], but the kinetics of dispersoid

formation is very slow in comparison to Mn containing alloys that may be under similar annealing conditions [104]. When alloyed with Mn and Cr, dispersoids are formed at the same temperature range as Mn-containing particles in the form of the α-Al(MnCrFe)Si phase [29,70]. The crystal structure of Mn/Cr containing dispersoids could either BCC or SC. Lodgaard and Ryum [30] pointed out that there was an effect of Cr on the crystal structure of dispersoids; only α-Al(CrFe)Si type dispersoids are present with 0.15 wt.% Cr, but an increase in the Cr content to 0.3 wt.% Cr led to the co-existence of FCC α'-AlCrSi with BCC/SC α-Al(CrFe)Si dispersoids. A summary from the literature of the chemical composition and crystal structure of dispersoids in frequently used AA6xxx alloys is presented in Table 2.3.

The nucleation of dispersoids during the homogenization process is an interesting phenomenon. The earlier literature on the subject indicates that these dispersoids nucleated on the metastable "MgSi" phase in the temperature range of 350 °C to 450 °C upon heating [104]. Further, the detailed study of Lodgaard and Ryum [70] suggested that the sequence of precipitation in Al-Mg-Si alloys with different Mn/Cr contents involved the nucleation of α-Al(MnFe)Si dispersoids on a transition phase of Mg_2Si, which they referred to as the "u-phase". Upon continued heating, the "u-phase" dissolved (i.e. when the temperature was above the Mg_2Si solvus temperature) leaving behind only the dispersoids. The detailed structure and composition of the dispersoids is rather complex as the Mn and Fe can substitute for each other, thus leading to a slight change in the lattice parameter [81,82]. However, it is a well established agreement that there are 138 atoms in the unit cell of α-Al(MnFe)Si dispersoids [68,81,82,105]. The stoichiometry is given as $Al_{100}(MnFe)_{24}Si_{14}$ [81,82], or $Al_{96}(MnFe)_{24}Si_{18}$ [68,105] where it can be noted that the atomic ratio between the transition elements (Mn and Fe) over the summation of Al and Si ratio actually stays unchanged.

Table 2.3 Summary of phases of dispersoids in frequently used 6xxx alloys

Alloys	Stoichiometry	Lattice parameters	Ref.
0.58Mg-0.99Si-0.21Mn 0.57Mg-0.95Si-0.5Mn	α-$Al_{12}Mn_3Si$	-	[34]
0.5Mg-0.65Si-0.12Fe-0.2Mn	bcc α-Al(MnFe)Si, Mn/Fe<1.6 sc α-Al(MnFe)Si, Mn/Fe>1.6	a=1.25nm	[28]
0.6Mg-0.94Si-0.22Fe-0.54Mn 0.6Mg-0.92Si-0.22Fe-0.55Mn-0.14Cr	bcc/sc α-Al(MnFe)Si bcc/sc α-Al(MnCrFe)Si	a=1.26nm	[70]
0.6Mg-0.92Si-0.22Fe-0.14Cr 0.6Mg-0.91Si-0.19Fe-0.32Cr	bcc/sc α-Al(CrFe)Si fcc α'-AlCrSi	a=1.26nm a=1.09nm	[30]

2.2.4 Influence of homogenization processing parameters

The size and spatial distribution of the dispersoids and dissolution of Mg_2Si are influenced by the chemistry and the homogenization processing parameters i.e. the heating rate, soaking temperature and time as well as cooling.

Heating rate

Low melting phase i.e. Mg_2Si dissolved through diffusion during the heat-up. However, the rapid heating rate will cause local melting leading to bad extrusion quality, which should be avoided [10,106]. The heating rate affects the morphology and spatial distribution of the dispersoids that are formed during homogenization [29,51,70,107]. Rapid heating (e.g. up quenching in salt bath at 530 °C) produces large needle-shaped dispersoids, while a slower heating rate (40 °C/h) produces homogeneous fine spherical shape dispersoids as shown in Figure 2.4 [51].

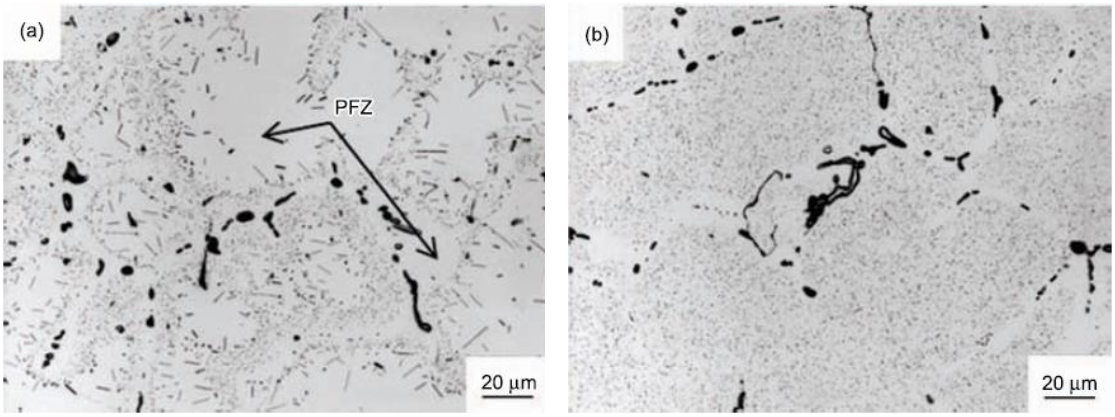

Figure 2-4 Optical micrographs of the AA6082 alloy after homogenization. (a) rapidly-heated specimen in salt bath to 530 °C, and (b) slowly-heated specimen (40 °C/h). (PFZ: Precipitation free zone) (Dark particles: constituent particles, grey particles: dipersoids) quenched when the sample reaches 530 °C [51]

As such, a slow heating rate to the homogenization temperature is preferred in the industry so that a uniform distribution of fine dispersoid across the microstructure can be produced. It is further suggested by Lodgaard and Ryum [29] that the dispersoid distribution is very much sensitive to the heating rate from around 250°C-350 °C to the homogenization temperature, i.e. the ramping rate from room temperature to 250 °C does not make much difference. The heating matters because the "u-phase" or β', containing faster diffusion element i.e. Mg and Si, formed during the range between heat-up to the homogenization temperature, serve as nucleation sites for α dispersoids [70].

Holding temperature and time

The dissolution of Mg-Si particles, growth/coarsening of dispersoids and the transformation of the constituent particles are some processes that occur during holding and are all diffusion controlled processes [108]. Mg_2Si phase dissolves very quickly when the alloy is held above its solvus temperature. For example, Kuijpers et al. [58] reported that the Mg_2Si precipitates were completely dissolved after homogenization at 540 °C for 20 min in an AA6005

alloy. However, they observed that the transformation from β-AlFeSi to α-Al(FeMn)Si was negligible at this temperature. A higher homogenization temperature of 590 °C for 32 h was necessary in order to transform all the β-AlFeSi phase to the α-Al(FeMn)Si phase. These results are consistent with the previously noted diffusion coefficients where Mg and Si had much higher values as compared to the transition metal Mn, Fe and Cr (see Table 2.2).

The homogenization temperature is also an important factor that affects the dispersoid density and size during homogenization [109] for alloys containing Mn, e.g. the Mn dispersoids density decreases markedly when comparing 2 h at 520 °C and 2 h at 585 °C as shown in Figure 2.5.

In the work of Lodgaard [65] and Strobel et al [31], the dispersoid mean radius was found to increase with a higher homogenization temperature and longer soaking time in a 0.50 wt.% Mn bearing alloy. Further, the number density of dispersoids was investigated by Lodgarrd [65] using TEM analysis on the same 0.50 wt.% Mn alloy. The heating rate for homogenization was 3 °C /min and the soaking temperature varied from 520 °C to 580 °C. It was found that the largest dispersoid density was observed at the end of the heating ramp (520 °C) in the alloy with 0.55 wt.% Mn and 0.15 wt.% Cr levels. The second highest dispersoid density was found in the 0.5 wt.% Mn alloy for the same homogenization condition. The mean dispersoid radius was 15 nm at the end of heating to 520 °C while the mean radius increased to 130 nm when homogenized at 580 °C for 50 h in 0.5 wt.% Mn alloy [65].

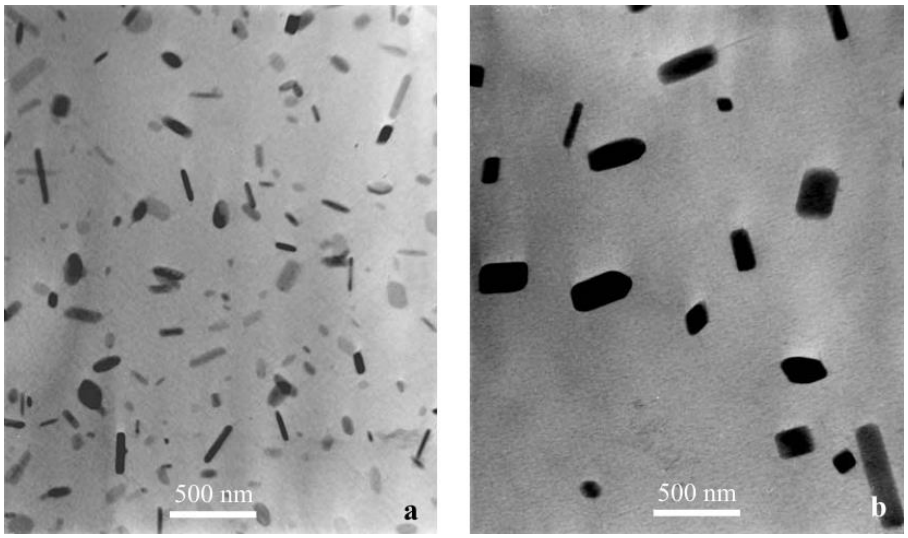

Figure 2-5 TEM images of 6082 alloy showing Mn containing dispersoids homogenized for 2 h at (a) 520 °C and (b) 585 °C [109]

Yoo et al [28] studied the chemical composition and crystal structure of the dispersoids in a 0.20 wt.% Mn alloy homogenized at 560 °C for 8 h. They found that a correlation between the Mn/Fe ratio, the disepersoid size and the crystal structure i.e. the simple cubic structure and BCC structure were related to higher Mn/Fe ratios and lower Mn/Fe ratios, respectively. Lodgaard [65] also reported the Mn/Fe and Fe/(Mn+Cr) ratios on dispersoids for the end of heating and also for long soaking times of 50 h at 520 °C and 580 °C, showing that the Mn/Fe ratios decreased with increasing soaking time. Yoo et al [28] and Strobel et al [31] also reported BCC and SC crystal structures for the dispersoids in two selected homogenization conditions (i.e. 8 h at 560 °C and 2 h at 570 °C).

Yoo et al [28] and Strobel et al [31] found that the chemistry of dispersoids, as characterized by Mn/Fe ratio, was observed to vary from one particle to another. Moreover, the Mn/(Mn+Fe) ratio was determined to be higher in the centre of a dispersoid for AA3xxx alloys [110]. Similar results were found by Flament et al for Cr in a 0.19 wt. % Cr bearing AA6xxx alloy [111].

The volume fraction of dispersoid is another important microstructure feature, but it is a rather challenging task to measure it correctly on micrographs, due to the well-known threshold issue. There are a few careful work dedicated to either measure or estimate it [71,112], which still exists some gap to reach a perfect solution. An alternative approach would be desirable to re-examine the measurement of dispersoid volume fraction, taking advantage of the experimental results from TEM/EDS, EPMA and electrical resistivity measurements. The approach performed in this thesis would be different from the approach of either tracing the particles [112] or counting the dispersoid particles in the TEM images [71].

In summary, the literature indicates a complex behaviour for the dispersoid precipitation, and systematic studies are still needed on the crystal structure and detailed distribution of alloying elements of the dispersoids for a wide range of homogenization conditions on alloys with a range of Mn/Cr additions.

Cooling path after holding

The cooling paths after homogenization can be broadly divided into two categories, interrupted cooling and continuous cooling. Cooling processes such as water quench and air cool belong to continuous cooling, which result in different mechanical properties and microstructure [113]. Microstructure evolution during cooling is due to the precipitation of Mg-Si particles when the temperature drops the below the solvus temperature [11]. One must be careful to avoid the precipitation of coarse Mg_2Si precipitates which may not dissolve during the subsequent reheating to the extrusion temperature. These coarse Mg_2Si precipitates together with β-AlFeSi intermetallics in microstructure may lead to incipient melting, which results in cracking during extrusion [9]. On the other hand, it may be possible to reduce the Mg/Si in solid solution by precipitation of fine Mg-Si particles which do not dissolve during the extrusion process, which

then results in a low extrusion force [35]. It is understood that decreasing the cooling rate (i.e. for large billet) results in more precipitation of coarse Mg_2Si and β'-MgSi plates which may not dissolve during extrusion and thus the Mg/Si are not able to contribute to subsequent age hardening [10].

Reheating and extrusion

While reheating to the extrusion temperature, two types of heating processes are generally adopted i.e. gas and induction heating, which typically take ≈ 20 min and ≈ 2 min to reach the extrusion temperature, respectively. During reheating, one may have precipitation of metastable β'' precipitates at 100-250 °C followed by dissolution above 350 °C [11]. The presence of undissolved Mg/Si phases leads to two important consequences. First, the extrusion force may be reduced due to the lowering of the Mg/Si solid solution level [14]. Second, the lower Mg/Si solid solution level can reduce the strengthening potential of the extrudates during artificial aging after extrusion. The dissolution of Mg/Si phase is closely related to the cooling condition employed in the homogenization process, i.e. slow cooling leads to coarse precipitation which may not dissolve during the reheating and extrusion processes [9].

2.3 Microstructure modeling during homogenization

Given the importance of microstructure development during homogenization, the following will review the current state of the modeling activities.

2.3.1 The β to α transformation of constituent particles

The β to α transformation was modeled by Haidemenopoulos et al. [78,87], using a diffusion based model (implemented by the DICTRA software) to study the microstructure evolution during homogenization in which, the dissolution of Mg_2Si precipitates and transformation of Fe bearing constituent particles are treated as a whole. The initial micro-

segregation of Mg, Si, Mn and Fe in the primary aluminum dendrite was calculated using the Scheil approach. The model requires inputs including the as-cast grain size and the volume fraction of the secondary phases from which the dissolution of Mg_2Si and β to α transformation are then simulated [87]. The model quantitatively predicted the evolution from β to α phase during homogenization in a 0.18Fe0.02Mn alloy at a range of temperatures from 540 °C to 580 °C and agreed with the experimental work from Kuijpers et al [27]. The drawback from the model is that the Mn diffusion into constituent particles is not taken into consideration and the application is not validated in a high Mn containing alloy.

Another approach by Kuijpers et al. [85,100] used a finite element model to study the transformation of β to α constituent particle as a function of homogenization temperature, as-cast microstructure and concentration of alloying elements in several AA6xxx alloys. The geometry of the model was described as an α nuclei on top of plate shape β phase, which broke up during homogenization [100]. The driving force for the β to α transformation was assumed to have taken effect largely due to the chemical potential differences of iron at α and β interfaces. This chemical potential difference caused a diffusion transportation of Fe from β to α phase, leading to the broken up of plate shape β phase. Although the model describes the β to α transition, it only works when the relative fraction of α is less than 80 %, nonetheless to say, providing an estimated fraction for the α phase during homogenization.

Apparently, the approaches of both Haidemenopoulos [87] and Kuijpers [100] did not consider the Mn diffusion and the interaction between Mn containing dispersoids and constituent particles during the homogenization in the AA6xxx alloys.

2.3.2 Modeling of dispersoid formation

The Alstruc homogenization model developed by the SINTEF group in Norway was an early attempt to model the dispersoid formation while simultaneously considering the transformation of constituent particles [12]. The model relied on published phase diagrams coupled with a large dataset of complementary experimental work, with a special interest for the region above 400 °C [12]. It is consisted of the phase diagrams, cyclic microsegreation long-range model, nucleation model and coarsening model. The model has subroutines for different types of wrought aluminum alloys, but required extensive experimental data of each alloy category to fit the subroutines of the model. The evolution of dispersoids and transformation of constituent particles were treated separately not in a coupled manner.

Cai et al. [66] simulated the width of the dispersoids free zone (DFZ) near grain boundaries in AA6069 alloy. A multicomponent Scheil model (calculating the concentration of Mg, Si, Fe and Mn) coupled with MTDATA [114] (a software used to calculate the phase equilibria and thermodynamic properties in multicomponent and multiphase systems) was used to calculate of dispersoid fraction and the width of DFZ. The critical level for forming Mn containing dispersoid was defined by a constant value (i.e. 0.2 wt. % Mn). Then, the width of DFZ is predicted for the regions where the Mn content is lower than the aforementioned criteria. It was predicted that the width of DFZ increases with an increasing homogenization temperature due to higher solubility of Mn at an elevated temperature. Because of higher Mn addition (i.e. 0.7 wt. %), Al_6Mn dispersoids were considered in the homogenization stage in the work of Cai et al. [66], but neither chemistry or the crystal structure experimental work was provided.

More recently, Du et al. [115] developed a CALPHAD (Computer Coupling Phase Diagrams)-coupled homogenization model to predict the microstructure evolution during the

homogenization of Al-Mn-Fe-Si alloys. The geometry of the model is one dimensional, and covers half a secondary dendrite arm with 10 cells; the last cell deals with the constituent particles, while the rest of the cells take care of the nucleation and coarsening of the dispersoids [115]. Two length scales of diffusion were taken into account including the dispersoid formation (short-range diffusion) and constituent particles transformation (long-range diffusion). A one-dimensional (1-D) pseudo front tracking (PFT) model was applied for the transformation of the constituent particles [116] and the Kampmann-Wagner numerical (KWN) [117] was adopted for the dispersoid formation. The two models are fully coupled to a CALPHAD database (via a look-up table based on the TTAL6 database) and successfully applied to investigate the effect of alloy chemistry and heat treatment conditions on the microstructure evolution of AA3xxx alloys [115]. A few important features of the dispersoid population such as the size distribution, number density and spatial distribution were predicted and were found to agree well with the experimental results. The DFZ could also be successfully modeled in this model by calculating the inhomogeneous spatial distribution of these dispersoids. The proposed idea of linking two length scale phase transformation from Du et al [115] has also been also adopted by Priya et al [118] to model the homogenization treatment for AA7050 alloy, where the Thermo-Calc is coupled as well. The prediction for the evolution of the mean radius of dispersoids in Priya et al [118] is still weak. It is also the weakness of all those models including the nucleation, effect of interfacial energy, complex precipitation path in AA6xxx alloys for dispersoids.

In summary, the current models show that the transformation of the primary constituent particles (particles of 0.5-5 μm) and the formation of dispersoids (20-200 nm) are extracted and are both affected by the composition and homogenization scenarios in a complex manner. Thus,

it would be desirable to have a chemistry-dependent homogenization model predicting the evolution of these particles.

2.4 High temperature constitutive behaviour of AA6xxx alloys

Extrudability is affected by the processing parameters as well as the alloying chemistry. The break-through force of high temperature extrusion is dependent on factors like homogenization treatment, pre-heat temperature and the ram velocity. Modeling the extrusion process, for instance, using FE models, requires robust models for the constitutive behaviour so that the effect of the process parameters such as temperature, strain, strain rate and initial microstructure can be examined [119]. The following section summarizes the different deformation mechanisms and corresponding constitutive equations in order to describe the high temperature flow behaviour in the Al alloys.

2.4.1 Empirical constitutive models

Zener-Hollomon (Z) Equation

The Zener-Hollomon (Z) equation, which is also known as temperature compensated strain rate parameter, was first proposed by Zener and Hollomon [120] in the 1940s while studying the flow stress behaviours of steels during hot deformation. i.e.

$$Z = \dot{\varepsilon} \exp(\frac{Q}{RT}) \qquad (2\text{-}4)$$

$$\sigma = f(Z) \qquad (2\text{-}5)$$

where Q is an effective activation energy (kJ/mol), R is the universal gas constant (8.314 $J \cdot mol^{-1} \cdot K^{-1}$); T is the absolute temperature (K), $\dot{\varepsilon}$ is the strain rate (s^{-1}) and A is the pre-exponential constant.

The Zener-Hollomon parameter is employed to predict the high temperature behaviour taking into account the strain rate and temperature. The temperature compensated strain rate factor proposed by Zener and Holloman [120] is the basis that describes the kinetic law during high temperature deformation. The stress can be described by the Z parameter (Zener-Hollomon parameter) at constant strain.

Modified hyperbolic sin laws were made on the Zener-Holloman equation at high strain rates based on the experimental results by conducting torsion or compression tests in order to have better flow stress prediction in metals including the aluminum alloys [119,121,122]. The initial microstructure is not explicitly included as an input to the model.

Sellars-Tegart Equation

The Sellar-Tegart equation was introduced in the 1960s [121] to relate the flow stress to strain rate and temperature at high temperatures and also to describe steady state deformation in the regime where there is no strain hardening.

$$\dot{\varepsilon} = A\left[\sinh\left(\frac{\sigma_{flow}}{\sigma_0}\right)\right]^{n_{Hn}} \exp(-\frac{Q}{RT}) \qquad (2\text{-}6)$$

where A is a pre-exponential constant, σ_{flow} is the steady-state flow stress, σ_0 and n_H are also constant, Q is the activation energy, R is the gas constant, and T is the deformation temperature in K. The application is limited to high temperature deformation where strain hardening is negligible [119]. The major limitation of these models is the failure of including of the initial microstructure information.

2.4.2 Physically-based constitutive models

Kocks and Chen' model

Kocks and Chen [123] developed a physically-based model to predict the flow stress under the regime where the solute drag mechanism dominant. This model integrating the microstructure information in the solute drag regime, Equation 2-7, is applicable to steady-state regime where no work hardening is observed.

$$\dot{\varepsilon} = A\left(\frac{\sigma}{\mu}\right)^{n} \frac{\mu b^{n}}{kT} \exp(-\frac{Q}{kT}) \qquad (2\text{-}7)$$

where A is the pre-exponential constant, n is the stress exponent (for solute drag, n=3), σ is the flow stress, μ is the temperature dependent shear modulus, b is the magnitude of the temperature dependent Burger's vector, k is the Boltzmann's constant, T is the deformation absolute temperature and Q is the activation energy for diffusion of the rate controlling alloy addition.

It is a physically based model in which the flow stress is related to as the strain rate, deformation temperature and microstructure. The stress component must be 3 so as to meet the original physical assumption. Two Al-Mg alloys with different Mg contents were tested and fitted with the model as shown in Figure 2.6 in the temperature range from 282 to 440 °C at strain rates between 10^{-5} and 10^{-1} [124].

Further, the model was used to conduct an analysis of the steady state flow stress of AA5182 alloy which had been determined from high temperature compression tests (deformation temperature between 350 and 550 °C and strain rate from 0.001 to 1 s^{-1}). The model was fit to the high temperature deformation data in AA5182 alloy, and was found to give a good fit when the stress exponent was modified to be 3.65, i.e. close to the theoretical value of 3 when solute drag is the dominant mechanism [125].

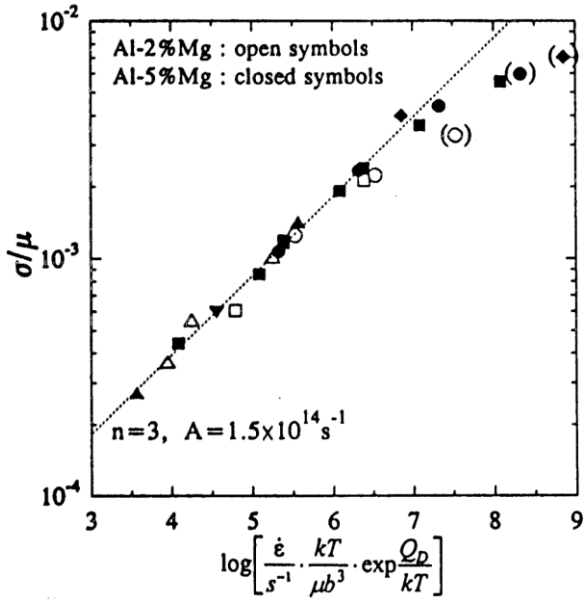

Figure 2-6 Two Al-Mg alloys deforming in steady state in the temperature regime 282 to 440 °C, at strain rates between 10^{-5} and 10^{-1} s^{-1} [124]**.**

Moreover, the high stress exponents were also observed from the extensive study in AA3xxx alloys when this model was applied to describe the high temperature compression behaviour. A satisfactory fit to experimental data was achieved only when the stress exponent was raised to a value of 8. Although the equation described the data well, the physical meaning was lost [126–128]. One reason for the high value of the exponent, *n*, could be attributed to the presence of Mn/Fe bearing constituent particles and dispersoids which provide an additional strengthening mechanism.

MPM model

Nes [129] developed a work-hardening model known as the MPM (multi-parameter microstructure model) by taking into account three microstructural elements i.e. cell/subgrain size, dislocation density within cells and cell boundary dislocation density or sub structure misorientation. The flow stress could be related to these internal state variables as:

$$\tau = \tau_i + \alpha_1 Gb\sqrt{\rho_i} + \alpha_2 Gb\frac{1}{\delta} \quad (2\text{-}8)$$

where τ_i is the frictional stress, α_1 and α_2 are constants, G is the shear modulus, b is the magnitude of the Burgers vector, ρ_i is the cell interior dislocation density and δ is the cell/substructure size.

In this model, the flow stress is mainly controlled by the spacing of the cell walls rather than their internal structure. With appropriate differential equations to describe the evolution of the state variables and the plastic strain, the model fitted well with the work hardening behaviour of FCC Cu alloys [130] and is often referred to as the MPM model (multi-parameter-microstructure) [131]. Although the stress-strain curves for different stain rates and temperatures could be modeled, the model has a large number of fit parameters and also incorporates some empirical elements for the sake of some poorly understood phenomena, such as dislocation cross-slip.

This model was further developed by Marthinsen and Nes [132] and the development led to the effects of grain size, precipitates and solute atoms in solutions.

$$\tau = \tau_t + \tau_p + \alpha_1 Gb\sqrt{\rho_i} + \alpha_2 Gb\left[\frac{1}{\delta} + \frac{1}{D}\right] \quad (2\text{-}9)$$

where τ_t is the thermal stress, τ_P is the stress caused by non-deformable dispersoids, α_1 and α_2 are constants, G is the shear modules, b is the magnitude of the Burgers vector, ρ_i is the cell interior dislocation density and δ is the cell/substructure size and D is the grain size. The term τ_t is assumed to be determined by the effects of solute atoms on the climb of jogs on the screw dislocations.

The model has been applied to predict the flow stress for AA6060, AA6082 and AA3104 alloys [133]. The Mg, Si and Mn in solid solution and Orowan by-passing stress are explicitly included. However, the combined effect of alloy additions could not be predicted since it has been suggested that the Mg, Si and Mn atoms share quite a complex interaction [133].

3IVM model

The 3IVM work-hardening model is another approach which has been developed by the group of Gottstein et al [134,135]. The model considers the mobile dislocation and immobile dislocations within the cells and on substructure boundaries [134,135] which are coupled to a set of differential equations for their evolution.

The model was applied to both a precipitation hardened Al-0.42Cu-0.14Mg alloy and precipitation free model alloy [135]. The model predictions seem to agree well with the experimental stress-strain curve. However, in multicomponent commercial alloys, factors like existing constituent particles, non-deformable dispersoids will also affect the shear stress which is not incorporated in these set of models.

2.4.3 Microstructure effect on high temperature flow stress behaviour

In AA6xxx alloys, Mg and Si in solid solution, Mg-Si precipitates and non-deformable Mn containing dispersoids, can all affect the flow stress during the high temperature compression. Sheppard and Jackson [119] clearly pointed out the effect of homogenization, in particular heating and cooling rates in AA6xxx, on the constitutive behaviour in aluminum alloys.

Effect of solid solution:

It has been shown that the amount of Mg and Si in the solid solution largely increases the flow stress (however, the effect of Mg is greater than that of Si) [133,136].

Effect of Mg-Si precipitates:

As the AA6082 alloys are very quench sensitive, their nature determines the formation and distribution of MgSi precipitates [109]. For example, the work conducted by Langkruis et al. [137] on a dilute AA6063 alloy shows the effect of β-Mg_2Si and its metastable forms β′- and β″-Mg-Si precipitates on the flow stress at 400 - 500°C. The work shows that the initial microstructure (mainly β-Mg_2Si precipitates) reduces the stress level quite significantly which is speculated to be a result of the absence of dynamic precipitation during high temperature deformation. The work of Anjabin et al [138] studied and confirmed the effect from MgSi precipitates on the deformation behaviour in the AA6063 alloy.

Effect of constituent particles:

The coarse constituent particles were found to have marginal effect on the high temperature flow stress in AA6xxx alloy from the work of Nes et al [139]. Geng [127] also found that the effect of the constituent particles on high temperature flow stress is negligible in AA3102.

Effect of dispersoids:

The fine dispersoids from various homogenization scenarios can also influence the constitutive behaviour where the strengthening effect from these fine intermetallics and MgSi precipitates is considered in an additive approach [140]. Dowling and Martin observed that the effect of Mn dispersoids strengthening in the form of interactions with dislocations in the slip planes [34]. The addition of an athermal strengthening component has been accounted by adding a threshold stress [141,142]. It has been proposed that the majority of the threshold stress comes from the presence of dispersoids, which contribute in the form of an Orowan stress [143,144]. In Mn containing alloys such as AA6082, a higher flow stress is found in samples with small

dispersoids (i.e. homogenized at a lower temperature) as compared to materials containing larger dispersoids (i.e. homogenized at high temperature) [65]. Further consideration would be about the shape and planar spacing of these dispersions, since these two factors are also capable of affecting the Orowan stress [145,146]. In the current context of deformation at high temperature, the detachment of dislocations from particles (i.e. dispersoids) should also be taken into account, as this will lower the magnitude of the Orowan stress [147,148].

2.5 Summary

As can be seen from this literature review, there is a considerable body of work on dispersoids and constituent particles in AA6xxx alloys. However, there is a dearth of systematic and quantitative studies on the effect of various Mn/Cr contents together combined with industrial related homogenization scenarios. The primary aim of this work is to conduct a comprehensive investigation on the constituent particle fraction, dispersoid size distribution, the (Mn+Cr)/Fe ratio and the crystal structure of dispersoids under different homogenization combinations for the AA6082 based alloys with varied Mn/Cr contents.

3. Scope and Objectives

The goal of this work is to study the chemistry dependent microstructure change during homogenization and the relationship of microstructure features to high temperature flow stress.

3.1 Scope

AA6062 based model alloys were cast with a range of Mn additions (0 - 0.75 wt.%) and in some cases 0.15 wt.% of Cr. The Mg content is common to all the alloys and their solid solution. The homogenization heat treatments are designed to be in the range of the industry processing windows, i.e. heating rate of ≈ 200 °C/h, soaking temperatures of 550 - 580 °C, and hold times of 2 - 168 h. The experimental high temperature deformation behaviour is examined in the temperature and strain rate where Mg and Si are in solid solution. A wide range of experimental characterization tools are used. For the characterization of the microstructure, FEGSEM, TEM, XRD and EPMA are employed. For the deformation response, high temperature compression tests are conducted.

3.2 Objectives

The objectives of this work are the following.

1) To quantitatively characterize the evolution of dispersoids and constituent particles during homogenization treatments by experimental methods. This includes the size, shape, volume fraction, crystal structure and chemical composition.

2) To experimentally measure the high temperature flow stress of different alloys with different homogenization treatments in the temperature range of 550 - 580 °C at strain rates of 1 and 10 s^{-1}.

3) To integrate the experimental observations on microstructure evolution during homogenization and modify an existing model to propose the mechanisms involved in dispersoids/constituent particles evolution during homogenization.

4) To develop a physically based constitutive model to describe the high temperature deformation response as a function of temperature, strain rate and microstructure.

4. Methodology

4.1 Materials and sample preparation

Four different Al-Mg-Si alloys of interest were cast as extrusion billets with 100 mm in diameter and 300 mm in length by Rio Tinto Aluminum Research and Development Center (ARDC) in Arvida, Quebec. The chemical composition of these alloys has been listed in Table 4.1. Alloy #1 (referred to as 0Mn alloy) is considered the base alloy, while alloys #2 - #4 were designed to investigate the effect of Mn/Cr additions on the microstructure evolution during homogenization and on the flow stress behaviour relevant to extrusion. For the base alloy, the Si/Mg ratio was designed to be 1.16, reflecting the recent knowledge that the β" strengthening precipitate has a stoichiometry Mg_5Si_6 [37,38]. It is worth noting that the chemistry of Si content was deliberately increased for the Mn and Cr alloys to account for Si loss to the constituent particles in these alloys. This was done on the basis of the Thermo-Calc (TTAL6 database) calculations. In this thesis, these alloys will be referred to by using the designations such as 0Mn, 0.25Mn, 0.5Mn and 0.5Mn0.15Cr as shown in Table 4.1.

Table 4.1 Chemical composition (from Rio Tinto Aluminum) of different Al-Mg-Si alloys in wt.%

Alloy	Designation	Mg	Si	Mn	Cr	Fe
1	0Mn	0.71	0.91	0.003	-	0.20
2	0.25Mn	0.71	0.95	0.25	-	0.21
3	0.5Mn	0.71	1.03	0.50	-	0.21
4	0.5Mn0.15Cr	0.70	1.04	0.49	0.15	0.23

Two types of samples were machined from the 20 mm to 40 mm positions in the radius of the initial as-cast billets; neither the centre within 10 mm nor the edge larger than 40 mm in radius were used. Samples with dimensions of 15 mm in diameter and 6.5 mm in height were

primarily used for homogenization heat treatments and observations of microstructure evolution; other samples of a diameter of 8 mm and 12 mm in height were cut for high temperature compression tests after the selected homogenization conditions shown in Figure 4.1.

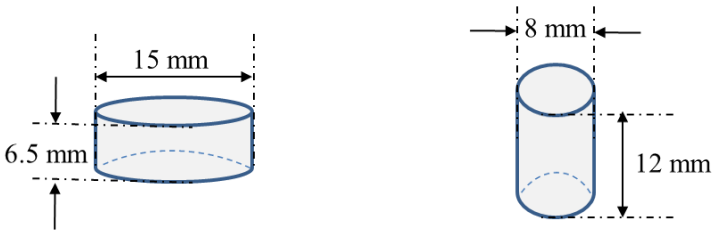

Figure 4-1 Schematic drawings of the samples for (a) microstructure evolution and (b) high temperature compression tests

4.2 Homogenization treatments

The homogenization temperature was chosen such that it would be below the melting temperature and above the Mg_2Si solvus temperature of the alloys. Thermo-Calc (TTAL6) was used to calculate the Mg_2Si solvus temperature and the equilibrium melting temperature of the four alloys of interest in this work. This defines the temperature window for homogenization as shown in Table 4.2. According to these calculations, two temperatures were chosen for the homogenization experiments, i.e. 550 ºC and 580 ºC.

Table 4.2 Solvus and melting temperatures of the Al-Mg-Si alloys by Thermo-Calc (°C)

Alloys	0Mn	0.25Mn	0.5Mn	0.5Mn0.15Cr
Solvus temperature	543	545	547	544
Equilibrium melting (°C)	592	592	590	595

Homogenization treatments were conducted on the as-cast samples using a Carbolite® (HRF) recirculating air furnace. A separate thermocouple was used in order to monitor the temperature and to record the thermocouple data via instruNet Model 100 DAQ system. An industrial heating rate of 200 °C/h was chosen for all the given samples. The soaking time at

specific target temperatures 550 ºC and 580 ºC varied between 10 minutes to 168 h (7 days), where the detailed homogenization conditions are shown in Table 4.3.

Table 4.3 Homogenization conditions for the Al-Mg-Si alloys

Designation	550 ºC	580 ºC
0Mn	10 min, 2 h, 4 h	2 h, 12 h, 168 h
0.25Mn	10 min, 2 h, 4 h	2 h, 12 h, 168 h
0.5Mn	10 min, 2 h, 4 h	2 h, 12 h, 168 h
0.5Mn0.15Cr	10 min, 2 h, 4 h	2 h, 12 h, 168 h

An example of the measured temperature history of heating and holding has been provided in Figure 4.2a, where the temperature error during soaking is ± 3 °C and has been measured from a separate K-type thermocouple and the holding error is ± 1 min depending on how long the samples were taken out of the box furnace. A closer look at the temperature history near the target temperature is shown in Figure 4.2b, where the temperature in the box furnace first dropped upon reaching the target temperature and then re-heated, but the change is small, and is within 5 °C. After the heat treatment, the samples were taken out of the box furnace and were water quenched at room temperature within 10 s.

It is worth noting that aluminum cubes with dimensions of 25.4 mm (1 inch) in length were used for the particular homogenization at 580 °C for 168 h (7 days) so that the surface layer could be removed, i.e. the layer where Mg is lost due to the formation of MgO in AA6082 alloys. After quenching, the cubes were cut into half, where the centre was characterized or examined using various experimental techniques in Section 4.3.

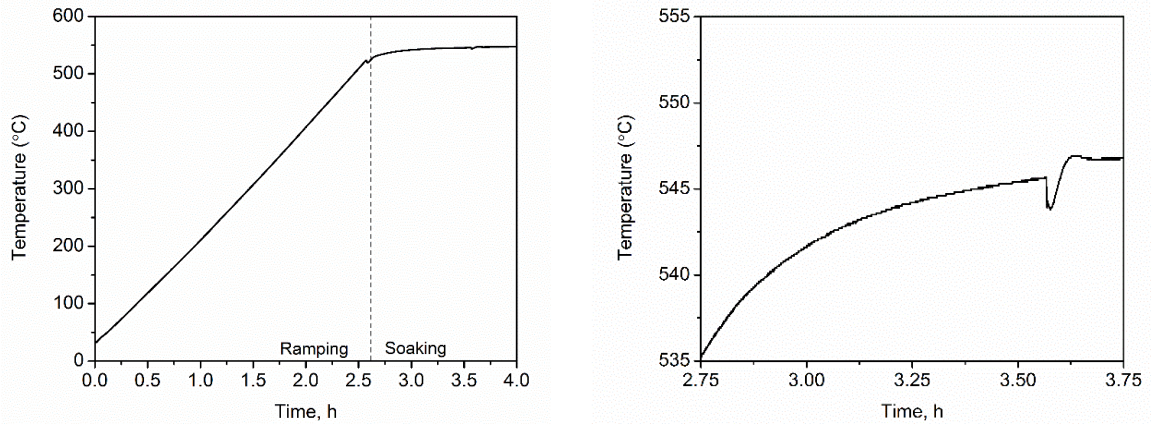

Figure 4-2 (a) an example of the monitored thermo history during homogenization treatment (b) a magnified area upon heating to the target temperature

4.3 Sample characterization

4.3.1 Initial grain size and secondary dendrite arm spacing (SDAS)

All the samples were cold mounted using the Cold Cure Epoxy Resin and Harder (Volume ratio 2:1 and cured for a day at room temperature). Then, the samples were ground using 320/600/1200 grit papers, where water was used as a lubricant. The polishing was conducted using Texmet® and Chemotexile® cloth with 6 µm and 1 µm diamond suspensions as lubricant, respectively. Colloidal silica was used as the final polishing using Chemotexile® cloth. Anodizing for the samples was conducted using Barker's reagent 3 vol.% HBF_4. The procedure was conducted at room temperature under 30 V for 100 seconds using pure aluminum as the cathode.

A Nikon Epiphot 300 series Optical Microscope was employed for the purpose of optical microscopy. The polarized light optical microscopy was also implemented using a trial and error approach in tuning the angle of the polarizer slide and the analyzer slide in the light path, with the aim to obtain the best image quality.

The initial grain size and inter-dendritic spacing were characterized for the four alloys using the anodized images captured under the polarized mode at the magnifications of x50. Grains are distinguished based on different colors from the polarized light images. An example is shown in Figure 4.3a and then traced for grain size measurements using the Clemex® software shown in Figure 4.3b, where more than 200 grains were chosen for grain size measurement at each of the samples.

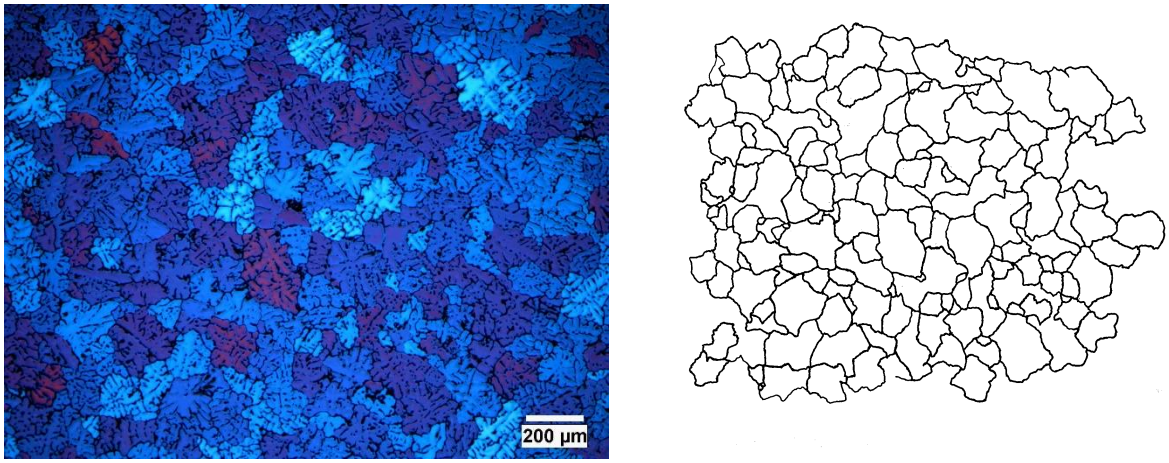

(a) **(b)**

Figure 4-3 Typical example of (a) an anodized image and (b) manually traced and scanned image of as-cast AA 6082

The secondary dendrite arm spacing (SDAS) was also measured from the anodized images using random line intercept method in Clemex®, shown illustrated in Figure 4.4a. A more detailed illustration of the measurements of SDAS has been shown in Figure 4.4b and Figure 4.4c, where the measurements for one and three secondary dendrite arms are revealed.

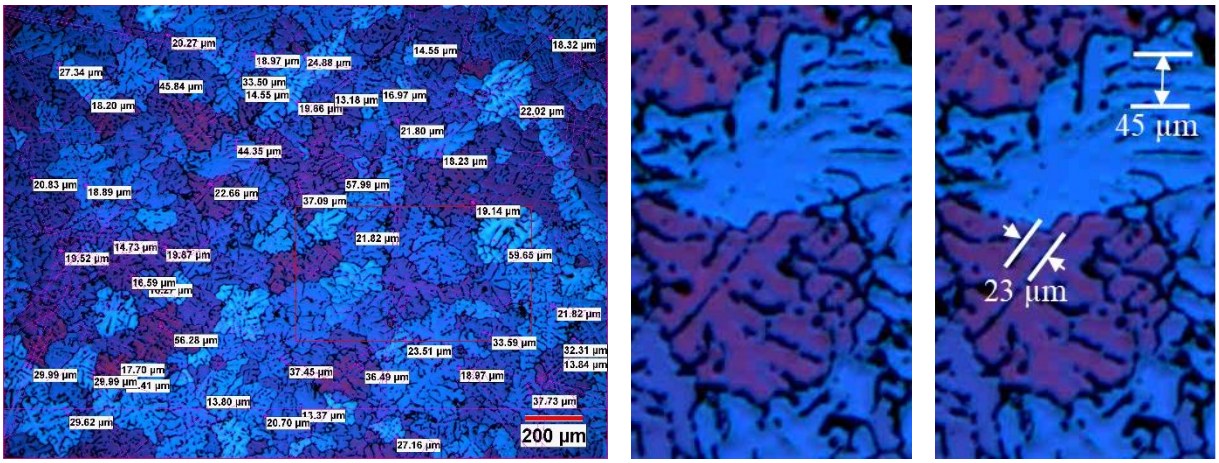

(a) **(b)** **(c)**

Figure 4-4 An illustration of the measurement of the SDAS (a) low magnification of a larger area, (b) high magnification of a few grains and (c) detailed examples depicting how the SDAS are measured where the measure of 23 µm is a single SDAS while that of 45 µm is for 3 SDAS.

4.3.2 Electrical resistivity

Electrical resistivity measurements were conducted using a Sigmatest 2.069® (Foerster Intrument Inc) eddy current conductivity meter for the as-cast and homogenized samples. Calibration using two standard samples and air point was implemented prior to each measurement. The samples used for resistivity measurement are the shown in Figure 4.1a i.e. with a diameter of 15 mm and thickness of 6.5 mm.

The frequency is set as 60 kHz for all the measurements. The output data is in the form of electrical conductivity (in MS/m) which is converted into electrical resistivity (in nΩ·m).

4.3.3 Constituent particles and dispersoids

A Zeiss Sigma field emission gun scanning electron microscope (FEGSEM) operated at 5 kV and a working distance of 5 mm was used for characterizing the dispersoids and constituent particles in the specimen. The samples were ground using 600/1200/4000 grit papers with water as lubricant. First polishing was step conducted using a Chemotexile® cloth lubricated with 1 µm

diamond suspension. Colloidal silica is used as the final polishing using Chemotec® cloth. The polished samples were characterized under secondary electron mode and backscattered electron (BSE) mode. The images collected for fine dispersoids quantification were conducted using the backscatter electron (BSE) mode, where Mn/Cr containing constituent particles and dispersoids were revealed due to their high atomic number contrast with aluminum. The magnifications of x1000 were selected for characterizing the coarse constituent particles; while higher magnifications up to x20000 were chosen for the much finer dispersoids. High magnification images, obtained at x1000, x10000 and x20000 times were selected for quantitative analysis using ImageJ® for constituent particles and dispersoids, where at least 10 fields of continuous BSE images were processed. An example of measuring fine dispersoids in ImageJ® is shown in Figure 4.5.

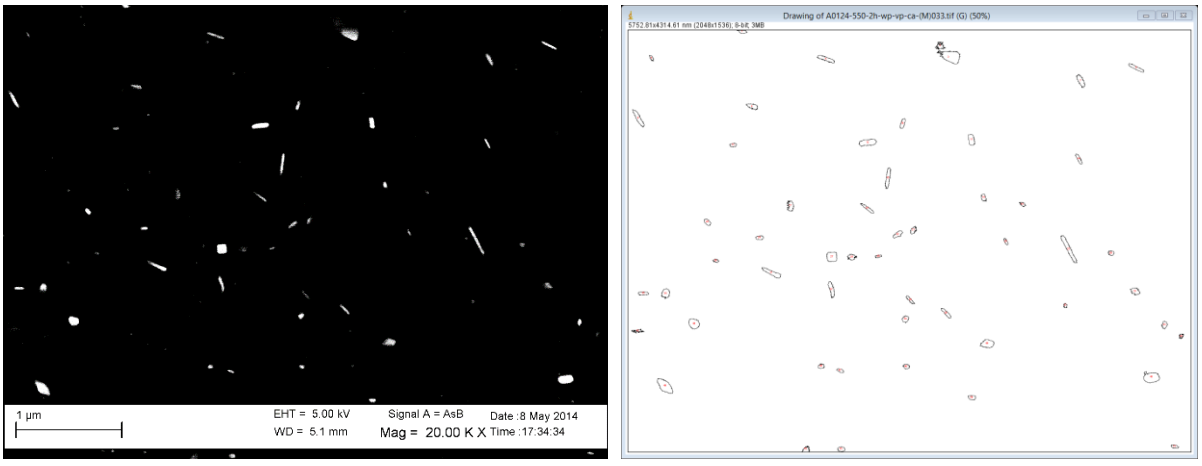

(a) **(b)**

Figure 4-5 An example of dispersoids (a) characterized under FEGSEM and (b) processed using ImageJ®

From Li and Arnberg [71,149] and Anselmino et al [112], the cut off value between dispersoids and constituent particles was at least above 240 nm in equivalent diameter, but the

upper boundary was not defined. Following the work of Lodgaard [65], 200 nm in equivalent radius was chosen as the cut off value for all the homogenized samples.

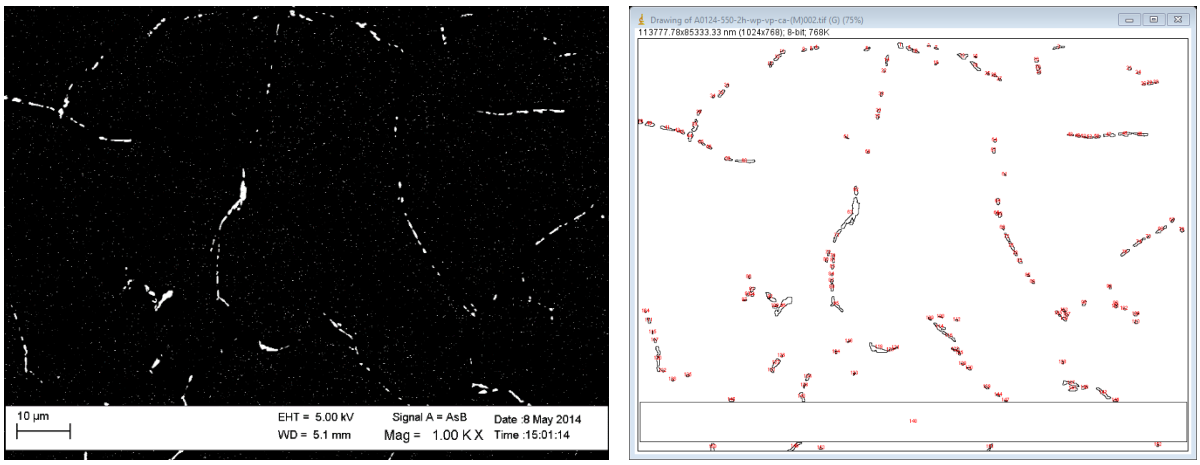

(a) **(b)**

Figure 4-6 An example of constituent particles (a) characterized under FEG-SEM and (b) processed using ImageJ®

TEM specimens were ground from 3 mm to ≈ 0.8 mm in thickness and were punched into 3 mm diameter discs. Jet electro-polishing was conducted in an electrolyte of 30 % nitric acid and 70 % methanol at -45 °C with a voltage of 15 V. The thin foils were examined in the Philips CM12 electron microscope operated at 120 kV for conducting crystallography (selected area diffraction patterns) and size measurements of the dispersoids, selected area diffraction patterns (SADP) analysis was performed using Philips CM12 with an operating voltage of 120 kV. An analysis of the chemical composition for dispersoids was conducted using a JEOL 2010F TEM operating at 200 kV. The STEM mode was utilized for an EDS chemical analysis. The EDS was performed by Oxford X-ray energy-dispersive spectrometer (Inca model 6498). One specific purpose is to characterize the same dispersoid by chemical composition using EDS and crystal structure using SAD patterns and to confirm if there is any correlation between them in the samples. The SAD pattern for crystal structure analysis was performed in CM12 convention

TEM, which has stage with a high rotation angle but without the EDS equipment. After obtaining SAD patterns and images of dispersoid at high magnifications, the same foil was transferred to JEOL2010F high resolution TEM equipped with EDS, to measure chemical composition cross dispersoid by using the STEM model for getting high resolution.

Quantitative measurements on the dispersoid size and distribution were conducted using ≈10 fields of observation in samples, where about 1000 dispersoids were measured for each of the conditions. For the sake of simplification, the measurements of projection area by using Image-Tool® software were converted to an equivalent radius and assuming that the orientation of dispersoids were distributed randomly.

In order to extract constituent particles for X-ray diffraction (XRD) analysis, the as-cast and homogenized samples were cut into thin slices with a thickness of 0.5 mm. The aluminum matrix was dissolved in phenol at 170 °C; dissolution was complete in ≈30 minutes. Benzyl alcohol was added to the warm phenol solution containing the constituent particles and it was centrifuged at 10,000 rpm for 10 minutes. The constituent particles were collected and dried for XRD analysis. A fine-focus Co X-ray tube (operated at 35 kV and 40 mA) was used in a Bruker D8 diffractometer and the sample of particles was scanned through a range of 2θ from 5 to 80° with CoK_{α} x-rays. X-ray powder-diffraction data was analyzed using the Rietveld approach (program Topas 4.2 Bruker AXS) to obtain quantitative content of each phase. One example for the quantitative analysis of the constituent particles using Rietveld method was shown in Figure 4.7 for 0.5Mn as-cast sample.

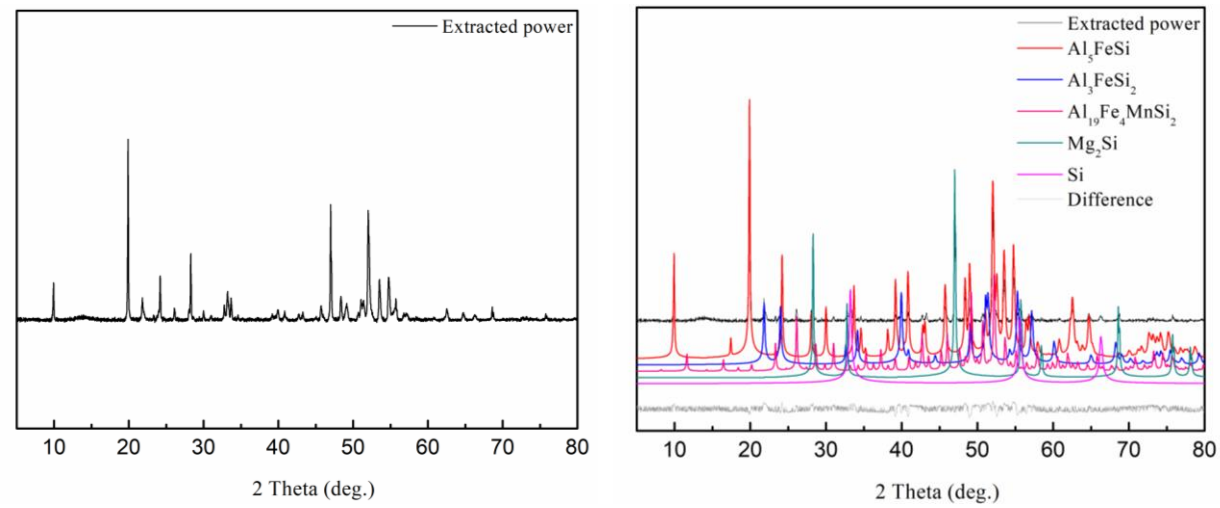

(a) **(b)**

Figure 4-7 XRD diffraction data measured for 0.5Mn alloy (a) on the as-cast sample and (b) on the as-cast sample with the Rietveld analysis

4.3.4 Microsegregation

Electro probe micro analysis (EPMA) is used to analyze the distribution of Mg, Si, Fe, Mn and Cr in the four alloys for the as-cast and homogenized conditions. The EPMA measurements were conducted on a fully automated CAMECA SX-50 instrument, operating in the wavelength-dispersion (WDS) mode. The samples were first cold mounted, grounded, polished and then carbon coated for a period of 24 h before the test. The accelerating voltage is 15 kV and beam current is 20 nA with a beam size of 1 μm. The interaction volume of each measurement was calculated based on the CASINO Monte Carlo software [150], where the interaction diameter is estimated to be 2 to 3 μm as shown in Figure 4.8.

Three to five random lines about 250-300 μm in length were selected in the samples for measurement. More than 200 points were covered in each specimen, where the contents of Al, Mg, Si, Mn, Fe and Cr were measured according to the standards of a known composition in the microprobe [151].

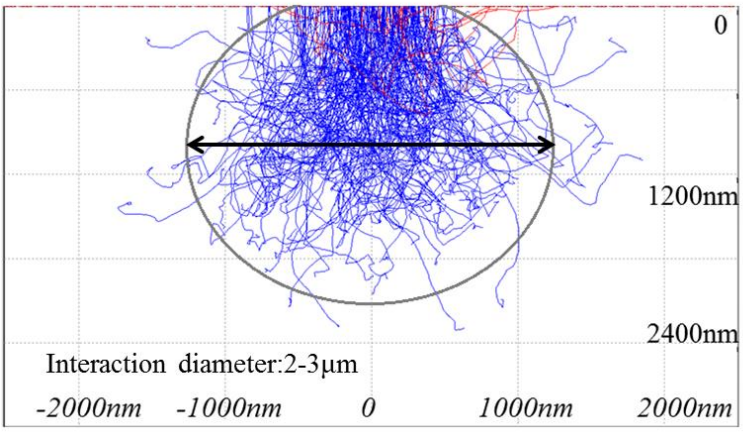

Figure 4-8 The interaction volume calculation with the CASINO Monte Carlo software

4.4 Flow stress measurements

A Gleeble® 3500 thermo-mechanical simulator with ISO-T compression plates was used for the high temperature compression tests, as shown in Figure 4.9. A small amount of nickel paste was manually and uniformly added between the tungsten carbide anvils and the compression samples, i.e. it served as the lubrication during the high temperature compression tests. The change in diameter of the compression sample was measured using a c-strain dilatometer.

The true strain and true stress are calculated using the following equations:

$$\varepsilon = 2\ln\left(\frac{d_0}{d_0 + \Delta d}\right) \tag{4-1}$$

$$\sigma = \frac{F}{\left(\frac{\pi(d_0 + \Delta d)^2}{4}\right)} \tag{4-2}$$

where d_0 is the initial diameter of before high temperature compression (where thermal expansion was considered and d_0 is the sum of initial diameter and the increase due to thermal

expansion at the target deformation temperature), Δd is the change of the diameter and F is the force.

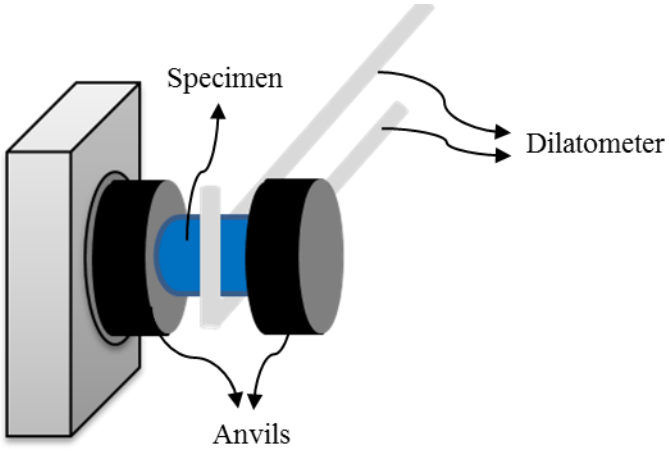

Figure 4-9 Schematic of the jaw set up for high temperature compression in the Gleeble® 3500

High temperature compression tests were conducted on the four alloys with four homogenization conditions shown in Table 4.4.

Table 4.4 Homogenization conditions for high temperature compression tests

	550 ºC	580 ºC
0Mn	2 h	2 h, 12 h
0.25Mn	2 h	2 h, 12 h
0.5Mn	2 h	2 h, 12 h
0.5Mn0.15Cr	2 h	2 h, 12 h, 168 h

Deformation temperatures of 550 °C and 580 °C were selected, i.e. above the Mg_2Si solvus and below the melting point; strain rates were chosen as 1 s^{-1} and 10 s^{-1}. A much lower strain rate of 0.01 s^{-1} was also used for the 0.5Mn0.15Cr alloy homogenized at 580 °C for 168 h. A constant heating rate of 5 °C/s was applied until the sample reached the test temperature where it was held for 1 minute prior to testing. A deformation true strain to 0.7 was imposed. The temperature history was controlled by a K-type thermocouple which was welded to the centre of the compression samples. An example of the thermal history is shown in Figure 4.10, where the

temperature deviation during holding and deformation was ± 1 ºC and ± 2 ºC for the strain rate 1 s^{-1}, respectively. The temperature increase during deformation was ≈5 ºC under the strain rate 10 s^{-1}.

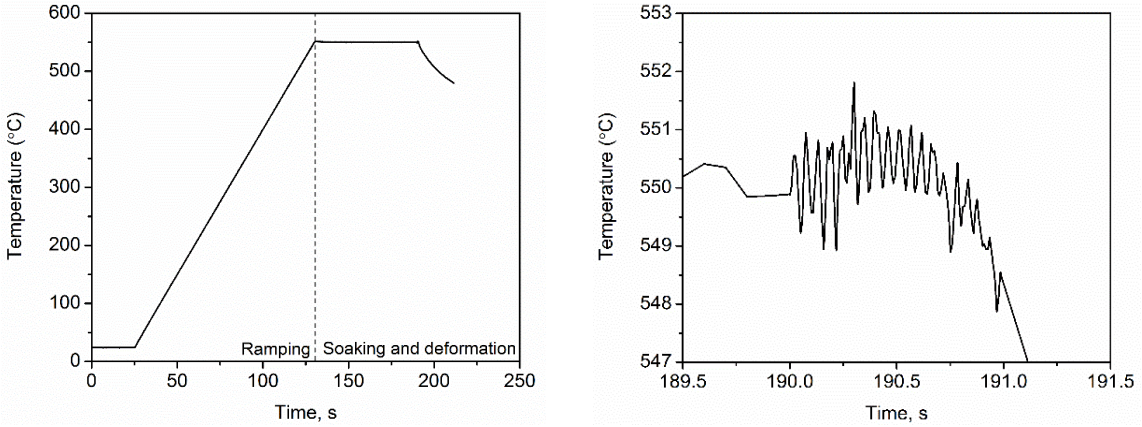

(a) **(b)**

Figure 4-10 An example of the monitored temperature history in the Gleeble® 3500 thermo-mechanical simulator (a) during ramping, soaking and deformation (b) during high temperature compression

Two compression tests were conducted for each of the conditions and Figure 4.11 shows an example of a sample before and after deformation.

Figure 4-11 Pictures of samples taken before and after the high temperature compression test

After each test, the maximum diameter and height of the sample were measured on the sample as shown in Figure 4.11, in order to calculate the degree of barreling due to the friction between the sample and the anvils.

The characterization of barreling was done using

$$B = \frac{h_0 \times d_0^2}{h_f \times d_f^2} \tag{4-3}$$

where h_0 and d_0 are the initial height and diameter of the compression sample; h_f and d_f are the corresponding dimensions after deformation at the centre of the samples. The barreling values were found to be in the range of 0.90 to 0.92, which according to previous work [152], is in the range where a correction for friction is not necessary.

4.5 Extrusion trials

The pilot scale extrusions trials were conducted in Rio Tinto Research and Development Centre (ARDC) in Arvida, Quebec with a fully instrumented 850-ton extrusion press. The extrusion billets were prepared according to the chemistry shown in Table 4. Two homogenization treatments, 2 h at 550 °C and 12 h at 580 °C, were conducted on the cast billets prior to the extrusion. Each billet was induction heated to 500 °C just before the extrusion trial. The ram speed of the extrusion trials varied from 3 mm/s to 8 mm/s. The mean strain rate during extrusion was calculated as:

$$\dot{\varepsilon}_m = \frac{6D_B^2 V_{ram} \ln R}{D_B^3 - D_E^3} \tag{4-4}$$

where V_{ram} is the extrusion speed (mm/s), R is the extrusion ratio (70), and D_B and D_E are the initial diameters of the billet and the extrudate diameter, respectively [9].

For each trial, the extrusion pressure and exit temperature were recorded. Later, the extrusion pressure P_{ext} was converted into extrusion force F_{ext} using

$$F_{ext} = P_{ext} \times (A_{main} + A_{side}) \quad (4\text{-}5)$$

where A_{main} is the surface area of the main cylinder (3318 cm^2) and A_{side} represents the two combined side cylinders (402 cm^2).

5. Experimental Results

This chapter provides a description of how the microstructure evolution occurs during different homogenization scenarios for four alloys (0Mn, 0.25Mn, 0.5Mn and 0.5Mn0.15Cr). This includes the dissolution of Mg_2Si, the transformation of the constituent particles and the formation of Mn/Cr containing dispersoids. The key microstructure features from different homogenization treatments are quantified, with a particular focus on the dispersoids. Finally, the high temperature flow stress of the alloys has been measured by the compression tests for a range of homogenization conditions.

5.1 Characterization of the initial materials

The samples cut from the as-cast billets were anodized to reveal the grain structure. Figure 5.1 shows optical micrographs for the microstructure of the four alloys under polarized light after anodizing. The as-cast microstructure consists of equiaxed grains with dendrites that are observed within the grains.

The grain size and secondary dendrite arm spacing were measured and have been summarized in Table 5.1. The results show that the initial average grain size for the four alloys ranges from 100-121 μm and the secondary dendrite arm spacing (SDAS) is 17-20 μm. As the cooling rate during solidification can be associated with the SDAS [41], it suggests that the solidification conditions were similar for the four AA6082 based alloys in this study. This is consistent with the information provided by Rio Tinto Aluminum [153].

It is generally understood that the as-cast microstructure has a range of non-equilibrium phases, since the DC casting process is far from the equilibrium [106]. Backscatter images were taken with a field emission gun scanning electron microscope (FEGSEM) in order to observe the

morphology of the constituent phases, which according to the literature, consist of α-Al(MnFe)Si, β-Al_5FeSi, Mg_2Si, Si and π-AlFeMgSi phases depending on the bulk chemistry [40,59,63].

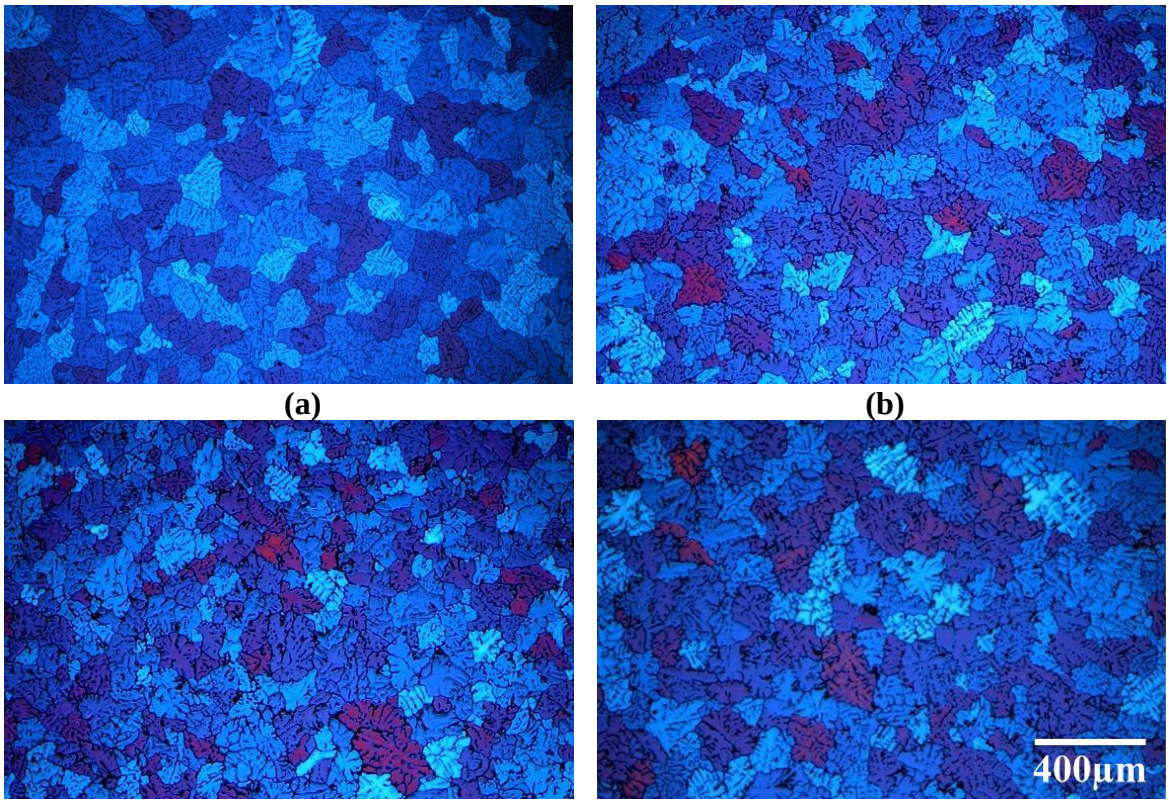

Figure 5-1 Anodized microstructure observed under polarized light with an optical microscope for the as-cast samples of (a) 0Mn alloy, (b) 0.25Mn alloy, (c) 0.5Mn alloy and (d) 0.5Mn0.15Cr alloy.

Table 5.1 Results for equivalent area diameter (EQAD) and the secondary dendrite arm spacing (SDAS) for the as-cast alloys

Designation	Grain size (µm)	SDAS (µm)
0Mn	121	19
0.25Mn	100	20
0.5Mn	103	17
0.5Mn0.15Cr	119	18

Since there is a considerable difference in the atomic number between Mn/Fe and Al, the Mn/Fe bearing constituent particles appear much brighter than the aluminum matrix while using

the backscatter mode. For example, in Figure 5.2a, thin plate Fe bearing constituent particles up to 20 μm in length can be observed in the as-cast sample of 0Mn alloy. These particles have been identified as β-Al_5FeSi using X-ray diffraction analysis (XRD) on extracted particles as shown in Table 5.2. In addition, the dark black particles indicated by white arrows can be seen to be located close to the Fe/Mn bearing constituent particles in Figure 5.2. Couto et al. [154] have identified that these particles are Mg_2Si. It is worth noting that these black particles could be caused by either selective etching of Mg_2Si from silica colloidal or pull-out of Fe bearing constituent particles. However, the presence of Mg_2Si is confirmed by the XRD analysis on the extracted particles after dissolving the aluminum matrix in Table 5.2. Thin plate constituent particles can also be observed in the as-cast samples for the alloys with Mn and Cr, see Figures 5.2b to 5.2d. These particles have been identified predominantly as the β-Al_5FeSi phase (see Table 5.2), and Mg_2Si particles were also found near the Fe/Mn constituent particles (see Figure 5.2b, 5.2c and 5.2d). The presence of the Mg_2Si is confirmed by the XRD analysis on the extracted particles as shown in Table 5.2.

Table 5.2 Results of quantitative phase analysis (wt.%) using the Rietveld approach for the fraction of phases in the extracted powder from the as-cast materials

Alloy	Mg_2Si	Si phase	β-Al_5FeSi	δ-Al_3FeSi_2	π-$Al_{8.64}FeMg_{3.36}Si_5$	α-$Al_{19}Fe_4MnSi_2$ (SC)
0Mn as-cast	16.8	10.5	57.9	5.3	9.5	-
0.25Mn as-cast	15.3	7.1	67.3	10.2	-	-
0.5Mn as-cast	18.4	6.1	52.0	13.3	-	10.2

Moreover, the XRD analysis also identifies the presence of Si, δ-Al_3FeSi_2 and π-$Al_{8.64}FeMg_{3.36}Si_5$ phases. The Si phase was determined to be in all the as-cast materials an observation that is consistent with the literature on as-cast materials [40,59,63]. The δ-Al_3FeSi_2

phase has a Fe to Si ratio of 1:2, which is close to the phase determined by EDS such as $Al_{21}Fe_3Si_5$ [63] and $AlFeSi_2$ [74], which have been observed in alloys having a high Si content similar to AA6082. The π-AlFeMgSi phase is only found in the 0Mn alloy from the XRD analysis in agreement with the work of Sweet et al [40] and Couper et al [59].

In summary, it can be said that the as-cast structure is dominated by plate-shaped constituent particles and a smaller fraction of Mg_2Si and Si particles in all alloys. It is understood that the plate shaped particles (α-AlFeMnSi and β-Al_5FeSi phases) are detrimental to high temperature extrusion [25]. As a result, the extrusion is always done after a homogenization treatment. The objectives of the homogenization treatment are i) To dissolve the coarse Mg_2Si particles so that Mg and Si are available to precipitate later in the process, ii) remove the micro segregation and iii) in some cases (Mn containing alloys) modify the constituent particles.

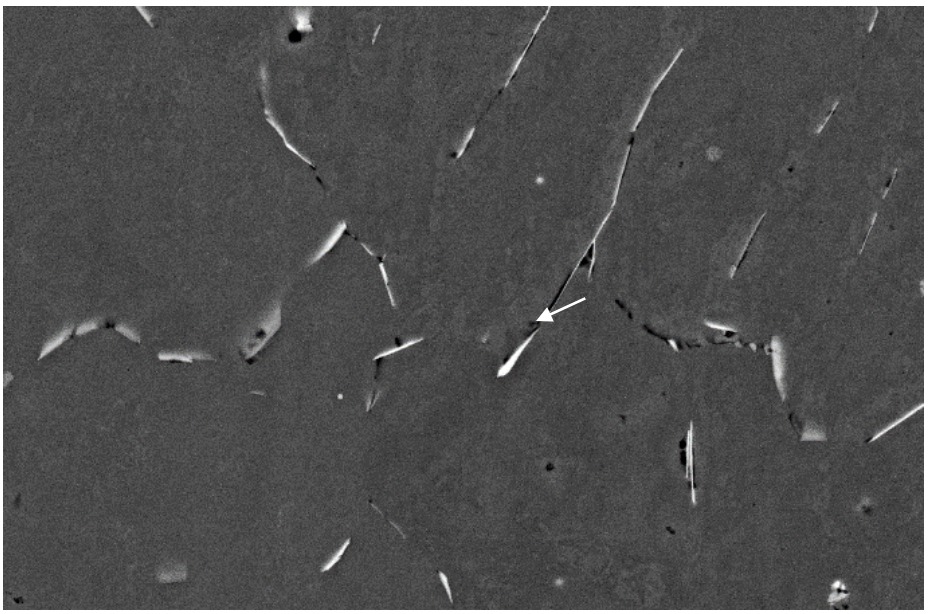

(a)

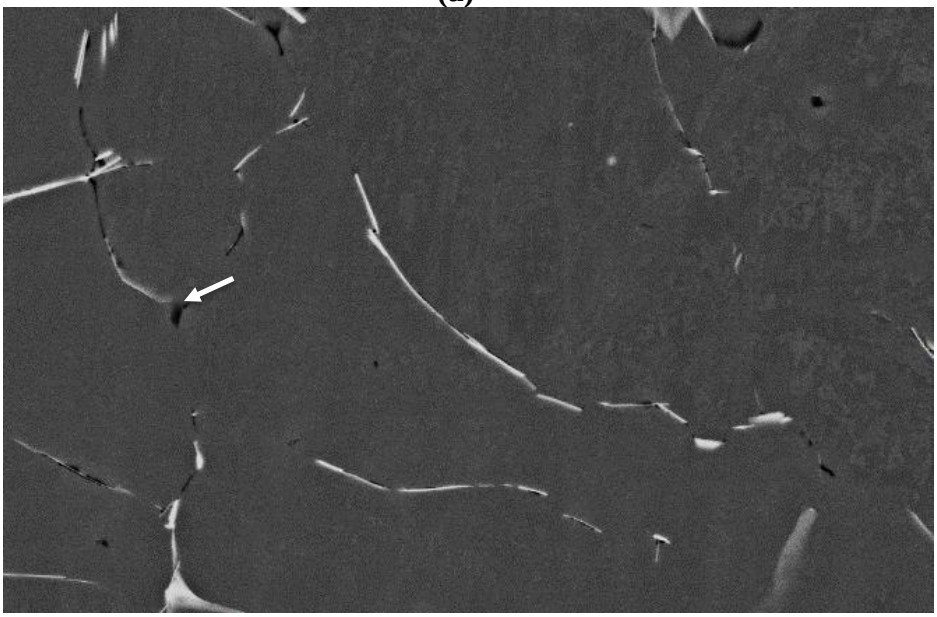

(b)

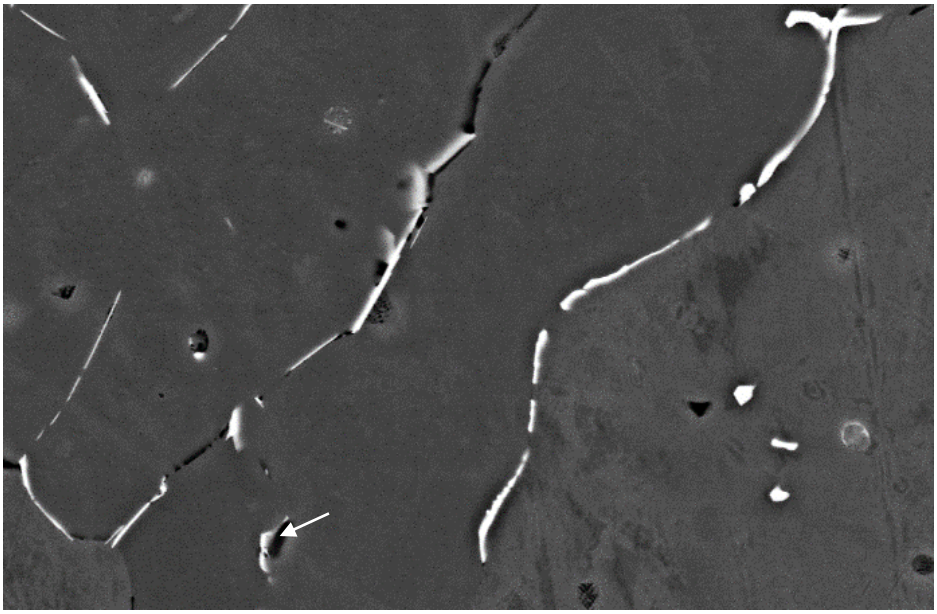

(c)

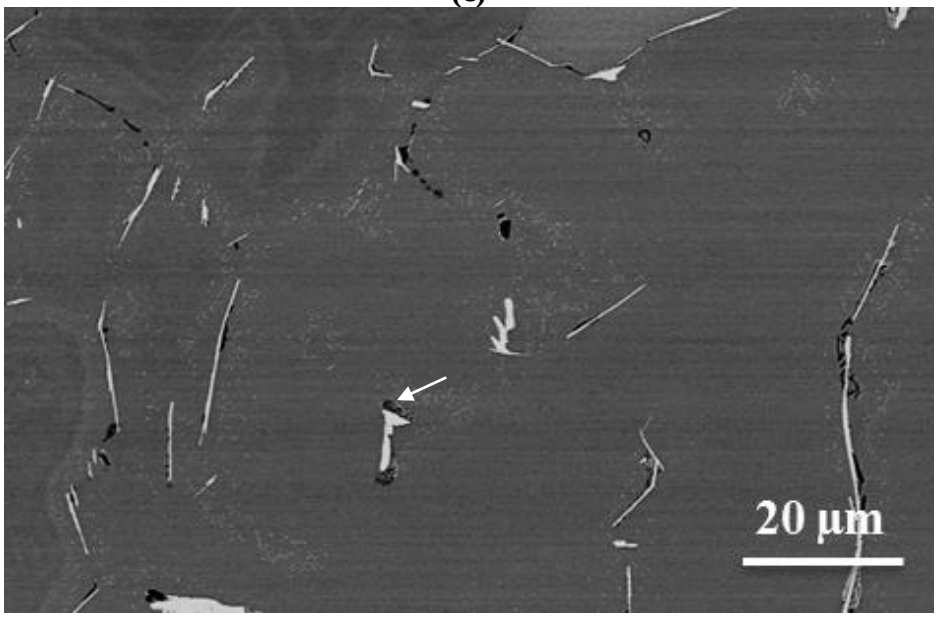

(d)

Figure 5-2 FEGSEM (backscatter mode) micrographs of constituent particles in the as-cast sample of (a) 0Mn alloy, (b) 0.25Mn alloy, (c) 0.5Mn alloy and (d) 0.5Mn0.15Cr alloy

5.2 Dissolution of Mg_2Si

The dissolution of the Mg_2Si particles formed during direct chill (DC) casting was investigated using the electron probe microanalysis (EPMA) and electrical resistivity measurements. As introduced earlier in the methodology (see section 4.2), the homogenization conditions were chosen above the Mg_2Si solvus, but below the solidus temperature. An industrial relevant heating rate 200 °C/h was chosen for all the homogenization scenarios. The backscatter images for the four alloys has been shown in Figure 5.3 (i.e. dark black particles) and it displays no evidence of undissolved Mg_2Si after the alloys were held for 10 minutes at 550 °C.

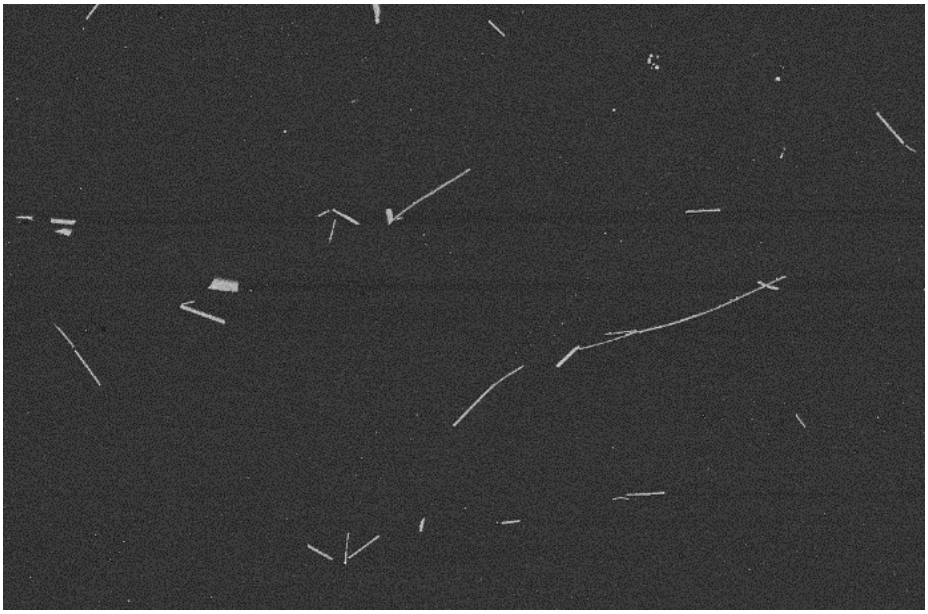

(a)

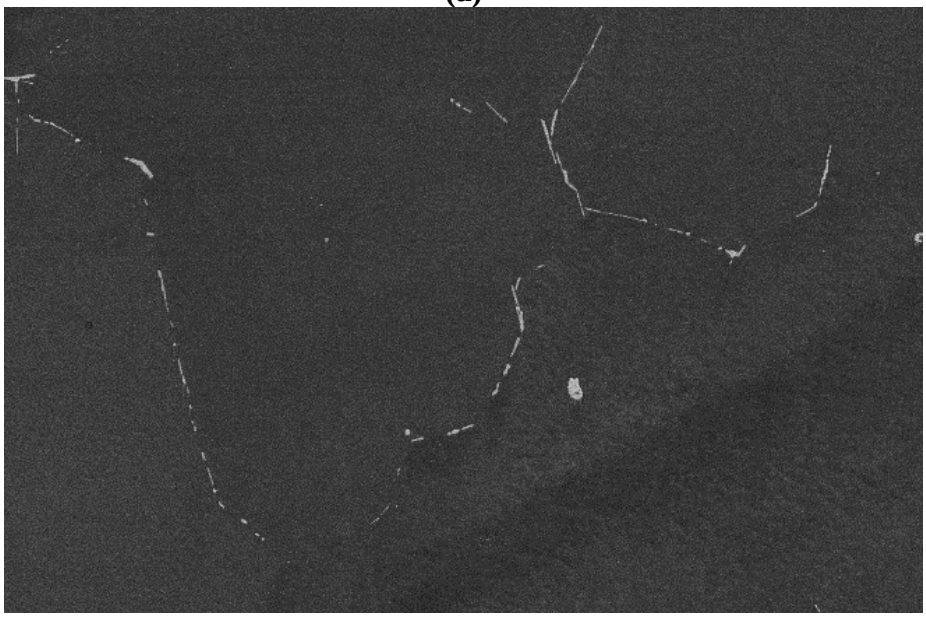

(b)

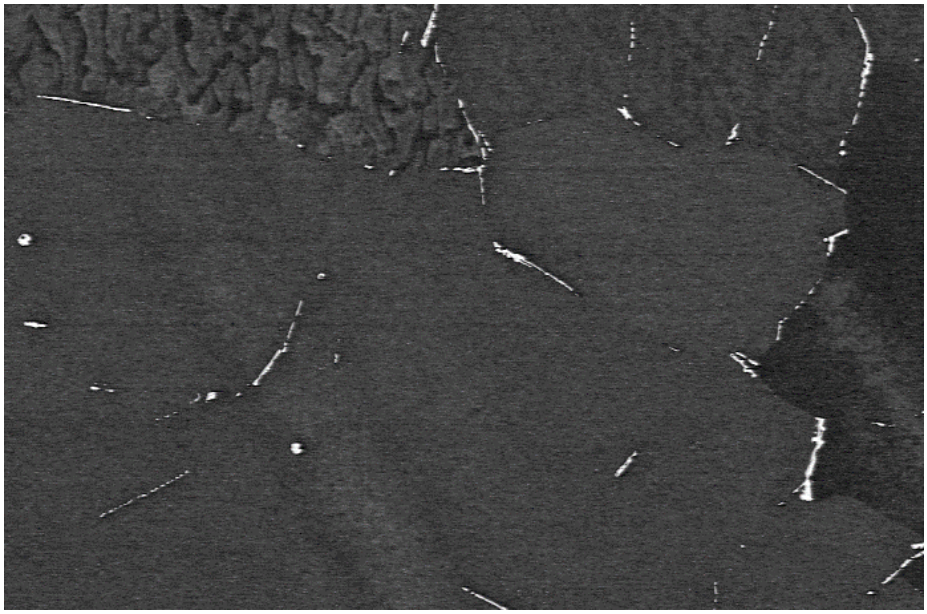

(c)

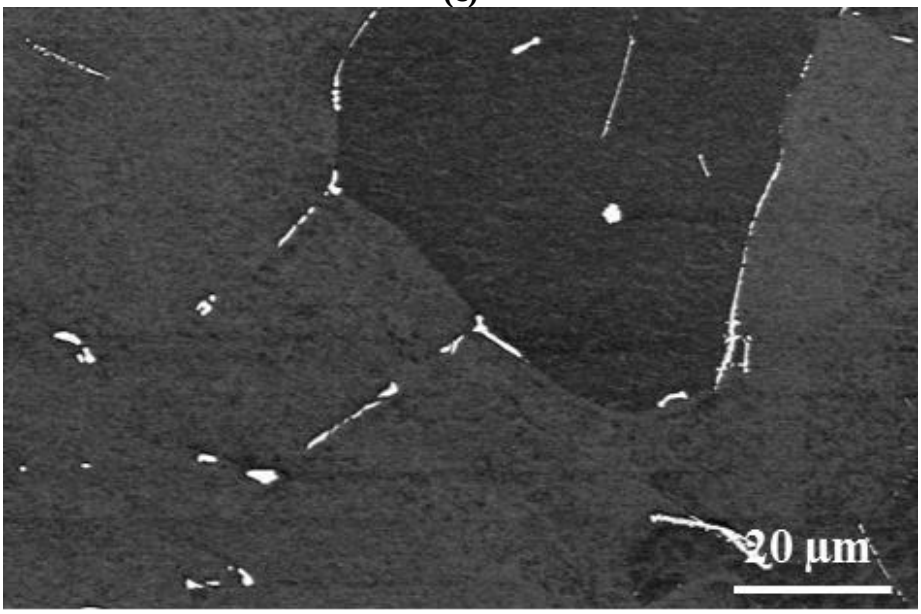

(d)

Figure 5-3 FEGSEM micrographs of constituent particles in the samples homogenized at 550 ºC for 10 min of (a) 0Mn alloy, (b) 0.25Mn alloy, (c) 0.5Mn alloy and (d) 0.5Mn0.15Cr alloy

The dissolution of Mg_2Si precipitates was further studied using the microprobe analysis (EPMA) and electrical resistivity measurements. To quantitatively determine the degree of micro-segregation for Mg, the EPMA line scans were conducted on the as-cast 0Mn samples, at the end of the heating ramp (i.e. 0 minute at 550 °C), and after 10 minutes and 2 h at 550 °C as shown in Figure 5.4a. Here, it can be observed in Figure 5.4a that there is a large range of Mg concentrations in the as-cast sample and there are four large peaks marked A to D. It should be noted that the average concentration of Mg from the microprobe measurements is 0.68 wt.%, i.e. very close to the nominal chemistry of 0.71 wt.% (see Section 4.1).

It can be observed in Figure 5.4b that the peaks marked A-D in Figure 5.4a also display high Si contents strongly suggesting that these peaks are associated with Mg_2Si. There are also peaks marked E-G in Figure 5.4b which do not have Mg associated with them, i.e. most likely Si particles or constituent particles. This is consistent with the results on the extracted particles in the as-cast material (Table 5.2). Ramping from room temperature to 550 °C leads to a significant reduction in the variation of the Mg content, and one large peak remains (denoted by D). This suggests that there is a redistribution of Mg and dissolution of Mg_2Si but indicates that the dissolution of Mg_2Si is not complete, i.e. peak D still remains both in Figure 5.4a and 5.4b.

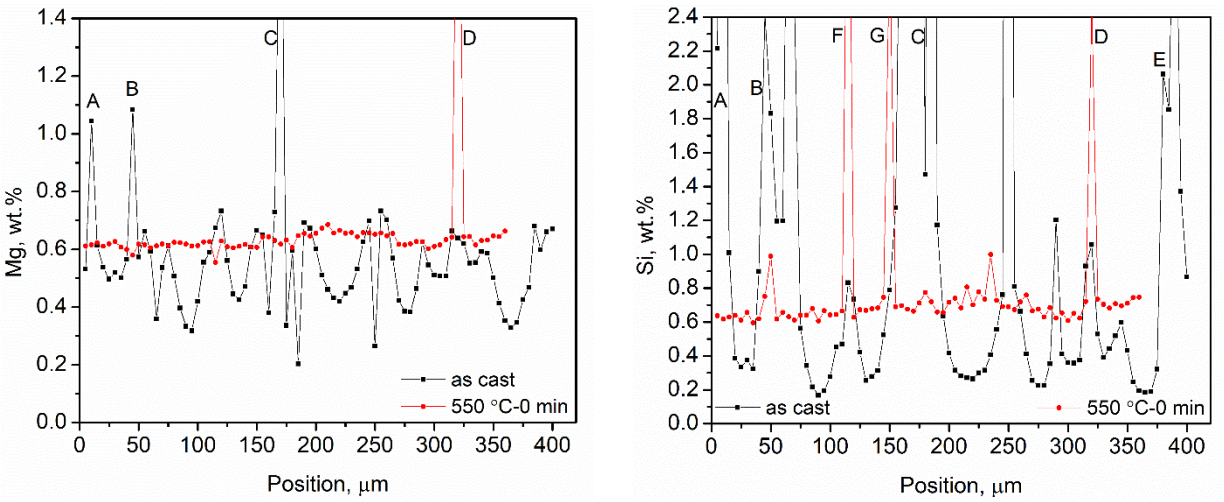

(a) **(b)**

Figure 5-4 (a) Evolution of the original Mg profiles and (b) Evolution of the corresponding Si profiles during homogenization at 550 °C in 0Mn alloy from EPMA line scans.

However, Figure 5.5a shows that holding at 550 °C for 10 minutes shows a slightly higher average Mg level and the absence of any Mg peaks. This is likely due to further dissolution of Mg_2Si in Figure 5.5a. A further increase of in the holding period to 2 h, results in little further change suggesting that the Mg_2Si was mostly dissolved after 10 minutes at 550 °C.

The dissolution of Mg_2Si particles was also inferred in an indirect manner from the electrical resistivity measurements. The resistivity values of the as-cast materials for 0Mn, 0.25Mn and 0.5Mn alloys are 37.0, 44.1 and 50.4 nΩ·m, respectively. The major difference in resistivity among the as-cast samples is due to the different Mn levels, where the resistivity increases with the higher Mn contents as shown in Figure 5.5b. The resistivity drops substantially after ramping from room temperature to 550 °C because of the decomposition of Mn from supersaturation to form dispersoids [70]. In comparison, it is observed that the resistivity change from as-cast to the end of the heating ramp is marginal for 0Mn alloy in Figure 5.5b. As can be seen, there is a small increase in the resistivity from the measurement made at the end of ramp to that after 10 minutes holding at 550 °C accounting for the dissolution of

Mg_2Si and then the resistivity shows a very little change as the holding time increases to 20 minutes.

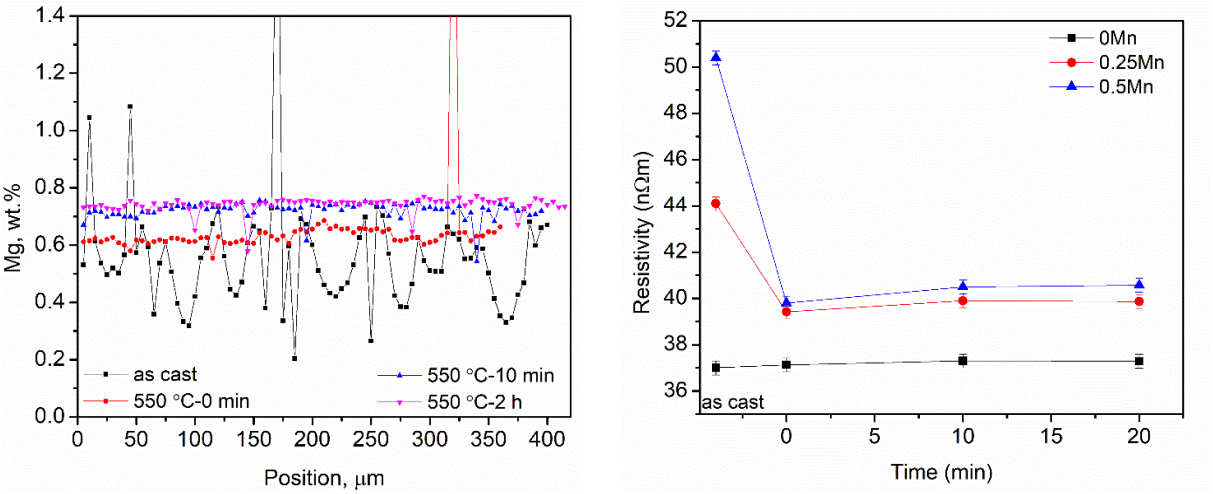

(a) **(b)**

Figure 5-5 (a) evolution of the Mg profiles during homogenization at 550 °C in the 0Mn alloy including the as-cast; (b) electrical resistivity measurement for the three alloys for up to 20 min soaking at 550 °C after the ramp.

It has been shown that during heating and holding at the homogenization temperature after that, the Mg content in the matrix increases as a result of the dissolution of Mg_2Si and the segregation profile of Mg/Si is flattened. Both the processes depend on the diffusion of Mg, and therefore it is of interest to compare the characteristic diffusion length $\sqrt{D_{Mg} \cdot t}$ with the scale of the microstructure as characterized by the SDAS, where D_{Mg} is the diffusion coefficient (see Table 2.2 in Section 2.2) at the relevant temperature [86]; i.e. in this case, it would be 550 °C. The determination of $\sqrt{D_{Mg} \cdot t}$ after holding at 550 °C for 10 minutes gives 21 μm, which is larger than half of the average SDAS (≈10 μm) that is measured in the as-cast samples, confirming that this is sufficient time for Mg redistribution to occur resulting in the almost flat Mg profile seen in Figure 5.5a.

5.3 Evolution of Fe bearing constituent particles during homogenization

As mentioned earlier, another objective of the homogenization practice is bringing about the modification of the Fe containing constituent particles. In order to examine the effect of the homogenization temperature and time on the evolution of the constituent particles, four homogenization conditions i.e. 2 h at 550 °C, 2 h at 580 °C, 12 h at 580 °C and 168 h (7 days) at 580 °C, were chosen for the study. These results for the four alloys will be presented in the following.

0Mn alloy

In the 0Mn alloy, Figure 5.6 shows that there is little obvious change in the morphology of the Fe containing intermetallic particles between the samples with different homogenization treatments. During the homogenization treatment for the 0Mn alloy, the β-Al_5FeSi phase is very stable. This is also consistent with the quantitative results in Table 5.3, which used XRD analysis on the extracted particles to show that almost all the constituent particles are the β-Al_5FeSi type and with less than 4 % of α-Al(FeMn)Si type constituent particles after homogenization for 12 h at 580 °C.

Table 5.3 Results of the quantitative phase analysis (wt.%) using the Rietveld approach for the fraction of constituent phases in the as-cast and homogenized materials after dissolving the aluminum matrix Note: only the Fe bearing particles are considered for the quantitative analysis.

Alloy	β-Al_5FeSi	δ-Al_3FeSi_2	π-$Al_{8.64}FeMg_{3.36}Si_5$	α-$Al_{19}Fe_4MnSi_2$ (SC)	α-$Al_{19}Fe_4MnSi_2$ (BCC)
0Mn as-cast	79.5	4.8	15.7	-	-
0Mn 580ºC-12h	96.4	-	-	3.6	-
0.25Mn as-cast	87.3	12.7	-	-	-
0.25Mn 550ºC-2h	16.8	-	-	76.9	6.3
0.25Mn 550ºC-4h	4.5	-	-	87.8	7.7
0.5Mn as-cast	71.2	16.8	-	12.0	-
0.5Mn 550ºC-2h	-	-	-	100	-

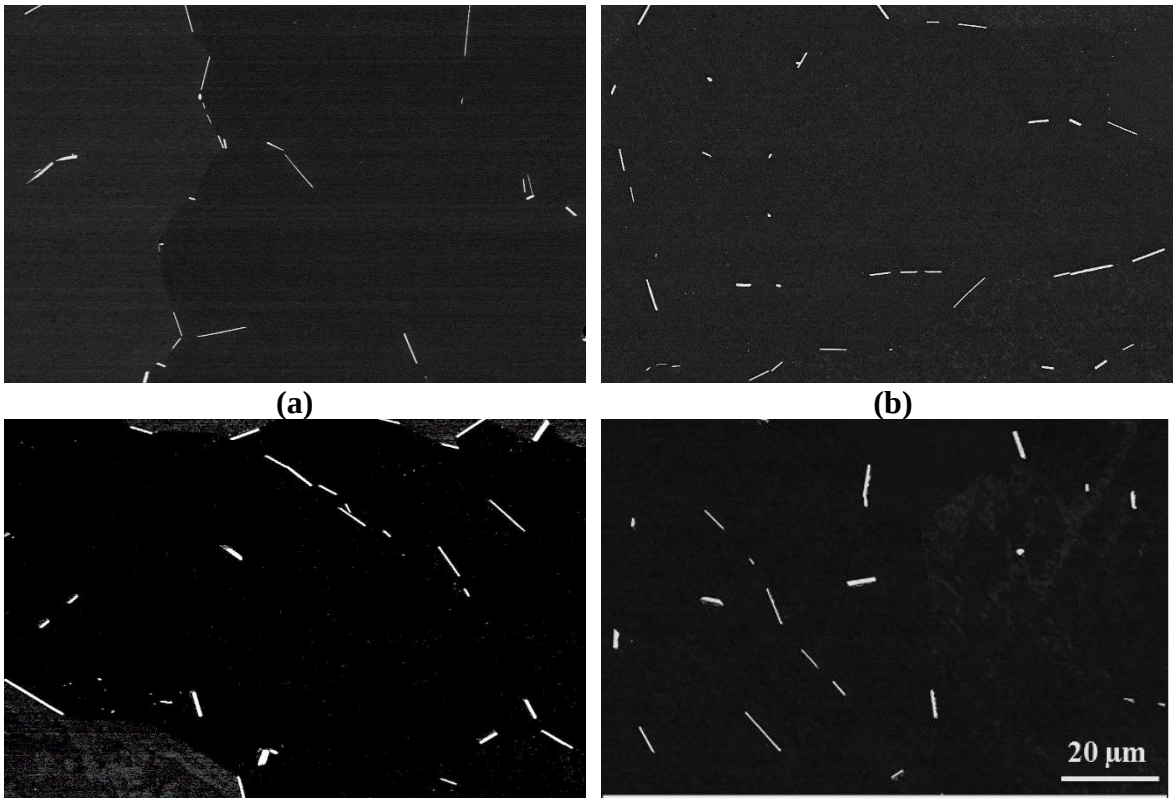

Figure 5-6 FEGSEM micrographs of constituent particles in 0Mn alloys homogenized at (a) 550 ºC for 2 h, (b) 580 ºC for 2 h, (c) 580 ºC for 12 h and (d) 580 ºC for 168 h

Further holding at 580 °C for 168 h (7 days) indicates that the constituent particles remain as plates albeit the appearing to be slightly thicker. The measured thickness and aspect ratio of the plates from the 2D images are reported in Table 5.4.

Table 5.4 Summary of the plate thickness and aspect ratio of the constituent particles in 0Mn alloy

Alloy and homo	Plate thickness, nm	Mean aspect ratio
0Mn-550ºC-2h	363	7.9
0Mn-580ºC-2h	424	6.6
0Mn-580ºC-12h	429	6.3
0Mn-580ºC-168h	619	5.8

0.25Mn alloy

In contrast, Figure 5.7 shows the spheroidization of the plate shaped constituent particles for 0.25Mn after the various homogenization treatments that it goes through. In parallel, the evidence for the phase transformation of the β-Al_5FeSi phase to α-Al(FeMn)Si phase can be observed with the help of the XRD analysis in Table 5.3. The as-cast material has ≈ 80 % of the β-phase, 2 h soaking at 550 °C results in 83% (77 % SC, ≈6 % BCC) of the α-Al(FeMn)Si constituent particles, leaving only 17 % β-Al_5FeSi phase. Further, it is also found that the transformation from β to α is almost complete after 4 h holding at 550 °C, i.e. there is less than 5 % β phase. After spheriodization, the constituent particles show slight coarsening in Figure 5.7 with an increased time at the temperature.

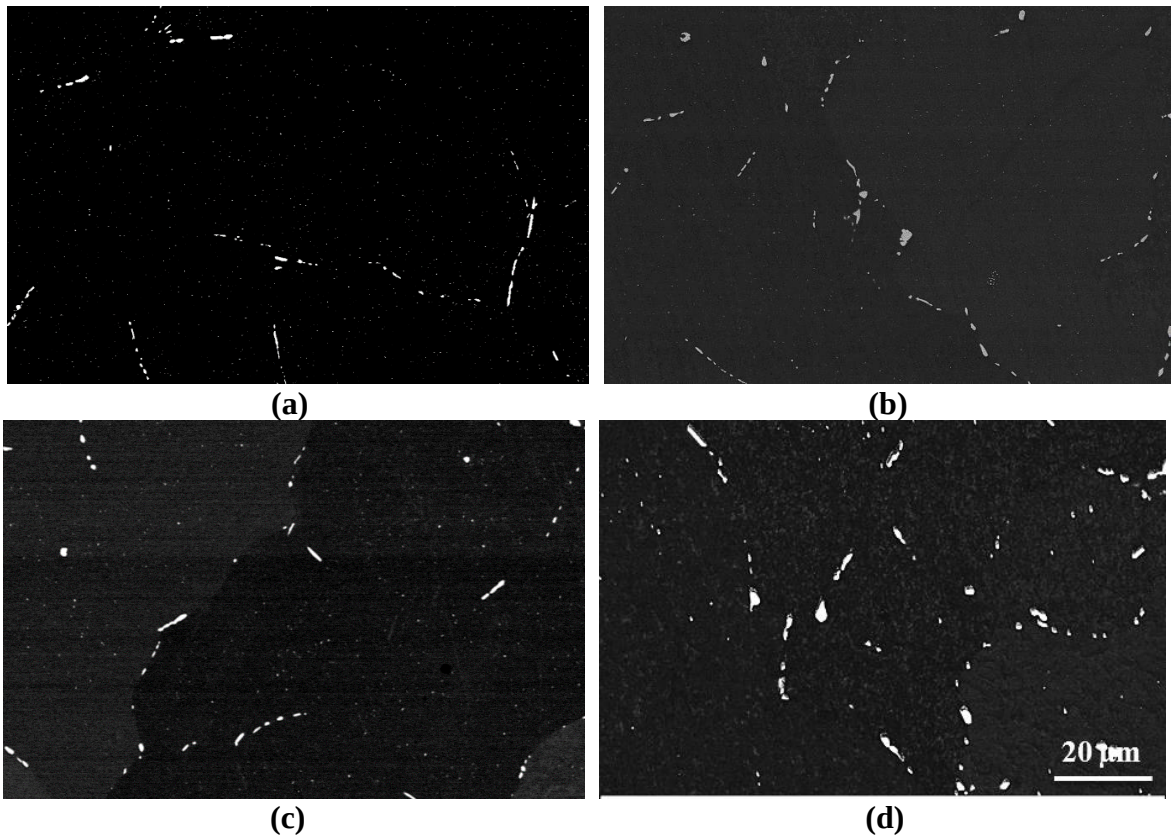

Figure 5-7 FEGSEM micrographs of constituent particles in 0.25Mn alloys homogenized at (a) 550 °C for 2 h, (b) 580 °C for 2 h, (c) 580 °C for 12 h and (d) 580 °C for 168 h

0.5Mn alloy

With an increase in the Mn content to 0.5 wt.%, there is only ≈10% α-Al(FeMn)Si (SC) in the as-cast sample (see Table 5.2) and the transformation kinetics from β-Al_5FeSi to α-Al(FeMn)Si is even faster. According to XRD results in Table 5.3, the complete transformation from β-Al_5FeSi to α-Al(FeMn)Si is observed for a homogenization of 2 h at 550 °C. The FEGSEM micrographs shown in Figure 5.8 illustrate the progression of the change in morphology and size during homogenization.

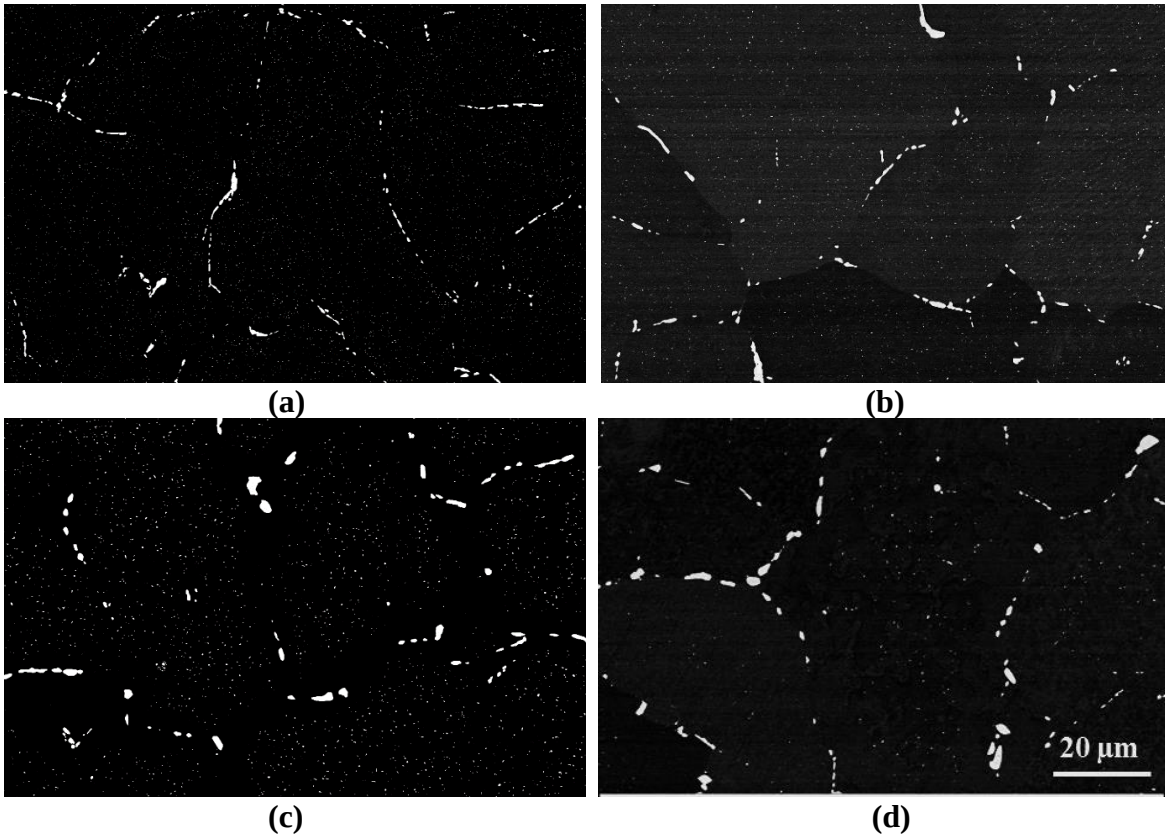

Figure 5-8 FEGSEM micrographs of constituent particles in 0.5Mn alloys homogenized at (a) 550 ºC for 2 h, (b) 580 ºC for 2 h, (c) 580 ºC for 12 h and (d) 580 ºC for 168 h

It can be observed that a higher degree of spheroidization was observed for the 0.5Mn alloy with increasing homogenization temperature from 550 ºC to 580 ºC and longer soaking time from 2 h to 12 h.

0.5Mn0.15Cr alloy

Spheriodization of the constituent particles was also found in the 0.5Mn0.15Cr alloy. The speriodization was essentially complete after 2 h at 550 °C.

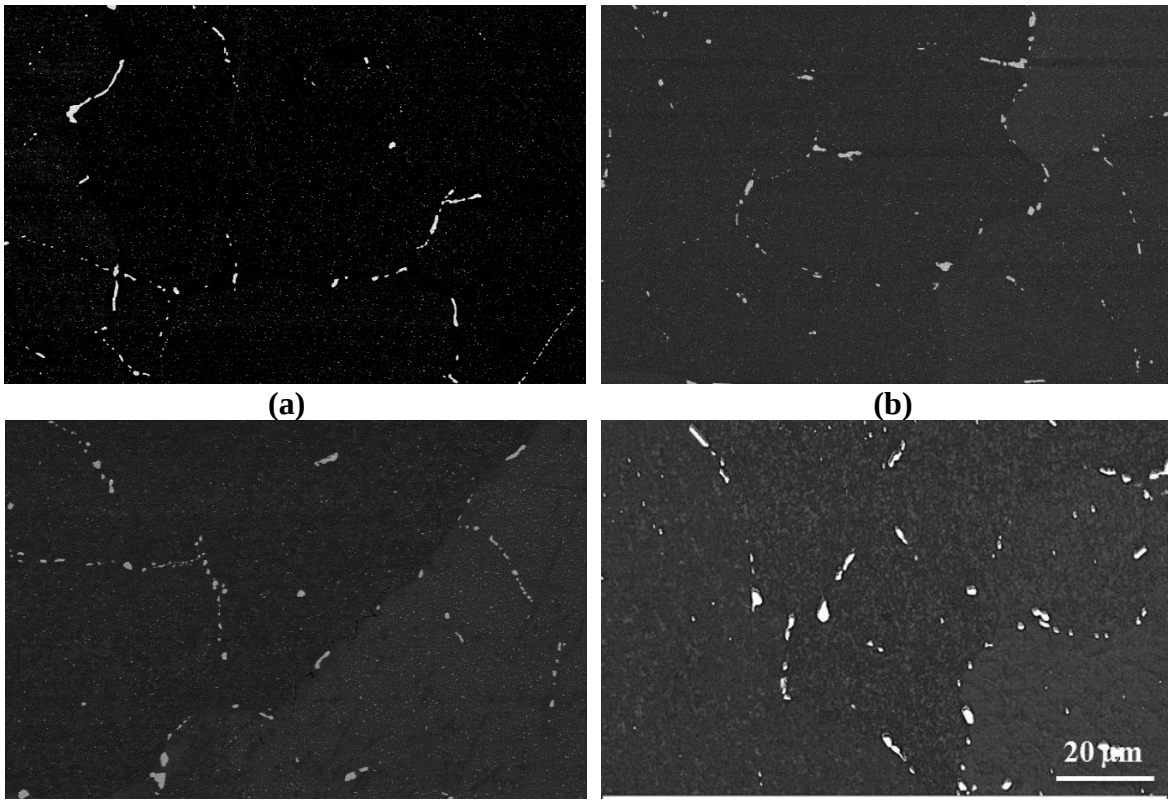

Figure 5-9 FEGSEM micrographs of constituent particles in 0.5Mn0.15Cr alloys homogenized at (a) 550 ºC for 2 h, (b) 580 ºC for 2 h, (c) 580 ºC for 12 h and (d) 580 ºC for 168 h

In order to quantify the evolution of the constituent particles during homogenizations, quantitative image analysis was conducted on the aspect ratio and mean radius for spherodized cases. One challenge here is to separate the constituent particles from dispersoids. A careful observation of Figure 5.7-5.9 shows that in some cases small particles (i.e. the dispersoids) can be seen in the background, i.e. 0.5Mn alloy homogenized at 550 °C for 2 h and 580 °C for 12 h. Figure 5.10 shows measurements using image analysis of all the bright particles for two cases

where dispersoids are clearly present. It can be seen in Figure 5.10 that by choosing a cut-off of >200 nm, the constituent particles can be readily separated from the dispersoids.

The size distributions in the equivalent radius of the constituent particles are shown in Figures 5.11-5.13.

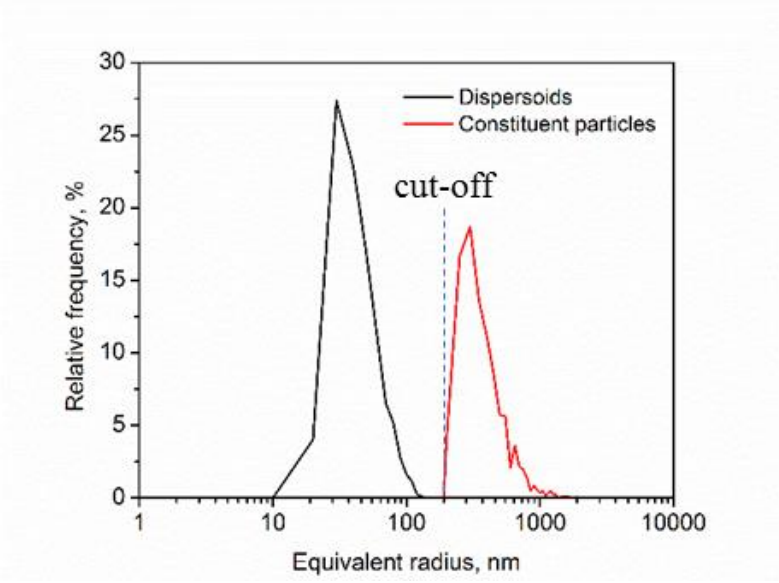

(a)

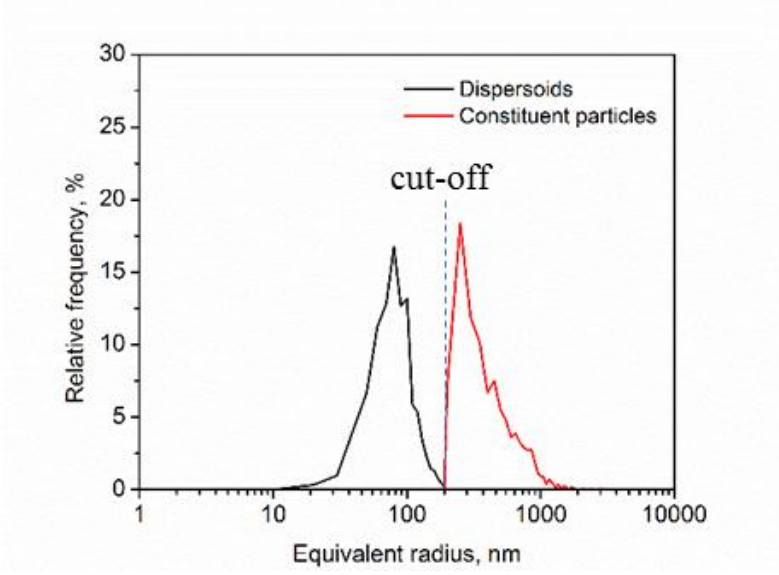

(b)

Figure 5-10 An example of the normalized size distribution of dispersoids and constituent particles (a) 0.5Mn alloy homogenized at 550 ºC for 2 h and (b) 0.5Mn alloy homogenized at 580 ºC for 12 h

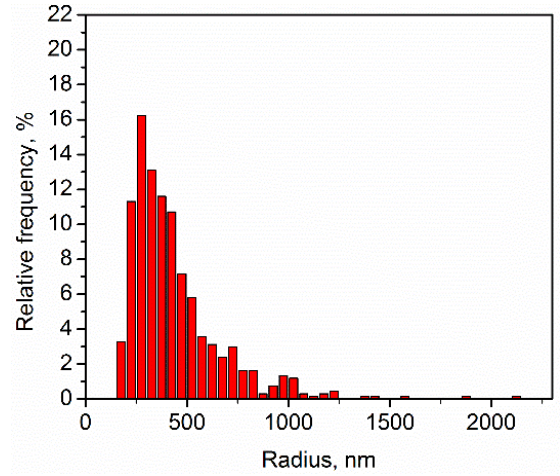

(a)

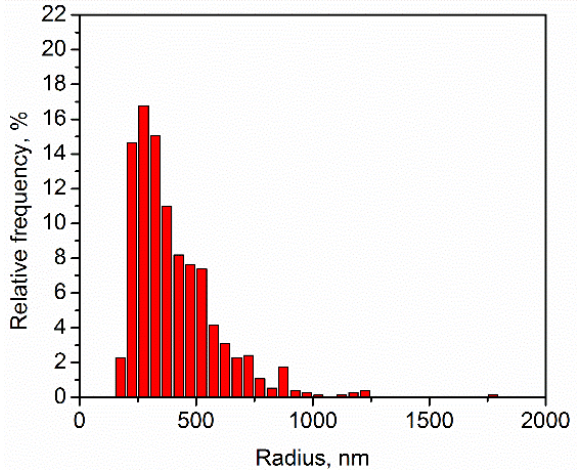

(b)

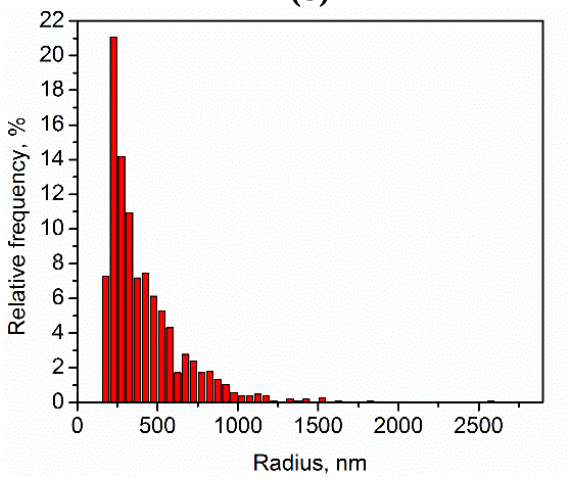

(c)

Figure 5-11 Equivalent radius size distribution of the constituent particles of 0.25Mn homogenized at (a) 550 ºC for 2 h, (b) 580 ºC for 2 h and (c) 580 ºC for 12 h

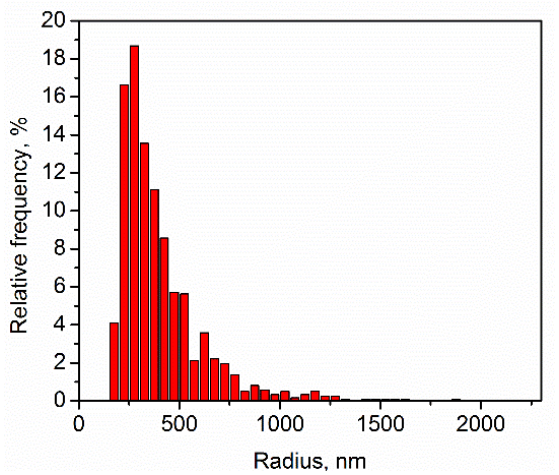

(a)

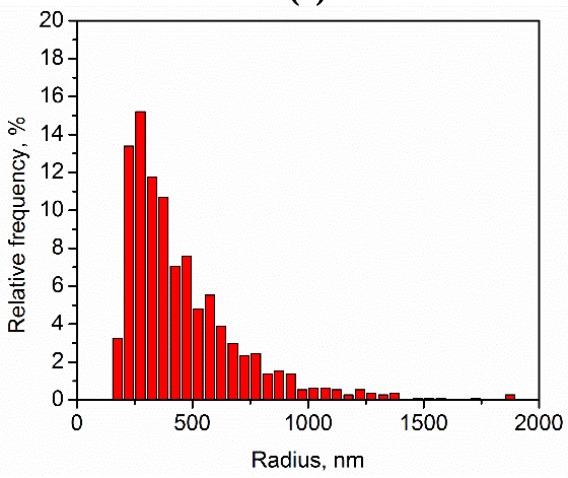

(b)

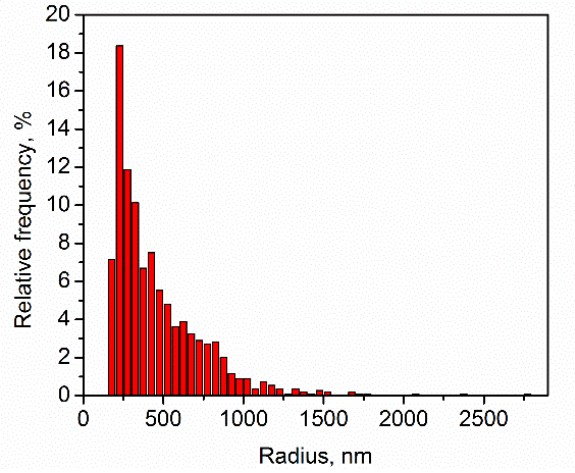

(c)

Figure 5-12 Equivalent radius size distribution of the constituent particles of 0.5Mn homogenized at (a) 550 ºC for 2 h, (b) 580 ºC for 2 h and (c) 580 ºC for 12 h

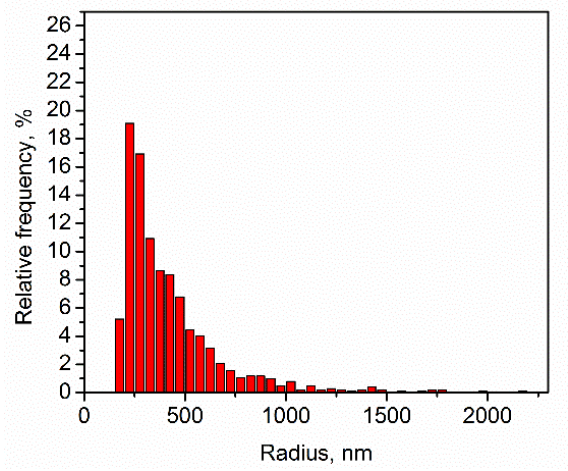

(a)

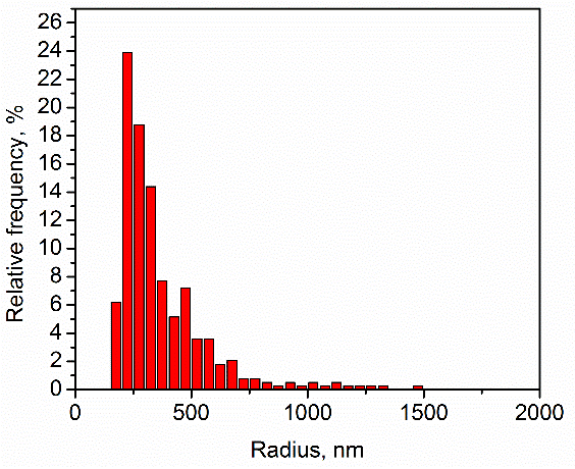

(b)

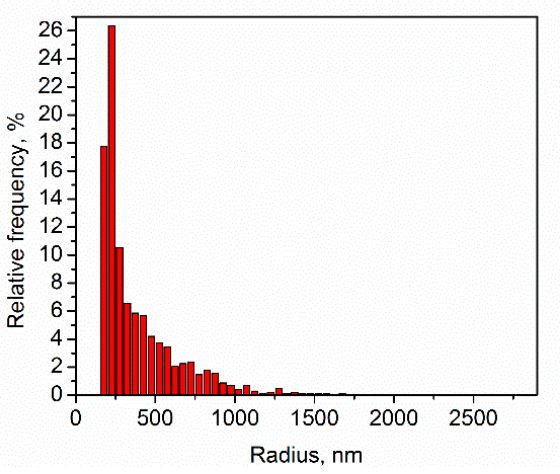

(c)

Figure 5-13 Equivalent radius size distribution of the constituent particles of 0.5Mn0.15Cr homogenized at (a) 550 ºC for 2 h, (b) 580 ºC for 2 h and (c) 580 ºC for 12 h

The mean equivalent radius is provided in Table 5.5, where a comparison of the results clearly indicates that there are only small differences in the equivalent mean radius among the different homogenization conditions. This indicates that the coarsening and growth of the Fe bearing constituent particles is minimal in the Mn and Mn/Cr alloys for homogenization temperatures from 550 ºC to 580 ºC and for a holding time from 2 h to 12 h. It can also be observed that the mean aspect ratio of the particles is ≈2-3 for all homogenization conditions. Finally, it was found that the determination of the volume fraction of the constituent particles from FEGSEM images was challenging due to the problem of choosing a suitable threshold. A new approach on the basis of a mass balance will be presented later in the next chapter (Section 6.1).

Table 5.5 Summary of the mean radius and aspect ratio of the evolution of the constituent particles

Alloy and homo	Mean radius, nm	Mean aspect ratio
0.25Mn-550ºC-2h	436	3.2
0.25Mn-580ºC-2h	405	2.6
0.25Mn-580ºC-12h	413	2.4
0.5Mn-550ºC-2h	399	3.1
0.5Mn-580ºC-2h	446	2.4
0.5Mn-580ºC-12h	459	2.3
0.5Mn0.15Cr-550ºC-2h	419	3.2
0.5Mn0.15Cr-580ºC-2h	367	2.4
0.5Mn0.15Cr-580ºC-12h	382	2.3

5.4 Dispersoids size, shape and volume fraction

In Mn containing alloys, another objective of the homogenization treatment is to form the dispersoids which will play a role in the modification of the grain structure during the subsequent extrusion process [29,30,65,70]. The dispersoids formed during homogenization have a strong effect on the processes, such as recovery, recrystallization and grain growth; moreover, they also affect the high temperature flow stress. This section presents a quantitative investigation of the

size of Mn-containing dispersoids where the particles were characterized using both the TEM and FEGSEM.

Figure 5.14 shows typical TEM micrographs for the samples with different Mn/Cr additions homogenized at 550 ºC for 2 h. It can be seen that the dispersoids appear with various shapes, which can be attributed to the projections of the plate shaped dispersoids in a 2D image [155]. In addition, the dispersoids may lie under or above the foil surface, which also leads to varying contrast. The morphology of the dispersoids projected in the micrographs varies to a considerable extent.

The sizes of the dispersoids in 0.25Mn homogenized at 550 ºC for 2 h are more or less similar to those in 0.5Mn and 0.5Mn0.15Cr alloys, which are homogenized under the same homogenization conditions. However, the number density appears to be higher with more addition of Mn and Cr, although one must be careful since the thin films may possess different thicknesses.

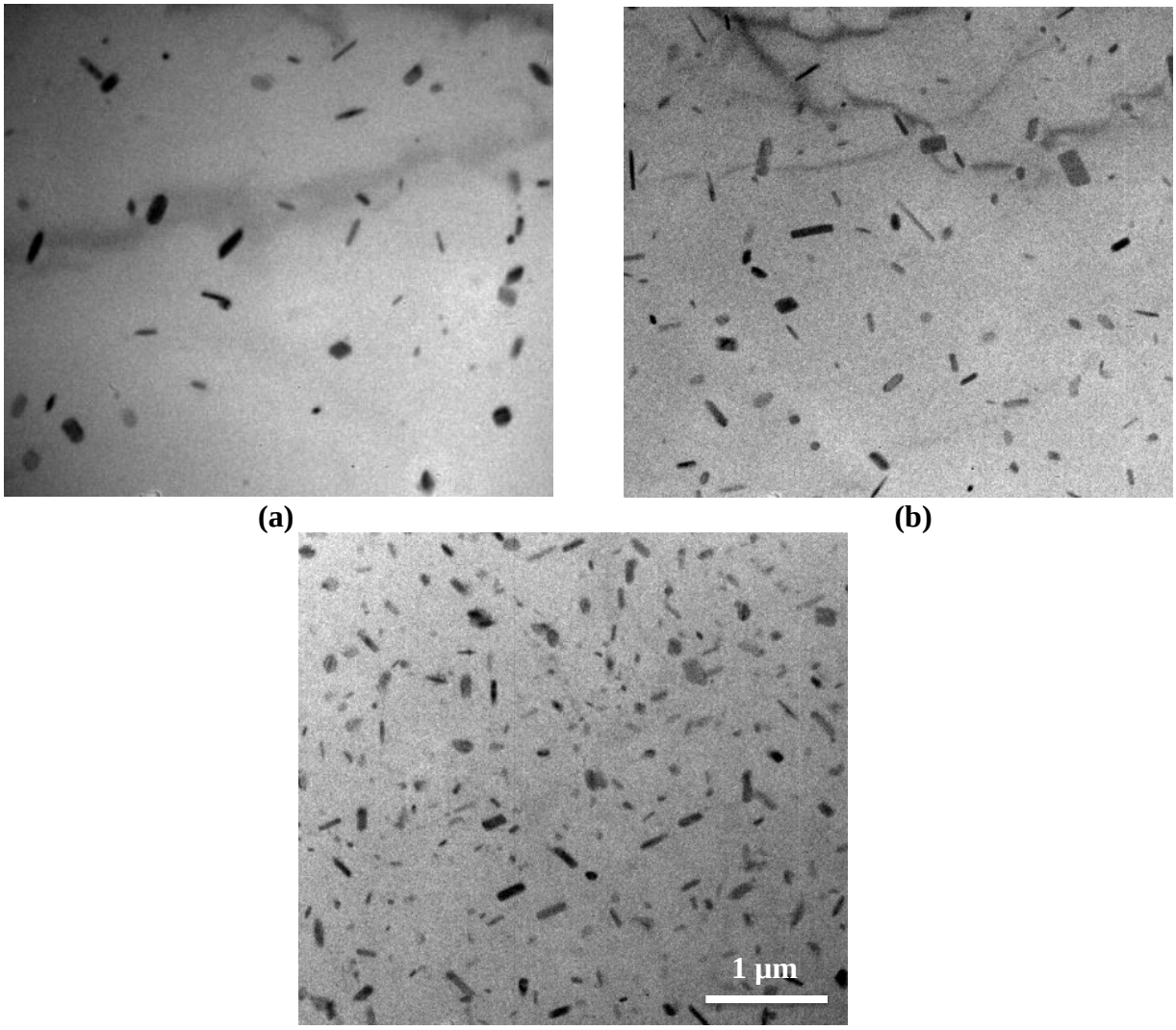

Figure 5-14 TEM micrographs for the samples homogenized at 550 ºC for 2 h of (a) 0.25Mn alloy, (b) 0.5Mn alloy and (c) 0.5Mn0.15Cr alloy

Figure 5.15 shows the examples of typical TEM micrographs for samples homogenized at 580 ºC for 12 h. The main differences that are observed are as follows: the size of the dispersoids from this heat treatment is generally larger as compared to the size of those in the samples homogenized at 550 ºC for 2 h; further, it again appears that qualitatively, the number density of dispersoids increases with an increase in the alloy content.

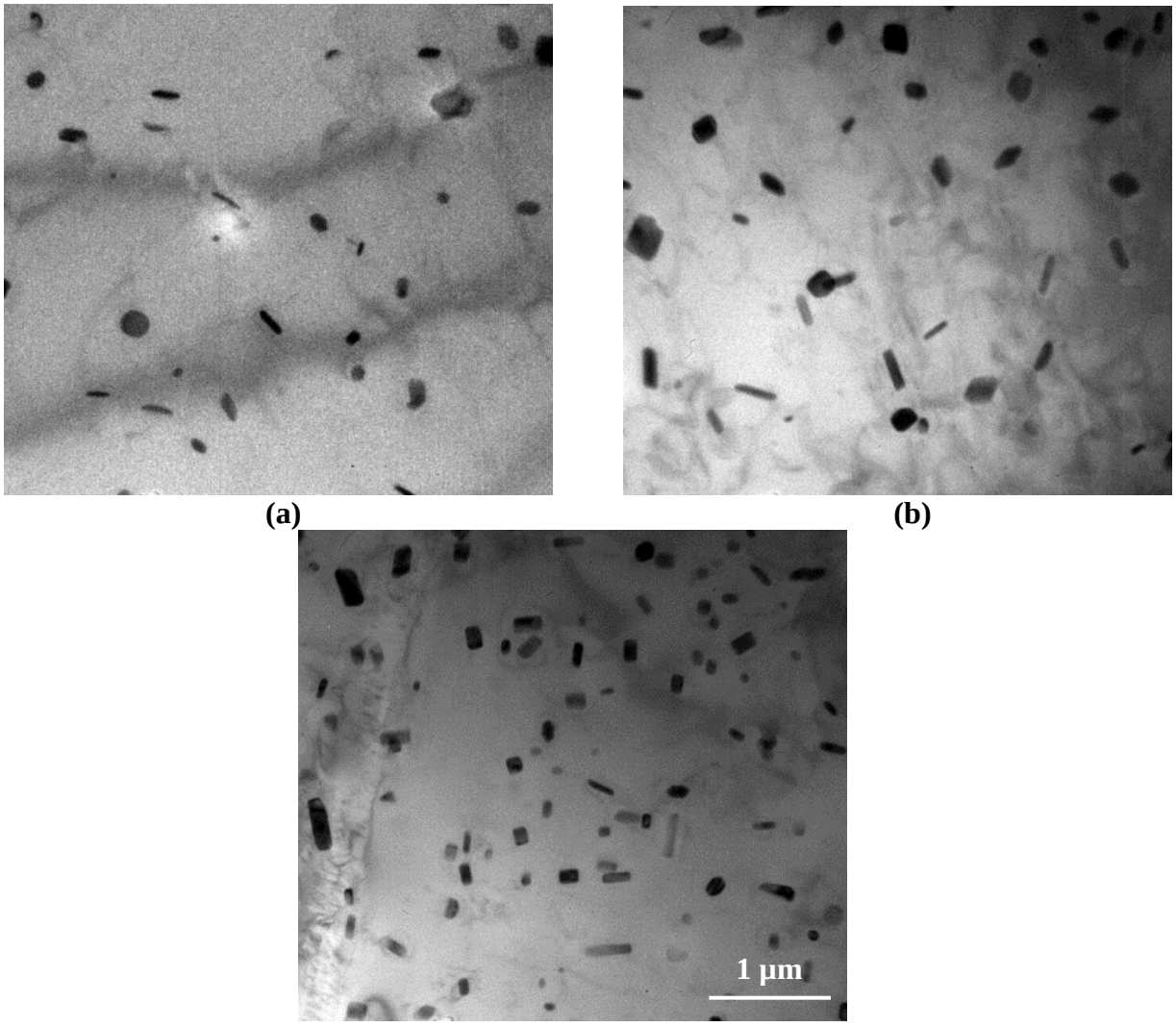

Figure 5-15 TEM micrographs for the samples homogenized at 580 ºC for 12 h of (a) 0.25Mn alloy, (b) 0.5Mn alloy and (c) 0.5Mn0.15Cr alloy

It is clear from Figures 5.14 and 5.15 that the projection of the dispersoids leads to the formation of different shapes and this would depend on the crystallographic orientation of the thin film. To simplify this, it can be said that the dispersoid size measurements were characterized by the equivalent area radius and by an average aspect ratio. The data of the average radius and aspect radios in the six samples are listed in Table 5.6.

Table 5.6 Summary of the average radius and aspect ratio of the evolution of the dispersoids from TEM

Alloy and homo	Average radius, nm	Average aspect ratio
0.25Mn-550ºC-2h	49	2.4
0.5Mn-550ºC-2h	46	2.6
0.5Mn0.15Cr-550ºC-2h	34	2.4
0.25Mn-580ºC-12h	82	1.9
0.5Mn-580ºC-12h	89	2.0
0.5Mn0.15Cr-580ºC-12h	76	2.2

From Figures 5.14 and 5.15 and Table 5.6, the main results have been summarized as follows. For 0.25Mn alloy, the average mean radius increases from 49 nm to 82 nm when the homogenization condition changes from 550 ºC for 2 h to 580 ºC for 12 h. For the samples homogenized at the same conditions, it can be seen that the average radius is almost the same for the 0.25Mn and 0.5Mn alloys in the case of 550 ºC for 2 h (49 nm vs 46 nm) or 580 ºC for 12 h (82 nm vs 89 nm). In contrast, the average radii for the 0.5Mn0.15Cr alloy are smaller than those in 0.25Mn and 0.5Mn alloys for each of the given homogenization conditions. These results are consistent with the qualitative observations that are seen in the TEM micrographs of Figures 5.14 and 5.15. The average aspect ratios for all the conditions are also reported in Table 5.6. Here, little difference appears amongst the alloys and the homogenized conditions, i.e. aspect ratios of 1.9-2.6.

Further size distributions were plotted as histograms, as shown in Figures 5.16 and 5.17 for the three alloys homogenized at 550 ºC for 2 h and 580 ºC for 12 h, respectively. Log-normal distribution was fit to each case and has been shown as the solid blue line.

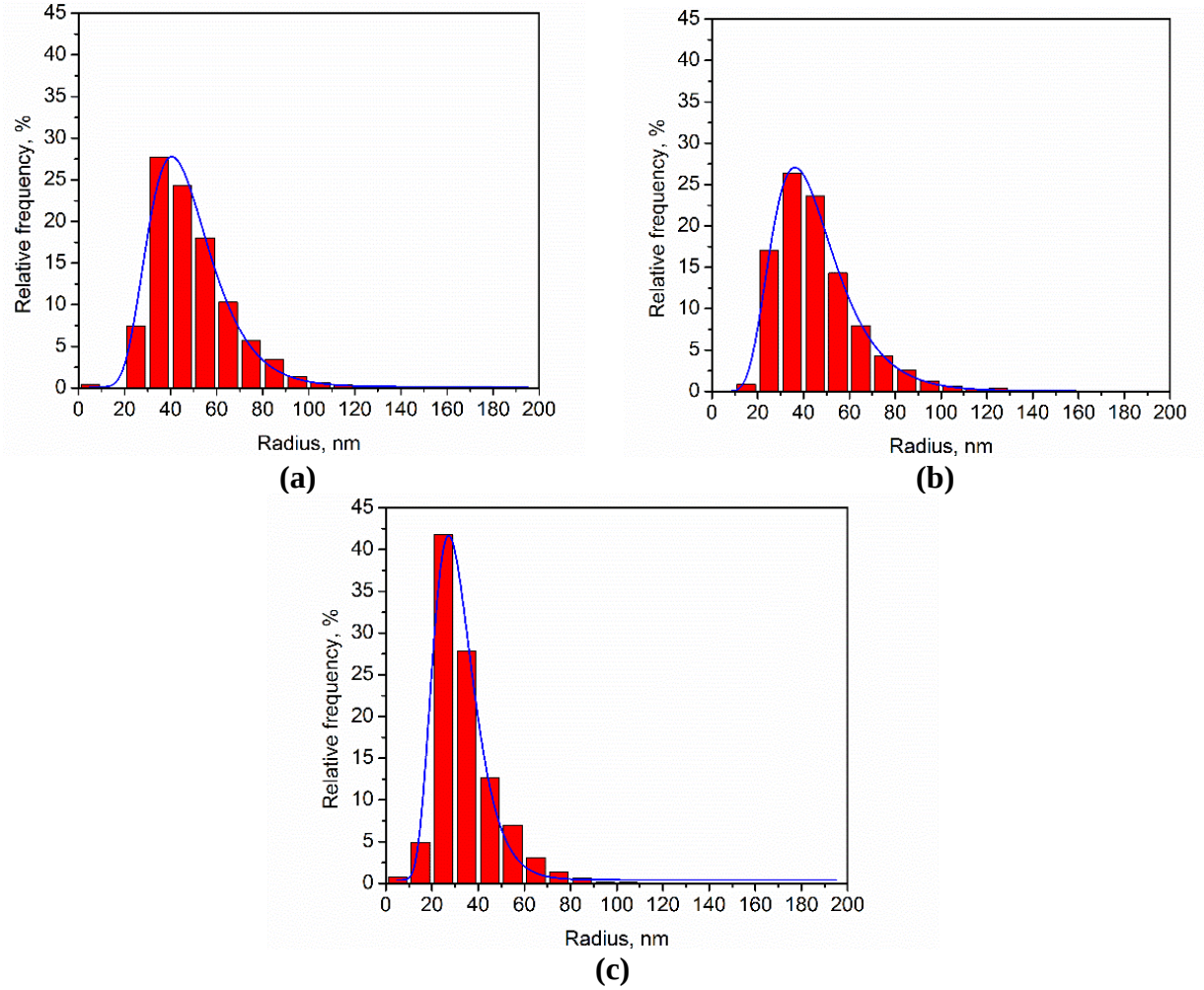

Figure 5-16 Equivalent radius size distribution of the dispersoids from TEM in the samples homogenized at 550 ºC for 2 h of (a) 0.25Mn alloy, (b) 0.5Mn alloy and (c) 0.5Mn0.15Cr alloy. The solid line is the fit of the log-normal distribution.

The size distributions of the dispersoids plotted were fit to a log normal distribution (Equation 5-1) following the least square root principle.

$$f(x) = \frac{1}{\sqrt{2\pi}\sigma x}\exp\left[-\frac{(\ln x - \mu)^2}{2\sigma^2}\right] \qquad (5\text{-}1)$$

where the mean is $e^{\mu+\frac{\sigma^2}{2}}$, and the variance is $\left(e^{\sigma 2}-1\right)e^{2\mu+\sigma^2}$.

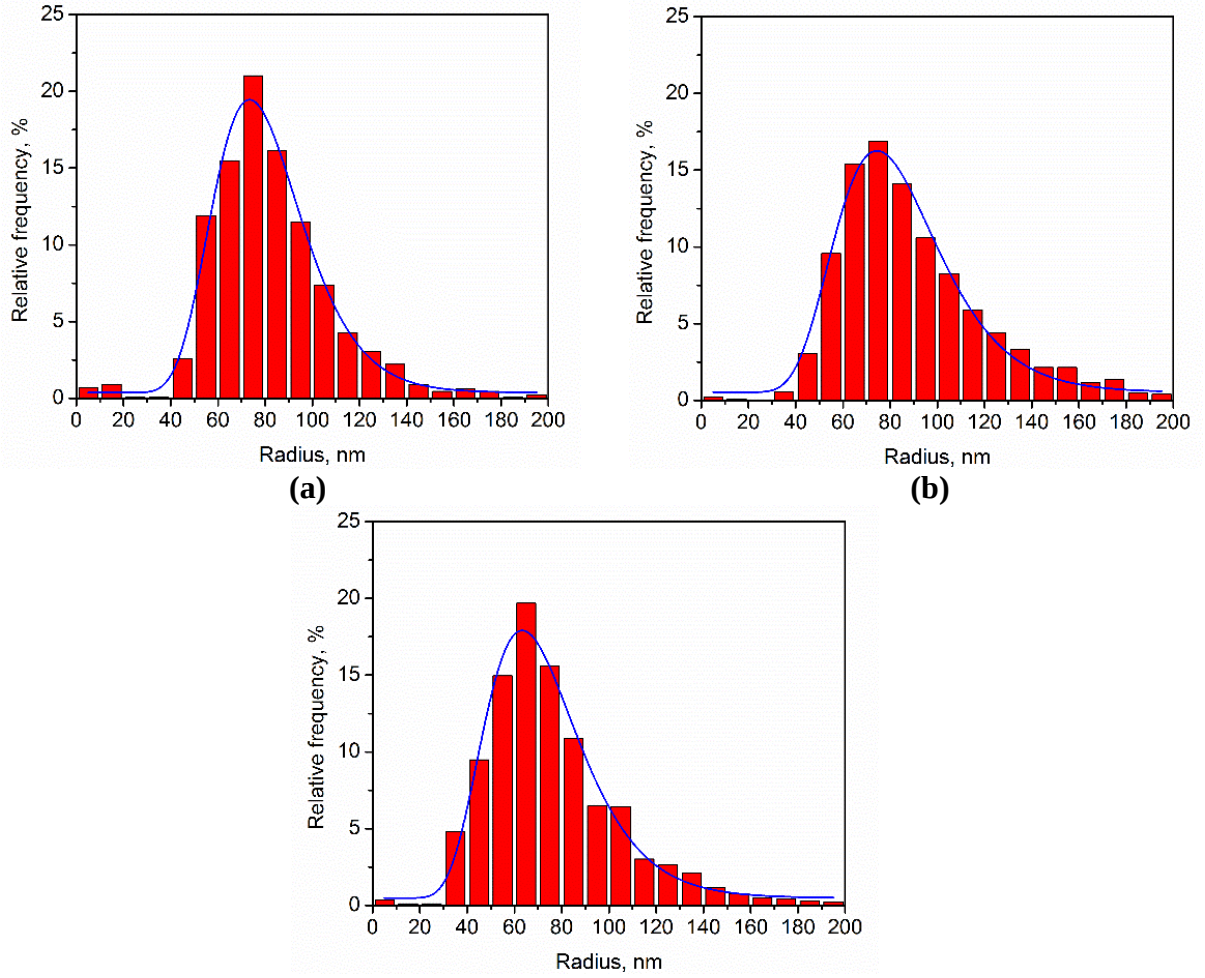

Figure 5-17 Equivalent radius size distribution of dispersoids from TEM in the samples homogenized at 580 ºC for 12 h of (a) 0.25Mn alloy, (b) 0.5Mn alloy and (c) 0.5Mn0.15Cr alloy. The solid line is the fit of the log-normal distribution.

The results for the mean value and variance from the fits to the log-normal distributions have been summarized in Table 5.7.

Table 5.7 Summary of the log normal fit for the equivalent radius of the dispersoids from TEM

Alloy and homo	Mean, nm	Variance, nm	Variance/mean
0.25Mn-550ºC-2h	48	16	0.34
0.5Mn-550ºC-2h	45	18	0.39
0.5Mn0.15Cr-550ºC-2h	32	10	0.32
0.25Mn-580ºC-12h	81	21	0.26
0.5Mn-580ºC-12h	85	25	0.30
0.5Mn0.15Cr-580ºC-12h	73	23	0.32

In order to further characterize the size of the dispersoids at earlier homogenization stage, in one alloy (0.5Mn alloy), the size of the dispersoids at the end of the heating ramp (i.e. heated from room temperature at 200 °C/h to to 550 °C) was examined and the results are shown in Figure 5.18a. As expected, the disperoids observed are of a much higher number density compared to the implemented homogenization conditions. Meanwhile, the sizes of the dispersoids are much smaller as expected. Quantitative analysis was also conducted on this sample with very fine dispersoids. The dispersoid frequency distribution is plotted in Figure 5.18b, where the log-normal fit was also applied, where the mean value is 20 nm and the variance is 12 nm.

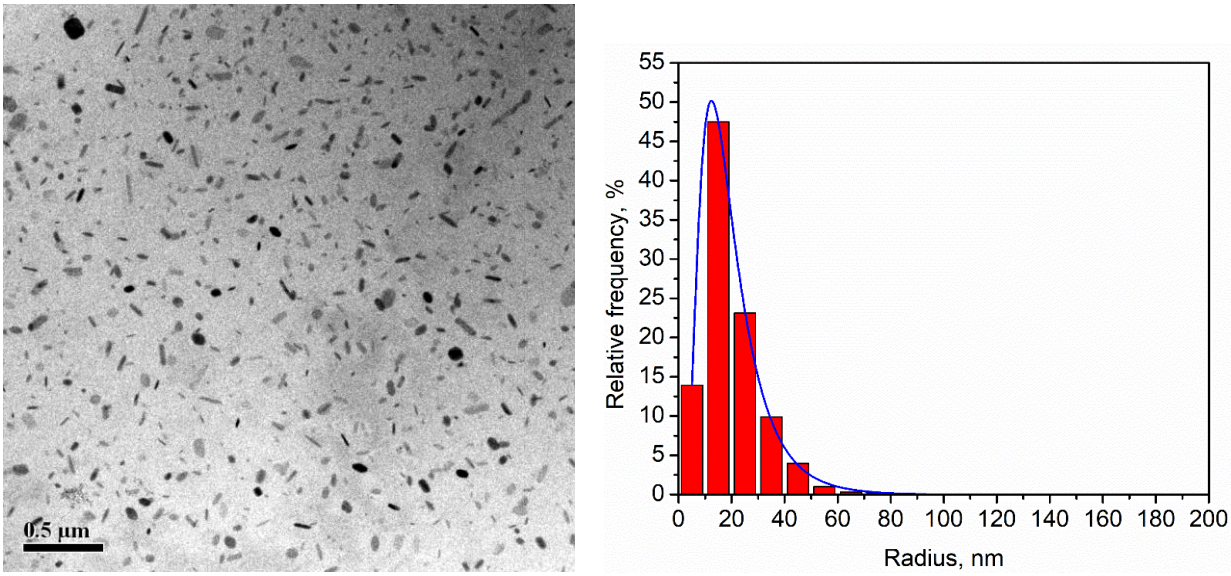

(a) **(b)**

Figure 5-18 (a) TEM micrograph for the sample ramped to 550 ºC of 0.5Mn alloy and (b) Equivalent radius size distribution of dispersoids from TEM in the sample ramped to 550 ºC of 0.5Mn alloy. The solid line is the fit of the log-normal distribution.

In parallel, the measurements were also conducted from FEGSEM micrographs. The reason to conduct size measurements using FEGSEM micrographs is due to the easier sample preparation for FEGSEM compared to TEM, i.e. it would be more convenient to use FEGSEM. Figures 5.19 to 5.22 shows the backscattered images for the 2 h at 550 ºC, 2 h at 580 ºC, 12 h at 580 ºC and 168 h at 580 ºC, respectively. As expected, an increase of Mn and or Cr leads to a higher number density of dispersoids.

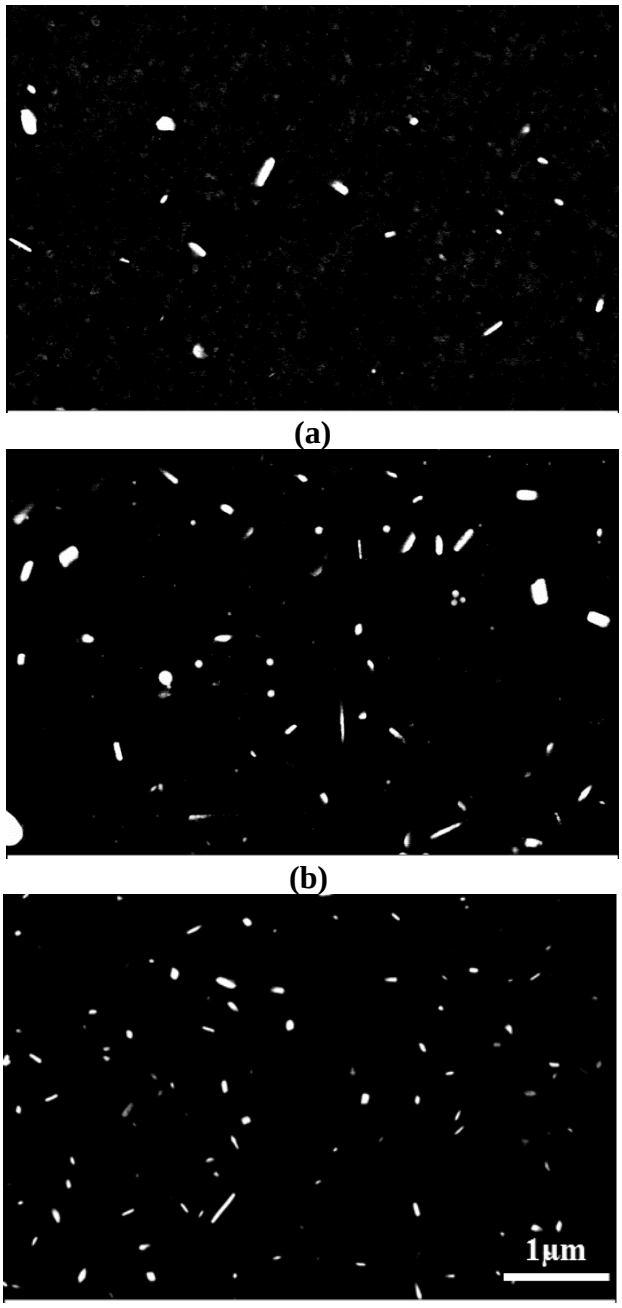

Figure 5-19 FEGSEM (backscatter mode) micrographs for the samples homogenized at 550 ºC for 2 h of (a) 0.25Mn alloy, (b) 0.5Mn alloy and (c) 0.5Mn0.15Cr alloy

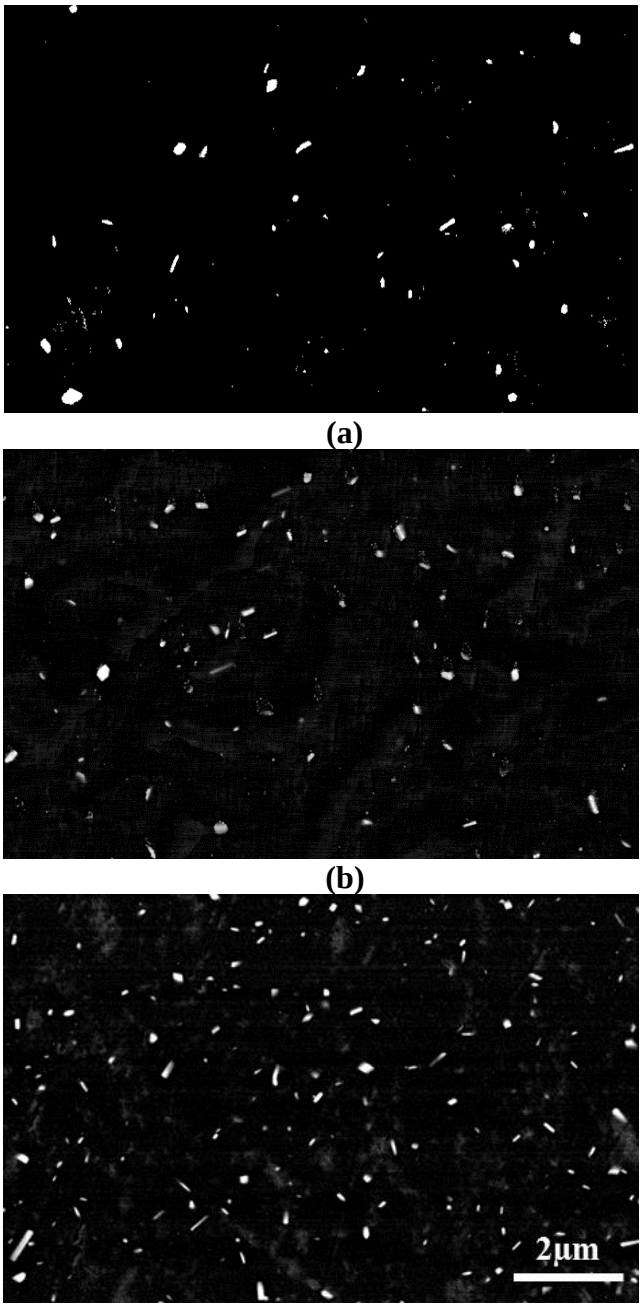

Figure 5-20 FEGSEM (backscatter mode) micrographs for the samples homogenized at 580 ºC for 2 h of (a) 0.25Mn alloy, (b) 0.5Mn alloy and (c) 0.5Mn0.15Cr alloy

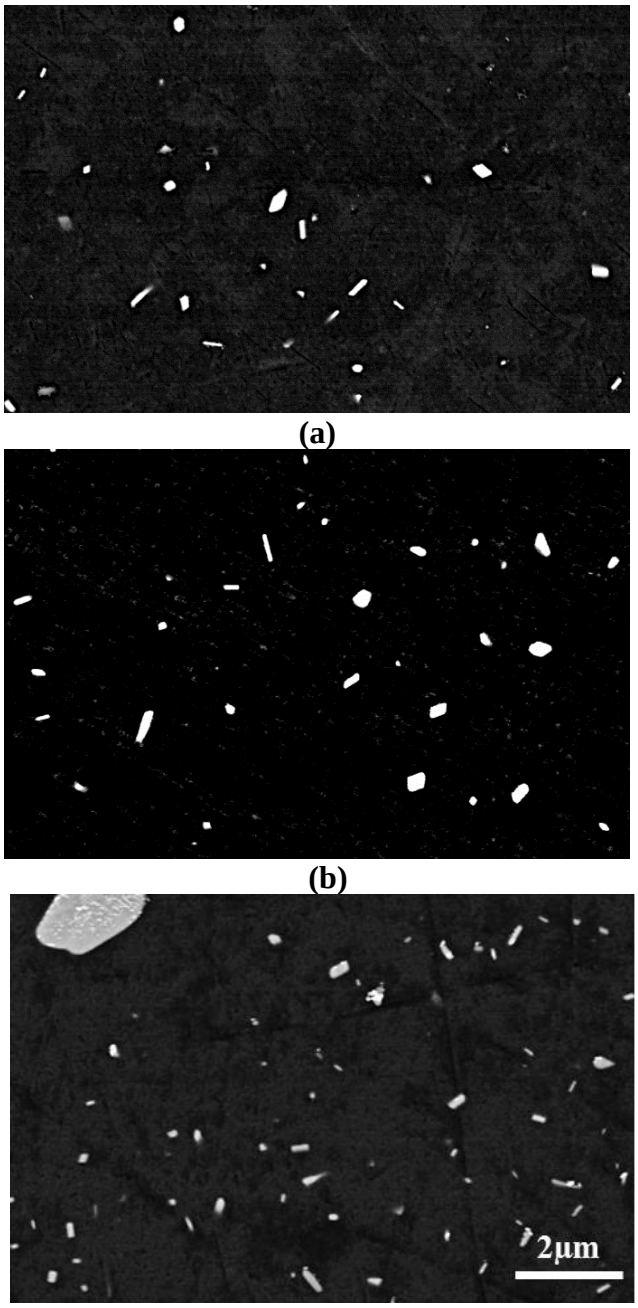

(a)

(b)

(c)

Figure 5-21 FEGSEM (backscatter mode) micrographs for the samples homogenized at 580 ºC for 12 h of (a) 0.25Mn alloy, (b) 0.5Mn alloy and (c) 0.5Mn0.15Cr alloy

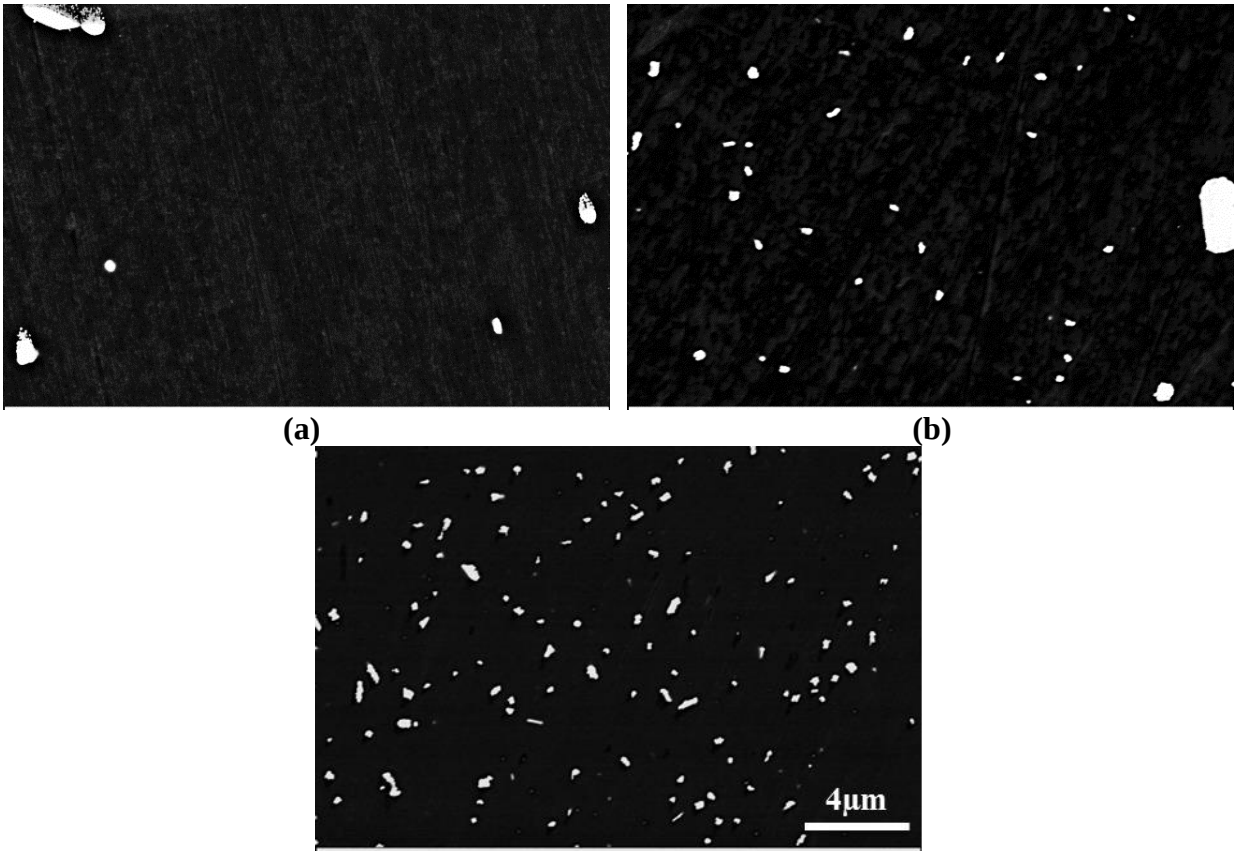

Figure 5-22 FEGSEM (backscatter mode) micrographs for the samples homogenized at 580 ºC for 168 h of (a) 0.25Mn alloy, (b) 0.5Mn alloy and (c) 0.5Mn0.15Cr alloy

The size distributions for the three selected homogenizations on 0.25Mn, 0.5Mn and 0.5Mn0.15Cr alloys have been plotted in Figure 5.23 to 5.25 and then fit to the log normal distribution (Equation 5-1). It is clear that the overall dispersoid size distribution shifted to a larger equivalent radius with an increasing homogenization temperature as well as time. At each homogenization condition, the 0.25Mn and 0.5Mn alloys have a similar size distribution, but the 0.5Mn0.15Cr size distribution has a smaller average value. However, the major difference in Mn/Cr content is the effect that it has on the dispersoid number density at a similar homogenization scenario.

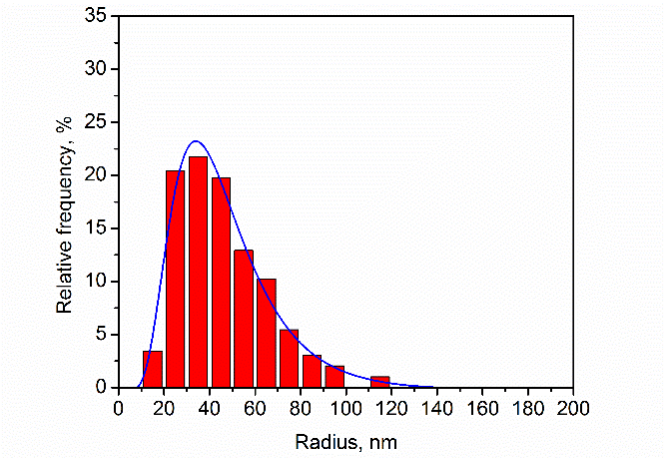

(a)

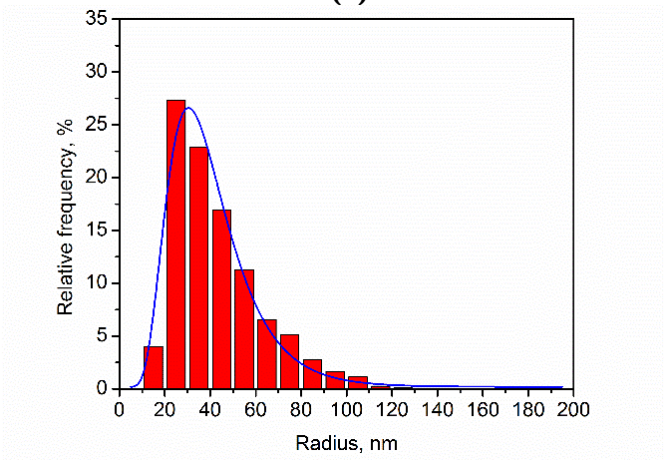

(b)

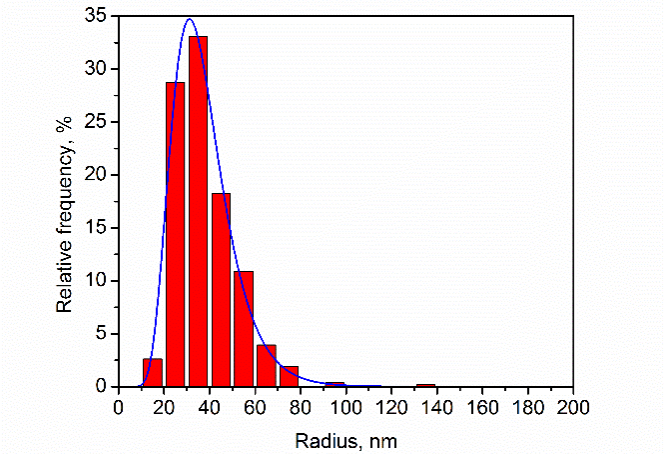

(c)

Figure 5-23 Equivalent radius size distribution of dispersoids from FEGSEM in the samples homogenized at 550 ºC for 2 h of (a) 0.25Mn alloy, (b) 0.5Mn alloy and (c) 0.5Mn0.15Cr alloy

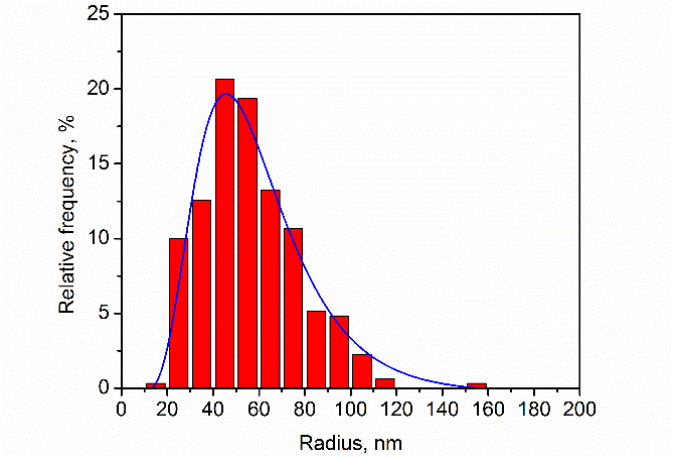

(a)

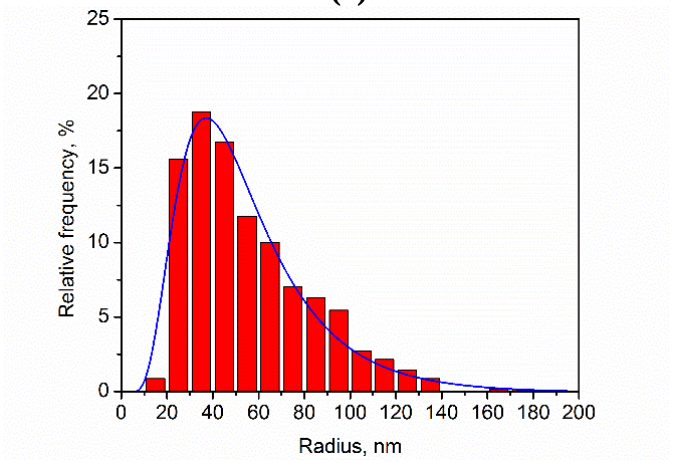

(b)

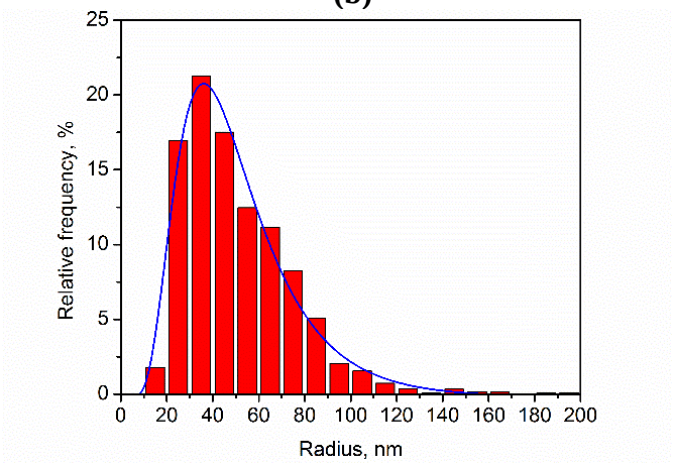

(c)

Figure 5-24 Equivalent radius size distribution of dispersoids from FEGSEM in the samples homogenized at 580 ºC for 2 h of (a) 0.25Mn alloy, (b) 0.5Mn alloy and (c) 0.5Mn0.15Cr alloy

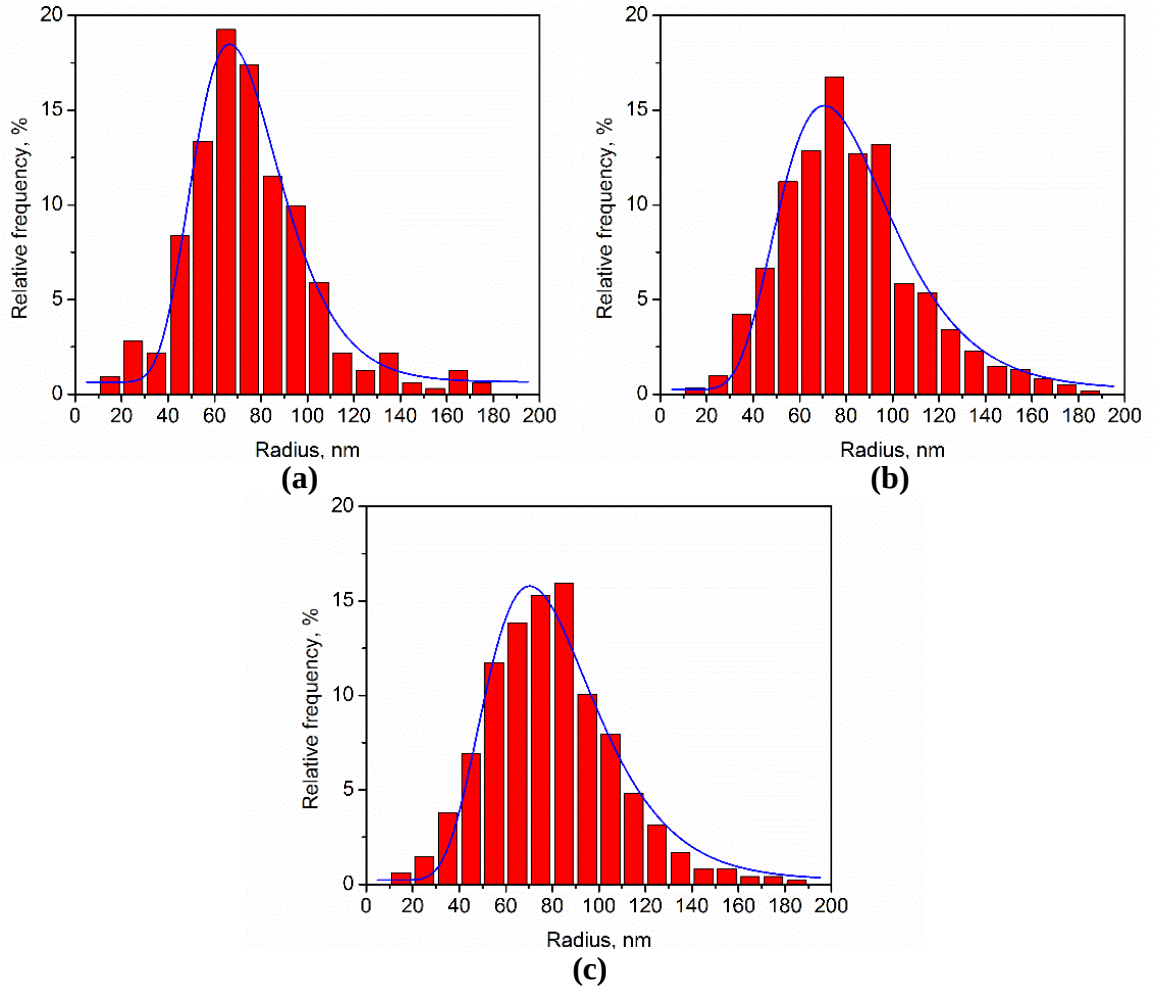

Figure 5-25 Equivalent radius size distribution of dispersoids from FEGSEM in the samples homogenized at 580 ºC for 12 h of (a) 0.25Mn alloy, (b) 0.5Mn alloy and (c) 0.5Mn0.15Cr alloy

The average mean size for the dispersoids in 0.25Mn, 0.5Mn and 0.5Mn0.15Cr alloys from five homogenization conditions has been summarized in Table 5.8 (Note, one additional homogenization condition has been added here, 24 h at 580 ºC). In order to compare the dispersoid size measurements, a cross plot has been made between the results from TEM and FEGSEM. It is clear that FEGSEM could obtain similar results for the dispersoid size measurements from homogenization at 550 ºC for 2 h and 580 ºC for 12 h compared to the TEM characterization in Figure 5.26. On one hand, the radius measurements from the TEM should be

larger than those from the FEGSEM because of the projection of dispersoid versus the section on the surface. On the other hand, it is challenging to use FEGSEM to clearly characterize for the very fine dispersoids i.e. smaller than 20 nm in equivalent radius skewing the average to large sizes. Practically, it appears that these two opposite effects counteract each other, thereby making for their near equivalence.

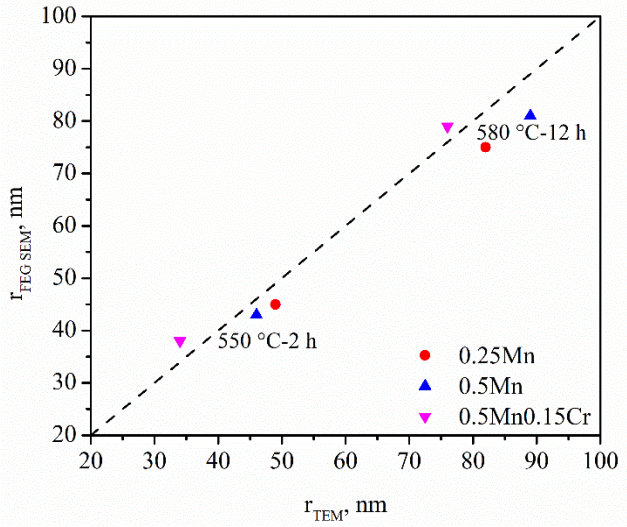

Figure 5-26 Comparison between the average dispersoid radii measured between TEM and FEGSEM

It should be noted that after one week of soaking at 580 ºC, the dispersoids could still be easily observed for 0.5Mn and 0.5Mn0.15Cr alloys as shown in Figure 5.22. In comparison, very few dispersoids could be observed in the 0.25Mn alloy.

Table 5.8 Summary of the average radius evolution of the dispersoids from SEM in nm

Alloy /homo	550ºC-0min	550ºC-2h	580ºC-2h	550ºC-12h	580ºC-24h	580ºC-168h
0.25Mn	-	45	56	75	105	-
0.5Mn	20	43	56	81	97	138
0.5Mn0.15Cr	-	38	51	79	83	119

The mean values and the standard deviation value for the fit of log normal distribution are summarized in Table 5.9, which shows similar results as the average mean radius measured directly from FEGSEM micrographs from the measurements in Table 5.8.

Table 5.9 Summary of the log normal fit parameters for the equivalent radius of dispersoids from FEGSEM

Alloy and homo	Mean, nm	Variance, nm	Variance/Mean
0.25Mn-550ºC-2h	47	23	0.50
0.5Mn-550ºC-2h	40	18	0.46
0.5Mn0.15Cr-550ºC-2h	37	13	0.36
0.25Mn-580ºC-2h	60	27	0.45
0.5Mn-580ºC-2h	56	31	0.56
0.5Mn0.15Cr-580ºC-2h	52	27	0.52
0.25Mn-580ºC-12h	75	22	0.29
0.5Mn-580ºC-12h	84	29	0.35
0.5Mn0.15Cr-580ºC-12h	83	28	0.34

Finally, it was noticed that in some cases, the spatial distribution of dispersoids showed an inhomogeneous nature. Figure 5.27 shows a FEGSEM backscattered image for the case of 0.5Mn alloy which had been homogenized for 12 h at 580 °C. It can be observed that there is a region around the constituent particles where no dispersoids are found. This area is referred to as the dispersoids free zone (DFZ).

The final parameter required for characterizing the physical nature of the dispersoids would be their volume fraction (or number density per volume). A number of attempts were made in order to achieve this in the current work, but it was found that this involved substantial uncertainty due to errors in the threshold of the particles to measure area fraction in the case of FEGSEM measurements or estimate of the volume for TEM measurements (i.e. film thickness). As such, a new approach has been proposed, which will be described in Section 6.1.

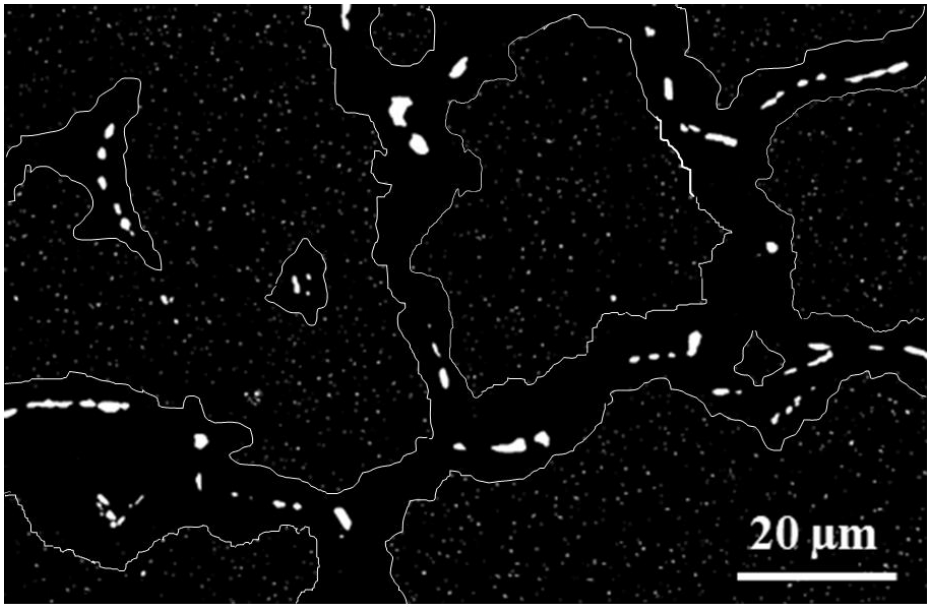

Figure 5-27 The microstructure of 0.5Mn alloy homogenized at 580 C for 12 h with the dispersoids free zone (DFZ) highlighted

5.5 Crystal structure and chemistry of dispersoids

Both the crystal structure and composition of the dispersoids in the alloys with different compositions and homogenization conditions were studied using transmission electron microscopy (TEM) and energy dispersive spectroscopy (EDS) in collaboration with Dr. Xiang Wang at the McMaster University. In the following, the crystal structure, the composition of dispersoids will be described for different alloys as well as different homogenization treatments.

5.5.1 Effect of alloy and homogenization on crystal structure

As discussed in Section 2.2, the α-Al(MnFe)Si dipsersoid in Al-Mg-Si-Mn alloys could have a simple cubic (SC) or BCC with the same lattice parameter a=1.26 nm. As many of the diffraction spots from the SC and BCC structure tend to overlap, the sample was tilted such that the <100> axis was aligned with the electron beam. When viewed along the <100> zone axis, the

absence for the spots of h+k+l≠2n (i.e. all spots are h+k+l=2n) indicates that structure is a BCC, while the presence of the diffraction spots of h+k+l≠2n indicates that structure is a SC [156].

Turning back to the observations on the crystal structure of the dispersoids, Table 5.10 summarizes the results. It should be noted that due to the difficulty and the time required to do these measurements, there are limited results. However, keeping this in mind, it is of quite some interest to consider some of the general trends that may be seen in this data.

Table 5.10 Number dispersoids with different crystal structures in 0.25Mn, 0.5 Mn and 0.5Mn0.15Cr alloys under three homogenization treatments

Alloy and homo	BCC	SC
0.25Mn-550ºC-2h	4	7
0.25Mn-580ºC-2h	8	2
0.25Mn-580ºC-12h	12	4
0.5Mn-550ºC-2h	5	5
0.5Mn-580ºC-2h	3	9
0.5Mn-580ºC-12h	1	11
0.5Mn0.15Cr-550ºC-2h	5	5
0.5Mn0.15Cr-580ºC-2h	4	9
0.5Mn0.15Cr-580ºC-12h	1	14

<u>0.25Mn</u>

Figure 5.28 provides a few examples of the diffraction patterns obtained from two of the dispersoids in the sample homogenized at 550 °C for 2 h. The diffraction pattern indicates that the strong spots are from aluminum matrix whereas the weaker spots can be attributed to the dispersoid which have either a simple cubic structure or BCC structure, both with a lattice parameter of 1.26 nm. According to the earlier work from Cooper et al. [81,82], BCC and SC are of a similar lattice parameter around 1.26 nm, but with different Mn and Fe contents.

The limited measurements suggest a transition from SC for 2 h at 550 ºC to BCC for 12 h at 580 ºC. Diffraction patterns of the dispersoids in the 0.25Mn alloy heat treated at high

temperature 580 ºC and much longer time for 12 h are shown in Figure 5.29. SAD patterns of dispersoids in Figure 5.29a and 5.29b can be indexed as SC and BCC unit cell, respectively.

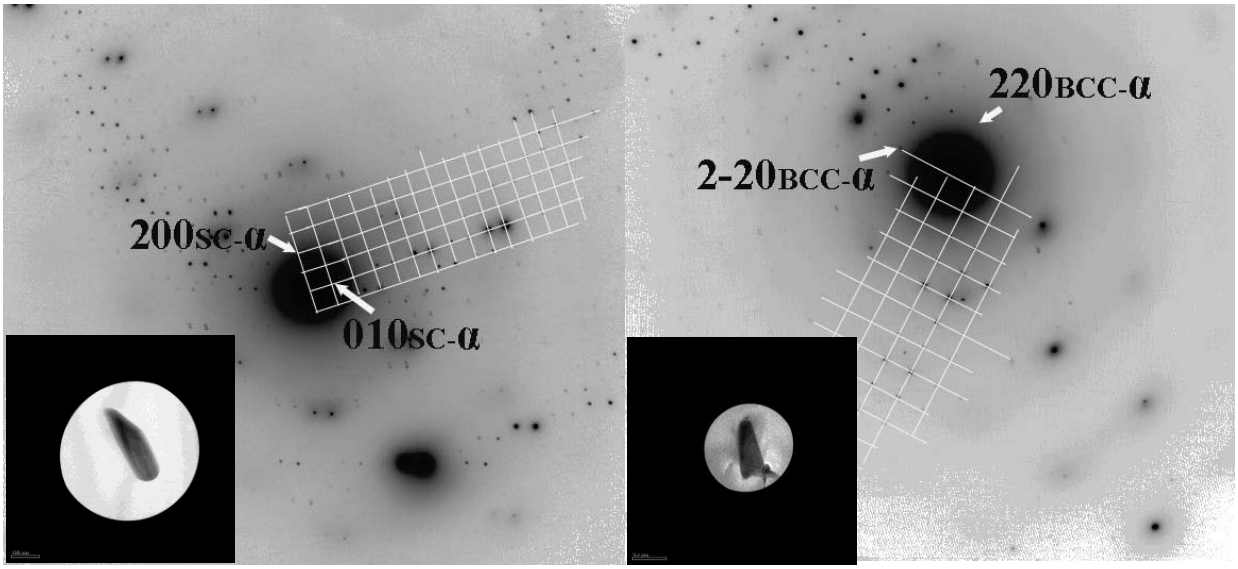

(a) **(b)**

Figure 5-28 Diffraction pattern of single α-Al(MnFe)Si dispersoids in 0.25Mn alloys homogenized at 550 ºC for 2 h (a) with SC crystal structure (b) with BCC crystal structure

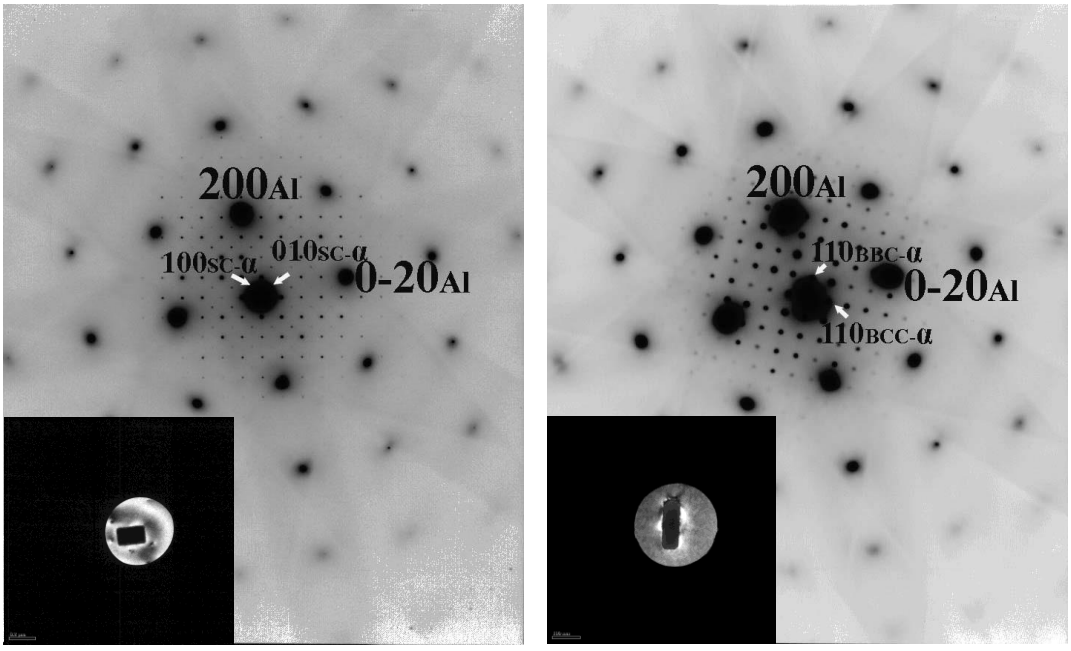

(a) **(b)**

Figure 5-29 Diffraction pattern of single α-Al(MnFe)Si dispersoids in 0.25Mn alloys homogenized at 580 ºC for 12 h (a) with SC crystal structure (b) with BCC crystal structure

0.5Mn alloy

When the 0.5Mn alloy is heated at 550 ºC for 2 h, the diffraction patterns for the dispersoids also shows either BCC or SC with a lattice parameter that is close to 1.26 nm. Examples are provided in Figure 5.30 and 5.31 for the homogenization at 550 ºC for 2 h and 580 ºC for 12 h, respectively.

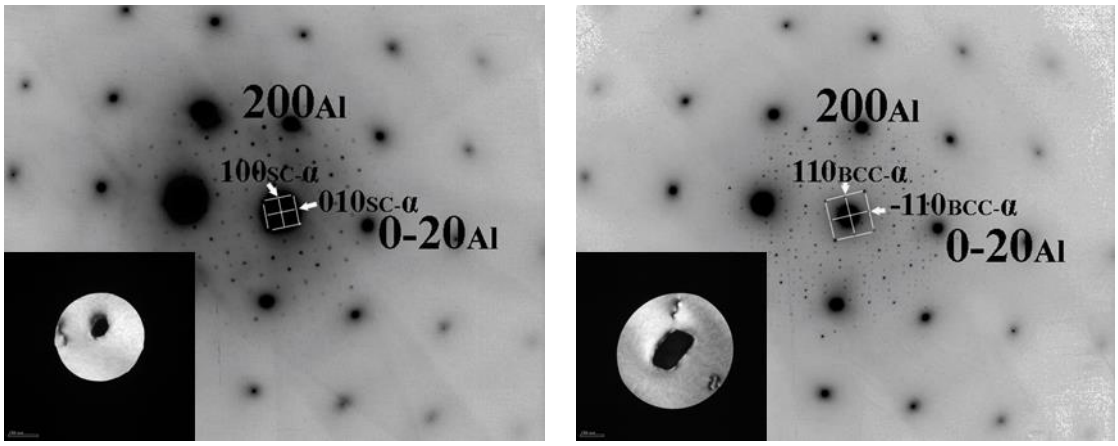

(a) **(b)**

Figure 5-30 Diffraction pattern of single α-Al(MnFe)Si dispersoids in 0.5Mn alloys homogenized at 550 ºC for 2 h (a) with SC crystal structure (b) with BCC crystal structure

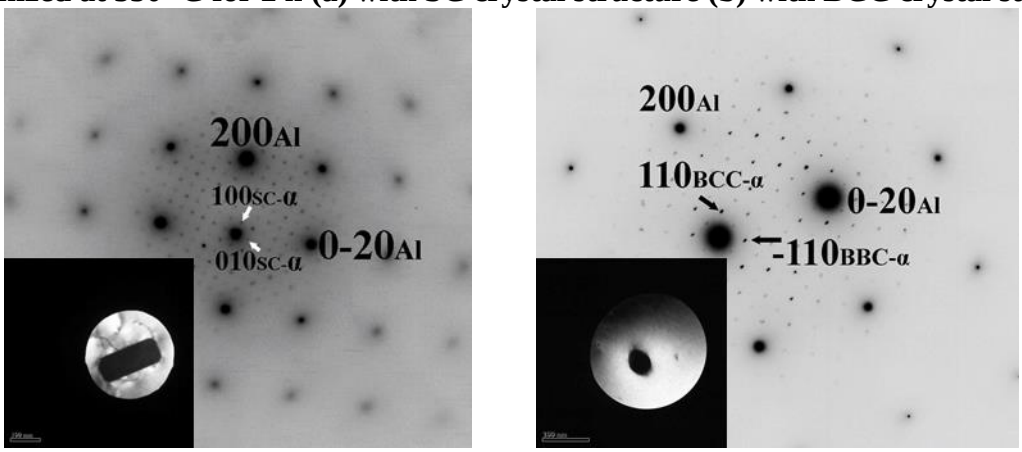

(a) **(b)**

Figure 5-31 Diffraction pattern of single α-Al(MnFe)Si dispersoids in 0.5Mn alloys homogenized at 580 ºC for 12 h (a) with SC crystal structure (b) with BCC crystal structure

There are also two kinds of crystal structures in all samples of 0.5Mn alloys, one is BCC, the other is simple cubic (SC). However, the trend is towards the SC structure with homogenization, i.e. the opposite of 0.25Mn alloy.

0.5Mn0.15Cr alloy

The typical images and related SAD patterns of dispersoids were provided of the 0.5Mn0.15Cr alloy homogenized at 550 ºC for 2 h and 580 ºC for 12 h, in which diffraction patterns can be indexed as SC and BCC respectively (see Figure 5.32 and 5.33). Addition of 0.15 wt.% of Cr in alloy with 0.5 wt.% Mn, the dispersoids were found to exhibit also either SC unit cell or BCC unit cell. The trend is also towards the SC structure with higher homogenization temperature and longer soaking time, i.e. similar to 0.5Mn alloy shown in Table 5.10. According to the results of EDS and SAD patterns, these dispersoids with combination of Mn and Cr are suggested to be α-Al(FeMnCr)Si phase. In addition, the SC/BCC evolution shows similar trend as 0.5Mn alloy.

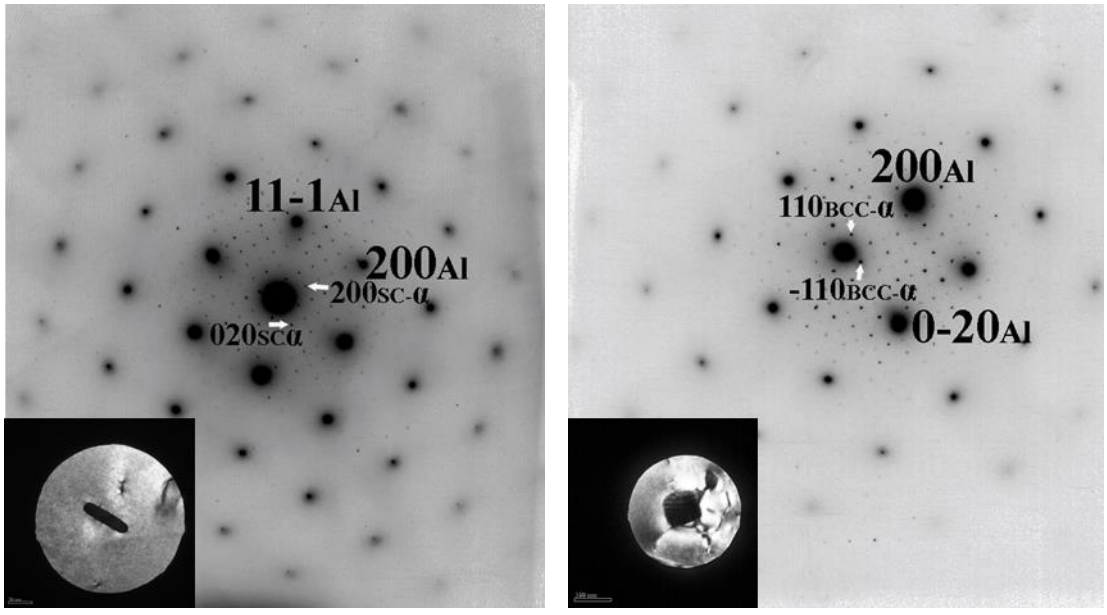

(a) **(b)**

Figure 5-32 Diffraction pattern of single α-Al(MnFe)Si dispersoids in 0.5Mn0.15Cr alloys homogenized at 550 ºC for 2 h (a) with SC crystal structure (b) with BCC crystal structure

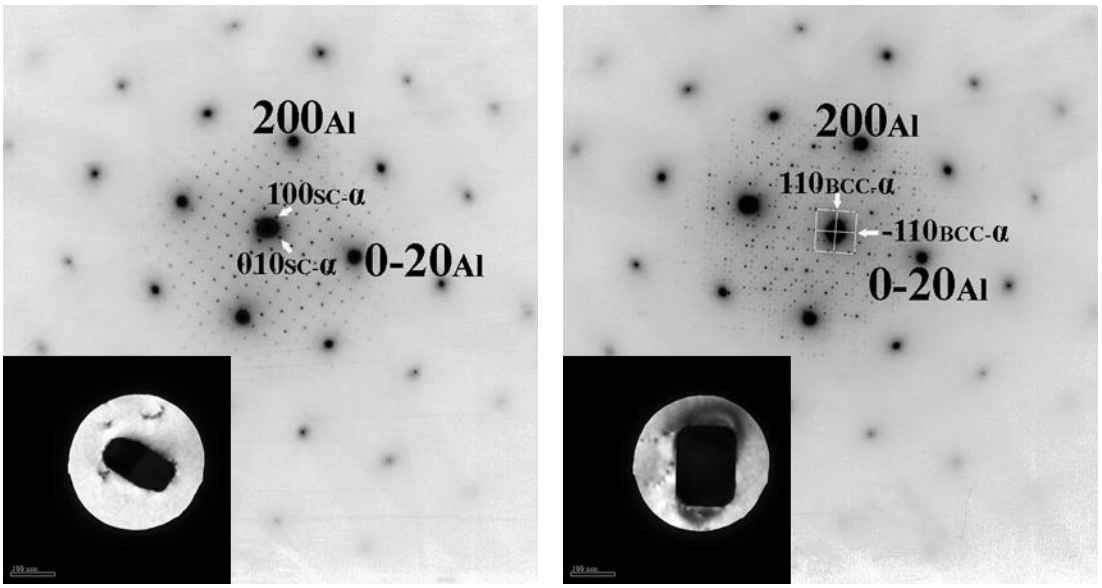

(a) **(b)**

Figure 5-33 Diffraction pattern of single α-Al(MnFe)Si dispersoids in 0.5Mn0.15Cr alloys homogenized at 580 ºC for 12 h (a) with SC crystal structure (b) with BCC crystal structure

Increasing the soaking time to 12 h at 580 ºC results in the dispersoids primarily exhibiting the SC unit. The number of the dispersoids examined using SAD and the corresponding crystal structure has been summarized in Table 5.10.

It appears that the BCC structure is favored with a higher homogenization temperature and longer soaking time for the 0.25Mn alloy. While in the case of 0.5Mn alloy and 0.5Mn0.15Cr alloy, the SC structure is observed to be the dominant crystal structure after long time soaking at a rather higher homogenization temperature. It indicates that the competition between the BCC and SC crystal structure is dependent both chemistry and processing.

5.5.2 Chemical composition (centre of dispersoid)

The chemical composition of the dispersoids has been analyzed by EDS of the TEM thin foils. When conducting the EDS on dispersoids, the spectrum chosen for collecting the information was on the centre for each of the measurements, as shown in Figure 5.34a. The

volume from which the X-rays are generated will also inevitably include some part of the aluminum matrix. Due to the contribution of the matrix to the composition of dispersoids, it is difficult to get the exact composition of dispersoids. Yoo et al [28], taking in consideration the very low contents of Mn, Fe and Cr in the matrix, the Mn/Fe or Mn/(Fe+Cr) ratios will not be affected significantly by those contributions from matrix. This atomic Mn/Fe ratio would reflect the characteristics of the dispersoids from various homogenization treatments. The EDS spectrum in Figure 5.34b shows that the dispersoid contains Al, Mn, Fe and Si elements for the 0.25Mn alloy homogenized at 550 ºC for 2 h.

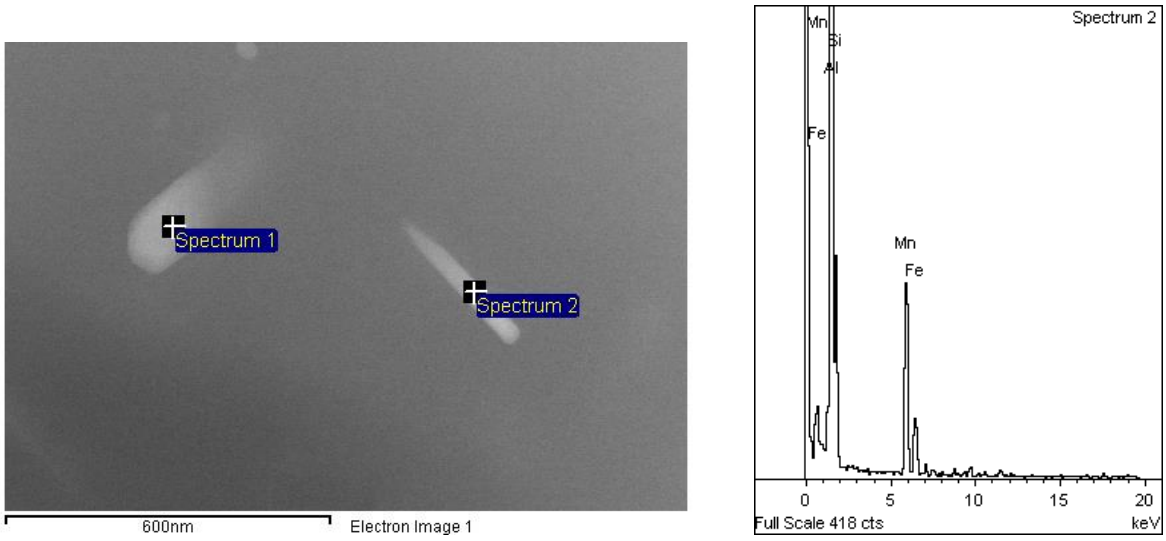

(a) **(b)**

Figure 5-34 (a) TEM micrograph (STEM mode) revealing dispersoids and (b) EDS spectrum on a dispersoid in 0.25Mn alloy homogenized at 550 ºC for 2 h.

EDS analysis of ≈ 30 dispersoids for each alloy has been performed in TEM with the spot probe (probe is around a few nm in diameter). The atomic ratio of Mn/Fe was estimated using the standardless quantification of spectra in all the alloys and conditions. The EDS measurements for each condition were plotted in the form of histograms.

In the 0.25Mn alloy, the Mn/Fe ratio distribution has been illustrated in the Figure 5.35a. It can be seen that the overall Mn/Fe ratio is higher for samples homogenized for 2 h at either 550 °C or 580 °C (≈2-4:1) compared to 12 h at 580 °C (less than 2:1). A similar trend is found in 0.5Mn alloy (See Figure 5.35b) with the highest Mn/Fe for 2 h at 550 °C (≈16:1) and then decreasing to the lowest value for 12 h at 580 °C (<6:1). The average Mn/Fe ratios from the EDS measurements have been reported in Table 5.11. The atomic ratio Mn/Fe of dispersoid in sample 0.25Mn alloy homogenized at 550 °C for 2 h is higher than that in the sample that have been homogenized at 580 °C for 12 h (Mn/Fe: 3.2 vs. 1.3). However, the Mn/Fe ratio in the sample with higher Mn content 0.5Mn homogenized at 550 °C for 2 h is 16.4, which is much higher than that in the samples with lower Mn content.

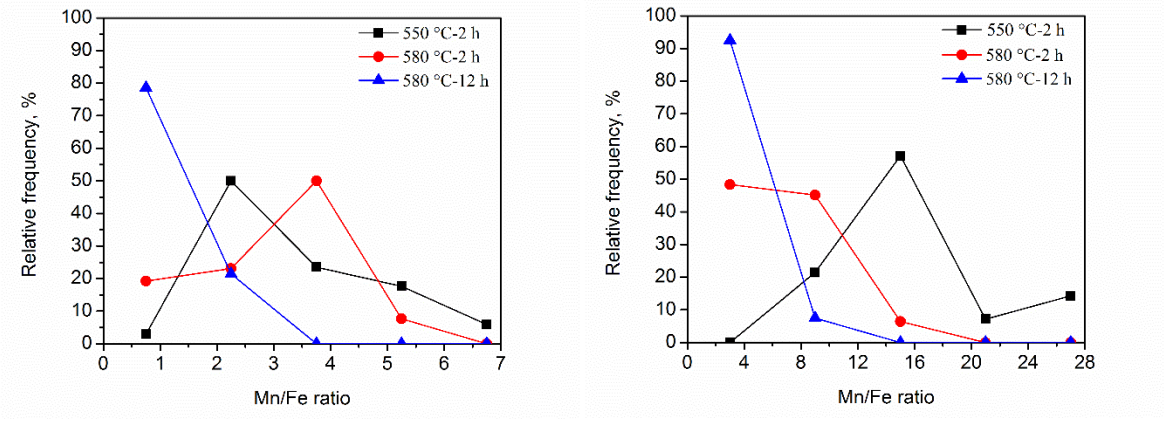

Figure 5-35 Mn/Fe ratios plotted in histogram for (a) 0.25Mn alloy and (b) 0.5Mn alloy from three homogenization conditions

In 0.5Mn0.15Cr alloy, the histogram is plotted for Mn/(Fe+Cr) ratio in Figure 5.36. The average Mn/(Fe+Cr) ratio also decreases with an increasing homogenization temperature and holding time. No dispersoids were found which contained only Cr without Mn and Fe. This is evident from the fact that Cr precipitates together with Mn and Fe as Al(MnCrFe)Si dispersoids.

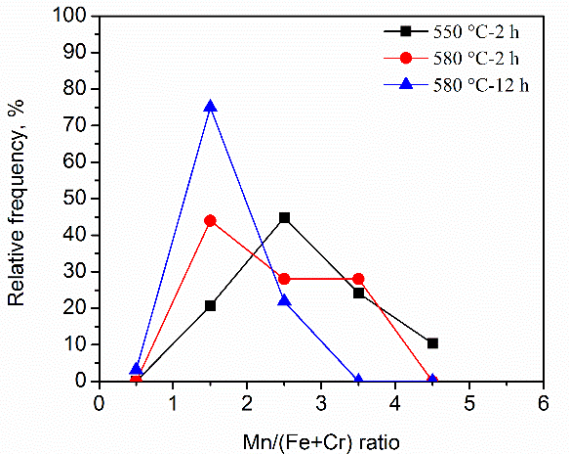

Figure 5-36 Mn/Fe ratios plotted in histogram for 0.5Mn0.15Cr alloy from three homogenization conditions

In summary, Figure 5.37 shows the results for the Mn/Fe or Mn/(Fe+Cr) ratio for all the conditions studied. It can be seen that these ratios are much higher for 0.5Mn alloy as compared to 0.25Mn alloy and the ratio decreases with both the time and temperature for homogenization.

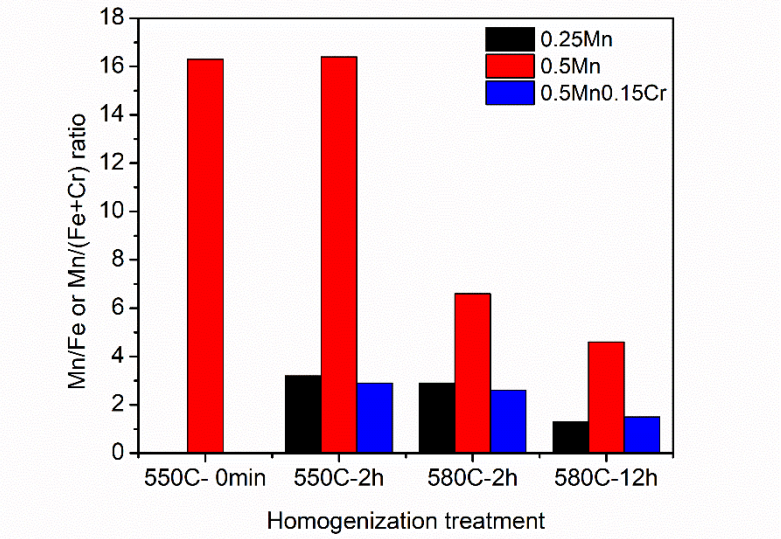

Figure 5-37 Mole Mn/Fe ratio measured from EDS in 0.25Mn, 0.5Mn and 0.5Mn0.15Cr alloys under different homogenizations

Table 5.11 Mole Mn/Fe, Mn/Cr, Mn/(Fe+Cr) and (Mn+Cr)/Fe ratios measured from EDS in 0.25Mn, 0.5Mn and 0.5Mn0.15Cr alloys under different homogenization treatments (Note that EDS analysis is also conducted on the dispersoids from the ramping heat treatment to 550 °C in 0.5Mn alloy)

Alloy and homo	Mn/Fe ratio	Mn/Cr ratio	Mn/(Fe+Cr) ratio	(Mn+Cr)/Fe ratio
0.25Mn-550ºC-2h	3.2	-	-	-
0.25Mn-580ºC-2h	2.9	-	-	-
0.25Mn-580ºC-12h	1.3	-	-	-
0.5Mn-Ramp to 550ºC	16.3	-	-	-
0.5Mn-550ºC-2h	16.4	-	-	-
0.5Mn-580ºC-2h	6.6	-	-	-
0.5Mn-580ºC-12h	4.6	-	-	-
0.5Mn0.15Cr-550ºC-2h	13.7	4.0	2.9	17.6
0.5Mn0.15Cr-580ºC-2h	11.8	3.4	2.6	15.2
0.5Mn0.15Cr-580ºC-12h	3.5	2.9	1.5	4.8

5.5.2.1 Spatial distribution of dispersoid chemistry within dispersoids

The chemistry information reported in the previous section is from the centre of the dispersoids. However, the non-homogeneous distribution of chemical composition in a single dispersoid has been observed in AA3xxx alloy by Muggerud et al. [110]. As this inhomogeneity will affect the average atomic Mn/Fe or Mn/Cr ratios and possibly also provide insight into the mechanism of dispersoid growth and coarsening, an attempt was made at this point to check the chemical composition profile across a single dispersoid in samples of the three Mn/Cr bearing alloys from two homogenization conditions 550 °C for 2 h and 580 °C for 12 h. The EDS measurements of the chemical composition of dispersoids were conducted along the long axis of the dispersoids. The step size of line scan ranges from 10 to 40 nm, depending on the size of dispersoid. A relatively large step size was used to avoid an overlapping of the investigated neighbor volume. In each condition, more than eight different dispersoids were analyzed. In parallel, the crystal structure of dispersoid was determined using SAD, since there are chances

that it may also relate to the ratio of Mn and Fe [28,157]. Figures 5.38a and 5.38b are High Angle Annular Bright Field (HAABF) micrographs revealing the dispersoids. Combining the results from the conventional TEM and high-resolution TEM, both crystal structure and corresponding Mn/Fe ratio were obtained from the same dispersoid. The dispersoids highlighted with red circles in Figures 5.38a and 5.38b were determined to be of SC structure and BCC structure, respectively. Typical examples of the concentration profile for Mn, Fe and Mn/Fe ratio are shown in Figure 5.38c and 5.38d.

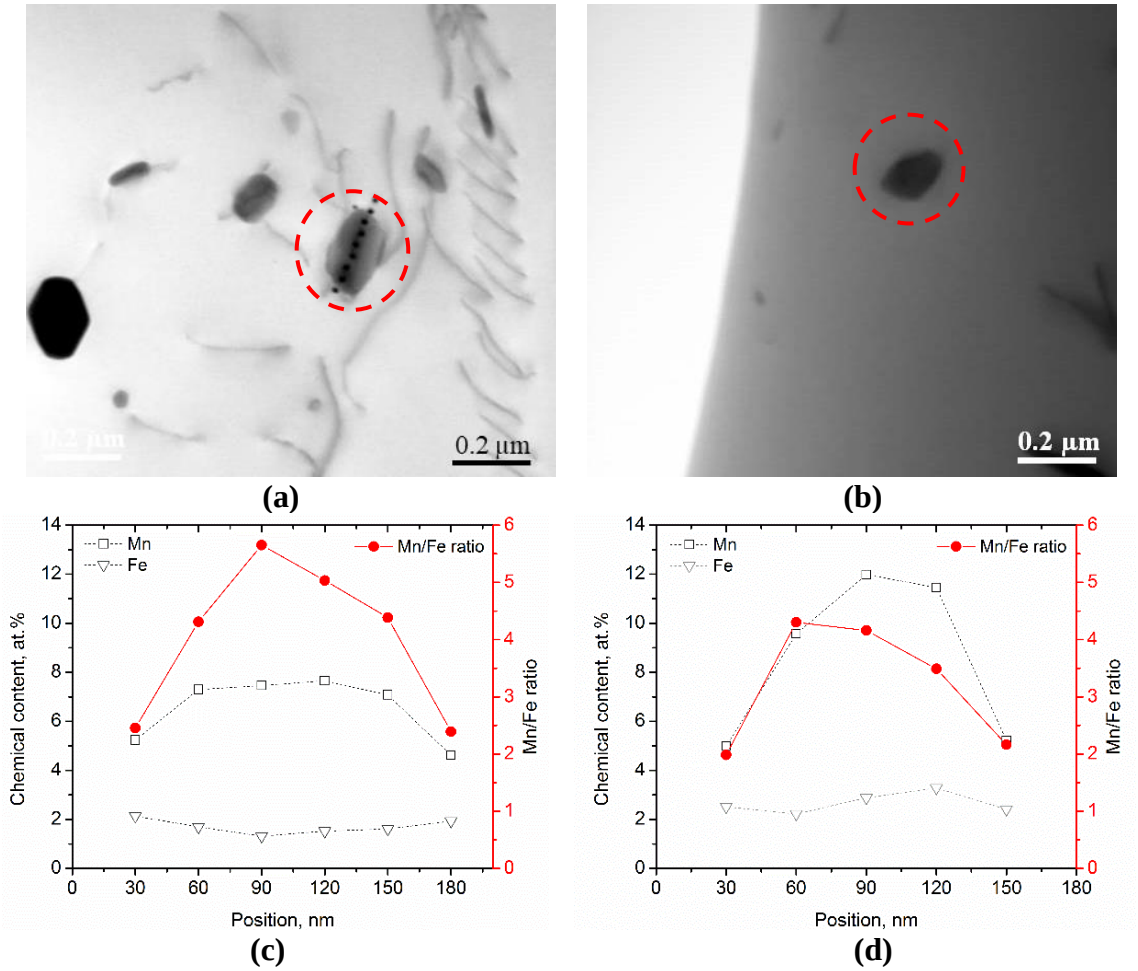

Figure 5-38 HAABF images of representative dispersoids in 0.25Mn alloy homogenized at 550 °C for 2 h (a) with SC crystal structure (b) with BCC crystal structure; Mn and Fe contents and also the Mn/Fe ratios measured along the length of a dispersoid in 0.25Mn alloy homogenized at 550 °C for 2 h (c) with SC crystal structure (d) with BCC crystal structure

The line scans across the dispersoids with different crystal structures correspond to the HAADF images in 5.39a and 5.39b. As seen from these two figures the Mn concentrations in the central area of dispersoid are higher than those in the edge area of dispersoid, while the change of the Fe concentrations across dispersoid has no obvious trend. With an increase in the homogenization temperature and soaking time to 12 h at 580 °C for 0.25Mn alloy, two dispersoids with SC and BCC structures were chosen, as shown in Figures 5.39a and 5.39b.

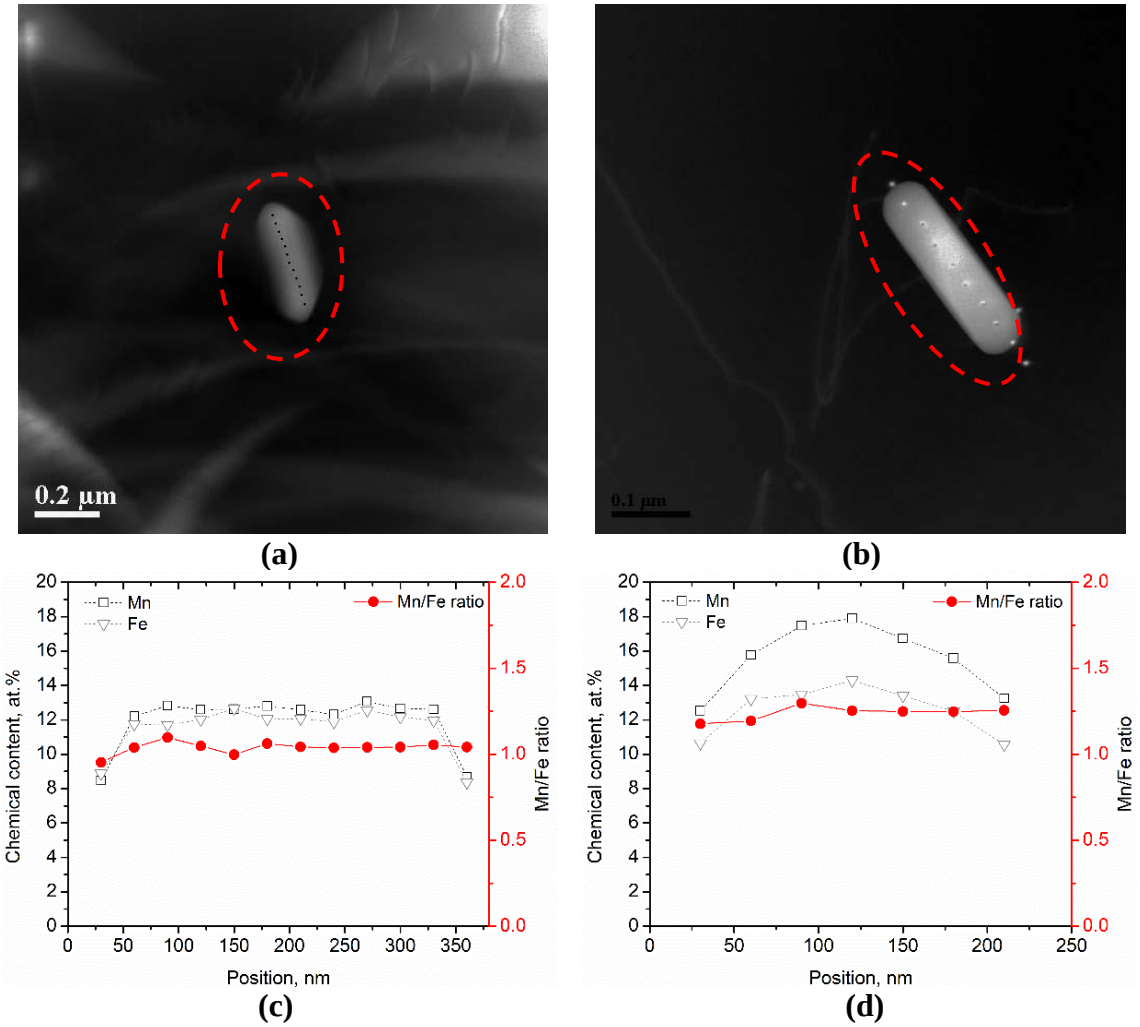

Figure 5-39 HAADF images of the representative dispersoids in 0.25Mn alloy homogenized at 580 °C for 12 h (a) with SC crystal structure (b) with BCC crystal structure; Mn and Fe contents and also the Mn/Fe ratios measured along the length of a dispersoid in 0.25Mn alloy homogenized at 580 °C for 12 h (c) with SC crystal structure (d) with BCC crystal structure

EDS line scans were conducted along the lengthways and were found to show little variation for the Fe and Mn levels between the central part and the edge, as has been shown in Figure 5.39c and 5.39d.

A similar kind of work was done on the 0.5Mn alloy. In Figure 5.40a, two dispersoids of interest have been circled in the sample homogenized at 550 ºC for 2 h.

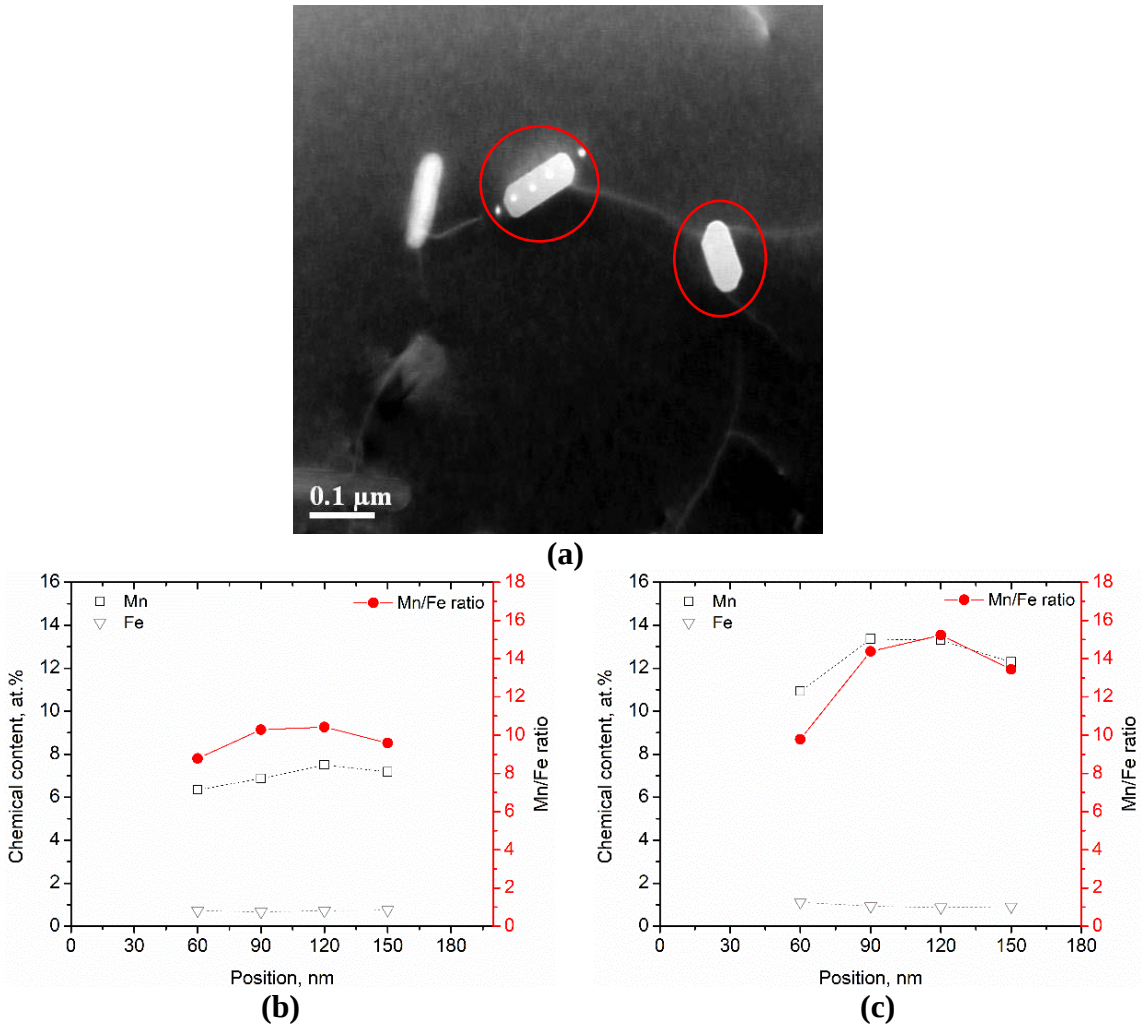

Figure 5-40 (a) HAADF image of representative dispersoids in 0.5Mn alloy homogenized at 550 °C for 2 h left circled dispersoid with SC crystal structure and right circled dispersoid with BCC crystal structure; Mn and Fe contents and also the Mn/Fe ratios measured along the length of a dispersoid in 0.5Mn alloy homogenized at 550 °C for 2 h (b) with SC crystal structure (c) with BCC crystal structure

Even though these two dispersoids display similar morphology, the left one was the determined to be of SC crystal structure while the right one was of BCC structure. EDS measurements were conducted on the two dispersoids and the results including Mn, Fe contents and Mn/Fe ratio are plotted in Figure 5.40b and 5.40c. The Mn/Fe ratio in both cases show higher Mn in the centre than near the edge resulting in a maximum Mn/Fe ratio near the centre of the dispersoid. With an increase of both homogenization temperature and time to 12 h at 580 °C, Figures 5.41a and 5.41b show typical results for the SC and BCC structures, respectively.

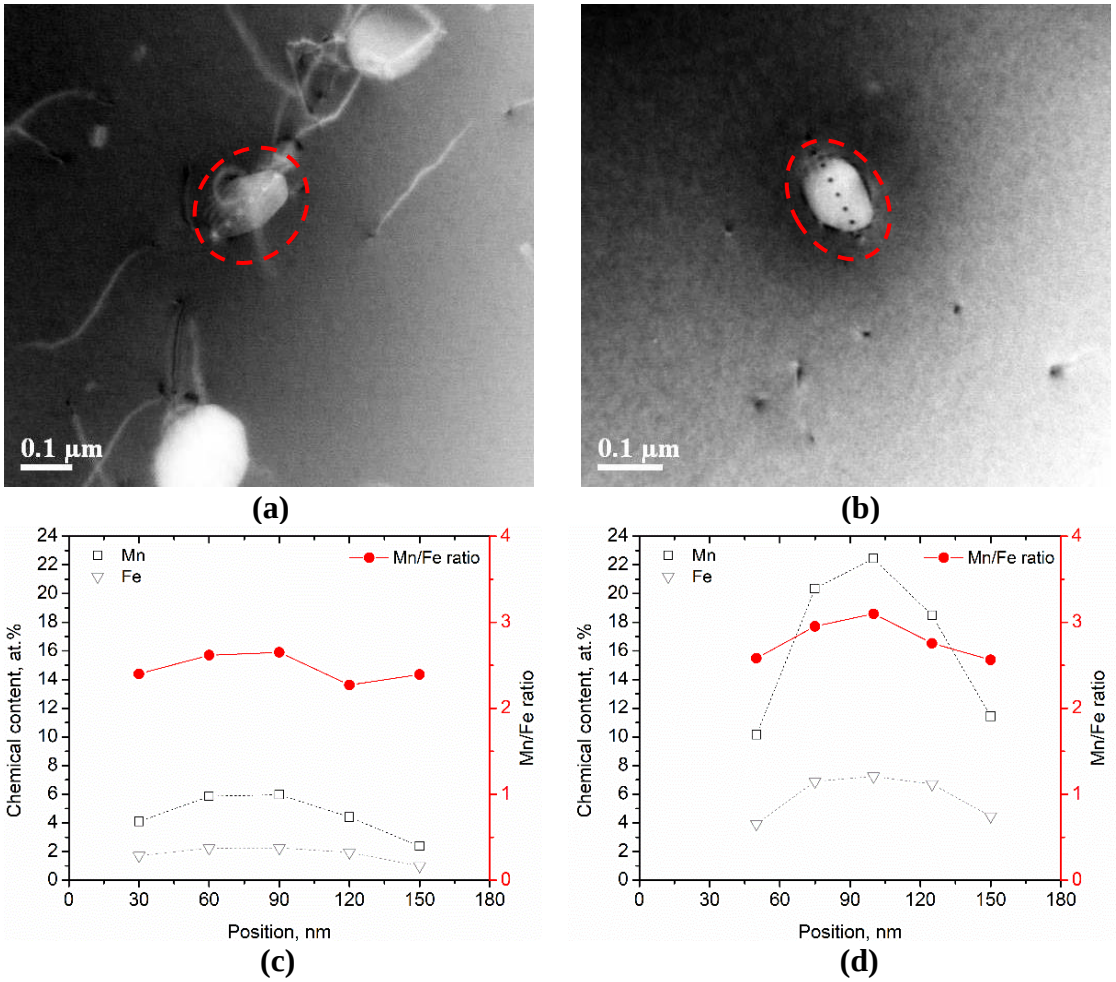

Figure 5-41 HAADF images of representative dispersoids in 0.5Mn alloy homogenized at 580 °C for 12 h (a) with SC crystal structure (b) with BCC crystal structure; Mn and Fe contents and also the Mn/Fe ratios measured along the length of a dispersoid in 0.5Mn alloy homogenized at 580 °C for 12 h (c) with SC crystal structure (d) with BCC crystal structure

The Mn and Fe contents together with the Mn/Fe ratio were plotted in Figure 5.41c and 5.41d. It is observed that the Mn/Fe ratio are both around 2.5, i.e. is similar for both SC and BCC, but much lower compared to the sample homogenized at 550 °C for 2 h.

The EDS line scans and crystal structure analysis were also conducted on the 0.5Mn0.15Cr alloy for homogenization of 2 h at 550 °C. Two dispersoids which were determined to be SC and BCC structures are shown in Figure 5.42a and 5.42b.

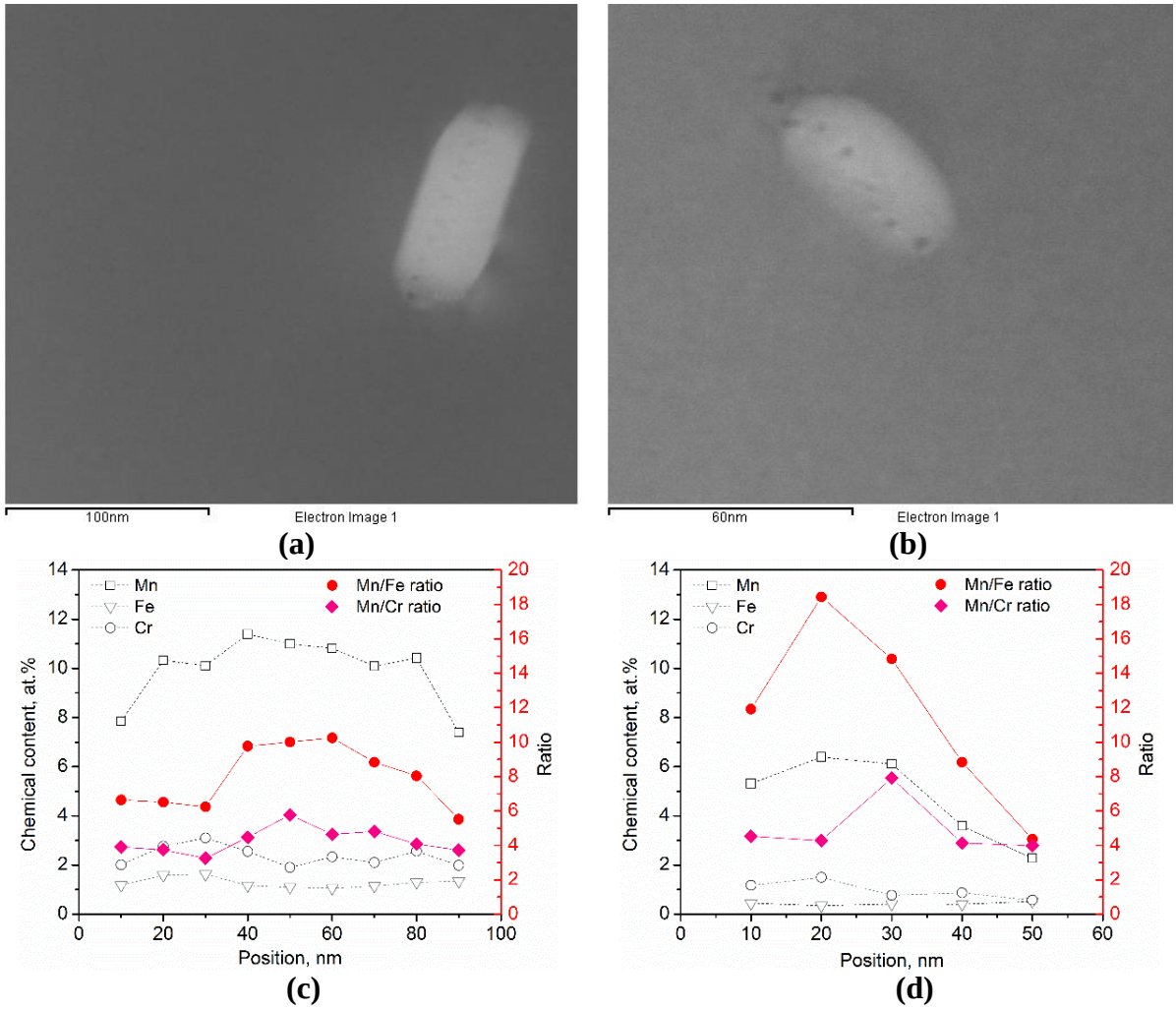

Figure 5-42 HAADF images of representative dispersoids in 0.5Mn0.15Cr alloy homogenized at 550 °C for 2 h (a) with SC crystal structure (b) with BCC crystal structure; Mn, Fe and Cr contents and also the Mn/Fe and Mn/Cr ratios measured along the length of a dispersoid in 0.5Mn0.15Cr alloy homogenized at 550 °C for 2 h (a) with SC crystal structure (b) with BCC crystal structure

The results from the EDS line scans for the Mn, Fe and Cr contents together with the Mn/Fe and Mn/Cr ratios are plotted in Figure 5.42c and 5.42d. It is observed that the Mn/Fe ratio is higher in the BCC structure than the SC structure, although it is not clear whether this is stastically significant or not.

After homogenization at 580 ºC for 12 h, it is very hard to find any dispersoids with BCC structure (see Table 5.10). Therefore, only a dispersoid determined to be SC structure was characterized under HAADF image shown in Figure 5.43a. From the chemistry distribution of Mn, Fe and Cr in Figure 5.43b, it clearly shows higher Mn in the centre of the dispersoids. The ratios of Mn/Fe and Mn/Cr also show the pronounced chemical inhomogeneity across the dispersoids.

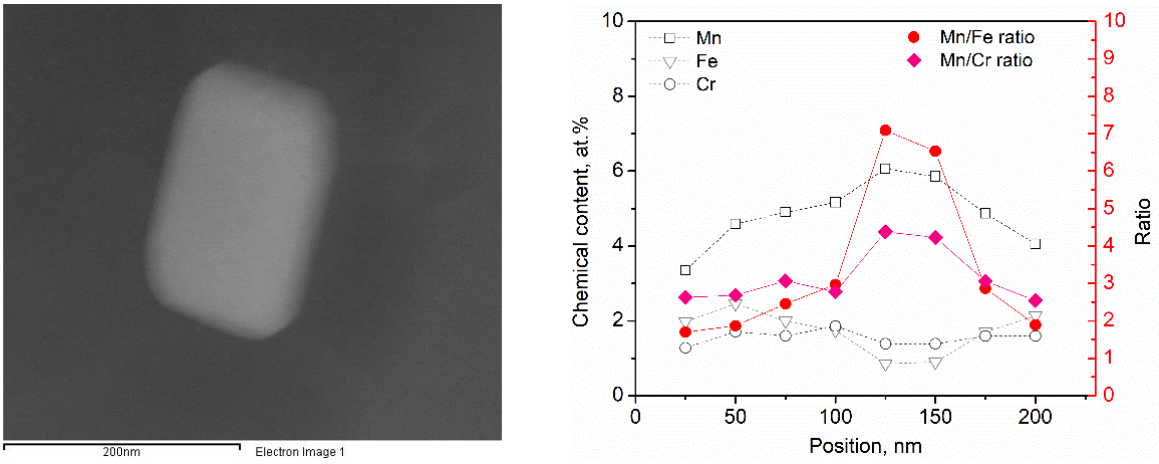

(a) **(b)**

Figure 5-43 (a) HAADF images of representative dispersoids in 0.5Mn0.15Cr alloy with SC crystal structure (b) Mn, Fe and Cr contents and also the Mn/Fe and Mn/Cr ratios measured along the length of a dispersoid in 0.5Mn0.15Cr alloy homogenized at 580 °C for 12 h

In summary, the ratios between the average and the centre for Mn/Fe and Mn/Cr from at least 8 EDS line scanning measurements are shown in Table 5.12.

Table 5.12 Ratios between the average and the centre for Mn/Fe and Mn/Cr from EDS line scanning in 0.25Mn, 0.5Mn and 0.5Mn0.15Cr alloys under two homogenization treatments

Alloy and homo	Mn/Fe (Ave/Centre)	Mn/Cr(Ave/Centre)
0.25Mn-550ºC-2h	0.69	-
0.25Mn-580ºC-12h	0.92	-
0.5Mn-550ºC-2h	0.77	-
0.5Mn-580ºC-12h	0.79	-
0.5Mn0.15Cr-550ºC-2h	0.72	0.86
0.5Mn0.15Cr-580ºC-12h	0.69	0.84

It is pretty clear that measuring the Mn/Fe or Mn/Cr ratio from the centre of a dispersoid would provide a higher value than the average ratio. Therefore, the Mn/Fe and Mn/Cr ratios obtained from the EDS measurements on the centre of the dispersoids in Table 5.11 could be corrected on the basis of the more detailed chemistry distribution from Table 5.12. After taking into account the chemical composition differences between the centre and the edge, the corrected average Mn/Fe and Mn/Cr ratios for the dispersoids are provided in Table 5.13.

Table 5.13 Average atomic Mn/Fe and Mn/Cr ratios after correction based on the difference between the centre and the average from EDS line scanning in 0.25Mn, 0.5 Mn and 0.5Mn0.15Cr alloys under two homogenization treatments

Alloy and homo	Atomic ratio Mn/Fe	Atomic ratio Mn/Cr
0.25Mn-550ºC-2h	2.2	-
0.25Mn-580ºC-12h	1.2	-
0.5Mn-550ºC-2h	12.6	-
0.5Mn-580ºC-12h	3.6	-
0.5Mn0.15Cr-550ºC-2h	9.8	3.5
0.5Mn0.15Cr-580ºC-12h	2.4	2.4

5.6 Estimation of Mn/Cr in solid solution

Having characterized the grain size, the constituent particles and the dispersoids, the next microstructure parameter that needs to be determined is the solid solution level in the primary aluminum. Electrical resistivity measurements were used for this purpose.

The measurements were done quickly on water quenched samples after the homogenization treatments for the base alloy and also Mn/Cr bearing alloys at 550 ºC and 580

ºC holding for different times. As discussed in Section 5.2, Mg_2Si was dissolved after approximately 10 min at 550 ºC and the effect of Mg_2Si on the change of electrical resistivity is negligible after this point. For the 0Mn alloy, the electrical resistivity change should be negligible once Mg_2Si is completely dissolved into the matrix. Based on this, an average electrical resistivity 37.3 nΩ·m was established as the base line value ρ_{base} (i.e. the average of all the homogenization conditions in for 0Mn alloy shown in row #1 of Table 5.14). In comparison, the resistivity values for the Mn/Cr bearing alloys from each of the homogenization condition are all higher and are summarized in Table 5.14.

Table 5.14 Electrical resistivity measurements on the homogenized samples of 0.25Mn, 0.5Mn and 0.5Mn0.15Cr alloys in nΩ·m

Alloys	550°C, 1h	550°C, 2h	550 °C, 4h	550 °C, 8h	550 °C, 24h	580 °C, 2h	580 °C, 12h	580 °C, 168 h
0Mn	37.5	37.6	37.3	37.4	37.0	37.0	37.0	37.5
0.25Mn	39.5	39.0	39.0	38.8	38.7	39.8	39.3	38.9
0.5Mn	40.4	40.1	39.9	39.0	39.0	41.0	40.6	40.4
0.5Mn0.15Cr	41.6	41.1	40.5	39.8	39.7	41.8	41.3	41.3

As described in the literature review (see Section 2.2), the resistivity has the following contributions:

$$\rho = \rho_{thermal} + \rho_{solutes} + \rho_{dislocations} + \rho_{precipitations} + \rho_{grainboundries} \quad (5\text{-}2)$$

where $\rho_{solutes} = \sum_{i=1}^{n} K_i C_i$ (K_i is the resistivity coefficient and C_i is the concentration)

In the current case, $\Delta\rho$ (ρ - ρ_{base}) has been utilized to remove the thermal component, in addition to any microstructure features such as the dislocation density, grain boundaries as well

as the constituent particles. Further, according to the work of Lodgaard and Ryum [65] and Lok[158], the effect of dispersoids on resistivity could be neglected to the first approximation as a result of their incoherency to the aluminum matrix. So, the change of resistivity compared to the base alloy is mainly caused by the solute in the solution.

$$\Delta\rho = \rho - \rho_{base} = K_{Mg}C_{Mg} + K_{Si}C_{Si} + K_{Mn}C_{Mn} + K_{Fe}C_{Fe} + K_{Cr}C_{Cr} \quad (5\text{-}3)$$

Mg is constant, as has been shown earlier, whereas all the Mg_2Si is dissolved, where ρ_{base}= 37.3 nΩ·m. The effect of Si is accounted for the Mn/Cr addition based on Thermo-calc (TTAL6). Finally, the solubility of Fe in the matrix for 0.25Mn alloy at 550 °C or 580 °C is 0.0029 and 0.0057 wt.%, respectively, i.e. it is so low ≈ 0.1 nΩ·m (given K_{Fe} ≈25.5 nΩ·m/wt.% [43]) as to have a negligible contribution to Δρ.

The differences in these electrical resistivity values from Table 5.14 are therefore found to be mainly caused due to the changes in Mn and Mn/Cr solid solution contents, which in turn, is caused by precipitation of Mn/Cr dispersoids. To quantitatively estimate the Mn in solid solution, the differences in the electrical resistivity were calculated between the Mn/Cr containing alloys and the base alloy as shown in Figure 5.44 and Figure 5.45.

It can be seen that in both Figure 5.44a and 5.44b, the change in resistivity is the largest for 0.5Mn0.15Cr alloy followed by the 0.5Mn alloy and 0.25Mn alloy. In addition, the change in the resistivity is also dependent on the homogenization temperature, as the solubility for Mn is higher at 580 ºC than 550 ºC.

Turning to the Mn alloys, the change of resistivity compared to the base alloy is the following.

$$\Delta\rho = K^{wt.}_{Mn,S.S}C^{wt.}_{Mn,S.S} \quad (5\text{-}4)$$

or $$C_{Mn,S.S}^{wt.} = \frac{\Delta\rho}{K_{Mn,S.S}^{wt.}} \quad (5\text{-}5)$$

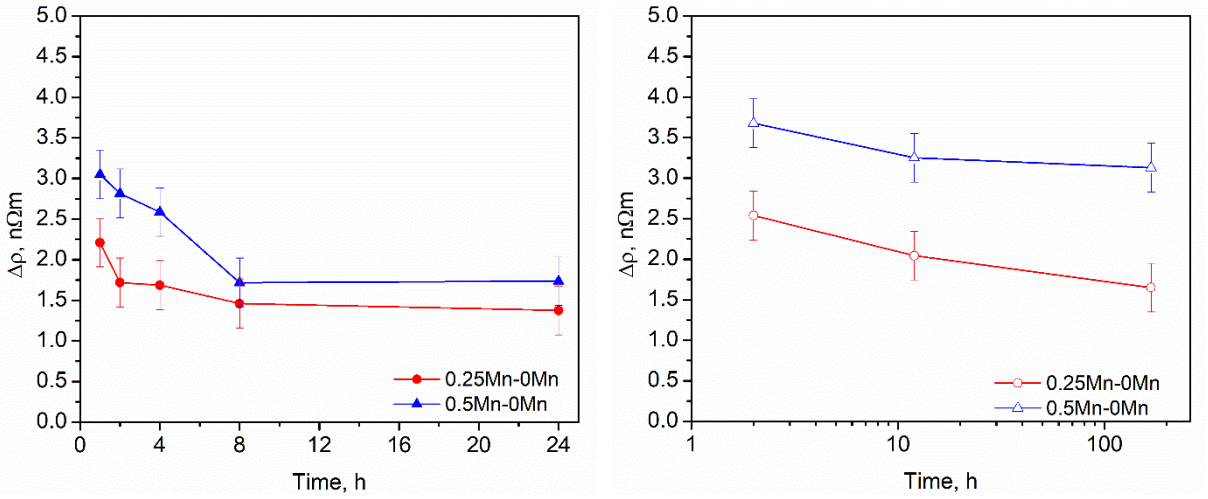

Figure 5-44 The electrical resistivity difference between the Mn bearing alloys and the 0Mn alloy (a) homogenized at 550 ºC and (b) homogenized at 580 ºC.

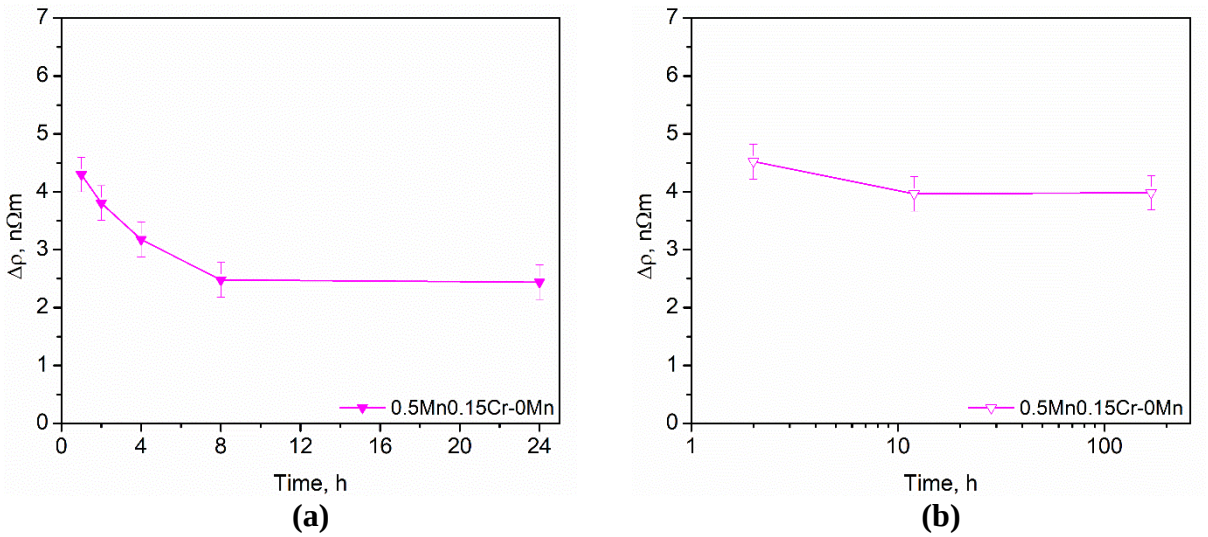

Figure 5-45 The electrical resistivity difference between the Mn and Cr bearing alloys and the 0Mn alloy (a) homogenized at 550 ºC and (b) homogenized at 580 ºC.

According to the previous literature (Modolfo [74] and Hatch [43]), a large range of coefficients can be found for Mn, from 24 to 36 nΩ·m/wt.%. Considering one week soaking at 580 °C, Thermo-Calc (TTAL6) thermodynamic database predicts 0.066 wt.% and 0.132 wt.%

for 0.25Mn and 0.5Mn, respectively. Given Δρ is 1.6 nΩ·m for 0.25Mn and 3.1 nΩ·m for 0.5Mn alloy. Then, K_{Mn} equals to 24.2 (i.e. 1.6/0.066) in 0.25Mn alloy and K_{Mn} equals to 23.5 (i.e. 3.1/0.132), which is close to the value from Modolfo [74] of 24 nΩ·m/wt.%. Therefore, the resistivity coefficient for Mn is chosen as 24 nΩ·m/wt.% in this thesis. Thus, the estimates of Mn in the solid solution are calculated from the change of resistivity and have been provided in Table 5.15.

Table 5.15 Estimations of Mn in solid solution in the homogenized samples of 0.25Mn and 0.5Mn alloys in wt.%

	550°C, 1h	550°C, 2h	550 °C, 4h	550 °C, 8h	550 °C, 24h	580 °C, 2h	580 °C, 12h	580 °C, 168 h
0.25Mn alloy	0.092	0.072	0.070	0.061	0.057	0.106	0.085	0.069
0.5Mn alloy	0.127	0.117	0.108	0.072	0.072	0.153	0.135	0.130

Now taking in consideration the case of the Mn/Cr alloy, it is clear that one cannot get two concentrations from one measurement. This will be returned to further in the discussion where an additional constraint is proposed.

5.7 Microprobe data (Solute redistribution of Mn, Fe and Cr)

Micro-segregation exists in the as-cast alloys where the dendrites are clearly visible in the anodized images of Figure 5.1 and in the literature review (Section 2.2), it was noted that Mn is initially supersaturated in the Al dendrites and that Mn diffuses to the constituent particles at long times and high temperatures. To quantitatively determine the degree of micro-segregation and its evolution during the process of homogenization, systematic electron probe micro analysis (EPMA) measurements were employed.

In Section 5.2, it was shown that the EPMA results could be used to examine the dissolution of Mg_2Si and Si phases in the as-cast material. This was a relatively fast process, which was complete within ≈10 min at 550 °C. In this section, the focus will be on the diffusing transition metals that diffuse at much slower rates, i.e. Mn, Fe and Cr.

As introduced in the methodology, three or four random lines of length 200-300 μm were examined by the EPMA with a distance of 5 μm between each of the measurements, such that about 200 data points were collected for each condition. The overall composition of the alloys from microprobe are about ± 0.1 wt.% to the nominal chemistry, and these results have been summarized in the appendix A from Tables A1 to A4. Since the beam size of the microprobe is ≈1 μm and the interaction volume in the aluminum is 2-3 μm in diameter [150], which makes it a challenge to clearly resolve the spatial distribution across a dendrite (1/2 the SDAS ≈ 10 μm). A schematic for one EPMA measurement has been shown in Figure 5.46. Due to the large size of the interaction volume, the chemistry information generated can involve a variety of sources, i.e. the matrix, one or more constituent particles, Mg_2Si or Si particles. Note: here, the term matrix refers to the summation of solid solution and dispersoids.

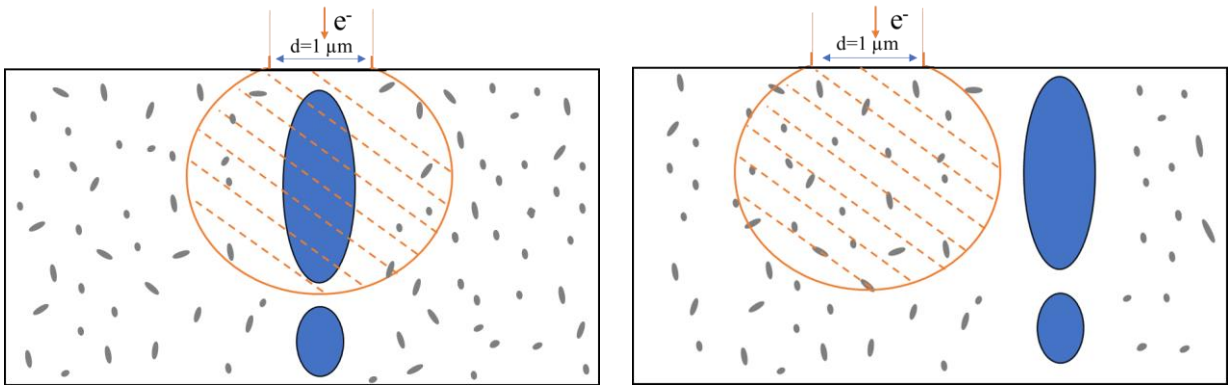

(a) **(b)**

Figure 5-46 Schematics of the interaction volume from EPMA and the scale of a homogenized microstructure. (a) on or partially on a constituent particle and (b) on the matrix including alloying elements in solid solution and in dispersoids (Note that the bigger blue particles in micro meters scale are constituent particles and the smaller grey particles in nano meters scale are dispersoids.)

Examples of EPMA line scans for Mn/Cr and Fe are shown in Figure 5.47a, 5.48a and 5.49a for the 0.25Mn, 0.5Mn and 0.5Mn0.15Cr alloys homogenized for 2 h at 550 ºC.

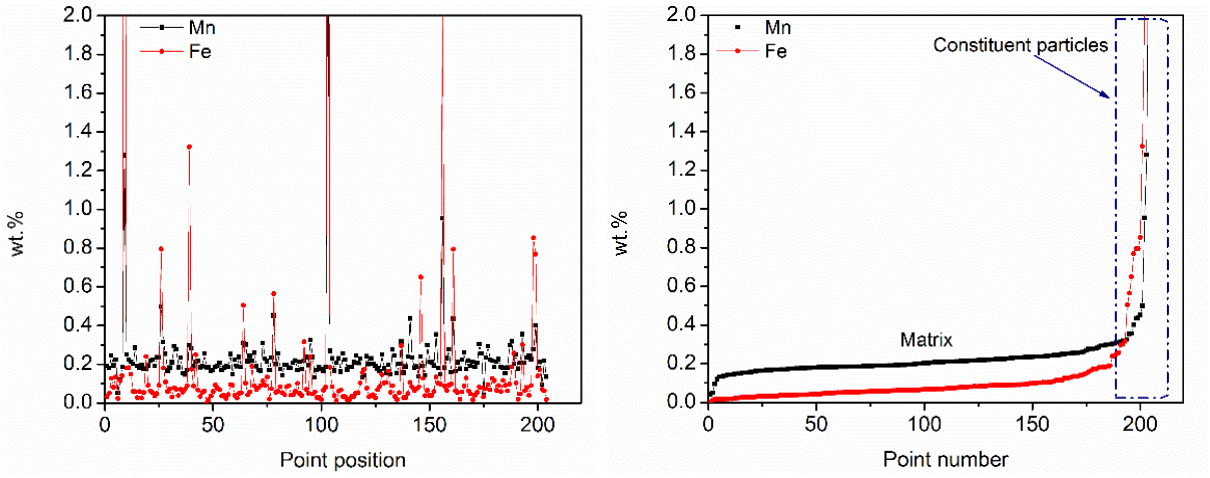

(a) **(b)**

Figure 5-47 Microprobe data measured for 0.25Mn alloy homogenized at 550 ºC for 2 h (a) unsorted showing spatial information and (b) Mn and Fe sorted ascendingly (constituent particles are found in the region marked by the box, i.e. high Fe and Mn levels.)

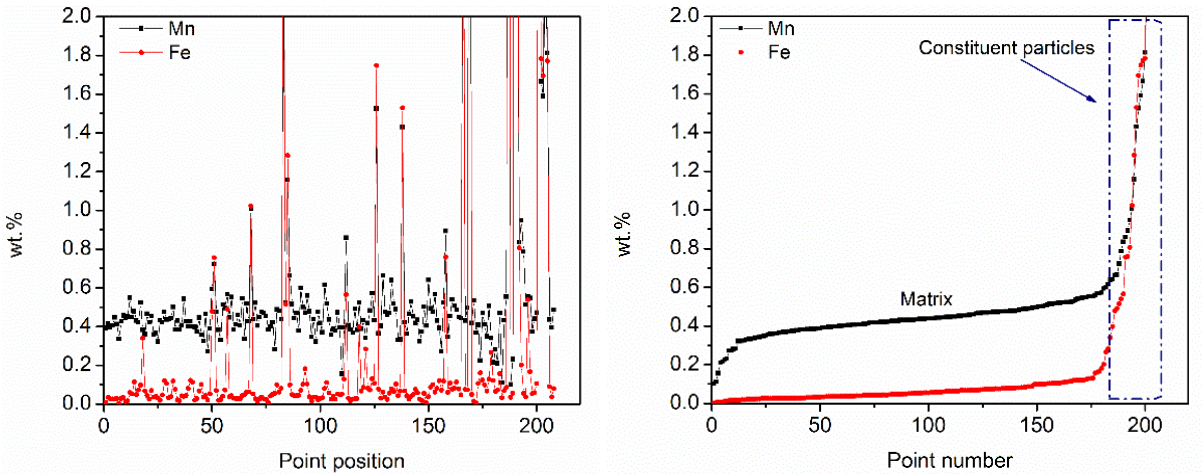

(a) **(b)**

Figure 5-48 Microprobe data measured for 0.5Mn alloy homogenized at 550 ºC for 2 h (a) unsorted showing spatial information and (b) Mn and Fe sorted in an ascending manner

The data of both Mn and Fe show that most of the points have lower concentrations (below 0.25 wt.%) with a small number of points having higher concentrations. Presumably, the points with high Mn and Fe levels come from the situations where the interaction volume includes a constituent particle, as shown schematically in Figure 5.46a. The same data for Mn/Cr and Fe were then sorted from the lowest to highest based on the approach from Gungor [159] and Ganesan et al. [160]; this arrangement is shown in Figure 5.47b, 5.48b and 5.49b. Although the spatial information is lost, plotting the data in this manner suggests that the data can be separated based on the Fe content, i.e. between the matrix measurements (note the matrix includes the Al rich solid solution and possible dispersoids) and the measurements that contain Fe rich constituent particles.

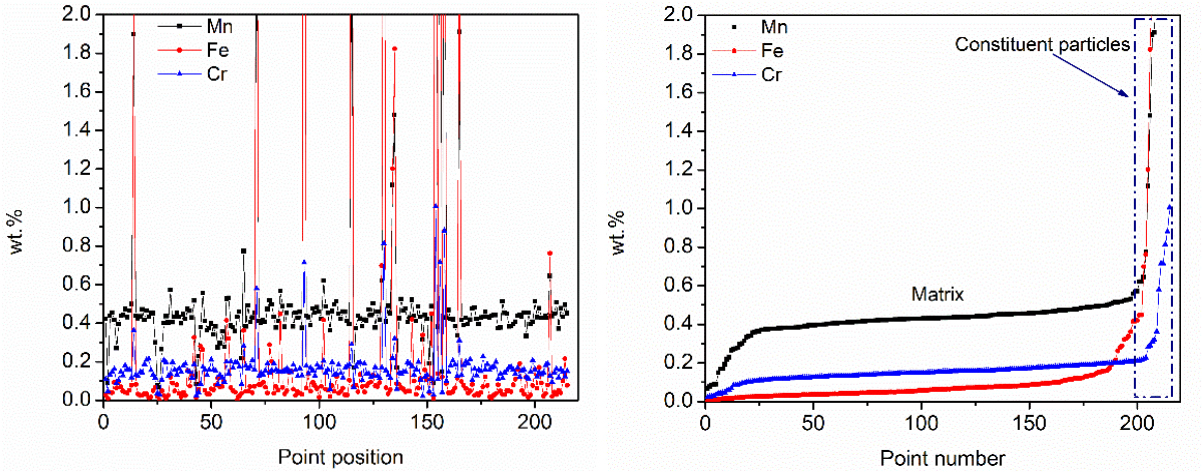

(a) **(b)**

Figure 5-49 Microprobe data measured for 0.5Mn0.15Mn alloy homogenized at 550 ºC for 2 h (a) unsorted showing spatial information and (b) Mn and Fe sorted in an ascending manner

5.7.1 Analysis of microprobe data

In the previous section, it was shown that after sorting the data from the lowest to highest, two groups of data were suggested, i.e. matrix and constituent particles. It has been noted that Fe is mostly segregated into the constituent particles after solidification as a result of its low solid solubility in Al matrix, i.e. 4.9×10^{-10} wt.% at room temperature, 2.3×10^{-3} wt.% at 580 °C and 0.04 wt.% at 655 ºC based on Thermo-Calc (TTAL6) for 0.5Mn alloy. Thus, it appears promising that the measured EPMA data can be separated based on the Fe content, i.e. matrix and Fe bearing constituent particles. In addition, Mg_2Si and Si phases are also present in the cast samples based on the quantitative XRD study on the extracted intermetallics shown in Table 5.2. Therefore, a rigorous way to separate the EPMA dataset into groups that contain Fe intermetallics, Mg_2Si and Si particles based on the local chemistry would seem valuable.

It is proposed that the first step is to separate the EPMA data points which possess a "high" Fe content and assign these as Fe intermetallics. Figure 5.50 shows the EPMA data sorted by the Fe content for 0.25Mn alloy which was homogenized for 2 h at 550 °C. In Figure 5.50b

(which is a magnified view of the data), it appears that there is a break in the slope of the data for the Fe content greater than 0.1 wt.%. It is proposed that this represents the boundary between the measurements that were fully in the matrix and those which contained part of a constituent particle.

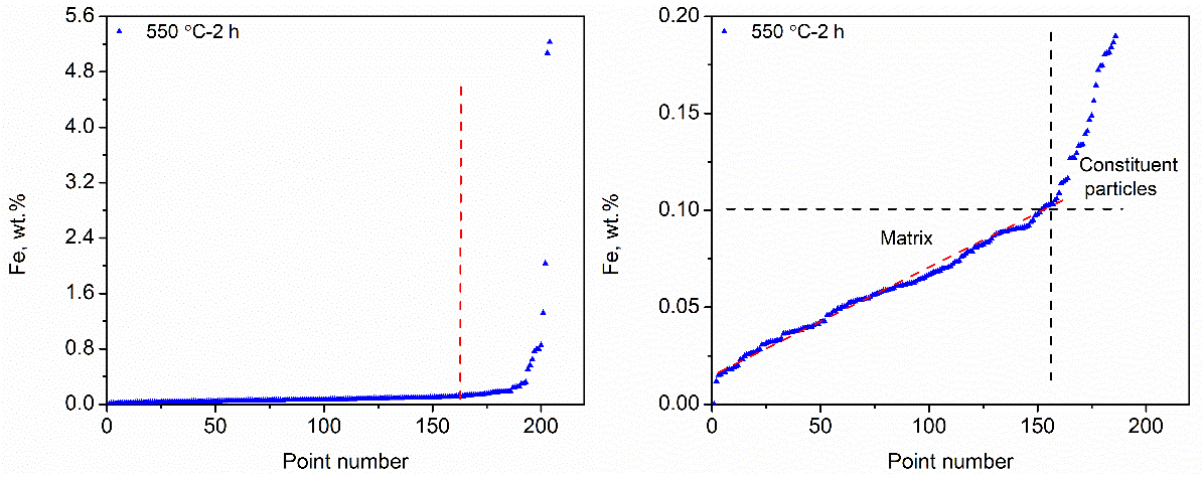

(a) **(b)**

Figure 5-50 Microprobe data of Fe after sorting in 0.25Mn alloy homogenized at 550 ºC for 2 h (a) Fe ranges from 0 to 5.6 wt.% and (b) Fe ranges from 0 to 0.2 wt.%

To further explain the separation cut-off, the histogram is plotted showing the relative frequency of the number points from the Fe range 0 to 0.35 wt.% as shown in Figure 5.51. A noticeable change in both the relative frequency and total Fe content was observed around 0.1 wt.%.

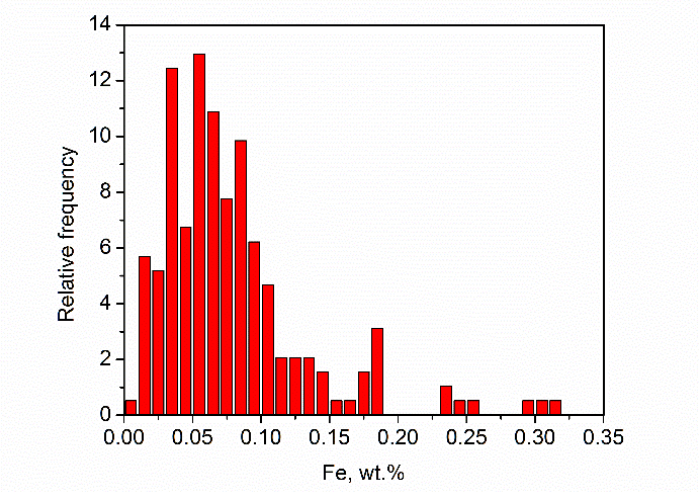

Figure 5-51 Histogram of Fe after sorting in 0.25Mn alloy homogenized at 550 ºC for 2 h based on the relative frequency of the number of points in each bin

Upon careful examination of the data, it became apparent that each case had a different Fe cut-off value. Therefore, the Fe cut-off value was determined similar to the example in Figure 5.51. The various cut-off values are indicated using the vertical solid lines in Figure 5.52. Further, the Fe cut-off values have been summarized in Table 5.16. It is observed that the Fe cut-off values first increase with higher homogenization temperature and longer soaking time, but then drop after reaching a certain homogenization scenario. The phenomenon was found in all the three alloys.

Table 5.16 Fe cut-off values for the three alloys of different homogenizations, wt.%

	As-cast	550°C-10min	550°C-2h	580°C-2h	580°C-12h	580°C-168h
0.25Mn alloy	0.04	0.06	0.10	0.09	0.10	0.03
0.5Mn alloy	0.04	0.05	0.09	0.10	0.11	0.04
0.5Mn0.15Cr alloy	0.05	0.05	0.09	0.16	0.17	0.15

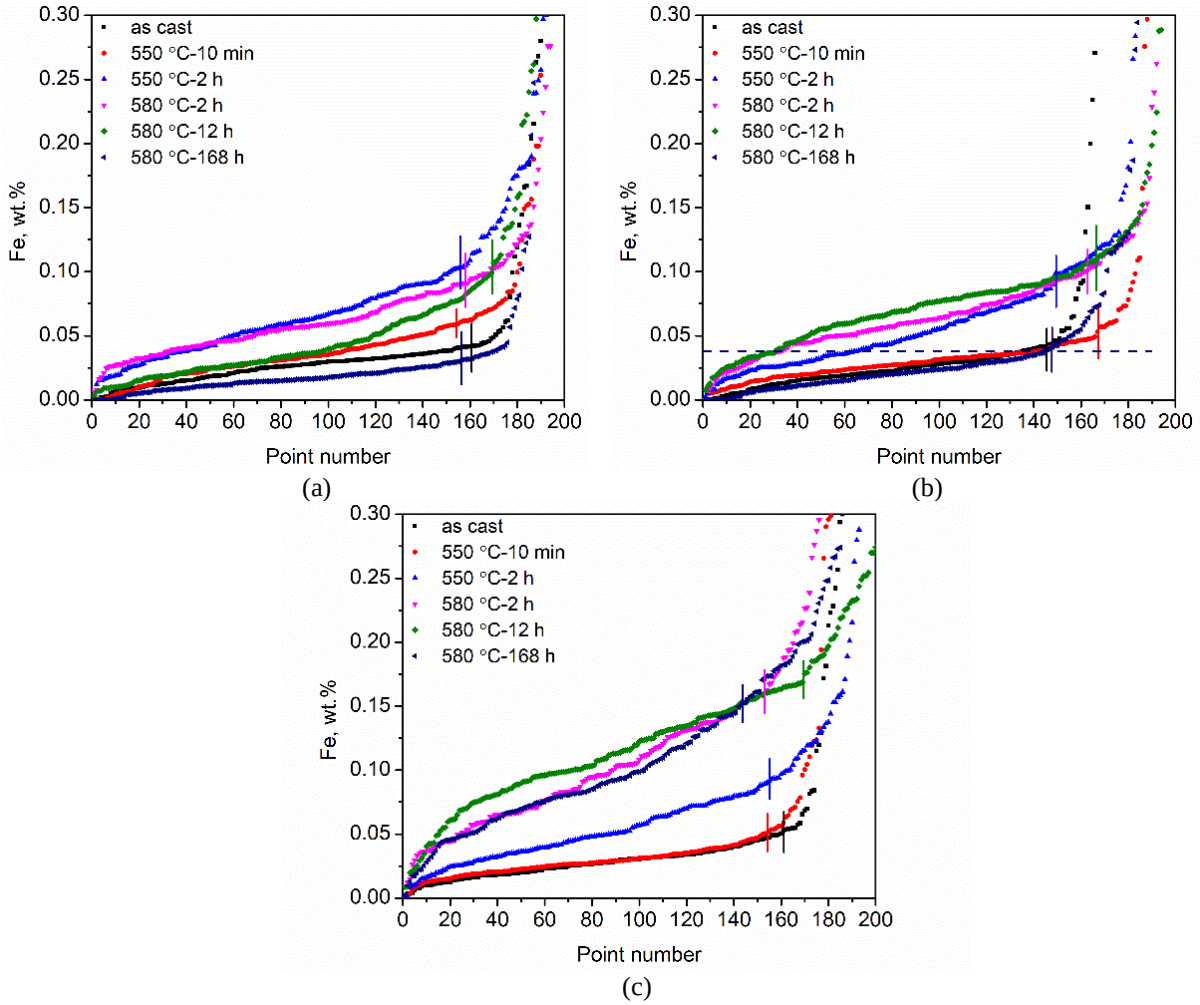

Figure 5-52 Microprobe data of Fe after sorting in (a) 0.25Mn alloy, (b) 0.5Mn alloy and (c) 0.5Mn0.15Cr alloy

Following this procedure, the EPMA points were separated into constituent particles and matrix. However, the presence of Mg_2Si and Si phases in the as-cast materials leads to a yet further complication. In the following, a method to separate these phases from the matrix data has been proposed.

The Mg sorted files and Si sorted files in 0.25Mn from various heat treatments were plotted individually in Figure 5.53a and 5.53b. It was confirmed that Mg and Si are dissolved and homogenized quickly almost after 10 min holding at 550 ºC. The change between 10 min and 2 h holding is very small at 550 ºC both for Mg and Si profiles. Apparently, the effect from

Mg_2Si and Si phases (i.e. points with higher Mg or Si concentrations) primarily exists in the as-cast samples when dealing the rigorous sorting approach. The separation numbers for Mg and Si are chosen as 0.8 wt.% and 1.0 wt.% as shown in Figure 5.53a and Figure 5.53b, respectively. It is because both these numbers are close to the nominal composition of Mg 0.71 wt.% and Si ≈ 1.0 wt.%, respectively.

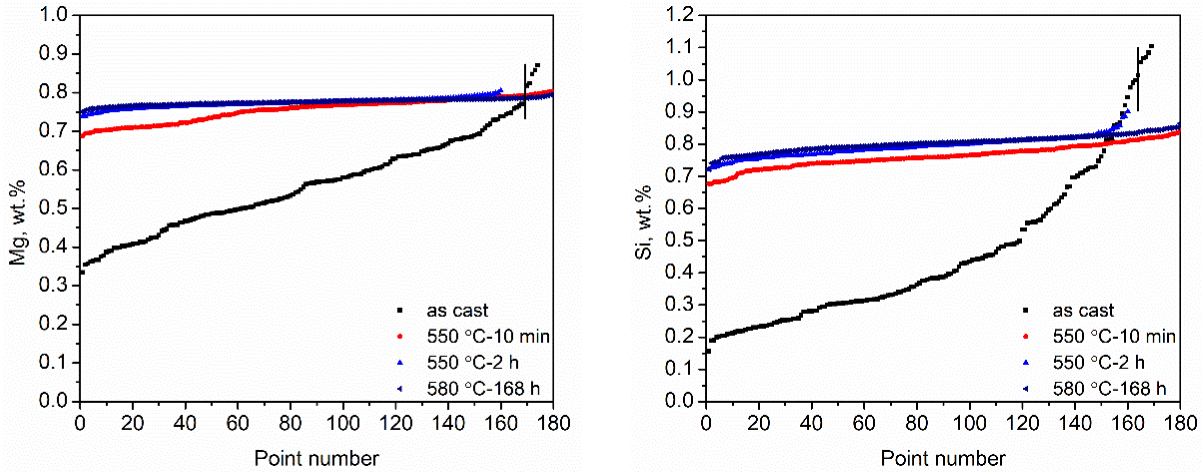

(a) **(b)**

Figure 5-53 Microprobe data of 0.25Mn alloy for (a) Mg sorted profiles and (b) Si sorted profiles both after separation based on Fe content

Therefore, the method introduced to sort the data can be summarized in the flow chart that is shown in Figure 5.54 into bins for the matrix, Fe bearing constituent particles, Mg_2Si and Si phases, even though the latter may only exist in the as-cast or very early stages of homogenization. Having separated the microprobe data, the data for each of the categories can be examined in a more detailed manner.

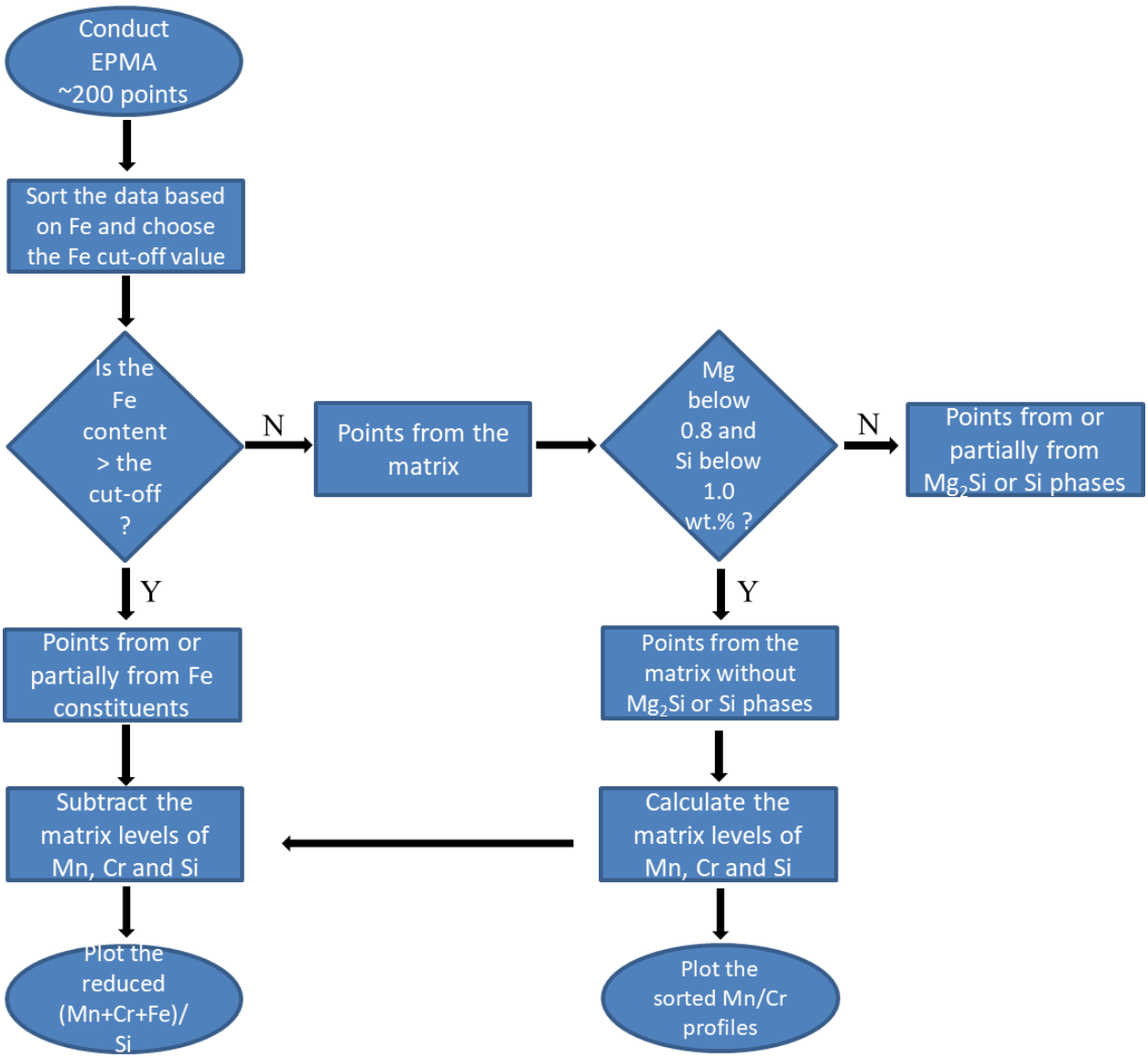

Figure 5-54 Flow chart showing the steps on how to separate the EPMA dataset into matrix and constituent particles

5.7.2 Dataset from constituent particles

In this section, the results from the microprobe will be presented for the constituent particles.

<u>0Mn alloy</u>

The transformation of Fe/Mn bearing constituent particles can be captured through EPMA measurements collected on or partially on the constituent particles in these aluminum alloys, as the Mn or Fe over Si ratio is different for the two main types of constituent particles. From the previous FEGSEM micrographs, the as-cast sample of 0Mn alloys shows the constituent particles are mostly of plate shape with very high aspect ratio (see Figure 5.2a). These particles are assumed to be primarily of β-AlFeSi type (which was confirmed by XRD on extracted particles in Section 5.3) and they still exist after a homogenization of 580 °C for 168 h. Figure 5.55 shows a cross plot of Fe vs reduced Si content for the five homogenizations (Note: the reduced Si is determined by taking the measured Si content and substracting 1 wt.%, i.e. the nominal Si level.). It can be observed that the Fe/Si ratio is close 1, which is consistent with the chemistry of the β-AlFeSi type constituent particles [41]. The ratio is close to 1 for all conditions suggesting that no phase transformation occurred to these plate phase constituent particles during the homogenization conditions, which is consistent with the results from XRD on extracted particles for the 12 h at 580 °C case shown in Table 5.3.

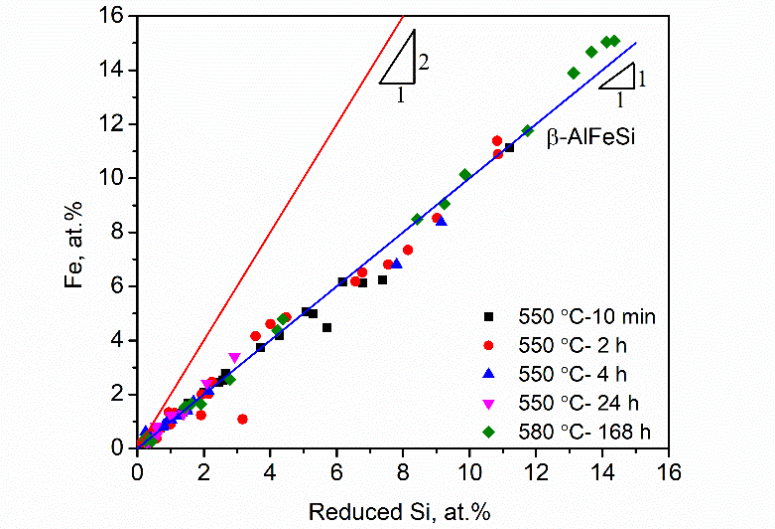

Figure 5-55 Reduced atomic Fe/Si ratio from microprobe data for constituent particles in 0Mn alloy

Further, it is noted that the α-Al(FeMn)Si phase has the general stoichiometry of $Al_{100}(FeMn)_{24}Si_{14}$.[81,82]. Sugiyama proposed a further refinement for the α phase as $Al_{100}Mn_{17.4}Si_{12.9}$ [105]. Further, it was noted in the literature review that although there is some uncertainty, it is generally believed that the (Fe+Mn) over Si ratio is ≈ 2 for the α phase. Clearly there are no data points found to match this ratio in the 0Mn alloy.

0.25Mn alloy

In the alloy with 0.25 wt.% Mn addition, the microprobe data suggests that β-AlFeSi phase is the dominant constituent particle for the homogenization condition of 10 min at 550 °C as seen in Figure 5.56a, i.e. all the data for this condition falls on the line with slope of 1. However, the transformation of β-AlFeSi phase to α-Al(FeMn)Si phase occurs during holding at 550 °C. Soaking for 2 h at 550 °C resulted the co-existence of α-Al(FeMn)Si and β-AlFeSi phase in the microstructure, i.e. there are data points on both the lines of slope 1 and slope 2 (Note: the value of the reduced Mn content were determined by substracting the Mn matrix levels from the measured Mn contents). In the cases of holding for 4 h at 550 °C or 12 h/168 h at 580 °C, only α-Al(FeMn)Si particles with chemistry consistent with the α-Al(FeMn)Si phase were found consistent with the XRD results shown in Table 5.3 (e.g. fraction of β-AlFeSi phase for 2 h at 550 °C is < 5%).

It is shown in Figure 5.56b that Mn/Fe ratio increases with a longer soaking period and higher soaking temperature, thus indicating that the Mn/Fe ratio is homogenization process dependent. The increase of Mn in the constituent particles is related to the diffusion of Mn from the matrix via dissolution of finer dispersoids to coarser constituent particles [115]. Since Mn diffusion is dependent both temperature and time, it is reasonable to see such an increase with a series of progressive homogenizations with a higher temperatures and longer soaking time.

Finally, the Mn/Fe ratio would reach a maximum level once the equilibrium condition is reached for a given composition.

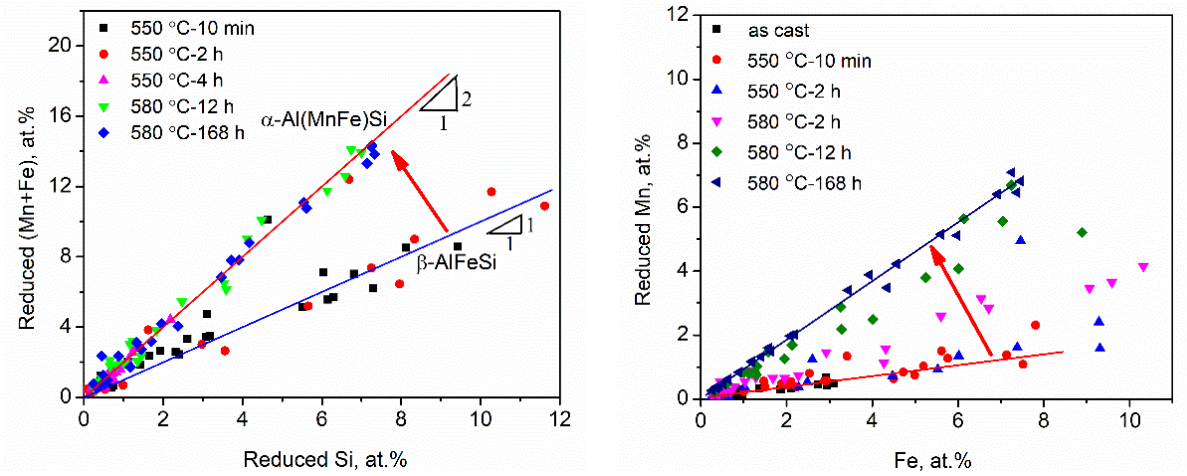

Figure 5-56 Microprobe data for constituent particles in 0.25Mn alloy (a) Reduced (Fe+Mn) over reduced Si ratio and (b) Reduced atomic Mn/Fe ratio

0.5Mn alloy

With an increasing Mn content to 0.5 wt.%, the transformation of β-AlFeSi to α-Al(FeMn)Si is even faster as shown in Figure 5.57. For the homogenization condition of 10 min at 550 °C, most of the data points fall on the line where the (Mn+Fe)/Si ratio is 2, although two points are seen on the line of slope 1. After holding for 2 h at 550 °C, all the data falls on α-Al(FeMn)Si line suggesting that the transformation is complete. This is consistent with the XRD results in Table 5.3 and the work from Zajac et al. [25], where it was reported that the addition of 0.8 wt.% Mn in AA6xxx alloys accelerates the transformation from long brittle β constituent particles to more rounded α ones.

It is also noted that similar to 0.25Mn alloy, the Mn/Fe ratio increases during the homogenization process. The Mn/Fe ratio is higher in 0.5Mn alloy than that of 0.25Mn alloy under a similar homogenization scenario in Figure 5.57b.

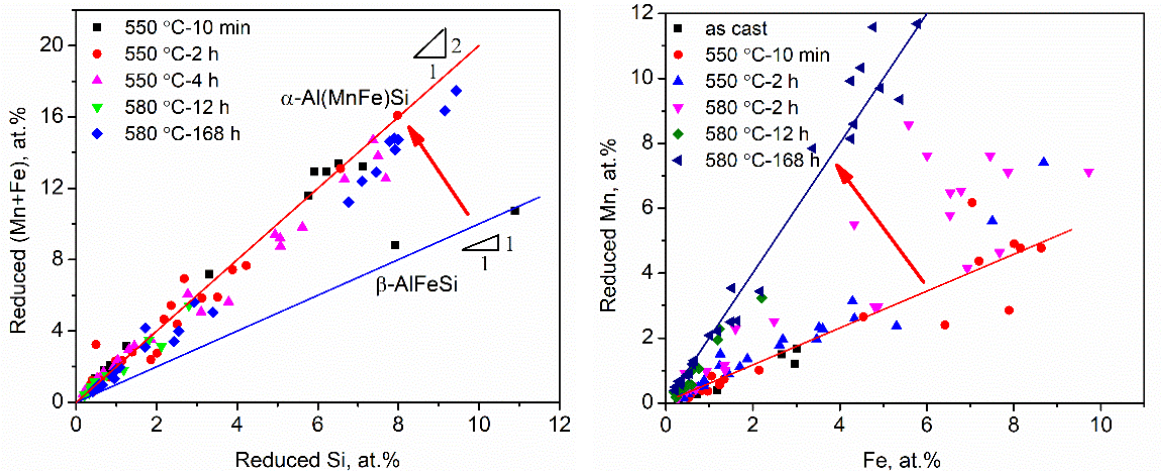

(a) **(b)**

Figure 5-57 Microprobe data for constituent particles in 0.5Mn alloy (a) Reduced (Fe+Mn) over reduced Si ratio and (b) Reduced atomic Mn/Fe ratio

0.5Mn0.15Cr alloy

The change in composition of the constituent particles was also observed in the 0.5Mn0.15Cr alloy. After a short holding period 550 °C for 10 min, it is observed in Figure 5.58a that most of the particles measured are of the (Mn+Fe+Cr)/Si ratio as 2, except only one point of the ratio as 1. This suggests the coexistence of α-Al(FeMn)Si and β-AlFeSi after ramping to 550 °C and held for a short period. After holding for 2 h at 550 °C or any of the conditions at 580 °C, it is found that all the particles measured are belong to α-Al(FeMn)Si phase.

Similar to the Mn bearing alloys, the Mn/Fe and Mn/Cr ratios are plotted in Figure 5.58b and 5.58c. In Figure 5.58b, Mn/Fe ratio generally increases with high homogenization temperature and longer soaking time, where lowest Mn/Fe ratio is found in the as-cast sample. During homogenization, the diffusion of Mn in the matrix to constituent particles occurred. The diffusion of Cr to constituent particles also occurred simultaneously via the dissolution of Mn/Cr containing dispersoids and growing of constituent particles. In Figure 5.58c, it shows that the Mn/Cr ratio is of little change with the increasing homogenization temperature and soaking time.

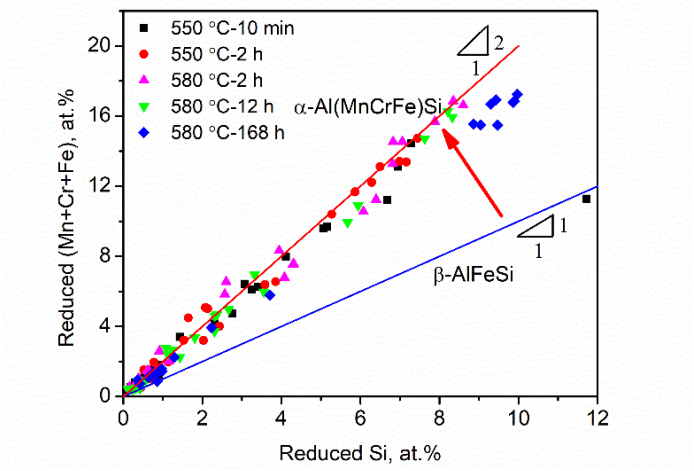

(a)

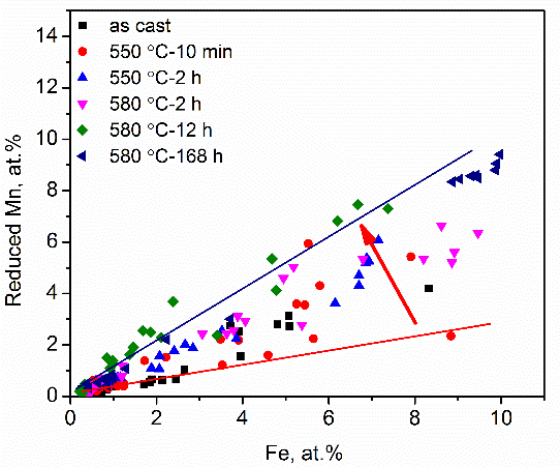

(b)

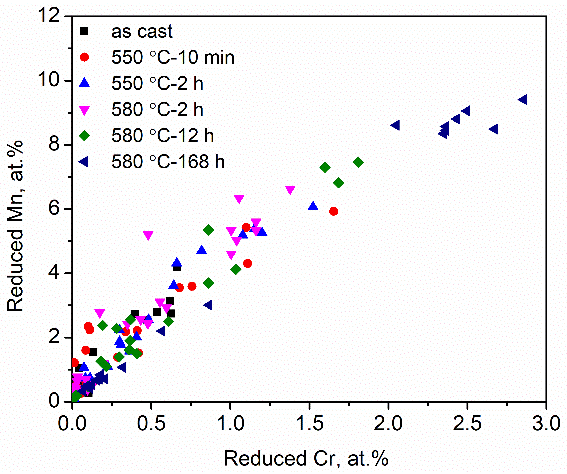

(c)

Figure 5-58 Microprobe data for constituent particles in 0.5Mn0.15Cr alloy (a) Reduced (Fe+Mn+Cr) over reduced Si ratio, (b) Reduced Mn/Fe ratio and (c) Reduced Mn/Cr ratio from EPMA

In summary, it appears that the microprobe data can be used to study the chemistry of the constituent particles and its evolution during homogenization. However, one problem here is that after sorting the data, there are really too few points for good statistics. So, the data is only qualitative. In order to make it quantitative, one would need much large data sets. On the other hand, compared with the XRD analysis, EPMA measurements are much easier to perform, as the extraction of the constituent particles in the homogenized conditions can be difficult.

5.7.3 Dataset from the matrix

This section will present the data for the matrix will be presented. There are about 150 to 180 points for each sorted curve after applying the cut-off values. It is must be reminded to the reader that the probe size is 1 µm and the interaction volume diameter is about 2 to 3 µm. Therefore, each measurement will include information from the solid solution as well as the dispersoids.

0.25Mn alloy

The histograms for Mn and Fe contents measured in 0.25Mn alloy by EPMA were plotted in Figure 5.59. Normal distribution was fit to Equation 5-6 following the least square root principle.

$$f(x) = \frac{1}{\sqrt{2\pi\sigma^2}} \exp\left[-\frac{(x-\mu)^2}{2\sigma^2}\right] \tag{5-6}$$

where µ is the mean and σ is the standard deviation.

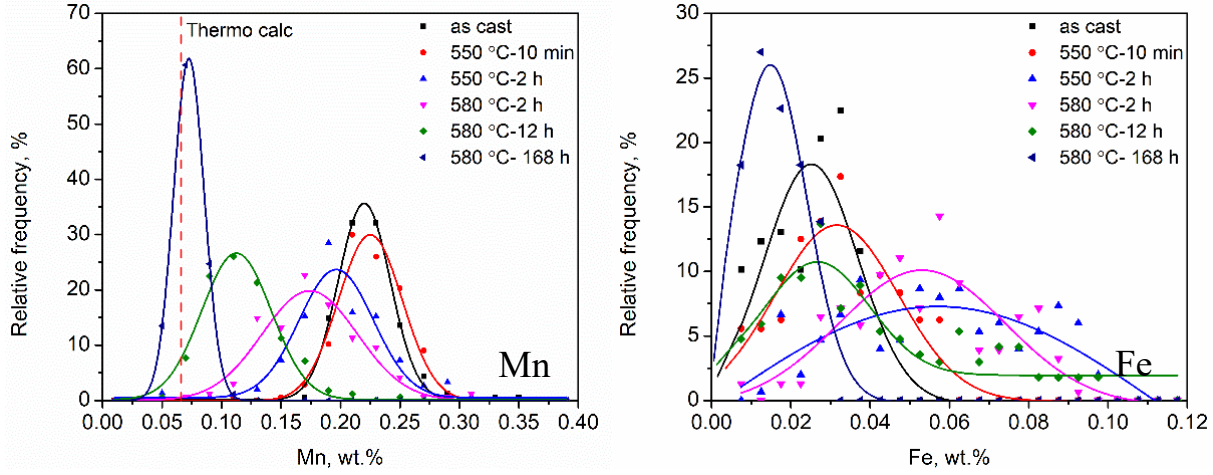

(a) **(b)**

Figure 5-59 Histograms with normal fittings from as-cast and different homogenization conditions for (a) Mn matrix levels and (b) Fe matrix levels in 0.25Mn alloy

The Mn is found more in the dendrite core area other than the interdendritic region, which consists of the constituent particles. It is observed that the Mn histogram shifts gradually

from the right to left with higher soaking temperature and longer soaking times as shown in Figure 5.59a. The Mn content histogram for the as-cast sample has a mean position of about 0.22 wt.%, which is close to the nominal Mn content of 0.25 wt.%. There is a very little distribution change after homogenization at 550 ºC for 10 min, as compared to the as-cast sample, i.e. the microprobe measurements are not affected by precipitation of dispersoids (see Figure. 5.18). However, the width of the histogram starts widening and has a small shift to the left for the homogenization condition of 550 ºC for 2 h, which may be due to the long-range diffusion of Mn from the dispersoids to the constituent particles. The Mn distributions further widen and shift to the left for homogenization at 580 ºC for 2 h, as Mn continues to diffuse to the constituent particles. Finally, the Mn distribution has shifted to a low value and becomes much narrower for homogenization at 580 ºC for 168 h. This is in agreement with the observation in Figure 5.22a (see Section 5.4) that there were almost no dispersoids left in the aluminum matrix. Further, the dashed red line represents the equilibrium value for Mn in the solid solution from TTAL6 and this is very close to the mean value of Mn, i.e. the system is close to the state of equilibrium.

Turning to the results for Fe shown in Figure 5.59b, one can observe that the Fe histogram for the 0.25Mn alloy shows a low value of Fe for the as-cast sample. While a pronounced change of Fe histogram was found in the sample held at 550 °C for 2 h, the Fe histogram possess a much wider span. Upon holding for 2 h at 580 °C, the width of the histogram shrinks a little, but still offers a very wide span. With an increase in the holding time, the width of the Fe containing histogram gets narrower and shifts from the right to the left. It could be observed in Figure 5.59b that the Fe histogram from the homogenization at 580 °C for one week has the narrowest width among the homogenizations studied and the mean position is even lower than the as-cast condition. In this case, the width of the distribution is probably due to

the measurement error for Fe in microprobe, as the true Fe content (i.e. 0.0057 wt.% at 580 °C for 0.25Mn from TTAL6) is below the resolution of the microprobe.

The evolution of the fitted mean values and standard deviations for Mn and Fe from the normal distributions are plotted in Figure 5.60. In Figure 5.60a, one can observe that the mean values of the Mn deceases steadily with an increase in the homogenization soaking temperature and time

It is also observed that the standard deviation changes differently compared to the Mn mean values, where the standard deviation first increases and then decreases. In comparison, the evolution of the standard deviation for Fe behaves in a similar manner to that of Mn, showing an increase and then decrease in Figure 5.60a. However, the mean value for Fe histogram firstly increases with higher homogenization temperature and longer soaking time and then it decreases after reaching a sufficient homogenization treatment in Figure 5.60b. A substantial decrease for Fe mean value was found in the homogenization at 580 °C for 12 h. The Fe results are unusual and this will be reflected upon further in the discussion.

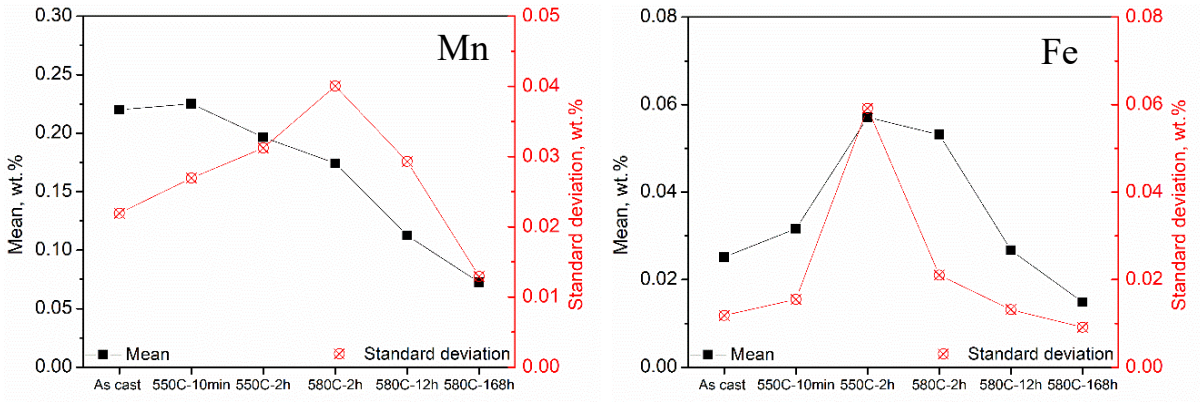

(a) **(b)**

Figure 5-60 Mean and standard deviations from the normal fitting for (a) the Mn matrix levels and (b) the Fe matrix levels in 0.25Mn alloy

0.5Mn alloy

The Mn and Fe histograms evolution in 0.5Mn alloy behaves in the same trend as that of 0.25Mn alloy as seen in Figure 5.61. As for Mn, the highest mean Mn position is found in the as-cast sample and then decreased with longer homogenization temperature and higher soaking temperature, shown in Figure 5.61a. It is not surprising that the lowest Mn mean position was found in the sample with a homogenization of 580 °C for one week. However, the mean value at this condition does not superimpose well with the Mn in solid solution calculated by Thermo-Calc (TTAL6) of 0.5Mn alloy. This shows that the equilibrium is still not established in 0.5Mn alloy even through such an extreme homogenization. There are surely more dispersoids with the equivalent radius of 100 nm or above left within grains than those of 0.25Mn alloy, as shown in Figure 5.22b (see Section 5.4). Turning back to Fe, a shift of the mean position from the left to right and then back to the very left was also observed in Figure 5.61b.

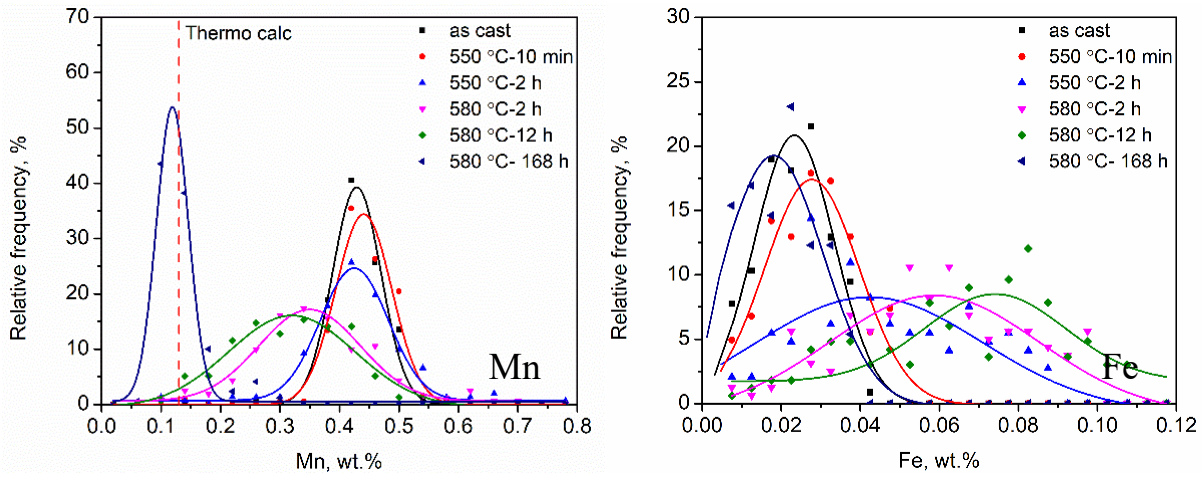

Figure 5-61 Histograms with normal fittings from as-cast and different homogenization conditions for (a) Mn matrix levels and (b) Fe matrix levels in 0.5Mn alloy

The fitted mean position values and standard deviations for Mn and Fe histogram in 0.5Mn alloy are also plotted as shown in Figure 5.62. As for Mn, both the evolutions of standard deviation and the mean positions are similar to 0.25Mn alloy, as shown in Figure 5.62a. The Fe

mean position in 0.5Mn alloy is observed to increase and then decrease in the same manner as found in 0.25Mn alloy, but the Fe mean position decease is only found in the extreme homogenization condition 580 °C for 168 h in Figure 5.62b. Apparently, addition of Mn to 0.5 wt.% changes the diffusion of Fe during homogenization. The standard deviation for Fe is also observed to rise and then falls back similarly to 0.25Mn alloy.

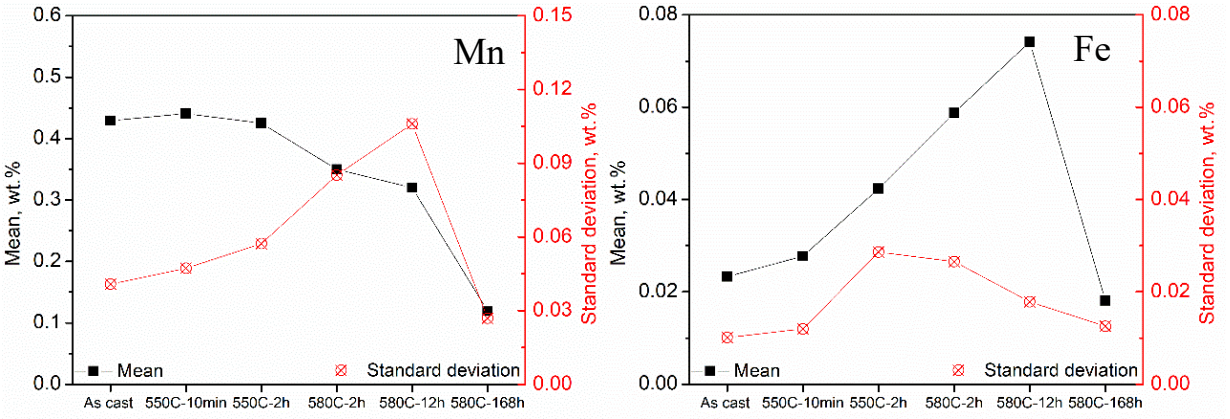

(a) **(b)**

Figure 5-62 Mean and standard deviations from the normal fitting for (a) the Mn matrix levels and (b) the Fe matrix levels in 0.5Mn alloy

The evolution of the mean position of Fe and Mn in 0.25Mn and 0.5Mn alloys are also reflected by the TEM EDS studies on the dispersoid chemistry. Referring to Figure 5.37 (see section 5.5), the decrease of the average mole Mn/Fe ratio indicated the exchange of Mn and Fe between the dispersoids and the constituent particles. It is because of the Fe diffusion from constituent particles driving the average Mn/Fe ratio.

The Mn matrix levels consist of the summation of Mn both in dispersoids and Mn in solid solution from several homogenizations summarized in Table 5.17. Each Mn matrix value was averaged from the measured data points done except on or partially on constituent particles. This manner of calculation would provide quantified information of the average Mn in the matrix under the assumption that the distribution is uniform in the micro meter scale. These quantitative

data will be used to estimate the dispersoid volume fraction in the aluminum alloys in the following discussion.

Table 5.17 Average Mn matrix levels obtained from EPMA results (wt.%) in 0.25Mn and 0.5Mn alloy (data taken from Figures 5.59a and 5.61a plus two other conditions not shown 550 °C for 4 h and 550 °C for 24 h)

	As-cast	550 °C, 10min	550 °C, 2 h	550 °C, 4h	580 °C, 2h	550 °C, 24h	580 °C, 12h	580 °C, 168 h
Mn level in 0.25Mn alloy	0.22	0.22	0.20	0.20	0.18	0.14	0.13	0.073
Mn level in 0.5Mn alloy	0.43	0.43	0.43	0.41	0.36	0.33	0.31	0.13

0.5Mn0.15Cr alloy

When Mn and Cr are added together, the histograms of Mn, Fe and Cr contents in the matrix were also plotted and fitted with the normal distributions fittings in Figure 5.63. For 0.5Mn0.15Cr alloy, the Mn histogram in Figure 5.63a shifted gradually from right to left with an increasing soaking temperature and time. The trend is also similar to the observation in 0.25Mn and 0.5Mn alloy, except the histogram from 168 h at 580 ºC with a much wider span. This is explained by the absence of a near equilibrium homogenization condition. It is speculated that with an even longer soaking time than 168 h at 580 ºC, a similar histogram like with a mean position on the very left and narrow width will be possible. In comparison, the evolution of Fe is similar to those in 0.25Mn and 0.5Mn alloy. However, the shifting back from the right to left is very slow as it has been seen in Figure 5.63b. Considering the Cr histograms in Figure 5.63c, it is observed that the mean position shift is similiar to the Mn histograms, but the change of the width is less pronounced than Mn. The reason is probably because of the low amount of Cr in solubility than Mn in aluminum alloys at a same temperature from Table A5 in the appendix.

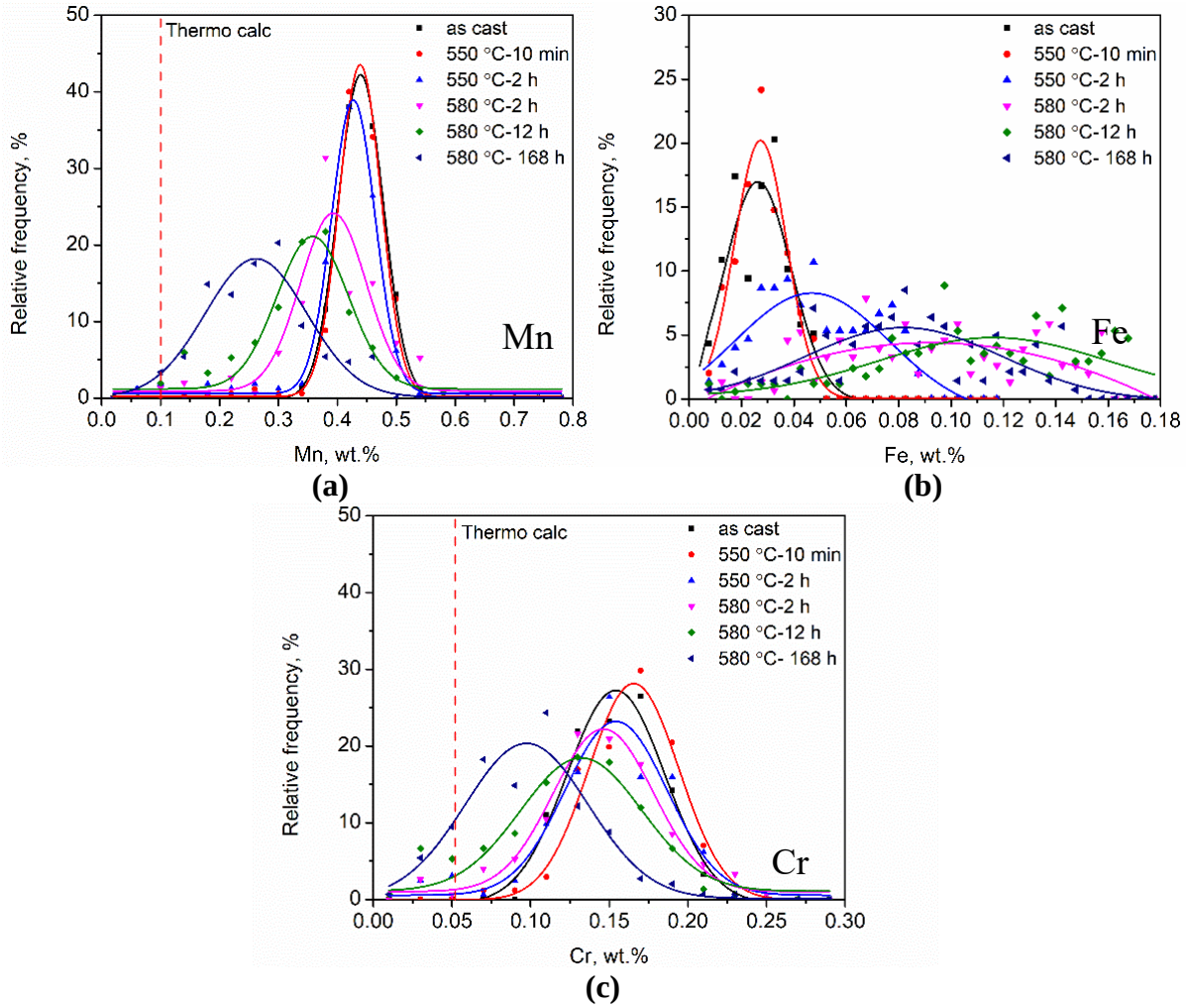

Figure 5-63 Microprobe data measured in 0.5Mn0.15Cr alloy from different homogenization conditions for (a) Mn histograms, (b) Fe histograms and (c) Cr histograms. The solid lines are normal fittings

The reason is probably because of the addition of Cr, which lowers the Mn in solid solution as shown in Table A5 in the appendix compared to the 0.5Mn alloy at both 550 °C and 580 °C calculated using Thermo-Calc (TTAL6). In addition, the solubility of Mn and Fe is also provided for comparison with the changing trends in chemistry and temperature.

Following Equation (5-6), the mean value and the standard deviation are also plotted for Mn, Fe and Cr levels of 0.5Mn0.15Cr alloy for the distributions in Figure 5.64. It is observed in Figure 5.64a and Figure 5.64c that the fitted mean values for Mn and Cr both decrease with

increasing homogenization temperature and time, indicating the similar trend of losing Mn and Cr from the matrix to the constituent particles. Moreover, the standard deviations are found to rise until the upper bound of homogenization 580 °C for 168 h in this work. This is also speculated to be due to the formation and expansion of dispersoids free zone (DFZ), gradually creating a more inhomogeneous spatial distribution.

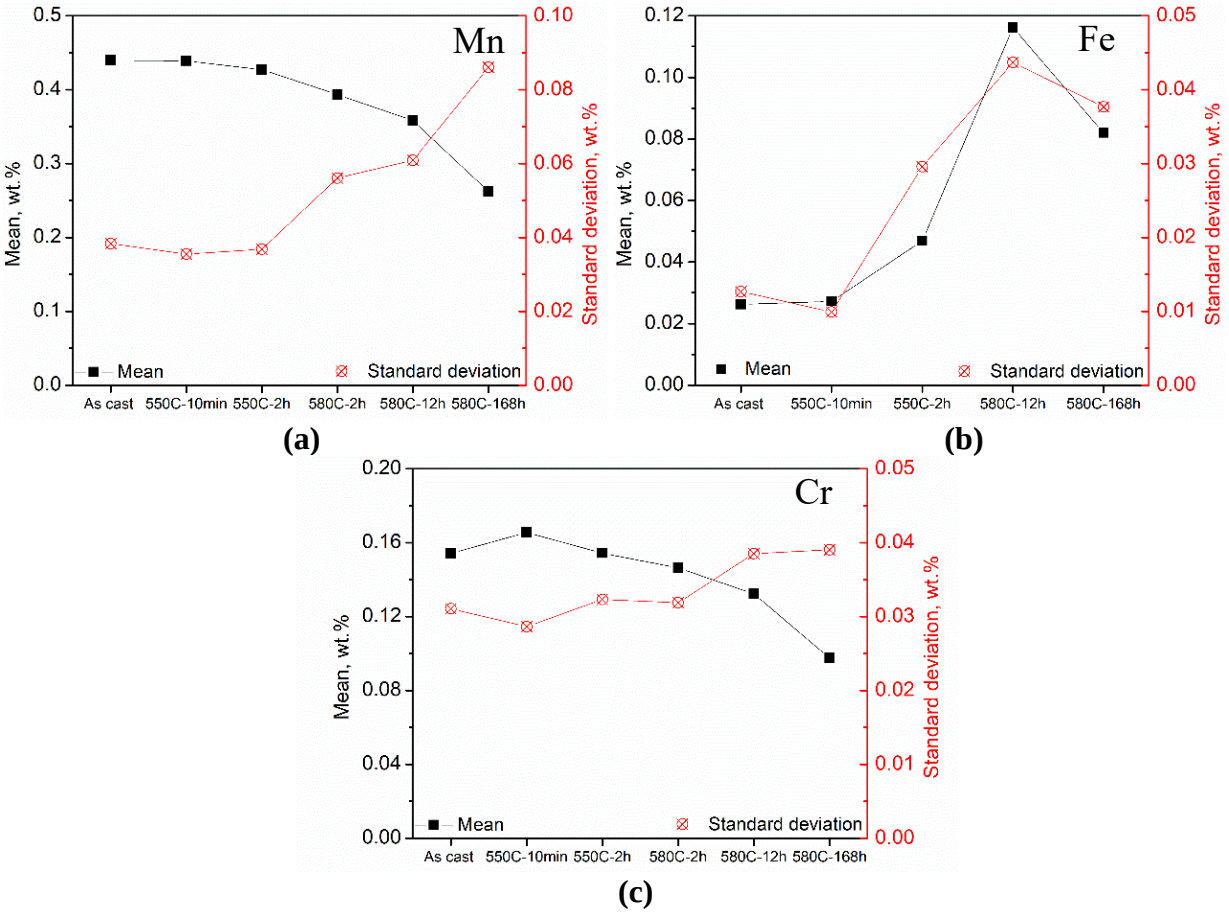

Figure 5-64 Mean and standard deviations from normal fitting in 0.5Mn0.15Cr alloy for (a) the Mn matrix levels, (b) the Fe matrix levels and (c) the Cr matrix levels

As discussed earlier, the addition of Cr will decrease the solubility of Mn in aluminum alloy, it would be reasonable to assume that a much longer soaking time than 168 h was desired to establish the equilibrium condition. i.e. dissolving all the dispersoids. That is why a decrease

in the standard deviation was not found in 0.5Mn0.15Cr alloy, compared to 0.25Mn and 0.5Mn alloys.

The matrix levels for Mn and Cr are calculated from the same approach as those for Mn bearing alloys and are summarized in Table 5.18 for further analysis, which clearly shows the loss of Mn and Cr in the matrix during homogenization.

Table 5.18 Average Mn and Cr matrix levels obtained from EPMA results (wt.%) in 0.5Mn0.15Cr alloy

	As-cast	550 °C, 10min	550 °C, 2 h	580 °C, 2h	580 °C, 12h	580 °C, 168 h
Mn level	0.43	0.43	0.40	0.39	0.34	0.27
Cr level	0.15	0.15	0.15	0.14	0.13	0.10

5.8 High temperature compression tests

5.8.1 Effect of homogenization on the flow stress of the base alloy (0Mn)

The microstructures of 0Mn alloy from three different homogenization conditions, 550 °C for 2 h, 580 °C for 2 h, and 580 °C for 12 h, were characterized under the FEGSEM in Section 5.3. For the three homogenization conditions, the Mg_2Si was dissolved leaving only the Fe bearing constituent particles. The Fe bearing constituent particles are the β phase and possess plate morphology for these homogenization conditions. The average plate thickness and aspect ratios were measured for these conditions in Section 5.3 and it was found that the particles had similar plate thickness and aspect ratios, which homogenization had little effect on the microstructure in this case.

High temperature compression tests were performed for strain rates 1 s^{-1} to 10 s^{-1} at the temperatures of 550 °C to 580 °C. The results for the stress-strain curves are shown in Figure 5.65. Comparing the flow curves from the four test conditions, it is clear that the flow stress is

both deformation temperature and strain rate dependent. The flow stress decreases with an increase of hot compression temperature under the same strain rate (compare Figure 5.65a and 5.65c) and increase with an increase in the strain rate (compare Figure 5.65a and 5.65b), as expected.

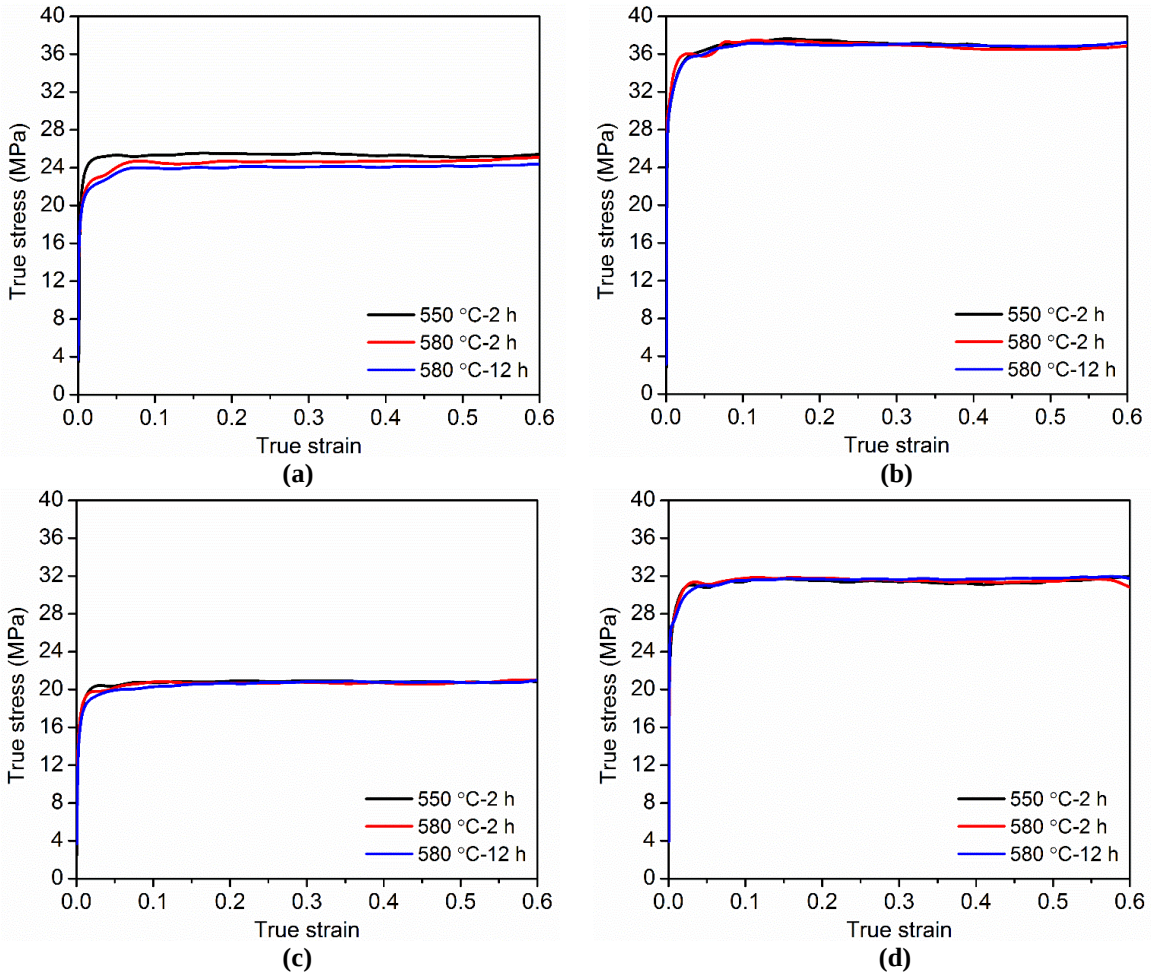

Figure 5-65 Flow stress curves of the 0Mn alloy with three initial homogenization treatments and then deformed at (a) 550 °C with strain rate 1 s^{-1}, (b) 550 °C with strain rate 10 s^{-1}, (c) 580 °C with strain rate 1 s^{-1} and (d) 580 °C with strain rate 10 s^{-1}

Figure 5.65a shows the results for the stress strain curves for deformation at 550 °C with a strain rate of 1 s^{-1}. The steady state flow stress of the sample homogenized at 550 °C for 2 h is of slightly higher flow stress than the other two homogenizations, 580 °C for 2 h and 580 °C for

12 h. However, the difference is quite small. Turning to Figures 5.65b to 5.65d, one can observe there is almost no difference in terms of flow stress. This is consistent with the observations that no dispersoids form in this alloy and the constituent particles do not evolve significantly during homogenization (see Figure 5.6 and Table 5.4)

5.8.2 Effect of homogenization on the flow stress in Mn/Cr alloys

In contrast, both the morphology and crystal structure of the constituent particles change in Mn bearing alloys due to the β to α transformation discussed in Sections 5.3 and 5.7. In addition to phase, the formation of nano-scale dispersoids also seemed to occur concurrently (see Section 5.5).

2 h at 550 °C

With these different initial microstructures, the high temperature deformation behaviour is examined using compression tests. Figure 5.66 shows the effect of chemistry on the flow stress where all the samples tested were homogenized at 550 °C for 2 h. The lowest flow stress was found in the 0Mn alloy.

With increasing additions of Mn/Cr, an increase of flow stress can clearly be observed. The flow stress increases proportionally with more Mn and Cr added under a given test condition in Figure 5.66. It can be clearly observed that the 0.5Mn0.15Cr alloy exhibits the highest flow stress. It is also noted that softening occurred in this alloy during the high temperature compression. This is probably due to the dynamic precipitation. Further compression results that were conducted at a much slower strain rate of 0.01 s^{-1} could be found in Figure A1 in the appendix, showing that the softening during high temperature deformation is gone with initial homogenization at 580 °C for 168 h.

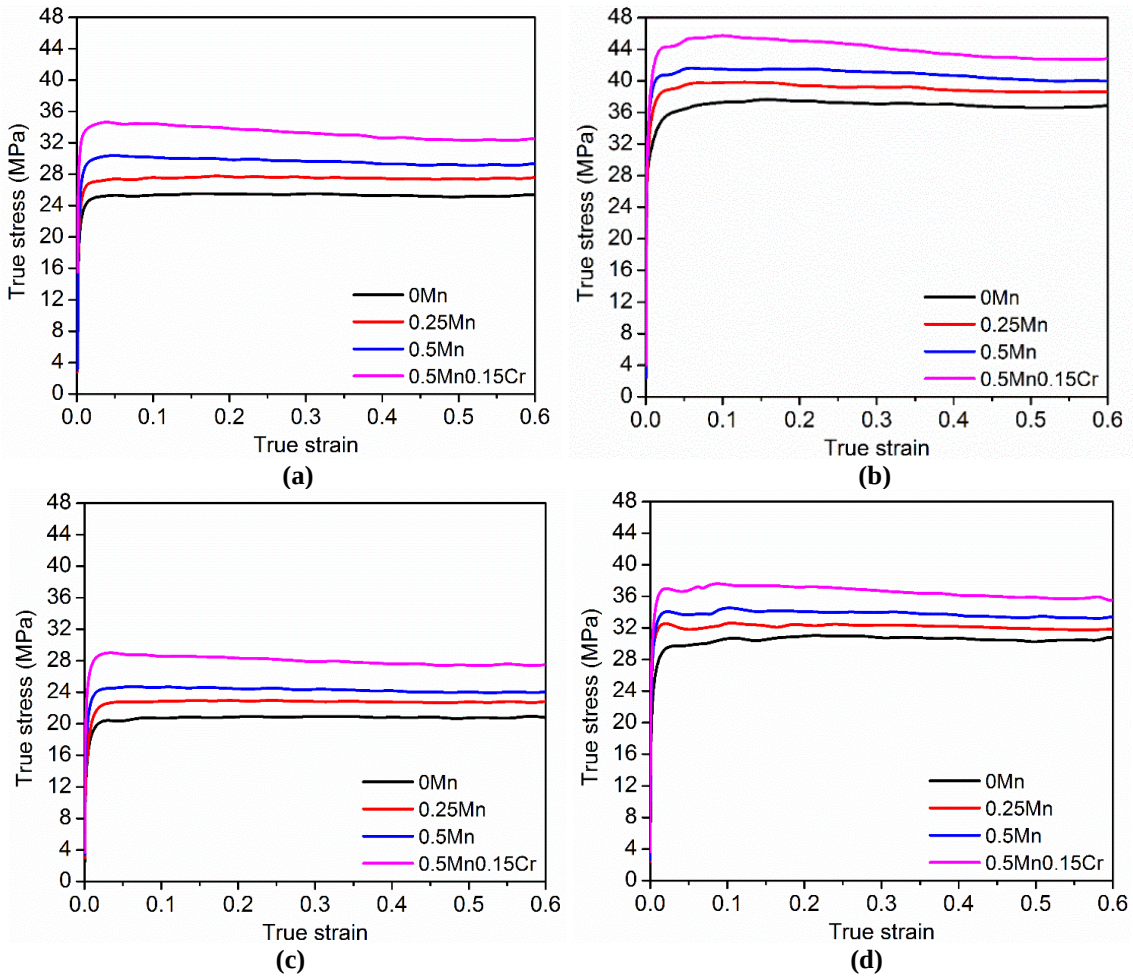

Figure 5-66 Flow stress curves of the four AA6082 based alloys with initial homogenization at 550 °C for 2 h and then deformed at (a) 550 °C with strain rate 1 s^{-1}, (b) 550 °C with strain rate 10 s^{-1}, (c) 580 °C with strain rate 1 s^{-1} and (d) 580 °C with strain rate 10 s^{-1}

2 h at 580 °C

When increasing the homogenization temperature, the flow stresses for the four alloys show the similar trend as the samples homogenized for 2 h at 550 °C, where the flow stress increases with more Mn/Cr addition. However, the differences for the four alloys at a given test condition are declining, as shown in Figure 5.67.

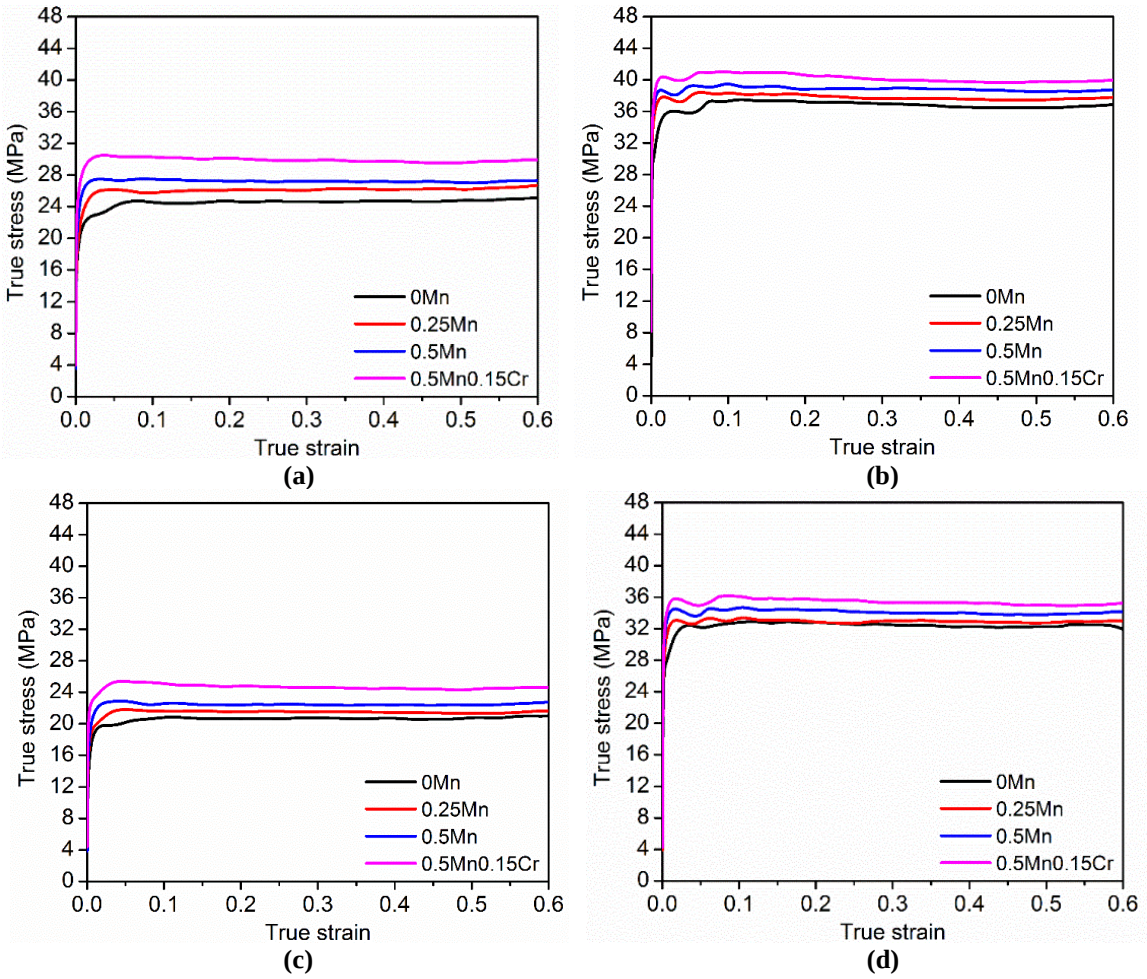

Figure 5-67 Flow stress curves of the four AA6082 based alloys with initial homogenization at 580 °C for 2 h and then deformed at (a) 550 °C with strain rate 1 s^{-1}, (b) 550 °C with strain rate 10 s^{-1}, (c) 580 °C with strain rate 1 s^{-1} and (d) 580 °C with strain rate 10 s^{-1}

12 h at 580 °C

It is also observed that the flow stress increases with an increase in the Mn/Cr addition. However, the flow stress difference between the Mn bearing samples and 0Mn samples is becoming less when gradually increasing the homogenization temperature to 580 °C and soaking time to 12 h as shown in Figure 5.69. The softening is also becoming less noticeable for 0.5Mn0.15Cr alloy.

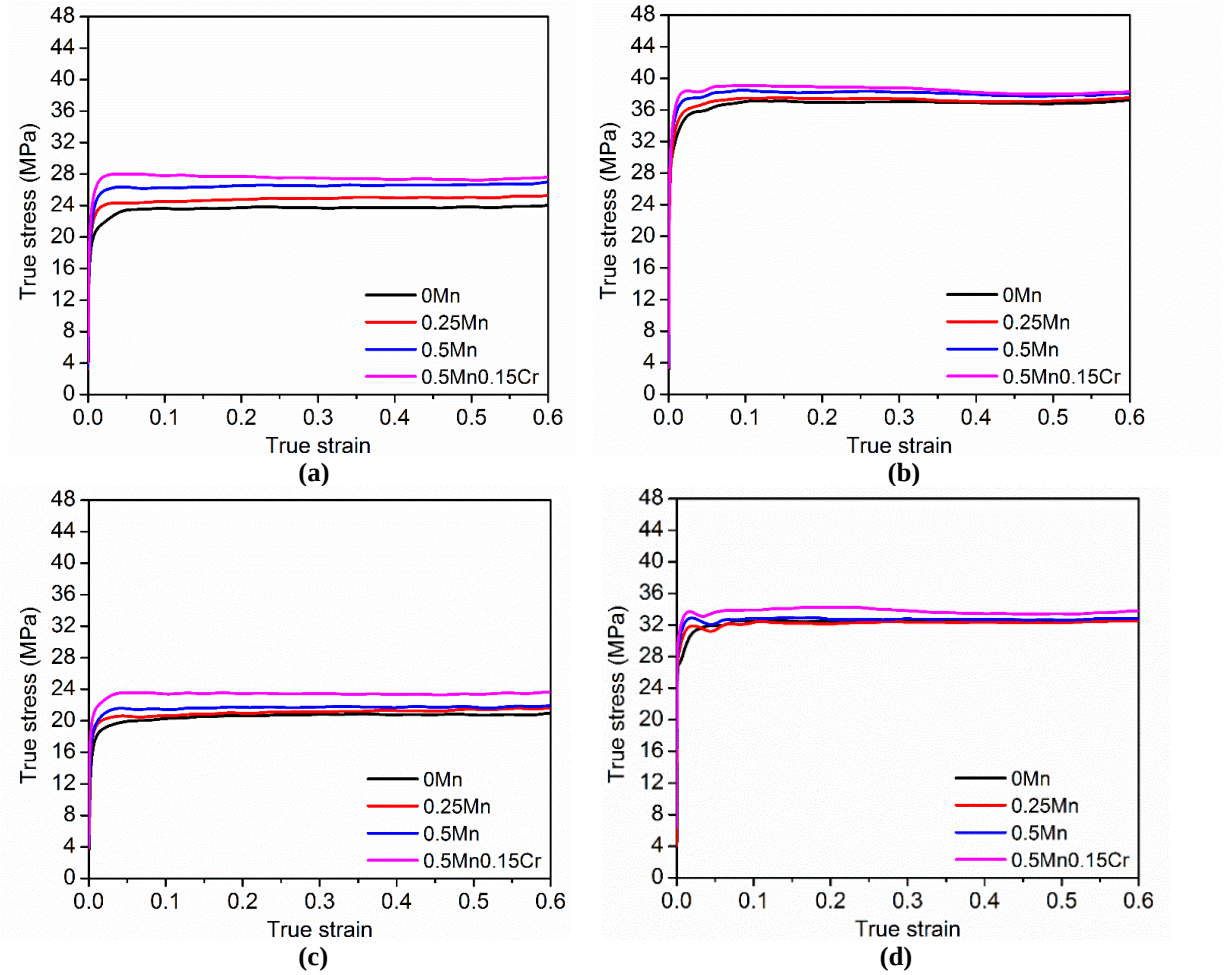

Figure 5-68 Flow stress curves of the four AA6082 based alloys with initial homogenization at 580 °C for 12 h and then deformed at (a) 550 °C with strain rate 1 s^{-1}, (b) 550 °C with strain rate 10 s^{-1}, (c) 580 °C with strain rate 1 s^{-1} and (d) 580 °C with strain rate 10 s^{-1}

It is apparent that a complex relationship exists between the initial homogenized microstructure and the subsequent influence on the flow stress. The steady state flow stress was chosen for further discussion, which is averaged from the strain of 0.4 to 0.6. The flow stresses determined from the Figures 5.66 to 5.68 are summarized from Tables 5.19 to 5.21.

Table 5.19 Steady state flow stresses for the fours alloys homogenized at 550 °C for 2 h, MPa

	550°C-1s^{-1}	550°C-10s^{-1}	580°C-1s^{-1}	580°C-10s^{-1}
0Mn alloy	24.9	36.7	20.8	31.3
0.25Mn alloy	27.4	38.4	22.7	32.3
0.5Mn alloy	28.7	40.2	24.0	33.4
0.5Mn0.15Cr alloy	32.1	42.6	27.2	35.9

Table 5.20 Steady state flow stresses for the fours alloys homogenized at 580 °C for 2 h, MPa

	550°C-1s^{-1}	550°C-10s^{-1}	580°C-1s^{-1}	580°C-10s^{-1}
0Mn alloy	25.0	36.8	20.9	32.3
0.25Mn alloy	26.4	38.0	21.7	32.8
0.5Mn alloy	27.3	38.5	22.4	33.4
0.5Mn0.15Cr alloy	29.6	39.7	25.0	34.8

Table 5.21 Steady state flow stresses for the fours alloys homogenized at 580 °C for 12 h, MPa

	550°C-1s^{-1}	550°C-10s^{-1}	580°C-1s^{-1}	580°C-10s^{-1}
0Mn alloy	24.0	37.4	21.0	32.6
0.25Mn alloy	25.0	37.3	21.3	32.3
0.5Mn alloy	26.3	37.9	21.9	32.7
0.5Mn0.15Cr alloy	27.5	38.1	23.3	33.4

6. Discussion and Analysis

The preceding chapter mainly focused on the experimental characterization of the microstructure evolution during the process of homogenization. It was noted that there was a particular challenge to measure the volume fraction of dispersoids and the constituent particles. This chapter will start by proposing a new combined approach using the TEM/EDS measurements on the dispersoids, the estimate of the alloy elements in solid solution and microprobe measurements to determine the volume fraction of dispersoids and constituent particles using a mass balance.

Given the difficulty of determining these microstructure parameters in an experimental manner, it would be of interest to predict these volume fractions from a CALPHAD database. Section 6.2 proposes a methodology to do this and a sensitivity analysis has been conducted on two of the experimental parameters which show uncertainty.

Next, the interesting observations on the evolution of the dispersoids chemistry during homogenization (i.e. the changes in the Mn/Fe ratio measured by EDS in TEM) and the redistribution of Mn, Fe and Cr measured by electron microprobe are revisited. A hypothesis to explain these results is proposed and then, it is compared to a multicomponent precipitation model which was modified for examining the current alloy chemistry. It will be shown that the consideration of multi-component thermodynamics and diffusion can thoroughly rationalize the current results.

Finally, the effect of dispersoids on the high temperature flow stress is considered by extending the Kocks-Chen model in order to include a contribution from dispersoids. It will be demonstrated that this model can be used to provide the steady flow stress to within ± 5 % for a

wide range of temperatures, strain rates and homogenization conditions. It is then shown that the alloys for the estimation of extrusion forces are also within ± 5 %.

6.1 Estimation of dispersoid and constituent particle volume fraction

As discussed in the literature review, the dispersoid size and volume fraction are of particular importance, as these parameters are willing to influence the high temperature deformation flow stress (i.e. the extrusion forces) and resulting grain structure after extrusion. As pointed out in the discussion, it is very challenging to measure the dispersoid volume directly from either TEM or FEGSEM images, due to issues related to the accuracy in measuring film thickness and area fraction, respectively. To avoid these errors, a new approach is proposed to estimate the volume fraction of dispersoids and constituent particles, based on the experimental measurements and a simple mass balance.

The analysis will start with the Mn containing alloy and then be extended to Mn/Cr alloys. Starting with the EPMA measurements from the matrix reported in Section 5.7.3, it is noted that the total amount of Mn measured ($C_{Mn,\ matrix}$) derives from the Mn in solid solution and the Mn in the dispersoids in aluminum.

$$C^{wt.}_{Mn,S.S} + C^{wt.}_{Mn,disp.} = C^{wt.}_{Mn,matrix} \tag{6-1}$$

The concentration of Mn in the solid solution was estimated with the help of electrical resistivity measurements, as described in Section 5.6, so that it would now be possible to calculate the amount of Mn in the dispersoids. However, the volume fraction of dispersoids depends on the molar volume of the dispersoids (i.e. crystal structure and lattice parameter) as well as on the stoichiometry.

The molar volume of dispersoids can be calculated with the lattice parameter determined from selected area diffraction work in Section 5.5, and the Al molar volume is known [43]. Whether or not it is BCC or SC, there are always 138 atoms in a unit cell (see Section 2.2.3). The number of Al and Si atoms can be determined based on the number of Mn and Fe atoms. Although it is agreed that there are 138 atoms in the unit cell, a slight difference in the Al and Si ratio has been reported, i.e. $Al_{100}(MnFe)_{24}Si_{14}$ and $Al_{96}(MnFe)_{24}Si_{18}$ (see Section 2.2.3) [68]. However, this small difference will not affect the following result in any manner. The Mn/Fe ratio has been determined from the EDX analysis of the dispersoid measured by TEM (Section 5.5). Thus, the volume fraction of dispersoids at any homogenization condition can be determined as:

$$f_{Al(FeMn)Si}^{disp.} = \frac{V_{molar}^{disp.}(C_{Mn,disp.}^{at.} + C_{Fe,disp.}^{at.} + C_{Si,disp.}^{at.} + C_{Al,disp.}^{at.})}{V_{molar}^{Al}} \quad (6\text{-}2)$$

In summary, the molar volume of the dispersoids was known, the Mn/Fe ratio was measured by TEM, the Mn in dispersoids was determined by Equation (6-1) and finally, the Al/Si levels follow from the stoichiometry of the dispersoids.

Turning to the alloy which also had Cr as an alloy addition, the approach to estimate the volume fraction Mn and Cr containing dispersoids is the same, but happens to be more complicated. As discussed in Section 5.6, the resistivity change for the 0.5Mn0.15Cr alloy derives from both Mn and Cr, such that Equation (6-1) can no longer be used. Instead, the resistivity equation can be modified as:

$$\Delta\rho = K_{Mn,S.S}^{wt.} C_{Mn,S.S}^{wt.} + K_{Cr,S.S}^{wt.} C_{Cr,S.S}^{wt.} \quad (6\text{-}3)$$

Cr is similar to Mn, in that it exists both in solid solution and in the dispersoids, so a mass balance can be calculated as:

$$C^{wt.}_{Cr,matrix} = C^{wt.}_{Cr,S.S} + C^{wt.}_{Cr,disp.} \quad (6\text{-}4)$$

The Cr matrix values were measured by the EPMA analysis in Section 5.7. As discussed in Section 5.5, the Cr and Mn are both present in the dispersoids. Thus, the average Mn/Cr ratio measured from the TEM/EDS analysis can be used to determine the Mn/Cr in dispersoids as:

$$C^{at.}_{Mn,dips.} / C^{at.}_{Cr,disp.} = R_{EDS} \quad (6\text{-}5)$$

Combining the equations, both Cr in solid solution and Cr in dispersoids together with Mn in solid solution and Mn in dispersoids could be calculated taking advantage of the resistivity measurements, EPMA analysis and TEM/EDS work. The amount of Fe in dispersoids could also be determined using the TEM/EDS and the calculated Mn and Cr content in dispersoids. Assuming 138 atoms per unit cell, the volume fraction of Mn/Cr bearing dispersoids could then be calculated as:

$$f^{disp.}_{Al(FeMnCr)Si} = \frac{V^{disp.}_{molar}(C^{at.}_{Mn,disp.} + C^{at.}_{Cr,disp} + C^{at.}_{Fe,disp.} + C^{at.}_{Si,disp.} + C^{at.}_{Al,disp.})}{V^{Al}_{molar}} \quad (6\text{-}6)$$

Figure 6.1 presents the results for the volume fraction of Mn/Cr bearing dispersoids. The errors are assessed from the resolution limit of EPMA (i.e. ± 0.05 wt.%) and accuracy of resistivity measurements (i.e. ± 0.3 nΩ·m).

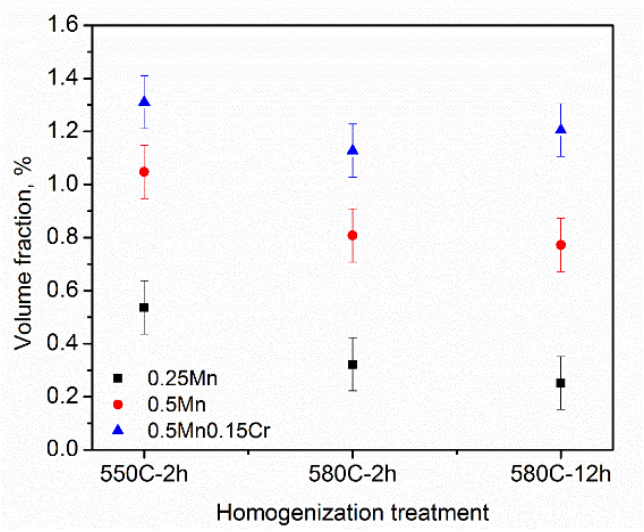

Figure 6-1 The dispersoid volume fraction estimated using the combined method for 0.25Mn, 0.5Mn and 0.5Mn0.15Cr alloys from three different homogenization treatments

It is observed that the dispersoid volume fraction is chemistry-dependent. As expected, the volume fraction increases with an increase in the Mn and Cr content. The dispersoid volume fraction is also affected by the homogenization temperature i.e. the fraction decreases with the increase of homogenization temperature as the solubility of Mn increases. The effect of holding time at 580 °C (2 h vs 12 h) has minimal effect, thus suggesting that the particles and the matrix are near equilibrium.

Another advantage of this approach is that the volume fraction of the constituent particles can also be estimated (i.e. it is also not easy to measure from micrographs due to the threshold issue) using the CALPHAD database (in this case TTAL6 in Thermo-Calc). From Thermo-Calc, the volume fraction of the second phase particles at a given homogenization temperature could be calculated using the equilibrium module. The volume fraction of constituent particles could also then be calculated as the difference between the equilibrium content of the α-phase and the dispersoid volume fraction, summarized in Table 6.1.

Table 6.1 Volume fraction of dispersoids and constituent particles estimated for for 0.25Mn, 0.5Mn and 0.5Mn0.15Cr alloys from three different homogenization treatments

Alloy and homo	Volume fraction of α-phase from TTAL6, %	Volume fraction of dispersoids, %	Volume fraction of constituent particles, %
0.25Mn-550ºC-2h	1.16	0.54	0.62
0.25Mn-580ºC-2h	1.09	0.32	0.77
0.25Mn-580ºC-12h	1.09	0.25	0.84
0.5Mn-550ºC-2h	1.75	1.05	0.70
0.5Mn-580ºC-2h	1.63	0.81	0.82
0.5Mn-580ºC-12h	1.63	0.77	0.86
0.5Mn0.15Cr-550ºC-2h	2.18	1.31	0.87
0.5Mn0.15Cr-580ºC-2h	2.04	1.13	0.91
0.5Mn0.15Cr-580ºC-12h	2.04	1.21	0.83

6.2 Simple model for dispersoid volume fraction

In the previous section, an approach was proposed to estimate the dispersoid volume fraction using a few experimental measurements, i.e. resistivity, EPMA and TEM/EDS. It would be advantageous to make predictions for the dispersoid fraction in an easier (and less expensive) manner. The method proposed here is to use Thermo-Calc (TTAL6) for this purpose. From Thermo-Calc (TTAL6), the equilibrium fraction of the α phase can be calculated at any given temperature. This includes both the volume fraction of dispersoids and of the constituent particles. The Scheil module in Thermo-Calc can then be used to predict the fractions of α and β phases under Scheil cooling conditions (diffusional mixing in liquid and no diffusion in solid) [161]. Table 6.2 shows an example of the results for 0.25Mn, 0.5Mn and 0.5Mn0.15Cr alloys at 550 °C.

Table 6.2 Volume fraction of different constituents at 550 °C from equilibrium and Scheil in Thermo-Calc (TTAL6)

Alloy	Equilibrium α-Al(MnFe)Si	Scheil α-AlFeSi	Scheil α-Al(MnFe)Si	Scheil β-Al_5FeSi	Estimation of α-Al(MnFe)Si dispersoids
0.25Mn	1.159	0.027	0.475	0.198	0.459
0.5Mn	1.751	-	0.877	0.008	0.866
0.5Mn0.15Cr	2.184	-	0.932	0.113	1.139

An upper bound for the dispersoid fraction can be obtained by subtracting the sum of α-Al(MnFe)Si, α-AlFeSi (formed possibly from the non-equilibrium reaction [79,80]), and β phase determined by Scheil calculation and equilibrium values at a given temperature.

$$f_{disp} = (f_{\alpha\text{-Al(MnFe)Si},eq} - f_{\alpha\text{-Al(MnFe)Si},Scheil} - f_{\alpha\text{-AlFeSi},Scheil} - f_{\beta\text{-AlFeSi},Scheil}) \quad (6\text{-}6)$$

The results have been shown in the last column of Table 6.2. Compared with the dispersoid fraction estimated from the experimental measurements described in Section 6.1, the predictions from the Thermo-Calc results tend to be smaller as shown in Figure 6.2. One possible reason behind this is that the Scheil calculation overestimates the volume fraction of the constituent phase as it does not take in account the details of the solidification path (i.e. cooling rate and second dendrite arm spacing, for example).

However, in Figure 6.2, it can be observed that with the exception of one point for 0.25Mn alloy, a linear relationship is found between the experiments and the Thermo-Calc predictions using the proposed approach. The slope of the line was found by a least square fit to be 1.11.

Thus, using this approach, one may predict the volume fraction of dispersoids for a given chemistry at a known soaking temperature using Equation 6-7.

$$V_{disp.} = 1.11 \times (V_{eq.} - V_{scheil}) \quad (6\text{-}7)$$

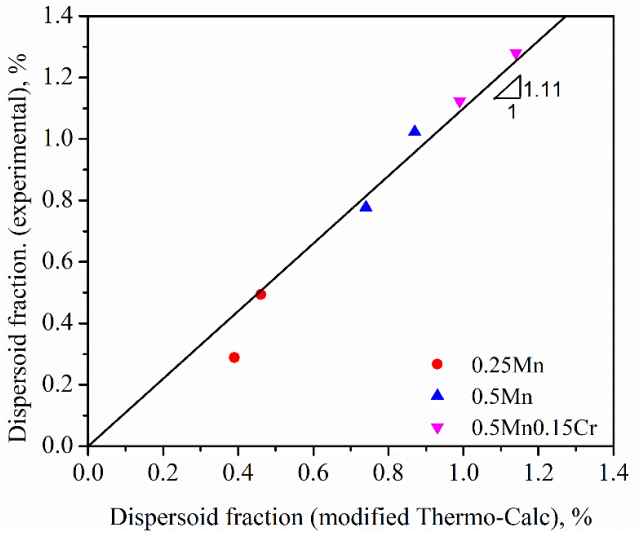

Figure 6-2 Dispersoid volume fraction prediction based on the equlibrium and scheil module from Thermo-Calc (TTAL6)

It is noted that this approach does not consider the homogenization time. For example, in the extreme of 168 h at the homogenization temperature, few or no dispersoids were observed (see Figure 5.22). In this case, as it will be shown in Section 6.3, the dispersoids have dissolved and Mn has been transported to the constituent particles. However, for most of the industrially relevant homogenization conditions (i.e. < 12 h at 580 °C), the long range diffusion of Mn to dispersoids is minimal (this will also be shown in Section 6.3). Therefore, this simple calculation may be very useful as a first order approximation for the industry scenarios.

In order to test the robustness of this simple approach, a new alloy with 0.75Mn alloy homogenized at 550 ºC for 2 h was proposed. The volume fraction of dispersoids was predicted using the Equation 6-7 to be 1.29 %. The alloy was then cast and homogenized followed by experimental characterization. The EPMA data was separated into two groups based on the iron content as shown in Figure 5.52 to derive the average Mn matrix level, while the resistivity difference compared to the base alloy was used to estimate the Mn in solid solution. The Mn/Fe atomic ratio is not directly measured from TEM/EDS, but it was estimated to be 13 to 23 based

the EDS work on the leaner alloys. A dispersoid range of 1.37 % to 1.41 % was determined which compares with the Thermo-Calc based estimate of 1.29 % in a favorable manner, i.e. a difference of ≈ 6-8 %. Considering the simplicity of the Thermo-Calc approach, this is considered to be quite reasonable.

In summary, a simple approach using a CALPHAD based approach is proposed. A test of its predictive capabilities yields a rather promising result. However, the approach is based on the assumption that the experimental data for volume fraction presented in Section 6.1 is reliable. The next section will explore two uncertainties in the analysis for volume fraction, i.e. i) the effect of the resistivity coefficient used to convert the changes in resistivity to the Mn solid solution content for the matrix and ii) the Mn/Fe ratio and Mn/Cr ratios for the composition of the dispersoids.

6.2.1 Sensitivity of the dispersoid volume fraction on Mn resistivity coefficient

As noted in the literature review (Section 2.1.4), a range of resistivity coefficient is reported; e.g. for Mn, 24-36 nΩ·m/wt.% and 26-41 nΩ·m/wt.% for Cr. In Section 5.6, the current work chose a value close to the lower range (i.e. 24 nΩ·m/wt.% for Mn and 36 nΩ·m/wt.% for Cr) and this was rationalized based on matching the Mn and Cr levels for materials homogenized for 168 h at 580 °C, i.e. assuming that this was close to the level of equilibrium.

In this analysis, the experimental volume fraction was re-calculated using a resistivity coefficient for Mn of 33 nΩ·m/wt.%, i.e. as suggested by Li and Arnberg [71] i.e. near the high end of values in the literature. Figure 6.3 shows the results where the solid symbols are the original experimental data reported in Section 6.1 (K_{Mn}=24 nΩ·m/wt.%) and the open symbols are re-calculated volume fractions (K_{Mn}=33 nΩ·m/wt.%).

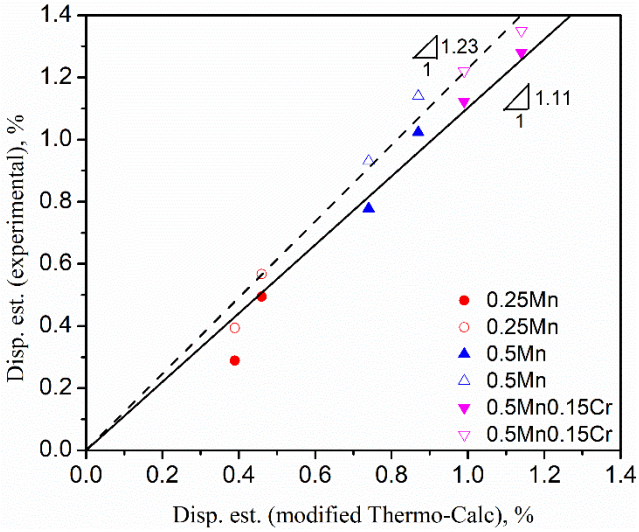

Figure 6-3 Comparison of dispersoid volume fractions based on the equlibrium and Scheil module from Thermo-Calc (TTAL6) and experimental estimates (solid symbols - experiments with K_{Mn}=24 nΩ·m/wt.%, open symbols - with K_{Mn}=33 nΩ·m/wt.%)

It is clear that changing the Mn resistivity coefficient only leads to changes in the slope of the best fit line. This results in a change of the volume fraction predictions of ≈ 10 %.

6.2.2 Sensitivity of the dispersoid volume fraction estimation to Mn/Fe and Mn/Cr ratios

The second factor for which there is uncertainty when calculating the dispersoid volume fraction is the Mn/Fe and Mn/Cr ratios. It was shown in Section 5.5 that there was a chemistry inhomogeneity within the dispersoids from the centre to surface. As such, the dispersoid volume fraction estimation was recalculated using values of Mn and Cr from the centre of the dispersoid and averages over the length of dispersoids (Table 5.11 and Table 5.13) and the results are plotted in Figure 6.4.

In this case it has been observed that, the slope changes from 1.11 to 1.14, indicating that the chemistry inhomogeneity only plays a marginal effect on the dispersoid volume fraction estimates.

Thus, it is suggested that both Mn and/or Cr coefficients and the effect of the Mn/Fe or Mn/Cr ratios will not significantly alter the proposal to use Thermo-Calc (TTAL6) so as to make predictions for the dispersoid volume fraction.

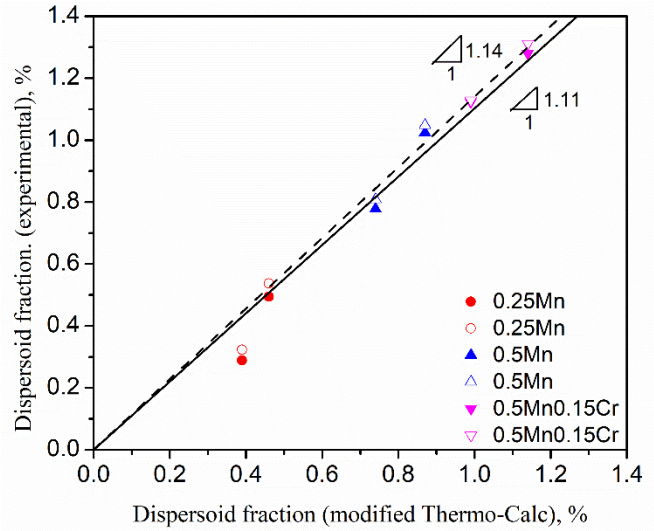

Figure 6-4 Comparison of dispersoid volume fractions based on the equlibrium and Scheil module from Thermo-Calc (TTAL6) and experimental estimates (solid symbols - Mn/Fe and Mn/Cr ratios taken from Table 5.11, open symbols – Mn/Fe and Mn/Cr ratios corrected from Table 5.13 in Section 5.5)

6.3 Discussion of dispersoid evolution during homogenization

Chapter 5 presented two important results on the evolution of the dispersoids. Of these, the first was that TEM/EDS measurements found that the Mn/Fe ratio was dependent on alloy composition but more significantly decreased during homogenization (See Table 5.11). For example, in the case of 0.5Mn alloy, the Mn/Fe ratio was ≈ 16 at early stages (at end of heating ramp and after holding for 2 h at 550 °C) and then decreased to 4.6 after 12 h at 580 °C.

Second, the EPMA measurements showed a rather different behaviour for Mn and Fe. Again, focusing on the 0.5Mn alloy, the mean concentration of the Mn decreased as homogenization progressed while the mean Fe concentration first increased and finally went on

to decrease for the final case of 168 h at 580 °C (see Figure 5.61). In the following, these results will be rationalized but first the overall sequence of dispersoid formation and dissolution and its impact on the microprobe measurements will be discussed.

The previous studies using microprobe have pointed out some advantages and disadvantages of using the techniques to study segregation. First, the technique has the advantages of measuring the composition accurately (for example, Mn levels to ± 0.05 wt.%) and being able to measure over large areas (in the present case a total line length of 1 mm was used). The disadvantage of the technique is the spatial resolution (i.e. interaction volume 2-3 μm). This comes into the problem in two different ways. First, the dispersoids are much smaller (20-100 nm) than the interaction volume so that when one measures a composition of Mn, for example, the measurement includes Mn in solid solution and in the dispersoids. It is known from other studies that solidification results in a segregation dendrite supersaturated in Mn and that, as the homogenization proceeds, Mn precipitates as dispersoids but then diffusion to the constituent particles occurs to approach equilibrium (see Qiang et al [115] and Gardin and Jacot [162]). This leads to a highly inhomogeneous distribution of Mn in the dendrites. With some cases of long homogenization, a dispersoid free zone (DFZ) adjacent to constituent particles is formed. The microprobe lacks spatial resolution to directly measure these phenomena.

Figure 6.5 summarizes schematically the overall evolution of dispersoids during the process of homogenization. Figure 6.5a shows the matrix supersaturated in Mn, Figure 6.5b shows the precipitation of dispersoids at the end of the heating ramp (see Figure 5.18 for an example from 0.5Mn alloy that had been heated to 550 °C and then quenched), Figure 6.5c shows an example where a dispersoid free zone (DFZ) has been generated (see Figure 5.27 for

an example) and finally, Figure 6.5d shows the situation for very long homogenization time where few or no dispersoids are observed (see Figure 5.22a).

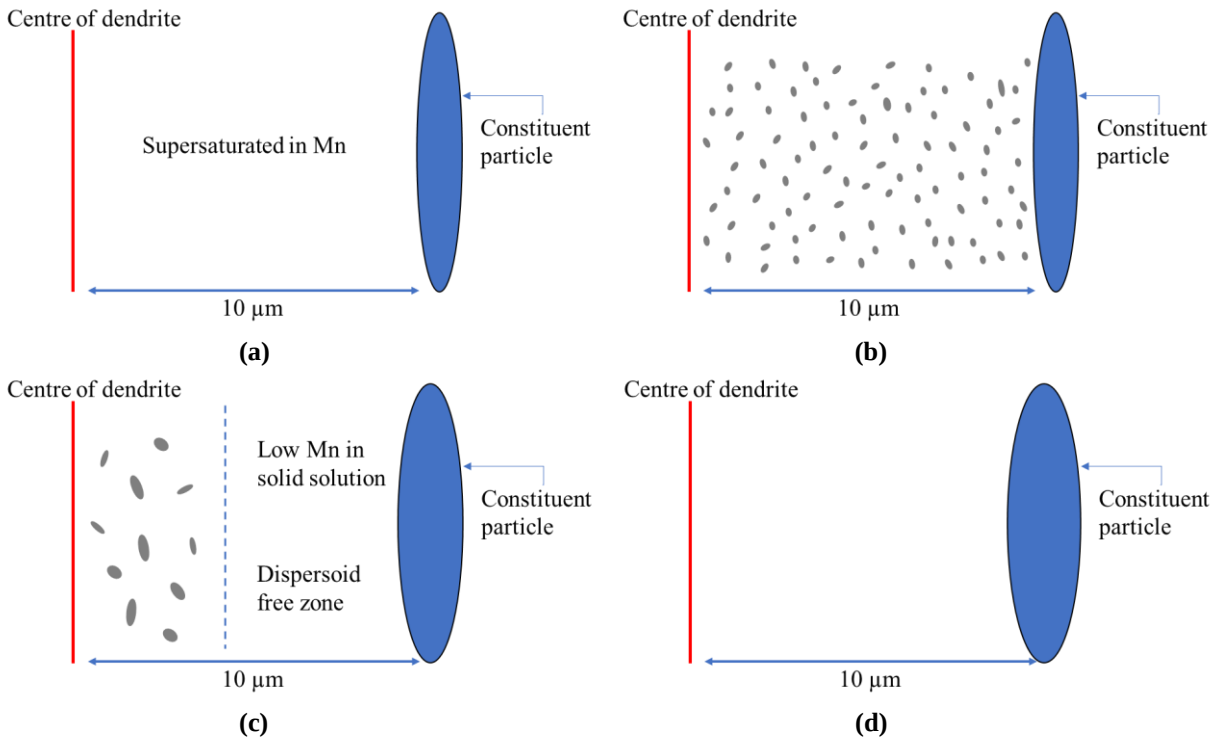

Figure 6-5 Schematic of the overal evolution of dispersoids during homogenization. (a) as-cast, (b) at the beginning of homogenization, (c) formation of DFZ during homogenization and (d) very long time homogenization

Returning to the microprobe results, Figure 6.6 schematically illustrates the data collected by the microprobe for each stage. For simplicity, only those cases were considered where the interaction volume of the electron beam is fully within the matrix (it was shown in Section 5.7 how the microprobe data was sorted into matrix data and data where constituent particles are present).

In Figure 6.6a, which is representative of the as-cast microstructure, i.e. the matrix is supersaturated in Mn and there are no dispersoids, one expects to get a range of Mn values where the Mn comes from the supersaturated solution and the width of the distribution is some measure

of the in homogeneity of Mn from solidification. This can be compared to the EPMA results in Figure 6.7 for 0.5Mn alloy (this is a copy of Figure 5.61 presented here for easy comparison). In Figure 6.7a, one can see a relatively narrow distribution for the Mn and Fe content (Mn=0.42 wt.% and Fe=0.02 wt.%)†.

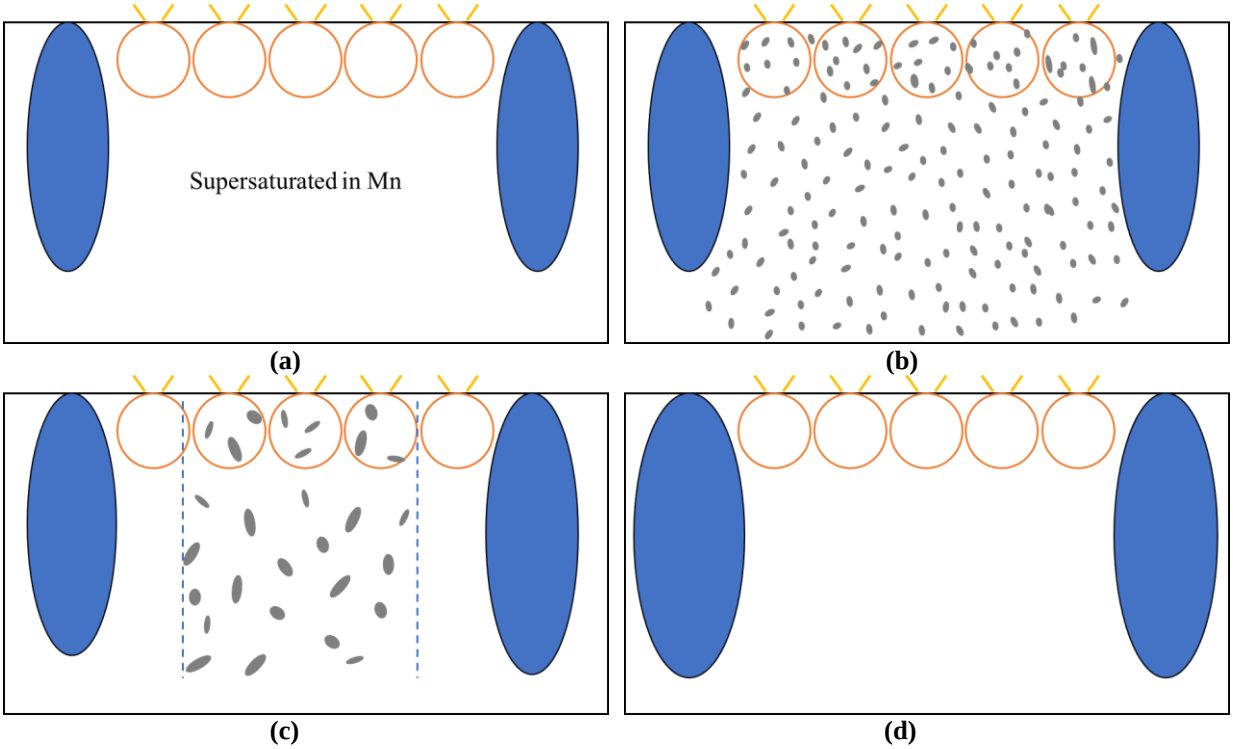

Figure 6-6 Schematic of the interaction volume from EPMA (a) as-cast, (b) at the beginning of homogenization, (c) formation of DFZ during homogenization and (d) very long time homogenization

Turning to Figure 6.6b, which is a representative of the situation after precipitation of dispersoids has occurred (around 450-550 °C) during heating to the homogenization temperature. One can see that from a chemical point of view, the microprobe samples the same composition (i.e. it cannot resolve whether Mn/Fe is in solid solution or in dispersoids).

---

† Fe solubility in Al after solidification is much lower than this [43], the represents the detection limit of the EPMA.

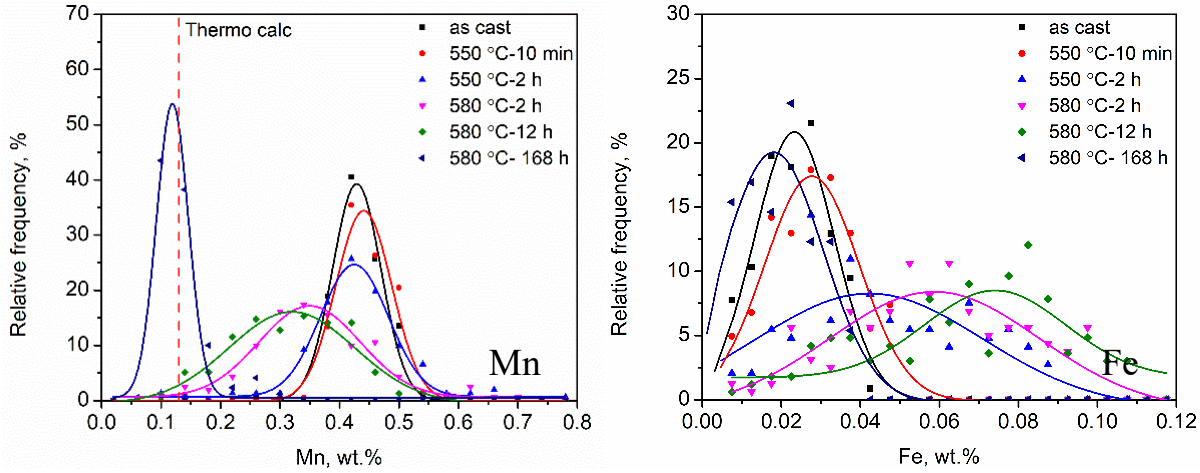

(a) **(b)**

Figure 6-7 Histograms with normal fittings from as-cast and different homogenization conditions for (a) Mn matrix levels and (b) Fe matrix levels in 0.5Mn alloy

A close examination of Figure 6.7 shows the data for 10 min at 550 °C show little change from the case of the as-cast for the Mn and Fe distributions. Next consider, the situation for 2 or 12 h at 580 °C. In Figure 6.7, there are two important observations. First, the average Mn level has decreased and the distribution is much wider and second the Fe level has *increased* as well as the distribution becoming wider. The change in the Mn profile can be rationalized by examining Figure 6.5.c and Figure 6.6c. One can see that the dispersoid free zone is very low in Mn and the region at the centre still has a high volume fraction of dispersoids. Thus, the microprobe on average samples a wide range of Mn contents. These two factors would explain the lower average Mn content and widening of the distribution. On the first observation, the situation for Fe seems rather unusual. However, if one considers the results that the Mn/Fe ratio in the case of 0.5Mn alloy decrease from 16:1 to ≈ 4:1, it is possible that Fe diffuses from the constituent particles to the dispersoids, thereby, decreasing the Mn/Fe ratio. It is worth noting that as shown in the literature review the diffusion coefficient for Fe at 580 °C is 2.1×10^{-14} m^2/s vs 1.5×10^{-15} m^2/s for Mn, i.e. it is almost 10 times faster. If the Fe diffuses to the dispersoids, this would

explain the EPMA results where the Fe level increased and the distribution widens. Due to the low solubility of Fe in Al (Thermocalc TTAL6 predicts less than 0.0023 wt.%), the Fe measured by EPMA would derive from the dispersoids.

Finally, if one looks at the results for the material that was homogenized for 168 h at 580 °C, one can see that in Figure 6.6d, there is an expected low value of Mn (i.e. near its solubility limit of 0.13 wt.%) and a very low value of Fe. Examination of Figure 6.7 shows the phenomena, i.e. an average Mn level of 0.13 wt.%. (Note: the width of the distribution is probably a measure uncertainty in the EPMA measurements). For Fe, the average composition is ≈ 0.02 wt.%. As the solubility of Fe is at least an order magnitude lower, as mentioned earlier, this probably represents the detection limit of the microprobe.

Finally, it also appears that in the late stages of homogenization, the Fe and Mn diffuse together to form the constituent particles. It is noted that the analysis of the volume fraction of constituent particles shown in Table 6.1 shows that this fraction does increase during homogenization for the 0.25Mn and 0.5Mn alloys that are consistent with this scenario.

6.3.1 Application of multi-component homogenization model

To examine the hypothesis related to how Mn and Fe behave, the multi-component model developed for Al-Mn-Fe-Si (AA3xxx) alloys by Du et al [115] was used. The model has a solidification module that predicts the initial distribution of alloy additions in the matrix and the type and fraction of the constituent particles for the as-cast material. The model accounts for long range diffusion of solutes in the matrix to or from the constituent particles using a 1D pseudo front tracking (PFT) approach and precipitation/dissolution of dispersoids (assumed to be spherical) at the local level using a KWN based model. The model is fully coupled to a CALPHAD database, either by calling the database or by extracting the appropriate

thermodynamic parameters from a look-up table. Finally, the conservation of alloying addition is ensured by using the splitting method, which has been taken from the combustion modeling literature. A full description of the model can be found in the references [115,117].

In order to apply the model to the current situation, a different chemistry of the current alloys must be considered. In the present case, a look-up table for composition dependent thermodynamic parameters was generated for Al-Mg-Si-Mn-Fe system from the TTAL6 database as this was computationally more efficient. The diffusion coefficients for Mn, Fe, Si, Mg were taken from the review of Du et al [86].

The model was applied to 0.5Mn alloy with a thermal profile that had a constant heating rate of 200 °C/h to the homogenization temperature of 580 °C where it was held for 24 h. For the KWN precipitation model, the number of nucleation sites per volume and the interfacial energy are required. As discussed in the literature review, the nucleation of dispersoids is complex in AA6xxx alloys, i.e. dispersoids nucleate on Mg-Si metastable phases formed during heating, which subsequently dissolve at the homogenization temperature. As such, the number of nucleation sites is quite an adjustable parameter. Further, the interfacial energy between the dispersoids and the matrix is not known. However, it is known that the dispersoids have a crystallographic relationship with the matrix and that there is a mixture of coherent and semi coherent interface area. As such, an effective interfacial energy was employed. Finally, the number of elements and the length scale of the finite volume based pseudo front tracking model must be defined. In the current case, the length from the centre of dendrite to the constituent particles was chosen based on one half of the SDAS, i.e. SDAS was reported in Section 5.1 as 17-20 µm so 10 µm was chosen as a representative length scale and the number of volume elements was chosen as 10 (i.e. 10 cells). The number of nucleation sites per volume and the

effective interfacial energy were chosen by trial and error with initial guesses based on the experiment (TEM measurements of ≈ 200/μm^3) and previous modeling of dispersoids in AA3xxx alloys (80 mJ/m^2). These two parameters were adjusted until a reasonable fit was obtained to the experimental measurements based on the average dispersoid radius at the centre of the dendrite. Using the values for the number of nucleation sites per volume of 100/μm^3 and an interfacial energy of 150 mJ/m^2 gives a reasonable result from the average dipsersoid radius (see Figure 6.8) for 0.5Mn alloy.

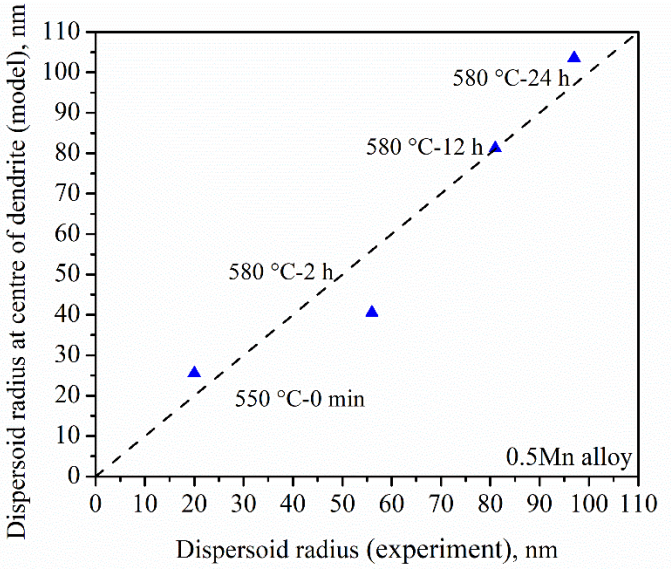

Figure 6-8 Comparison of the dispersoid radius at centre of dendrite from the model and dispersoid radius from the experiment in 0.5Mn alloy

Figure 6.9 shows the model predictions for the spatial distribution of Mn and Fe in solution for different points in the homogenization cycle. The matrix information is reflected from cell 1 to cell 9 (with cell #1 representing the centre of the dendrite) whereas cell 10 contains the information for the constituent particle. It is noted that the total 10 cells representing a half SDAS, i.e. 10 μm. In Figure 6.9a, the black square symbols show the Mn predictions from the centre to the interdendritic area of a dendrite arm of the as-cast microstructure. Since Mn is

supersaturated in the primary aluminum phase during solidification, the highest level of Mn in solid solution was found in the as-cast sample and the segregation profile shows that the Mn in solution increases from ≈ 0.38 of the centre of the dendrite to ≈ 0.65 adjacent to the constituent particle. A similar trend is found in the Fe segregation profile in the as-cast condition but at a much lower concentration level. It was found in Figure 6.9b that the Fe in solution increases from ≈ 0.011 of the centre of the dendrite to ≈ 0.018 close to the constituent particles.

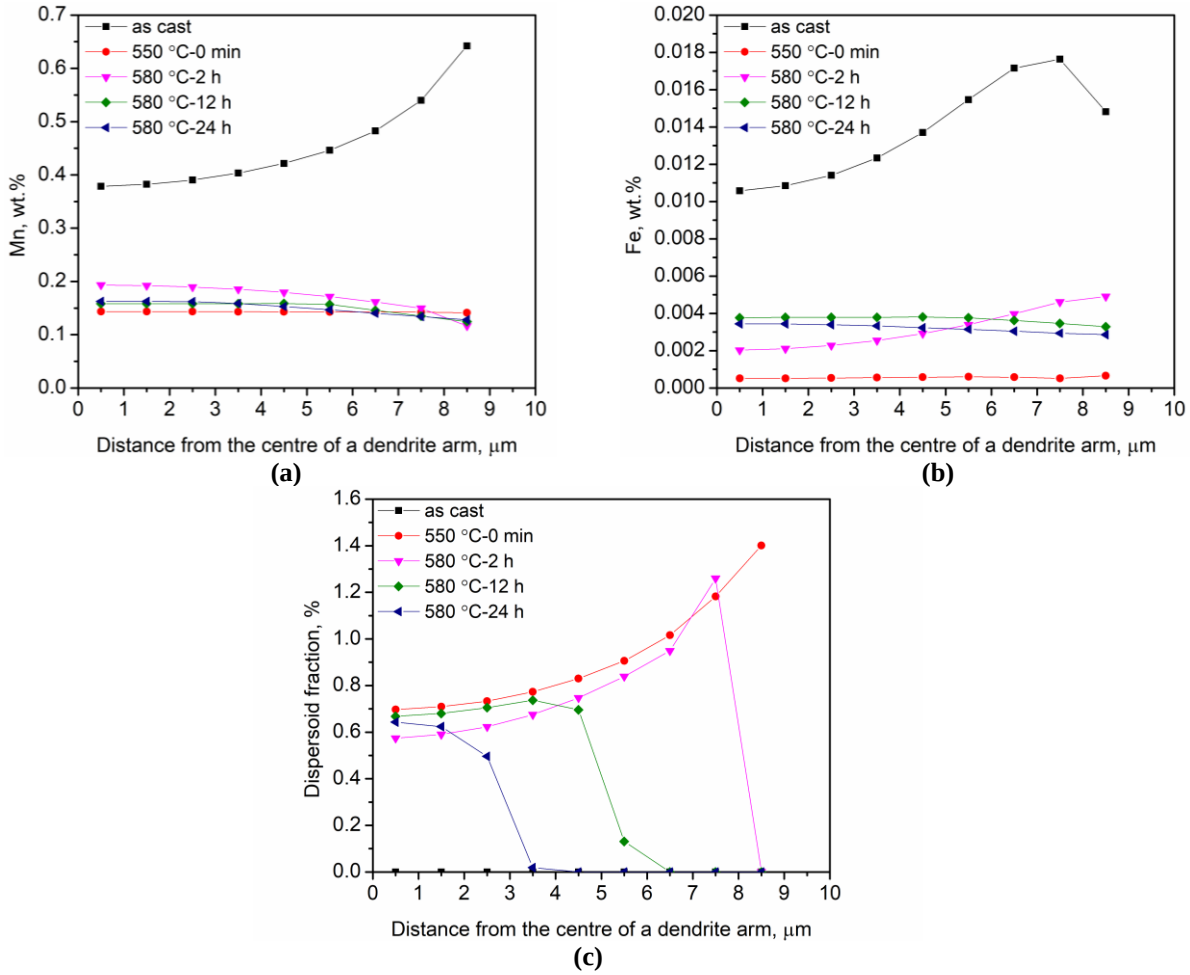

Figure 6-9 (a) Mn solid solution spatial distribution, (b) Fe solid solution spatial distribution and (c) volume fraction of dispersoids spatial distribution in the matrix from the centre of a dendrite to the constituent particles

Turning to the model results from near the end of the heating ramp (i.e. 550 °C - 0 min), one can observe that the Mn and Fe solution levels have dropped to a lower level (0.15 - 0.2 for Mn and <0.001 for Fe) due to the precipitation of dispersoids (Figure 6.9c). The volume fraction of dispersoids varies from 0.7 % at the centre of the dendrite to 1.4 % in the volume element adjacent to the constituent particles, i.e. reflecting the initial spatial distribution of Mn and Fe in the as-cast condition. With an increase in homogenization to 2 h at 580 °C, there is little change in the Mn profile (Figure 6.9a), however, the Fe profile changes significantly thus showing a slight gradient from the centre of the dendrite to the constituent particles. The level of Fe in solution *increases* across the dendrite with the largest value near the constituent particle (i.e. 0.002 at the centre of the dendrite and 0.005 near the constituent particle). For 12 and 24 h at 580 °C, the Mn and Fe profiles are similar; each has a small variation across the dendrite (i.e. ≈ 0.004 at the centre of the dendrite and ≈ 0.003 near the constituent). On the other hand, the volume fraction of dispersoids now shows a region besides the constituent particles where no dispersoids are found. For 12 h at 580 °C, this region is approximately 30 - 40% of the distance across the dendrite. This is qualitatively similar to Figure 5.27, but a larger DFZ is predicted than observed in the experiments.

A significant advantage of the model is that one can extract the information which is difficult or impossible to obtain from the experiments. For example, the Mn and Fe fluxes from one cell to an adjacent cell (note positive flux is diffusion from left to right, negative flux is form right to left) are plotted in Figure 6.10. It is observed in Figure 6.10a that for all the cases, Mn moves from left to right; i.e. from the centre of the dendrite to the constituent particles. For holding at 580 °C (2 h,12 h, and 24 h), the flux is the range of $0.25\text{-}30\times10^{-8}$ m^2/s and reflects the long range diffusion of Mn to the constituent particles.

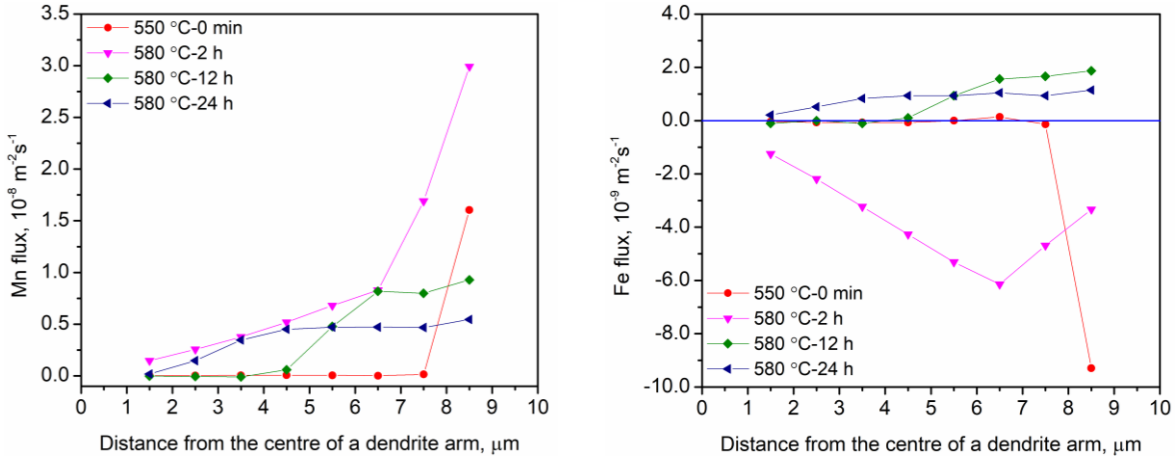

Figure 6-10 (a) Mn flux and (b) Fe flux spatial distribution in the matrix from the centre of a dendrite to the constituent particles

However, the results for the Fe flux put forth a more complicated behaviour which can be seen in Figure 6.10b. The Fe first diffuses from the constituent particles to the matrix as shown for the condition of heating to 550 °C and homogenization at 580 °C for 2 h (i.e. negative values). Then, the Fe flux reverses as the Fe moves back to the constituent particles as seen for the longer soaking time at 580 °C, i.e. soaking for 12 h and 24 h.

The results for the Mn and Fe content and the Mn/Fe in dispersoids are plotted in Figure 6.11a, 6.11b and 6.11c, respectively. It can be observed that the Mn content in the dispersoids decreases slightly as the homogenization progresses (e.g. at the centre of dendrite Mn decreases from 28% to 24%). In contrast, the Fe content in the dispersoids increases from ≈ 1.5 % for 550 °C- 0 min (i.e. during heating) to ≈ 7.5 % for 12 h at 580 °C.

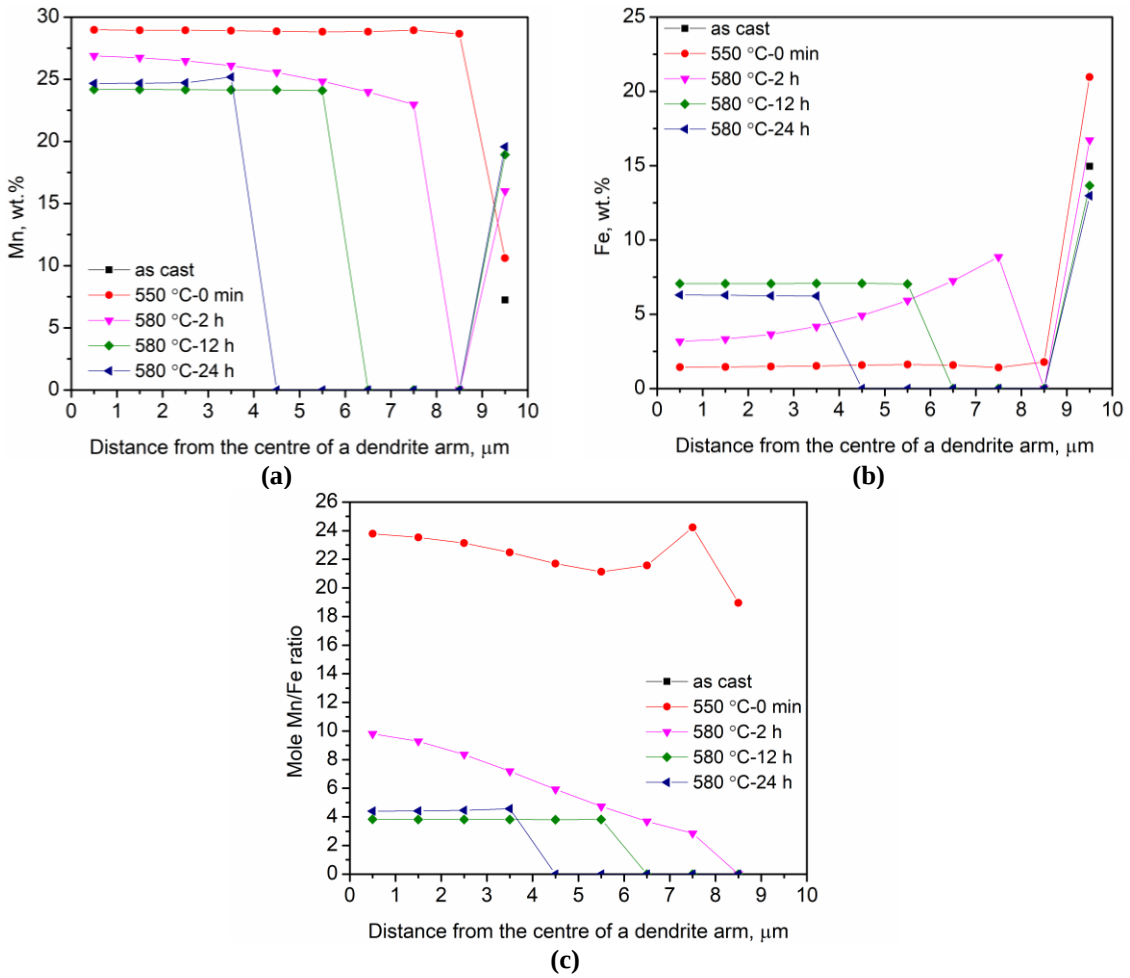

Figure 6-11 Spatial distributions from the homogenization model for (a) Mn in dispersoids, (b) Fe in dispersoids and (c) mole Mn/Fe ratio from the centre of a dendrite to the constituent particles

The evolution of the Mn/Fe ratio provided in Figure 6.11c shows that the Mn/Fe ratio decreases during the process of homogenization. The results Mn/Fe ratio for 550 °C - 0 min is ≈ 20 which compares to a ratio of 16.3 from TEM/EDS. For homogenization of 2 h at 580 °C, the Mn/Fe ratio is 6.6 from the experiments and 6.6 from the model. While for 12 h at 580 °C, the Mn/Fe ratio is 4.6 and 3.8 from the experiments and the model, respectively. In summary, the model calculations are consistent with the hypothesis that Fe first diffuses to the dispersoids from the constituent particles, thereby decreasing the Mn/Fe ratio.

In Figure 6.12, the evolution of the total Mn and Fe in each cell (i.e. solid solution plus dispersoids which is similar to that measured by EPMA) is plotted. As Mn is supersaturated during the solidification process, the highest level of Mn in solid solution was found in the 0.5Mn as-cast sample, as expected. Soaking the as-cast samples at 550 °C promotes the formation of the Mn-containing dispersoids and mass transfer by the diffusion of Mn to the large constituent particles. The depletion of Mn in the matrix at the vicinity of constituent particles results in a local decrease of the Mn content as can be clearly seen for the green curve corresponding to the homogenization at 580 °C for 12 h. Upon holding for 24 h, the simulated Mn profile shows a further loss of Mn to the constituent particles.

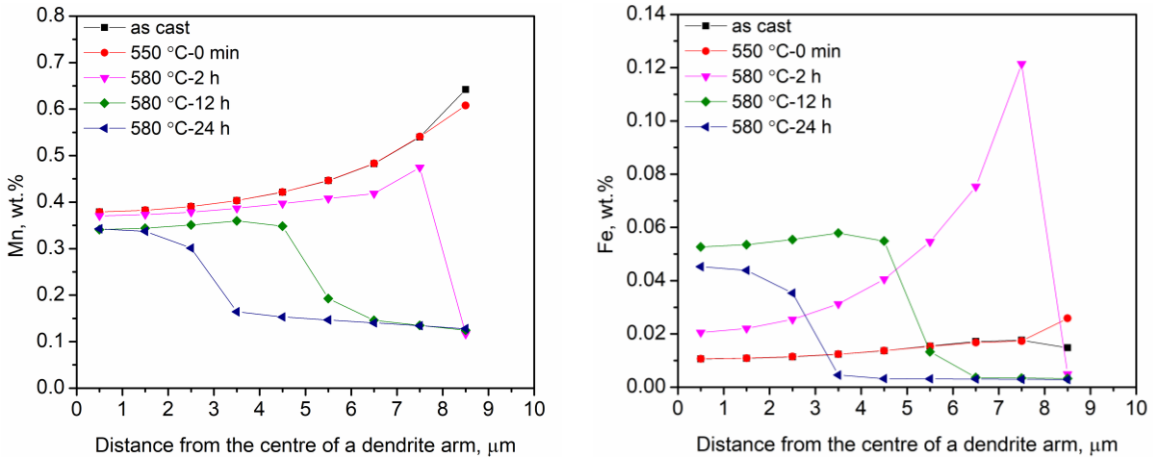

Figure 6-12 (a) Mn spatial distribution and (b) Fe spatial distribution in the matrix from the centre of a dendrite to the constituent particles

In contrast, the Fe profiles behave in a different manner as compared to the Mn profiles. Instead of showing a continuous decrease like Mn, the Fe content first increases i.e. compare the homogenization 580 °C for 2 h with the sample heated to 550 °C. Then the Fe profile decreases with an increase in the soaking time at 580 °C. This indicates the Fe first diffuses from the constituent particles to the matrix and then diffuses back to the constituent particles with Mn.

The rationale could be due to the change of Mn in the solid solution results the increase of Fe in solid solution. A calculation of $\sqrt{Dt}$ for Fe at 580 °C (see Table 2.2 in Section 2.2) soaking for 2 h gives 9.7 µm, which is about the size of half a SDAS in the as-cast microstructure.

Figure 6.13 shows the comparison of the matrix levels of Mn and Fe in 0.5Mn alloy between the EPMA measurements and the model (this is a copy of Figure 5.62, but superimposed with the matrix levels of Mn and Fe calculated from cell #1 to cell #9 from the model). Note, the data in the last column in Figure 6.13 from the model shows the homogenization condition of 24 h soaking at 580 °C. In Figure 6.13a, the mean values and standard deviations from the model for Mn showed similar trend to the experiments with a continuous decrease of the mean values and a first increase and then decrease for the standard deviation. Turning to Fe in Figure 6.13b, the model predictions for the mean and standard deviation also in line with the trend measured from the EPMA. To summarize it, a reasonable agreement is found between the model and the experiments in terms of the evolution for Mn and Fe during homogenization.

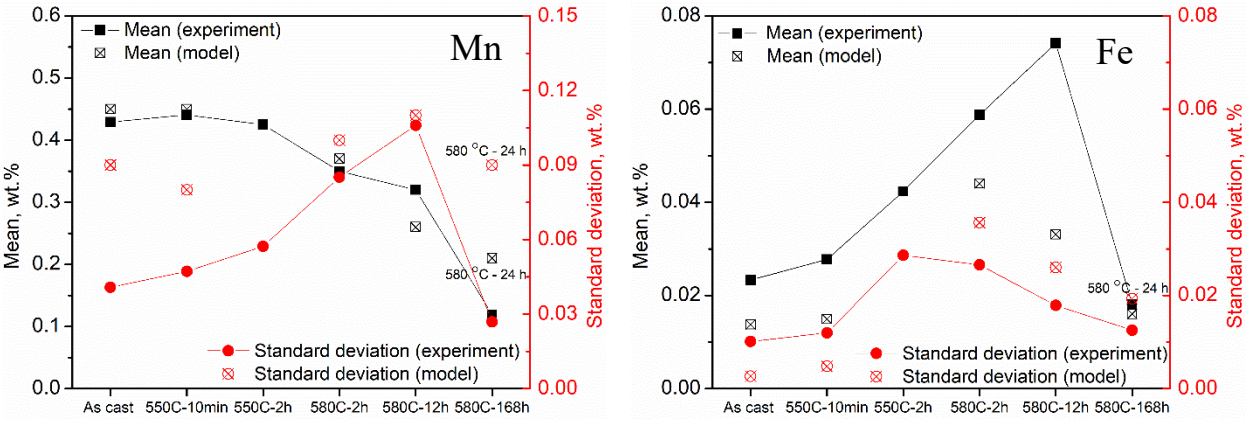

Figure 6-13 Comparison of the mean and standard deviations from the experiment and the model for (a) the Mn matrix levels and (b) the Fe matrix levels in 0.5Mn alloy

6.4 Constitutive model for AA6082 alloys

The steady state flow stresses were measured for a range of temperatures, strain rates as well as homogenization conditions (see Section 5.8). In this section, the steady flow stresses are used to fit and construct a constitutive model. The constitutive model developed by Kocks-Chen [123] is adopted here as a starting point to describe the flow stress behaviour at high temperatures. A modification is made to the original Kocks-Chen model to include an athermal contribution to the flow stress. This term is assumed to have been derived from the contribution of grain boundaries and the large constituent particles, i.e.:

$$\sigma_{flow} = \sigma_{athermal} + \sigma_{thermal} \tag{6-8}$$

where $\sigma_{thermal}$ is described by the Kocks-Chen model. The model is physically based (solute drag on mobile dislocations), as formulated to give the strain rate as a function of temperature and the flow stress, i.e.

$$\dot{\varepsilon} = A\left(\frac{\sigma_{flow} - \sigma_{athermal}}{\mu}\right)^n \frac{\mu b^3}{kT} \exp\left(-\frac{Q_D}{RT}\right) \tag{6-9}$$

where, $\dot{\varepsilon}$ is the strain rate, A is the pre-exponential, n is the stress component (n=3 in the solute drag regime), μ is the temperature dependent shear modulus, k is the Boltzman constant 1.3807×10^{-23} J·K^{-1}, R is the universal gas constant 8.314 J·mol^{-1}·K^{-1} and b is the magnitude of temperature dependent Burgers vector.

In the following, the stress exponent, n, has been assumed to be 3 consistent with the solute drag controlled plasticity. In this work, Mg and Si, in the solid solution are the atoms dragging on the dislocations. As such, Q_D was chosen as 131 kJ/mol which is the activation energy for Mg following Kocks and Chen [123]. The base athermal stress for this case, σ_0, is estimated to be 11.35 MPa by using the results from the 12 compression conditions for the 0Mn

alloy (i.e. the case with no dispersoids). Figure 6.14 illustrates that a good fit is attained using the Kocks-Chen model for the 0Mn base alloy.

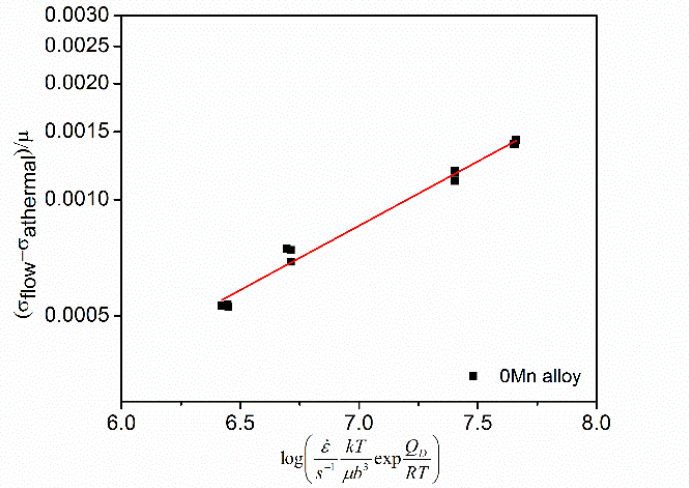

Figure 6-14 Flow stress data plotted using consitituitive model for the 0Mn alloy with 550 °C for 2 h, 580 °C for 2 h and 580 °C for 12 h homogenizations (n=3, Q_D=131 kJ/mol, $\sigma_{athemal}$=11.35 MPa)

Going forward, the athermal component derived from 0Mn alloy will be used as the base athermal for the Mn/Cr bearing alloys as they have similar average grain sizes (Table 5.1) and volume fractions of constituent particles does not vary much (Table 6.1).

It has been proposed that the presence of dispersoids will also contribute to the athermal stress in the form of Orowan stresses, i.e.

$$\sigma_{athermal} = \sigma_0 + \sigma_{Orowan} \tag{6-10}$$

where σ_0 is the athermal stress derived from the 0Mn alloy i.e. σ_0=11.35 MPa. A trial and error approach was adopted to find the Orowan stresses using the Kocks-Chen model with n=3 and Q_D=131 kJ/mol. Figure 6.15 illustrates the fit to the model after obtaining estimating the best value for Orowan stress. In addition, the Orowan stresses for all the alloys are summarized in Table 6.3.

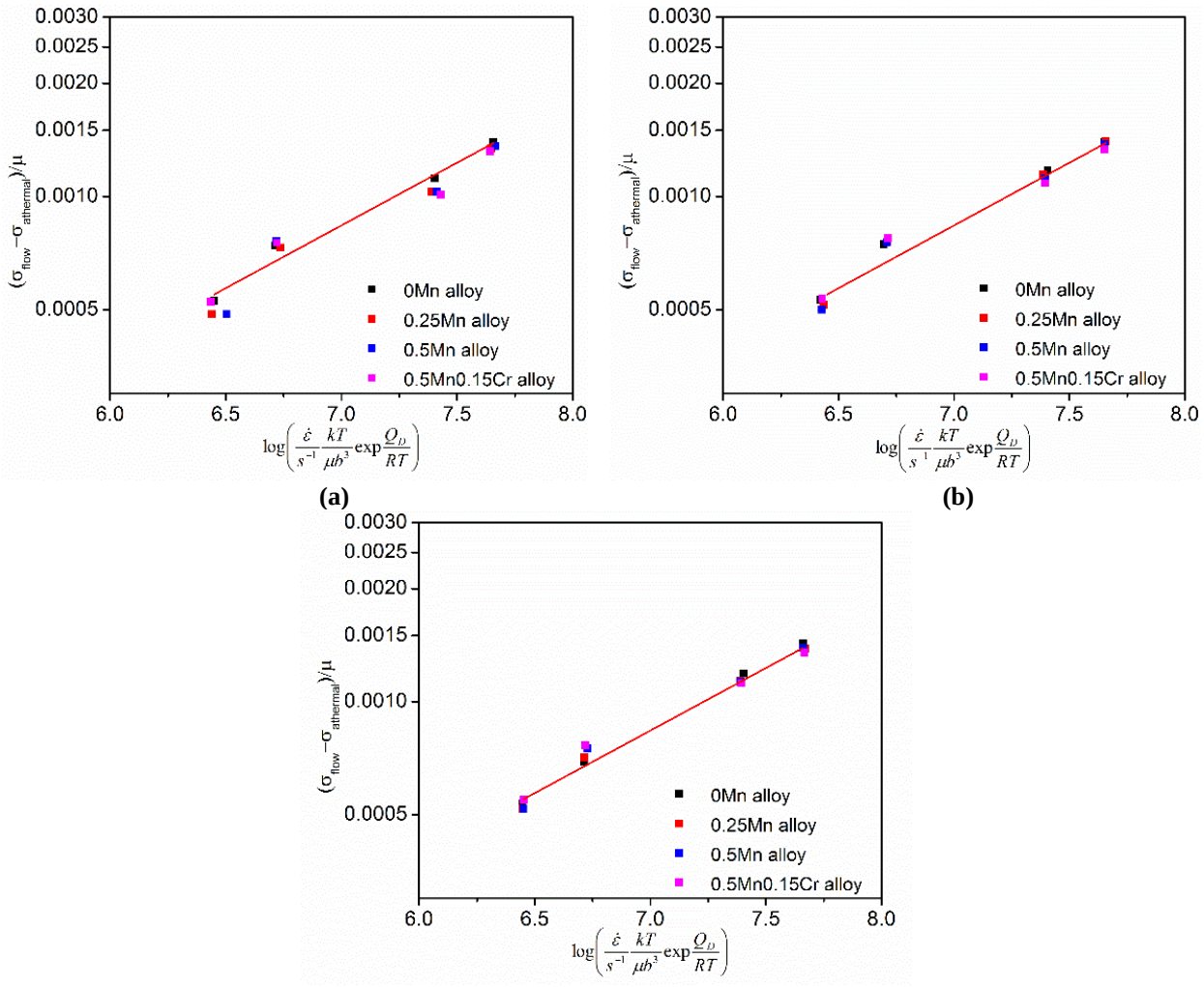

Figure 6-15 Flow stress data plotted using consitituitive model for the four AA6082 alloys with homogenizations (a) 550 °C for 2 h, (b) 580 °C for 2 h and (c) 580 °C for 12 h

Table 6.3 Orowan stresses for all the alloys determined using Kocks-Chen model by trial and error approach

Alloy and homo	σ_0, MPa	σ_{Orowan} , MPa	$\sigma_{athermal}$, MPa
0Mn-550ºC-2h	11.35	-	11.35
0Mn-580ºC-2h	11.35	-	11.35
0Mn-580ºC-12h	11.35	-	11.35
0.25Mn-550ºC-2h	11.35	2.60	13.95
0.25Mn-580ºC-2h	11.35	1.10	12.45
0.25Mn-580ºC-12h	11.35	0.65	11.95
0.5Mn-550ºC-2h	11.35	3.90	15.25
0.5Mn-580ºC-2h	11.35	2.10	13.45
0.5Mn-580ºC-12h	11.35	1.20	12.55
0.5Mn0.15Cr-550ºC-2h	11.35	6.65	17.95
0.5Mn0.15Cr-580ºC-2h	11.35	4.05	15.40
0.5Mn0.15Cr-580ºC-12h	11.35	2.10	13.45

The next step is to build a model in order to describe the Orowan stresses from the dispersoids at high temperatures. The approach adopted here starts with the simple line tension model assuming that the dispersoids are by passed by dislocation, i.e. the Orowan process. The line tension of the dislocation is decribed by Ashby [163] and Kelly [145].

$$T = \frac{\mu b^2}{4\pi}\left(\frac{1+\nu-3\nu\sin^2\theta}{1-\nu}\right)\ln\left(\frac{2r}{b}\right) \tag{6-11}$$

where, r is the dispersoid mean radius, b is the magnitude of the Burgers vector, μ is the shear modulus, θ is the angle between the Burgers vector and the line of the dislocation and ν is Poisson's ratio.

Assuming that the dispersoids are spatially, randomly distributed on the glide plane, the Orowan stress is given by:

$$\tau = 0.76 \cdot \frac{T}{bR} \tag{6-12}$$

where the factor of 0.76 is the correction for a random spatial distribution [164] and R is the critical radius of curvature, i.e. the planar particle spacing L is twice the radius of the curvature. The planar spacing for spherical particles is given as [146].

$$L = \sqrt{\left(\frac{2\pi}{3f}\right)} \cdot r \tag{6-13}$$

where f is the volume fraction of dispersoids. The critical resolved stress on the glide plane was converted to a polycrystal flow stress, σ, as:

$$\sigma = M\tau \tag{6-14}$$

where M is the Taylor factor, here assumed to be 3.06 [165].

Thus, the Orowan stress for a random distributed spherical particle is derived in given by combining equation 6-11 to 6-14.

$$\sigma_{ppt} = 0.76 \cdot \frac{M\mu b\sqrt{3}}{2\pi\sqrt{2\pi}}\left(\frac{1+\nu-3\nu\sin^2\theta}{1-\nu}\right)\frac{\sqrt{f}}{r}\ln\left(\frac{2r}{b}\right) \tag{6-15}$$

With the above equation, the Orowan stress can be calculated based on the volume fraction and average radius of the dispersoids, where θ was π/2. Figure 6.16 shows a plot comparing the results from Equation 6-15 and the experimental results using the results for the mean dispersoid radius presented in Section 5.4 and the volume fractions calculated in Section 6.1 (see Table 6.1). It is clear from this plot that Equation 6-15 over predicts the Orowan stress. The probable reason for this is due to the detachment of dislocation around dispersoids at high temperature which will reduce the magnitude of the Orowan stress. The correction factor for detachment has been reported by Artz and co-workers [147,148] to be in the range of 0.3 to 0.4. Therefore, the Orowan stress should be corrected in order to be used for the current situation of

high temperature deformation. A correction factor of 0.42 was found to give the best fit to the experimental results, i.e. the final flow contribution is:

$$\sigma_{ppt(HT)} = 0.42\sigma_{ppt} = 0.018M\mu b\frac{\sqrt{f}}{r}\ln\left(\frac{2r}{b}\right) \quad (6\text{-}16)$$

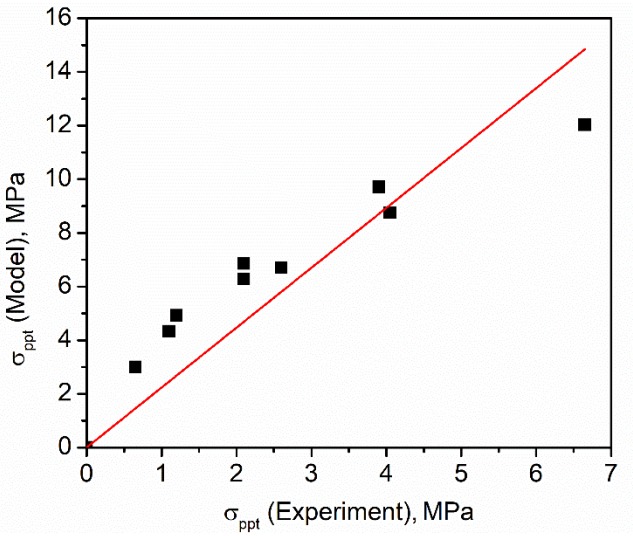

Figure 6-16 The athermal flow stress calculated using the Orowan equation based model plotted against for the experimental flow stress increase compared to the base alloy for 0.25Mn, 0.5Mn and 0.5Mn0.15Cr alloys (The red line is a plot of equation 6-16)

From these considerations, the flow stress consists of three components: i) the base athermal stress (grain boundaries and constituent particles), ii) the athermal stress due to dispersoids and iii) the thermal stress:

$$\sigma_{flow} = \sigma_0 + \sigma_{thermal} + \sigma_{ppt(HT)} \quad (6\text{-}17)$$

The base athermal stress is derived based on the 0Mn alloy and assumed to be independent of chemistry as well as the homogenization scenario. The athermal stress due to the dispersoids is expressed using a modified Orowan equation taking into account dislocation detachment at high temperature. The Orowan stress is chemistry and processing dependent i.e. the dispersoid mean radius and volume fraction are unique for an alloy under a certain

homogenization condition. The thermal stress is described by Kocks-Chen model taking into consideration the viscous dislocation glide in the solute drag regime. Taking a linear addition law, the flow stress is now described by:

$$\sigma_{flow} = \sigma_0 + \mu \cdot \left[\frac{1}{A} \frac{\dot{\varepsilon}}{s^{-1}} \frac{kT}{\mu b^3} \exp\left(\frac{Q_D}{RT}\right) \right]^{\frac{1}{n}} + 0.018 M \mu b \frac{\sqrt{f}}{r} \ln\left(\frac{2r}{b}\right) \qquad (6\text{-}18)$$

where, M is the Taylor factor (M=3.06), f is the disperosid volume fraction, and r is the dispersoid mean radius.

Here, the dispersoid mean size and volume fraction are the primary quantitative characteristics of the initial microstructure, which were given in the Sections 5.4 and 6.1. Figure 6.17 shows the flow stresses calculated using Equation 6-18 versus the experimentally measured values for the four alloys under different homogenization conditions. The error between the model and 95 % of the experimental results are within 5 % error, thereby showing the capacity of the flow stress model to describe the experimental data.

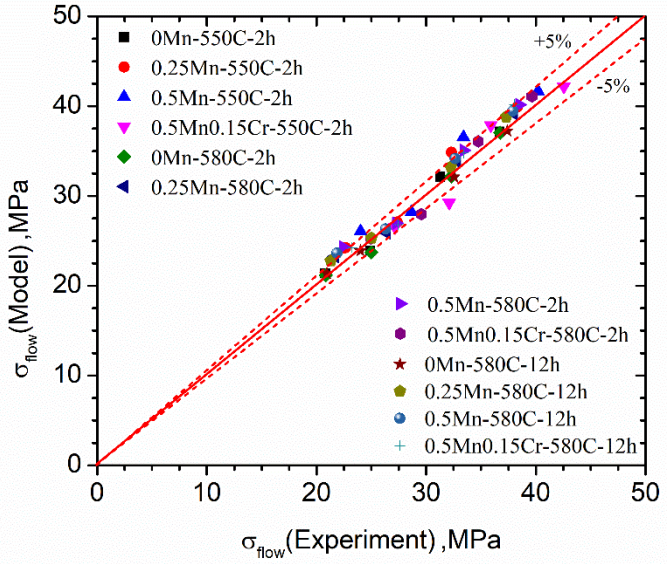

Figure 6-17 The flow stress calculated from the constituive model plotted against for the experimental flow stress for 0Mn, 0.25Mn, 0.5Mn and 0.5Mn0.15Cr alloys from three homogenization conditions

In order to test the predictive capability of the model, a new alloy with 0.75 wt.% Mn was cast and homogenized at 550 °C for 2 h. The mean radius was measured to be 46 nm and the volume fraction of dispersoids was calculated to be 1.29 % using the method described in Section 6.1. High temperature compression tests were performed under 550 ºC at strain rates of 1 and 10 s^{-1} shown in Figure 6.18. From the constitutive model (Equation 6-18), the flow stresses predicted for these deformation conditions were 28.4 MPa and 41.3 MPa, respectively. In comparison, the flow stresses measured from the flow curves (average in the range of true strain 0.4 to 0.6) were 29.4 MPa and 39.8 MPa, i.e. model prediction within 4% of the experiments.

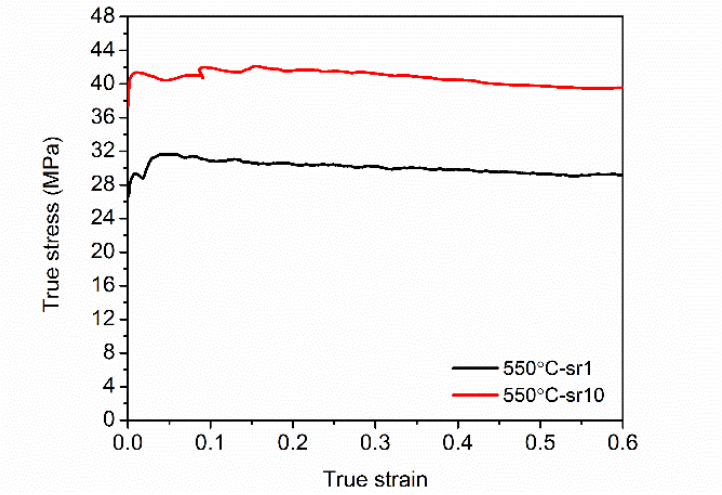

Figure 6-18 The flow stress curves measured at 550 °C at strain rate 1 and 10 s^{-1} for 0.75Mn alloy homogenized at 550 °C for 2 h

6.5 Relation between flow stresses and extrusion forces

The plant scale extrusion trials were conducted at Rio Tinto Aluminum's Arvida Research and Development Centre. The billet temperature was 500 ºC and the extrusion ram speed was varied between 3 mm/s and 10 mm/s using the 0Mn, 0.25Mn, 0.5Mn and 0.5Mn0.15Cr alloys homogenized at 550 ºC for 2 h and 580 ºC for 12 h. Using the Equation 4-2 from the methodology, the mean strain rate for each of the extrusion trials was calculated.

Furthermore, the corresponding flow stresses could be arrived using Equation 6-18 with the extrusion parameters (temperature and mean strain rate) and the dispersoid radius and volume fraction. In the meantime, the extrusion forces are converted on the basis of the extrusion pressure measured at the 800-mm position of the extrusion ram. Figure 6.19 plots the extrusion force versus corresponding flow stress. It can be seen that the extrusion force is proportional to the flow stress with ≈ 90% of the results within ± 5%. Therefore, the current work has the capacity to be used to predict the extrusion forces for a given AA6062 alloy using the microstructure information from this work and together with a constitutive model. In addition, the constitutive model can also be used for extrusion simulation by Finite Element Method (FEM), which is another application of the model.

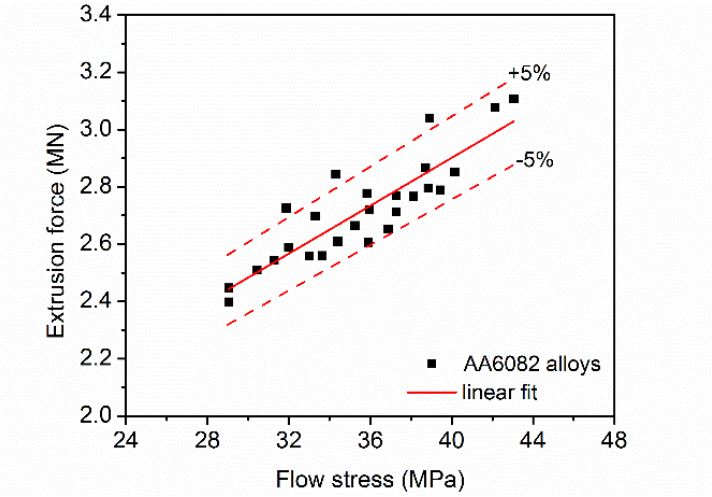

Figure 6-19 The correlation between the flow stresses calculated from the constituive model and the extrusion forces measured during plant scale exrusions for 0Mn, 0.25Mn, 0.5Mn and 0.5Mn0.15Cr alloys with the initial homogenizations 550 °C for 2 h and 580 °C for 12 h

7. Conclusion and Future Work

7.1 Conclusions

The present work investigated the microstructure evolution during the homogenization in AA6082 alloys and its effect on high temperature deformation behaviours. A wide range of characterization tools were employed in order to quantify the microstructure changes (including constituent particle and dispersoids) and a modified homogenization model was tuned to rationalize the microstructure evolution. The quantified microstructure information was integrated into building a constitutive law. The two models from homogenization and high temperature deformation are closely linked and worked in the form of a through process modeling support for the industry. The major findings and contributions have been summarized as follows:

1) The addition of Mn accelerates the transformation of the constituent particles from β-AlFeSi to α-Al(FeMn)Si phase. The β-AlFeSi to α-Al(FeMn)Si phase transformation and dispersoids formation were not observed in the 0Mn alloy, where the transformation happens faster in the 0.5Mn alloy than that in 0.25Mn alloy soaking at 550 °C, indicating that transformation is dependent on the local chemistry dependent.

2) The addition of Mn/Cr favors the dispersoid formation. It is found that dispersoid mean radius is primarily dependent on the homogenization scenarios other than Mn contents up to 0.75 wt.% in AA6082 alloys.

3) Dispersoids are determined to be of either simple cubic (SC) or body centre cubic (BCC) crystal structure in Mn/Cr containing alloys from the homogenization 550 °C for 2 h to 580 °C for 12 h. In both disperoids and constituent particles, Mn/Fe atomic ratio is bulk

chemistry dependent. However, the ratio in dispersoids decreases with higher homogenization temperatures and longer soaking time, which is due to the transportation of the transition metal between dispersoids and constituent particles i.e. Fe firstly diffuses from constituent particle to dispersoids and then diffuses with Mn back to the constituent particles.

4) A new combined experimental method was introduced to indirectly estimate the Mn/Cr containing dispersoid volume fraction and also the volume fraction of the constituent particles, which also depends on the chemistry and decreases with higher homogenization temperature and soaking time. In the meantime, a simple dispersoid volume fraction model was proposed based on Thermo-Calc (TTAL6).

5) A chemistry dependent multi-component homogenization model developed for AA3xxx alloys was adapted to examine the microstructure evolution during homogenization of AA6xxx alloys. A range of characterization techniques were employed to validate the model. It was found that the model could capture the major microstructure feature such as the Mn composition profiles, the dispersoid mean size in the centre of the dendrites, and the evolution of Mn and Fe in solid solution and dispersoids with good agreement found for the 0.5Mn alloy.

6) It was quantified that the chemistry and homogenization effect on the subsequent high temperature deformation behaviour. In 0Mn alloy, the flow stress is not affected by the homogenization scenario above the solvus temperature. In Mn/Cr containing alloys, homogenization condition has a significant effect on the measured flow stress above solvus temperature, which will contribute in the form of athermal Orowan stress. In this high temperature deformation regime, the Orowan component is about 0.42 of that at room temperature because of much easier clime and detachment of dislocations around the dispersoids.

7) A physically-based constitutive model was developed on the basis of the solute drag deformation, but with modifications taking dispersoids as an additional input. The flow stress can be well described by this model in the industrial temperature range, where n equals to 3 and the athermal stress from dispersoids as a function of dispersoid volume fraction and average mean radius.

7.2 Recommended future work

1) The quantification of dispersoid free zone (DFZ) during homogenization in AA6xxx alloys would be useful to further study the effect of chemistry and homogenization scenario on Fe and Mn transportation between dispersoids and the constituent particles

2) There is some room for further improvement of the homogenization model. The inhomogeneity of dispersoids density should also be carefully treated in the model from the centre to the constituent particle. The effect of heating rate on the nucleation of dispersoids should be taken into consideration. The role of the dispersoid shape should be examined as well. The model's predictive power would be improved in the future if these considerations are taken into account. It would also be of great interest to study the effect of changing chemistry (i.e. using different Fe contents) on the behaviour of the model.

3) It would be interesting to conduct high temperature compression tests below the solvus temperature of Mg_2Si. It would be also desirable to quantify the microstructure feature of Mg_2Si right before the high temperature deformation, as the flow stress is dependent on the size and distribution for all types of second phase particles.

4) It would be also interesting to characterize the microstructure evolution during high temperature compression tests, especially comparison of dispersoids before and after high temperature deformation.

References

[1] J. Hirsch, Recent development in aluminium for automotive applications, Trans. Nonferrous Met. Soc. China (English Ed. 24 (2014) 1995–2002.

[2] E.A. Starke, J.T. Staley, J.T. Staleyt, Application of modern aluminum alloys to aircraft, Prog. Aerosp. Sci. 32 (1996) 131–172.

[3] A. Wimmer, B. Schwarz, Production Routes for Impact Extruded Aluminum Parts for the Automotive Industry, Key Eng. Mater. 710 (2016) 222–227.

[4] T. Moons, P. Ratchev, P. De Smet, B. Verlinden, P. Van Houtte, A comparative study of two Al-Mg-Si alloys for automotive applications, Scr. Mater. 35 (1996) 939–945.

[5] W.S. Miller, L. Zhuang, J. Bottema, A.J. Wittebrood, P. De Smet, A. Haszler, A. Vieregge, Recent development in aluminium alloys for the automotive industry, Mater. Sci. Eng. A. 280 (2000) 37–49.

[6] J.P. Immarigeon, R.T. Holt, A.K. Koul, L. Zhao, W. Wallace, J.C. Beddoes, Lightweight materials for aircraft applications, Mater. Charact. 35 (1995) 41–67.

[7] R.C. Dorward, T.R. Pritchett, Advanced aluminium alloys for aircraft and aerospace applications, Mater. Des. 9 (1988) 63–69.

[8] G.S. Cole, A.M. Sherman, Lightweight Materials for Automotive Applications, Mater. Charact. 35 (1995) 3–9.

[9] T. Sheppard, Extrusion of Aluminium Alloys, Springer, 1999.

[10] O. Reiso, Extrusion of AlMgSi alloys, Mater. Forum. 28 (2004) 32–46.

[11] N.C. Parson, H.L. Yiu, The effect of heat-treatment on the microstructure and properties of 6000 series alloy extrusion ingots, in: J. Met., 1989: pp. 713–724.

[12] A.L. Dons, The Alstruc homogenization model for industrial aluminum alloys, J. Light

Met. 1 (2001) 133–149.

[13] H.J. McQueen, O.C. Celliers, Application of hot workability studies to extrusion processing. Part III: Physical and mechanical metallurgy of Al-Mg-Si and Al-Zn-Mg alloys, Can. Metall. Q. 36 (1997) 73–86.

[14] H. Zhu, M.J. Couper, A.K. Dahle, Effect of process variables on Mg-Si particles and extrudability of 6xxx series aluminum extrusions, Jom. 63 (2011) 66–71.

[15] E.D. Sweet, S.K. Caraher, N. V Danilova, X. Zhang, C.A. Limited, Effects of Extrusion Parameters on Coarse Grain Surface Layer in 6xxx Series Extrusions, Proc. 8th Alum. Ext. Sem. Inum Extrus. Technol. Semin. (2004) 115–126.

[16] M. Schikorra, L. Donati, L. Tomesani, A.E. Tekkaya, Microstructure analysis of aluminum extrusion: Prediction of microstructure on AA6060 alloy, J. Mater. Process. Technol. 201 (2008) 156–162.

[17] S. Karabay, M. Zeren, M. Yilmaz, Investigation extrusion ratio effect on mechanical behaviour of extruded alloy AA6063, J. Mater. Process. Technol. 135 (2003) 101–108.

[18] J.S. Ajiboye, M.B. Adeyemi, Effects of extrusion variables on temperature distribution in axisymmetric extrusion process, Int. J. Mech. Sci. 50 (2008) 522–537.

[19] S. Tomovic-Petrovic, O. Jensrud, Extrusion of silicon-rich AlMgSi alloys, J. Mater. Process. Technol. 212 (2012) 1437–1442.

[20] T. Ishikawa, H. Sano, Y. Yoshida, N. Yukawa, J. Sakamoto, Y. Tozawa, Effect of extrusion conditions on metal flow and microstructures of aluminum alloys, CIRP Ann. - Manuf. Technol. 55 (2006) 275–278.

[21] A.J. Bryant, D.J. Field, E.P. Butler, Al-Mg-Si extrusion alloy and method, US Patent, 1989.

[22] N. Parson, A. Maltais, C. Jowett, The influence of die bearing geometry on surface recrystallisation of 6xxx extrusions, ET. 12 (2012) 15–18.

[23] N.C. Parson, J.D. Hankin, K.P. Hicklin, Al-Mg-Si alloy with good extrusion properties, (2002).

[24] A.J. Bryant, D.J. Field, E.P. Butler, Al-Mg-Si extrusion alloy and method, EU Patent, 1987.

[25] S. Zajac, B. Hutchinson, A. Johansson, L.-O. Gullman, Microstructure control and extrudability of Al-Mg-Si alloys microalloyed with manganese, Mater. Sci. Technol. 10 (1994) 323–333.

[26] H. Tanihata, T. Sugawara, K. Matsuda, S. Ikeno, Effect of casting and homogenizing treatment conditions on the formation of Al-Fe-Si intermetallic compounds in 6063 Al-Mg-Si alloys, J. Mater. Sci. 34 (1999) 1205–1210.

[27] N.C.W. Kuijpers, F.J. Vermolen, C. Vuik, P.T.G. Koenis, K.E. Nilsen, S. Van Der Zwaag, The dependence of the β-AlFeSi to α-Al (FeMn) Si transformation kinetics in Al–Mg–Si alloys on the alloying elements, Mater. Sci. Eng. A. 394 (2005) 9–19.

[28] J.E. Yoo, A. Shan, I.G. Moon, S.J. Maeng, A study on composition and crystal structure of dispersoids in AlMgSi alloys, J. Mater. Sci. 34 (1999) 2679–2683.

[29] L. Lodgaard, N. Ryum, Distribution of Mn and Cr containing dispersoids in Al-Mg-Si-alloys, Mater. Sci. Forum. 331–337 II (2000) 945–950.

[30] L. Lodgaard, N. Ryum, Precipitation of chromium containing dispersoids in Al–Mg–Si alloys, Mater. Sci. Technol. 16 (2000) 599–604.

[31] K. Strobel, E. Sweet, M. a. Easton, J.F. Nie, M. Couper, Dispersoid Phases in 6xxx Series Aluminium Alloys, Mater. Sci. Forum. 654–656 (2010) 926–929.

[32] P. Priya, M.J.M. Krane, D.R. Johnson, A Numerical and Experimental Study of Homogenization of Al-Si-Mg Alloys, Light Met. 2014. (2014) 423–428.

[33] P. Priya, D.R. Johnson, M.J.M. Krane, Numerical Study of Microstructural Evolution During Homogenization of Al-Si-Mg-Fe-Mn Alloys, Metall. Mater. Trans. A Phys. Metall. Mater. Sci. 47 (2016) 4625–4639.

[34] J.M. Dowling, J.W. Martin, The influence of Mn additions on the deformation behaviour of an AlMgSi alloy, Acta Metall. 24 (1976) 1147–1153.

[35] Y. Birol, Homogenization of en AW 6005A Alloy for Improved Extrudability, Metall. Mater. Trans. A Phys. Metall. Mater. Sci. 44 (2013) 504–511.

[36] S.J. Andersen, Quantification of the Mg_2Si β ″and β′ phases in AlMgSi alloys by transmission electron microscopy, Metall. Mater. Trans. A. 26 (1995) 1931–1937.

[37] C.D. Marioara, S.J. Andersen, J. Jansen, H.W. Zandbergen, The influence of temperature and storage time at RT on nucleation of the β ″phase in a 6082 Al–Mg–Si alloy, Acta Mater. 51 (2003) 789–796.

[38] J.H. Chen, E. Costan, M.A. Van Huis, Q. Xu, H.W. Zandbergen, Atomic pillar-based nanoprecipitates strengthen AlMgSi alloys, Science (80-.). 312 (2006) 416–419.

[39] Rio Tinto, Confidential document, (2011).

[40] L. Sweet, S.M. Zhu, S.X. Gao, J.A. Taylor, M.A. Easton, The effect of iron content on the iron-containing intermetallic phases in a cast 6060 aluminum alloy, Metall. Mater. Trans. A Phys. Metall. Mater. Sci. 42 (2011) 1737–1749.

[41] S. Kumar, P.S. Grant, K.A.Q. O'Reilly, Evolution of Fe Bearing Intermetallics During DC Casting and Homogenization of an Al-Mg-Si Al Alloy, Metall. Mater. Trans. A. 47 (2016) 3000–3014.

[42] J.A. Blind, J.W. Martin, The effect of dispersoids on the ductile fracture toughness of AlMgSi alloys, Mater. Sci. Eng. 57 (1983) 49–54.

[43] J.E. Hatch, Aluminium Properties and Physical Metallurgy, Handb. Alum. Vol. 1 - Phys. Metall. Process. (1984).

[44] R.P. Garrett, J. Lin, T.A. Dean, An investigation of the effects of solution heat treatment on mechanical properties for AA 6xxx alloys: Experimentation and modelling, Int. J. Plast. 21 (2005) 1640–1657.

[45] S. Karabay, M. Yilmaz, M. Zeren, Investigation of extrusion ratio effect on mechanical behaviour of extruded alloy AA-6101 from the billets homogenised-rapid quenched and as-cast conditions, J. Mater. Process. Technol. 160 (2005) 138–147.

[46] G. Mrówka-Nowotnik, Influence of chemical composition variation and heat treatment on microstructure and mechanical properties of 6xxx alloys, Arch. Mater. Sci. Eng. 46 (2010) 6–13.

[47] M. Kolar, K.O. Pedersen, S. Gulbrandsen-Dahl, K. Marthinsen, Combined effect of deformation and artificial aging on mechanical properties of Al-Mg-Si Alloy, Trans. Nonferrous Met. Soc. China (English Ed. 22 (2012) 1824–1830.

[48] K.C. Prince, J.W. Martin, The effects of dispersoids upon the micromechanisms of crack propagation in AlMgSi alloys, Acta Metall. 27 (1979) 1401–1408.

[49] D.H. Lee, J.H. Park, S.W. Nam, Enhancement of mechanical properties of Al-Mg-Si alloys by means of manganese dispersoids, Mater. Sci. Technol. 15 (1999) 450–455.

[50] F.J. Humphreys, M. Hatherly, Recrystallization and Related Annealing Phenomena, Elsevier, 2012.

[51] R. Hu, T. Ogura, H. Tezuka, T. Sato, Q. Liu, Dispersoid formation and recrystallization

behavior in an Al-Mg-Si-Mn alloy, J. Mater. Sci. Technol. 26 (2010) 237–243.

[52] A.R. Eivani, H. Ahmed, J. Zhou, J. Duszczyk, Correlation between electrical resistivity, particle dissolution, precipitation of dispersoids, and recrystallization behavior of AA7020 aluminum alloy, Metall. Mater. Trans. A Phys. Metall. Mater. Sci. 40 (2009) 2435–2446.

[53] J. Røyset, M.M. Rødland, U. Tundal, O. Reiso, Effect of Alloy Chemistry and Process Parameters on the Extrudability and Recrystallization Resistance of 6082 Aluminum Alloy, Hydro Alum. R&D Technol. (2008) 91–99.

[54] R. Jeniski, B. Thanaboonsombut, T.H. Sanders, The effect of iron and manganese on the recrystallization behavior of hotrolled and solution-heat-treated aluminum alloy 6013, Metall. Mater. Trans. A. 27 (1996) 19–27.

[55] Q. Zhao, B. Holmedal, Y. Li, Influence of dispersoids on microstructure evolution and work hardening of aluminium alloys during tension and cold rolling, Philos. Mag. 93 (2013) 2995–3011.

[56] J.D. Evensen, N. Ryum, J.D. Embury, The intergranular fracture of Al- Mg-Si alloys, Mater. Sci. Eng. 18 (1975) 221–229.

[57] A.L. Dons, O. Lohne, Quench Sensitivity of Almgsi-Alloys Containing Mn or Cr, MRS Proc. 21 (1983).

[58] N.C.W. Kuijpers, W.H. Kool, P.T.G. Koenis, K.E. Nilsen, I. Todd, S. Van der Zwaag, Assessment of different techniques for quantification of α-Al (FeMn) Si and β-AlFeSi intermetallics in AA 6xxx alloys, Mater. Charact. 49 (2002) 409–420.

[59] M.J. Couper, B. Rinderer, J.Y. Yao, Characterisation of AlFeSi intermetallics in 6000 series aluminium alloy extrusions, Mater. Sci. Forum. 519–521 (2006) 303–308.

[60] N.C.W. Kuijpers, J. Tirel, D.N. Hanlon, S. Van Der Zwaag, Characterization of the α-Al

(FeMn) Si nuclei on β-AlFeSi intermetallics by laser scanning confocal microscopy, J. Mater. Sci. Lett. 22 (2003) 1385–1387.

[61] J.H. Li, A. Wimmer, G. Dehm, P. Schumacher, Intermetallic phase selection during homogenization for AA6082 alloy, Philos. Mag. 94 (2014) 830–846.

[62] M.H. Mulazimoglu, a. Zaluska, J.E. Gruzleski, F. Paray, Electron microscope study of Al-Fe-Si intermetallics in 6201 aluminum alloy, Metall. Mater. Trans. A. 27 (1996) 929–936.

[63] M. Qian, J.A. Taylor, J.Y. Yao, M.J. Couper, D.H. StJohn, A practical method for identifying intermetallic phase particles in aluminium alloys by electron probe microanalysis, J. Light Met. 1 (2001) 187–193.

[64] F.H. Samuel, A.M. Samuel, H.W. Doty, S. Valtierra, Decomposition of Fe-intermetallics in Sr-modified cast 6XXX type aluminum alloys for automotive skin, Metall. Mater. Trans. A. 32 (2001) 2061–2075.

[65] L. Lodgaard, N. Ryum, Precipitation of dispersoids containing Mn and/or Cr in Al–Mg–Si alloys, Doctoral thesis, NTNU, 2000.

[66] M. Cai, J.D. Robson, G.W. Lorimer, Simulation and control of dispersoids and dispersoid-free zones during homogenizing an AlMgSi alloy, Scr. Mater. 57 (2007) 603–606.

[67] Y.J. Li, A.M.F. Muggerud, A. Olsen, T. Furu, Precipitation of partially coherent α-Al (Mn, Fe) Si dispersoids and their strengthening effect in AA 3003 alloy, Acta Mater. 60 (2012) 1004–1014.

[68] A.M.F. Muggerud, Transmission electron microscopy studies of dispersoids and constituent phases in Al-Mn-Fe-Si alloys, Doctoral thesis, NTNU, 2014.

[69] M. Dehmas, E. Aeby-Gautier, P. Archambault, M. Serrière, Interaction between eutectic

intermetallic particles and dispersoids in the 3003 aluminum alloy during homogenization treatments, Metall. Mater. Trans. A Phys. Metall. Mater. Sci. 44 (2013) 1059–1073.

[70] L. Lodgaard, N. Ryum, Precipitation of dispersoids containing Mn and/or Cr in Al–Mg–Si alloys, Mater. Sci. Eng. A. 283 (2000) 144–152.

[71] Y.J. Li, L. Arnberg, Quantitative study on the precipitation behavior of dispersoids in DC-cast AA3003 alloy during heating and homogenization, Acta Mater. 51 (2003) 3415–3428.

[72] P. Olafsson, R. Sandstrom, Å. Karlsson, Comparison of experimental, calculated and observed values for electrical and thermal conductivity of aluminium alloys, J. Mater. Sci. 32 (1997) 4383–4390.

[73] E. Louis, C.G. Cordovilla, Resistivity of aluminium binary alloys in annealed condition, Met. Sci. 14 (1980) 597–600.

[74] L.F. Mondolfo, Aluminum alloys: Structure and properties, London-Bost. Butter Worths Co Ltd. (1976).

[75] F. Kutner, G. Lang, The inflnence of alloying constituents and heatment on the resistivity, Aluminium. 5 (1976) 322.

[76] F.R. Fickett, Aluminum—1. A review of resistive mechanisms in aluminum, Cryogenics (Guildf). 11 (1971) 349–367.

[77] R. Nadella, D.G. Eskin, Q. Du, L. Katgerman, Macrosegregation in direct-chill casting of aluminium alloys, Prog. Mater. Sci. 53 (2008) 421–480.

[78] S.N. Samaras, G.N. Haidemenopoulos, Modelling of microsegregation and homogenization of 6061 extrudable Al-alloy, J. Mater. Process. Technol. 193 (2007) 63–73.

[79] C. Hsu, K.A.Q. O'Reilly, B. Cantor, R. Hamerton, Non-equilibrium reactions in 6xxx series Al alloys, Mater. Sci. Eng. A. 304–306 (2001) 119–124.

[80] G. Sha, K. O'Reilly, B. Cantor, J. Worth, R. Hamerton, Growth related metastable phase selection in a 6xxx series wrought Al alloy, Mater. Sci. Eng. A. 304–306 (2001) 612–616.

[81] M. Cooper, K. Robinson, The crystal structure of the ternary alloy α (AlMnSi), Acta Crystallogr. 20 (1966) 614–617.

[82] M. Cooper, The crystal structure of the ternary alloy α(AlFeSi), Acta Crystallogr. 23 (1967) 1106–1107.

[83] N.C.W. Kuijpers, J. Tirel, D.N. Hanlon, S. Van der Zwaag, Quantification of the evolution of the 3D intermetallic structure in a 6005A aluminium alloy during a homogenisation treatment, Mater. Charact. 48 (2002) 379–392.

[84] S. Onurlu, A. Tekin, Effect of heat treatment on the insoluble intermetallic phases present in an AA 6063 alloy, J. Mater. Sci. 29 (1994) 1652–1655.

[85] N.C.W. Kuijpers, Kinetics of the β-AlFeSi to α-Al (FeMn) Si transformation in Al-Mg-Si alloys, TU Delft, Delft University of Technology, 2004.

[86] Y. Du, Y.A. Chang, B. Huang, W. Gong, Z. Jin, H. Xu, Z. Yuan, Y. Liu, Y. He, F.Y. Xie, Diffusion coefficients of some solutes in fcc and liquid Al: Critical evaluation and correlation, Mater. Sci. Eng. A. 363 (2003) 140–151.

[87] G.N. Haidemenopoulos, H. Kamoutsi, A.D. Zervaki, Simulation of the transformation of iron intermetallics during homogenization of 6xxx series extrudable aluminum alloys, J. Mater. Process. Technol. 212 (2012) 2255–2260.

[88] S. Fujikawa, K. Hirano, Diffusion of 28 Mg in aluminum, Mater. Sci. Eng. 27 (1977) 25–33.

[89] G. Moreau, J.A. Cornet, D. Calais, Acceleration de la diffusion chimique sous irradiation dans le systeme aluminium-magnesium, J. Nucl. Mater. 38 (1971) 197–202.

[90] S.J. Rothman, N.L. Peterson, L.J. Nowicki, L.C. Robinson, Tracer diffusion of magnesium in aluminum single crystals, Phys. Status Solidi. 63 (1974).

[91] S. Fujikawa, K. Hirano, Y. Fukushima, Diffusion of silicon in aluminum, Metall. Trans. A. 9 (1978) 1811–1815.

[92] D. Bergner, E. Cyrener, Diffusion of Foreign Elements in Aluminum Solid Solutions. Pt. 2. Diffusion of Zinc and Manganese in Aluminum, Neue Hutte. 18 (1973) 9–12.

[93] G.M. Hood, R.J. Schultz, The diffusion of manganese in aluminium, Philos. Mag. 23 (1971) 1479–1489.

[94] Y. Minamino, T. Yamane, S. Nakagawa, H. Araki, K. Hirao, Atomic size effect in interdiffusion of aluminum alloys, J. Japan Inst. Light Met. 37 (1987) 72–82.

[95] S. Fujikawa, K.-I. Hirano, Impurity diffusion of manganese in aluminum, in: Mater. Sci. Forum, Trans Tech Publ, 1987: pp. 539–546.

[96] G. Rummel, T. Zumkley, M. Eggersmann, K. Freitag, H. Mehrer, Diffusion of implanted 3d-transition elements in aluminium. I: Temperature dependence, Zeitschrift Für Met. 86 (1995) 122–130.

[97] N.L. Peterson, S.J. Rothman, Impurity diffusion in aluminum, Phys. Rev. B. 1 (1970) 3264.

[98] W.G. Fricke Jr, K.R. Van Horn, Aluminium, (1967).

[99] W.B. Alexander, L.M. Slifkin, Diffusion of solutes in aluminum and dilute aluminum alloys, Phys. Rev. B. 1 (1970) 3274.

[100] N.C.W. Kuijpers, F.J. Vermolen, K. Vuik, S. Van Der Zwaag, A Model of the b-AlFeSi to

a-Al(FeMn) Si Transformation in Al- Mg-Si Alloys, Mater. Trans. 44 (2003) 1448–1456.

[101] D. Lassance, M. Schmitz, F. Delannay, T. Pardoen, Linking microstructure and high temperature ductility in aluminium alloys AA6xxx, 15th Eur. Conf. Fract. Adv. Fract. Mech. Life Saf. Assess. (2004).

[102] M. V. Kral, A crystallographic identification of intermetallic phases in Al-Si alloys, Mater. Lett. 59 (2005) 2271–2276.

[103] R.A. Jeniski, Effects of Cr addition on the microstructure and mechanical behavior of 6061-T6 continuously cast and rolled redraw rod, Mater. Sci. Eng. A. 237 (1997) 52–64.

[104] H. Hirasawa, Precipitation process of Al-Mn and Al-Cr supersaturated solid solution in presence of age hardening phases, Scr. Metall. 9 (1975) 955–958.

[105] K. Sugiyama, N. Kaji, K. Hiraga, Re-refinement of α-(AlMnSi), Acta Crystallogr. Sect. C Cryst. Struct. Commun. 54 (1998) 445–447.

[106] B. Rinderer, The Metallurgy of Homogenisation, Mater. Sci. Forum. 693 (2011) 264–275.

[107] M.S. Remøe, K. Marthinsen, I. Westermann, K. Pedersen, J. Røyset, O. Reiso, The Effect of Heating Rate on the Density and Spatial Distribution of Dispersoids during Homogenisation of 6xxx Aluminium Alloys, Mater. Sci. Forum. 877 (2016) 322–327.

[108] Y. Birol, The effect of homogenization practice on the microstructure of AA6063 billets, J. Mater. Process. Technol. 148 (2004) 250–258.

[109] P.A. Rometsch, S.C. Wang, A. Harriss, P.J. Gregson, M.J. Starink, The effect of homogenizing on the quench sensitivity of 6082, in: Mater. Sci. Forum, 2002: pp. 655–660.

[110] A.M.F. Muggerud, Y. Li, R. Holmestad, Composition and orientation relationships of constituent particles in 3xxx aluminum alloys, Philos. Mag. 94 (2014) 556–568.

[111] C. Flament, J. Ribis, J. Garnier, T. Vandenberghe, J. Henry, A. Deschamps, Electron irradiation-enhanced core/shell organization of Al(Cr, Fe, Mn)Si dispersoids in Al–Mg–Si alloys, Philos. Mag. 95 (2015) 906–917.

[112] E. Anselmino, A. Miroux, S. Van Der Zwaag, Dispersoid quantification and size distribution in hot and cold processed AA3103, Mater. Charact. 52 (2004) 289–300.

[113] B. Liscic, H.M. Tensi, L.C.F. Canale, G.E. Totten, Quenching theory and technology, CRC Press, 2010.

[114] R.H. Davies, A.T. Dinsdale, J.A. Gisby, J.A.J. Robinson, S.M. Martin, MTDATA - Thermodynamic and phase equilibrium software from the national physical laboratory, Calphad Comput. Coupling Phase Diagrams Thermochem. 26 (2002) 229–271.

[115] Q. Du, W.J. Poole, M.A. Wells, N.C. Parson, Microstructure evolution during homogenization of Al-Mn-Fe-Si alloys: Modeling and experimental results, Acta Mater. 61 (2013) 4961–4973.

[116] A. Jacot, M. Rappaz, A pseudo-front tracking technique for the modelling of solidification microstructures in multi-component alloys, Acta Mater. 50 (2002) 1909–1926.

[117] Q. Du, W.J. Poole, M.A. Wells, A mathematical model coupled to CALPHAD to predict precipitation kinetics for multicomponent aluminum alloys, Acta Mater. 60 (2012) 3830–3839.

[118] P. Priya, D.R. Johnson, M.J.M. Krane, Modeling phase transformations kinetics during homogenization of 7xxx series aluminum alloys, Comput. Mater. Sci. 138 (2017) 277–287.

[119] T. Sheppard, a. Jackson, Constitutive equations for use in prediction of flow stress during extrusion of aluminium alloys, Mater. Sci. Technol. 13 (1997) 203–209.

[120] C. Zener, J.H. Hollomon, Effect of strain rate upon plastic flow of steel, J. Appl. Phys. 15 (1944) 22–32.

[121] C.M. Sellars, W.J. McTegart, On the mechanism of hot deformation, Acta Metall. 14 (1966) 1136–1138.

[122] T. Sheppard, D.S. Wright, Determination of flow stress: part1 constitutive equation for aluminum alloys at elevated temperatures, Met. Technol. (1979) 215–223.

[123] U.F. Kocks, S.R. Chen, Constitutive laws for deformation and dynamic recrystallization in cubic metals, Aspects of High Temperature Deformation and Fracture in Crystalline Materials, (JIMIS-7), Y. Hosoi, H. Yoshinaga, H. Oikawa, and K. Maruyama, eds. (Jap. Inst. Metals), 1993.

[124] U.F. Kocks, Solute drag as an upper bound to high-temperature strength, Scr. Mater. 39 (1998) 431–436.

[125] S.R. Chen, M.G. Stout, U.F. Kocks, S.R. MacEwen, A.J. Beaudoin, Constitutive modeling of a 5182 aluminum as a function of strain rate and temperature, Hot Deformation of Aluminum Alloys II: Proceedings of the Second Symposium Held at the 1998 TMS Fall Meeting, 1998.

[126] A.D. Kubiak, Effect of homogenization on high temperature deformation behaviour of AA3xxx aluminum alloys, Masters thesis, The University of British Columbia, 2009.

[127] G. Yuanyuan, Microstructure evolution during extrusion of AA3xxx aluminum alloys, Masters thesis, The University of British Columbia, 2011.

[128] L.M. Grajales, Effect of high temperature extrusion conditions on the microstructure of AA3003 aluminum alloy, Masters thesis, The University of British Columbia, 2013.

[129] E. Nes, Modelling of work hardening and stress saturation in FCC metals, Prog. Mater.

Sci. 41 (1997) 129–193.

[130] K. Marthinsen, E. Nes, A general model for metal plasticity, Mater. Sci. Eng. A. 234–236 (1997) 1095–1098.

[131] E. Nes, T. Pettersen, K. Marthinsen, On the mechanisms of work hardening and flow-stress saturation, Scr. Mater. 43 (2000) 55–62.

[132] K. Marthinsen, E. Nes, Modelling strain hardening and steady state deformation of Al–Mg alloys, Mater. Sci. Technol. 17 (2001) 376–388.

[133] E. Nes, K. Marthinsen, B. Rønning, Modelling the evolution in microstructure and properties during processing of aluminium alloys, J. Mater. Process. 117 (2001) 333–340.

[134] M. Goerdeler, G. Gottstein, A microstructural work hardening model based on three internal state variables, Mater. Sci. Eng. A. 309 (2001) 377–381.

[135] F. Roters, D. Raabe, G. Gottstein, Work hardening in heterogeneous alloys—a microstructural approach based on three internal state variables, Acta Mater. 48 (2000) 4181–4189.

[136] B. Rønning, K. Nord-Varhaug, T. Furu, E. Nes, The Effect of Chemical Composition and Microstructure on the Flow Stress during Hot Deformation of Aluminium Alloys, Mater. Sci. Forum. 331–337 (2000) 571–576.

[137] J. Van De Langkruis, W.H. Kool, C.M. Sellars, M.R. Van Der Winden, S. Van Der Zwaag, The effect of β, β′ and β ″precipitates in a homogenised AA6063 alloy on the hot deformability and the peak hardness, Mater. Sci. Eng. A. 299 (2001) 105–115.

[138] N. Anjabin, A.K. Taheri, H.S. Kim, Constitutive Modeling of Hot Deformation Behavior of the AA6063 Alloy with Different Precipitates, Metall. Mater. Trans. A. 44 (2013) 5853–5860.

[139] E. Nes, K. Marthinsen, Modeling the Evolution in Microstructure and Properties During Plastic Deformation of F.C.C. - Metals and Alloys – an Approach Towards a Unified Model, Mater. Sci. Eng. A. 322 (2002) 176–193.

[140] C. Poletti, T. Wójcik, C. Sommitsch, Hot deformation of AA6082 containing fine intermetallic particles, Metall. Mater. Trans. A. 44 (2013) 1577–1586.

[141] P.S. Follansbee, U.F. Kocks, A constitutive description of copper based on the use of the mechanical threshold stress as an internal state variable, Acta Mater. 36 (1998) 81–93.

[142] S. Spigarelli, E. Evangelista, H.J. McQueen, Study of hot workability of a heat treated AA6082 aluminum alloy, Scr. Mater. 49 (2003) 179–183.

[143] N. Hansen, Dispersion strengthening of aluminium-aluminium-oxide products, Acta Metall. 18 (1970) 137–145.

[144] E.W. Hart, Theory of Disperpersion Hardening In Metals, Acta Metall. 20 (1972) 275–289.

[145] A. Kelly, Strengthening methods in crystals, Elsevier Publishing Company, 1971.

[146] A.J. Ardell, Precipitation hardening, Metall. Trans. A. 16A (1985) 2131–2165.

[147] E. Arzt, M.F. Ashby, Threshold stresses in materials containing dispersed particles, Scr. Metall. 16 (1982) 1285–1290.

[148] E. Arzt, D.S. Wilkinson, Threshold stresses for dislocation climb over hard particles The effect of an attractive interaction, Acta Metall. 34 (1986) 1893–1898.

[149] Y.J. Li, L. Arnberg, Evolution of eutectic intermetallic particles in DC-cast AA3003 alloy during heating and homogenization, Mater. Sci. Eng. A. A347 (2003) 130–135.

[150] H. Demers, N. Poirier-Demers, A.R. Couture, D. Joly, M. Guilmain, N. de Jonge, D. Drouin, Three-dimensional electron microscopy simulation with the CASINO Monte

Carlo software, Scanning. 33 (2011) 135–146.

[151] J.L. Pouchou, F. Pichoir, Procedure for improved quantitative microanalysis. in: Microbeam Analysis (JT Armstrong, editor), (1985) 104–106.

[152] B. Roebuck, J.D. Lord, R.K. Varma, Guidelines for the Measurement of Flow Stress in Hot Axisymmetric Compression Tests, National Physical Laboratory. Great Britain, Centre for Materials Measurement and Technology, 1997.

[153] N.C. Parson, Personal communication, 2012.

[154] K.B.S. Couto, S.R. Claves, W.H. Van Geertruyden, W.Z. Misiolek, M. Goncalves, Effects of homogenisation treatment on microstructure and hot ductility of aluminium alloy 6063, Mater. Sci. Technol. 21 (2005) 263–268.

[155] A.M.F. Muggerud, J.C. Walmsley, R. Holmestad, Y. Li, Combining HAADF STEM tomography and electron diffraction for studies of α-Al(Fe,Mn)Si dispersoids in 3xxx aluminium alloys, Philos. Mag. 95 (2015) 744–758.

[156] Z.H. Lai, C.H. Li, The disorder-order transformation of Al(Mn,Fe)Si phase, Scr. Metall. Mater. 29 (1993) 895–900.

[157] P. Donnadieu, G. Lapasset, T.H. Sanders, Manganese-induced ordering in the α-(Al-Mn-Fe-Si) approximant phase, Philos. Mag. Lett. 70 (1994) 319–326.

[158] Z.J. Lok, Microchemistry in aluminium sheet production, TU Delft, Delft University of Technology, 2005.

[159] M.N. Gungor, A statistically significant experimental technique for investigating microsegregation in cast alloys, Metall. Trans. A. 20 (1989) 2529–2533.

[160] M. Ganesan, D. Dye, P.D. Lee, A technique for characterizing microsegregation in multicomponent alloys and its application to single-crystal superalloy castings, Metall.

Mater. Trans. A. 36 (2005) 2191–2204.

[161] D.A. Porter, K.E. Easterling, Phase Transformations in Metals and Alloys, CRC Press, 1992.

[162] C.A. Gandin, A. Jacot, Modeling of precipitate-free zone formed upon homogenization in a multi-component alloy, Acta Mater. 55 (2007) 2539–2553.

[163] M.F. Ashby, Results and consequences of a reclaculation of the Frank-Read and the Orowan stress, Acta Mater. 14 (1966) 679–681.

[164] A. de Vaucorbeil, On the origin of cluster strengthening in aluminum alloys, Doctoral thesis, The University of British Columbia, 2015.

[165] H. Mecking, U.F. Kocks, Kinetics of flow and strain-hardening, Acta Metall. 29 (1981) 1865–1875.

Appendix

Table A1. Average composition from EPMA on about 200 points in 0Mn alloy, wt.%

	Mg	Si	Mn	Fe
Nominal composition	0.71	0.91	0.003	0.2
As-cast	0.62	1.08	0.006	0.39
550C-10min	0.72	0.91	0.006	0.31
550C-2h	0.74	0.91	0.005	0.30
550C-4h	0.73	0.93	0.005	0.33
550C-24h	0.68	0.81	0.005	0.15
580C-168h	0.74	0.90	0.004	0.22
Mean	0.71	0.92	0.005	0.28

Table A2. Average composition from EPMA on about 200 points in 0.25Mn alloy, wt.%

	Mg	Si	Mn	Fe
Nominal composition	0.71	0.95	0.25	0.21
As-cast	0.68	1.00	0.28	0.34
550C-10min	0.75	0.92	0.30	0.35
550C-2h	0.77	0.84	0.23	0.17
580C-2h	0.68	0.94	0.27	0.24
580C-12h	0.73	0.92	0.31	0.29
580C-168h	0.77	0.91	0.28	0.24
Mean	0.73	0.92	0.28	0.27

Table A3. Average composition from EPMA on about 200 points in 0.5Mn alloy, wt.%

	Mg	Si	Mn	Fe
Nominal composition	0.71	1.03	0.5	0.21
As-cast	0.61	0.75	0.51	0.19
550C-10min	0.76	0.90	0.50	0.16
550C-2h	0.76	0.97	0.60	0.32
580C-2h	0.73	0.93	0.55	0.23
580C-12h	0.77	0.95	0.47	0.16
580C-168h	0.76	0.95	0.51	0.22
Mean	0.73	0.91	0.52	0.22

Table A4. Average composition from EPMA on about 200 points in 0.5Mn0.15Cr alloy, wt.%

	Mg	Si	Cr	Mn	Fe
Nominal composition	0.70	1.04	0.15	0.49	0.23
As-cast	0.70	1.03	0.16	0.52	0.24
550C-10min	0.69	0.90	0.18	0.58	0.27
550C-2h	0.74	0.94	0.17	0.55	0.28
580C-2h	0.71	1.03	0.17	0.60	0.38
580C-12h	0.70	0.93	0.16	0.52	0.23
580C-168h	0.75	0.96	0.15	0.44	0.19
Mean	0.71	0.97	0.16	0.53	0.27

Table A5. Mn, Cr and Fe in solid solution calculated from Thermo-Calc (TTAL6) in wt.%

	Mn (550°C)	Fe (550°C)	Cr (550°C)	Mn (580°C)	Fe (580°C)	Cr (580°C)
0Mn alloy	-	0.0066	-	-	0.012	-
0.25Mn alloy	0.045	0.0029	-	0.066	0.0057	-
0.5Mn alloy	0.090	0.0011	-	0.13	0.0023	-
0.5Mn0.15Cr alloy	0.068	0.0013	0.037	0.10	0.0024	0.052

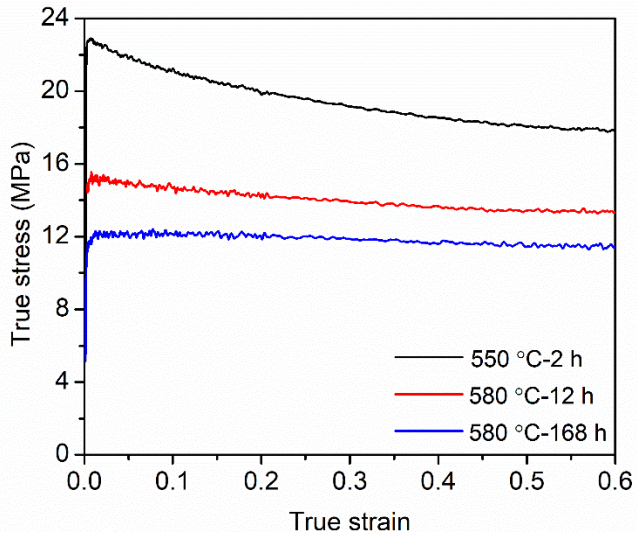

Figure A1. Flow stress curves of the 0.5Mn0.15Cr alloy with three homogenization treatments and then deformed at 550 °C with strain rate 0.01 s^{-1}.